



**HAL**  
open science

# Locale structure around heteroatoms in alumino- and borosilicates for catalysis

Mounesha Nagendrachar Garaga

► **To cite this version:**

Mounesha Nagendrachar Garaga. Locale structure around heteroatoms in alumino- and borosilicates for catalysis. Other. Université d'Orléans, 2013. English. NNT : 2013ORLE2013 . tel-00919192

**HAL Id: tel-00919192**

**<https://theses.hal.science/tel-00919192>**

Submitted on 16 Dec 2013

**HAL** is a multi-disciplinary open access archive for the deposit and dissemination of scientific research documents, whether they are published or not. The documents may come from teaching and research institutions in France or abroad, or from public or private research centers.

L'archive ouverte pluridisciplinaire **HAL**, est destinée au dépôt et à la diffusion de documents scientifiques de niveau recherche, publiés ou non, émanant des établissements d'enseignement et de recherche français ou étrangers, des laboratoires publics ou privés.

**THÈSE PRÉSENTÉE A L'UNIVERSITÉ D'ORLÉANS  
POUR OBTENIR LE GRADE DE  
DOCTEUR DE L'UNIVERSITÉ D'ORLÉANS**

PAR

**Mounesha N. GARAGA**

ÉCOLE DOCTORALE EMSTU

Discipline: Chimie

Soutenue le Mardi 28 Mai 2013

**Structure locale autour d'Hétéroatomes  
dans des Matériaux Alumino- et  
Borosilicates pour la Catalyse**

**THÈSE dirigée par:**

**M. Dominique MASSIOT**  
**M. Sylvian CADARS**

Directeur de Recherches, CEMHTI Orléans, UPR3079-CNRS  
Chargé de Recherches, CEMHTI Orléans, UPR3079-CNRS

**RAPPORTEURS:**

**M. Darren BROUWER**  
**M<sup>me</sup> Corine GERARDIN**

Associate professor, Redeemer University College, Canada  
Directeur de Recherches ICGM, CNRS-UMR5253, Montpellier

**JURY:**

**M. Darren BROUWER**  
**M<sup>me</sup> Corine GERARDIN**

Associate professor, Redeemer University College, Canada  
Directeur de Recherche, Institut Charles Gerhardt (ICG) -  
UMR5253 - CNRS / Ecole Nationale Supérieure de Chimie de  
Montpellier / Université Montpellier 1 / Université Montpellier 2

**M<sup>me</sup> Florence BABONNEAU**

Directeur de Recherche, Laboratoire de Chimie de la Matière  
Condensée (LCMCP) – UMR 7574 – CNRS / UPMC / Chimie-  
ParisTech / Collège de France

**M. Fabrice LEROUX**

Directeur de Recherche, Institut de Chimie de Clermont-Ferrand,  
UMR6296-CNRS / Université Blaise Pascal

**M. Dominique MASSIOT**

Directeur de Recherche, CEMHTI Orléans – UPR3079 – CNRS;  
*Directeur de thèse*

**M. Sylvian CADARS**

Chargé de Recherche, CEMHTI Orléans – UPR3079 – CNRS;  
*Co-Encadrant de thèse*

*To my beloved parents for their love,  
endless support and encouragement...*

## Abstract

Much attention has been paid to the structural investigation of aluminosilicates and borosilicates because of their paramount importance in catalysis, ion exchange and gas separation. Unfortunately, there still lacks fundamental understanding of the molecular origins of the catalytic activity of these materials. This is mainly because of the incorporation of Al and B heteroatoms into the silicate framework deteriorates the molecular order by generating local compositional (Al/Si or B/Si substitutions) and geometric disorder (variation in bonding geometry) to extents that are particularly difficult to establish. Since diffraction methods are often limited to powder analyses in these systems due to generally small crystal sizes, solid-state nuclear magnetic resonance (NMR) can play a key complimentary role to solve this long-standing issue. Surfactant-directed layered silicate materials with short-range molecular order are particularly interesting model systems to study the local structures around Al or B hetero atoms that confer their acidity and catalytic activity to porous silicates. The synthesis and local molecular structures in the pure-silicate form of these layered silicates are indeed well understood, and they have simple and well-resolved  $^{29}\text{Si}$  NMR signatures specific of each individual framework crystallographic sites. Various amounts of Al and B atoms, including some small enough to yield well-isolated defects have been incorporated into the framework of such layered silicates. This is demonstrated by novel multidimensional NMR measurements that unambiguously establish spatial proximities (via  $J$ - and dipolar-couplings) between  $^{29}\text{Si}$  and  $^{11}\text{B}$  or  $^{27}\text{Al}$  nuclei, and hence make it possible to distinguish incorporated hetero atoms from extra-framework sites or side products. Such advanced NMR studies revealing the local structure are further extended to atomic substitution of Al and B heteroatoms in other materials, for example, in montmorillonites and calcium borosilicate phase, respectively. Interestingly, the contemporary studies, in addition, provide the nature of cation ordering. On the other hand, NMR parameters are calculated by Density Functional Theory (DFT) calculations, a computational method, which, in combination to solid-state NMR spectroscopy, offers many opportunities to explore, evaluate, and validate various structural models that capture the local structure distortions and/or rearrangements of the frameworks that results from the presence of various (Si/B, Si/Al, or even Al/Mg in clays) atomic substitutions. Despite the absence of long-range crystallinity of these systems, our work sets the bases of the understanding, to a level of detail never before attained, of the chemical composition, local framework distortions, and sometimes more profound re-arrangements of the local structures around hetero-atom environments in silicates. The remarkable differences between the consequences of the incorporation of a given heteroatom into two distinct frameworks of otherwise strongly related materials, or of the incorporation of Al or B in a given material provide a unique opportunity to identify the properties that drive the incorporation.

## Acknowledgements

*This doctoral thesis would have not been possible without the support of many individuals who contributed in one way or other throughout my thesis. First and foremost, I am very thankful to my thesis supervisor Dr. Dominique Massiot for providing me an opportunity to work and learn solid-state NMR in an esteemed research group. I am grateful and indebted for his support, encouragement and the guidance throughout this thesis.*

*I would like to express the deepest appreciation to my co-supervisor Dr. Sylvian Cadars for his guidance, immense knowledge and patience during discussions and in reading my thesis. I have been extremely lucky to have such a person who encouraged, cared and responded to all my queries and questions so promptly. His support and motivation throughout this thesis was unimaginable and invaluable.*

*I wish to express my sincere thanks to Dr. Zalfa Nour who was the backbone of DFT calculations used in this thesis. I would also like to thank Dr. Michael Deschamps for his support and valuable discussion during my studies.*

*I owe my heartiest gratitude to Dr. Catherine Bessada, Dr. Frank Fayon, Dr. Valérie Montouillout, Dr. Pierre Florian, Dr. Mallory Gobet, Dr. Aydar Rakhmatullin, Dr. Vincent Saroukhanian, Mr. Thomas Poumeyrol and all other colleagues of CEMHTI who directly or indirectly helped me in many ways during my tenure in the laboratory.*

*I would like to take this opportunity to record my sincere thanks to Dr. Emmanuel Véron and Dr. Mathieu Allix for their help and guidance in the “New Calcium Borosilicate” project. I would like to extend my thanks to Dr. Régis Guégan for his support and great work in ‘Montmorillonites’.*

*My stay at University of California, Santa Barbara over a period of 5 months to learn synthesis of porous silicate materials under the guidance of Prof. Bradley F. Chmelka was one of the best phases of this thesis that I will cherish for my lifetime. It would not have been possible unless the support and discussion with him and his research group, Mr. Ming-Feng Hsieh, Dr. Robert J. Messinger and Mr. Matthew T. Aronson, other colleagues and friends. I owe a lot of credit for their contribution towards this thesis and for providing the samples.*

*I would like to express my gratitude to all the jury members for accepting to be a member of the evaluating committee and for reviewing my manuscript.*

*I would like to sincerely acknowledge the financial support provided by CNRS through ANR-NSF grant and their invaluable contribution to the scientific research in France.*

*I would like to extend my sincere thanks to Prof. N. Suryaprakash, Prof. K.V. Ramanathan, Dr. S. Ragothama, Prof. H.S. Atreya and all members of NMR research centre, IISs, India for the guidance and support during my trainee period at SIF, IISc Bangalore.*

*Last but not the least I am very grateful to my parents, family members and friends for their everlasting love, encouragement and support throughout my career.*

# Table of Contents

<b>Abstract</b>	<b>2</b>
<b>Acknowledgements</b>	<b>3</b>
<b>Introduction</b>	<b>7</b>
<b>Chapter A. A literature study of porous and lamellar silicate materials</b>	<b>13</b>
A.1 Introduction	13
A.2 Porous silicate materials and solid-state NMR	14
A.3 Layered silicate composites	26
A.4 Heteroatoms in porous silicate materials and their importance	36
A.5 Conclusions	43
<b>Chapter B. Methods and Materials</b>	<b>45</b>
B.1 Introduction	45
B.2. Measuring or Exploiting solid-state NMR interactions	45
B.3 Other Experimental and Computational Methods	67
B.4 Synthesis of materials	75
B.5 Conclusions	77
<b>Chapter C. Structural study at the local level around Al heteroatoms in surfactant-directed layered silicates</b>	<b>79</b>
C.1 Introduction	79
C.2 Placement of Al heteroatoms in surfactant-directed layered silicates	80
C.3 Distribution of Al heteroatoms in C <sub>16</sub> H <sub>33</sub> Me <sub>2</sub> EtN <sup>+</sup> -directed layered silicate	82
C.4 Distribution of Al heteroatoms in C <sub>16</sub> H <sub>33</sub> Me <sub>3</sub> N <sup>+</sup> -directed layered silicate	94
C.5 Conclusions	109

<b>Chapter D. Probing the local structure upon boron incorporation in non-crystalline layered silicates</b>	<b>111</b>
D.1 Introduction	111
D.2 Incorporation of boron heteroatoms into surfactant-directed layered silicates	112
D.3 Boron heteroatoms distribution in C <sub>16</sub> H <sub>33</sub> Me <sub>3</sub> N <sup>+</sup> -directed layered borosilicate	118
D.4 Distribution of B heteroatoms in C <sub>16</sub> H <sub>33</sub> Me <sub>2</sub> EtN <sup>+</sup> -directed layered silicates	129
D.5 Conclusions	142
<b>Chapter E. Extension to the study of atomic substitution in other materials</b>	<b>143</b>
E.1 Introduction	143
E.2 Exploiting the local structure of 2:1 clay minerals: Montmorillonites	144
E.3 Solid-state NMR study of the new calcium borosilicate phase	156
E.4 Conclusions	168
<b>Conclusions and Perspectives</b>	<b>169</b>
<b>References</b>	<b>175</b>
<b>Appendices</b>	<b>187</b>
Experimental section	188
Symbols and Abbreviations	195

## Introduction

The impact of advancements in science and technology are being greatly inter-linked with our daily life routines. For instance, several revolutionary inventions have been made in modern-material chemistry including the synthesis, characterization, and broad usage of biomaterials, catalysts, semiconductors, ceramics, polymers and plastics etc. Deep understanding of materials at the molecular level is a key aspect in many industrial applications in order to cope with increasing demands of modern materials. In the case of hybrid materials, a combined knowledge of the molecular-level structure, dynamics, and properties of both the organic and inorganic components and of their mutual interactions is often crucial for the general understanding, and ultimately the control of the macroscopic physico-chemical properties. It is in part the ability of such structural insights to help controlling the materials properties that have made Material Science so popular.

Silicate ( $\text{SiO}_2$ )-based materials are among the class of materials that have attracted the most attention in the area of material science for many decades. The main reasons for this are their relatively easy and versatile synthesis, little or no toxicity in most of the cases, availability of cheap precursors and their ability to condense and form chains, sheets, rings and framework structures etc. It has been speculated that 30% of all minerals are silicate-based materials. These mainly include as important and well-known classes as zeolites, mesoporous silica, and clays etc.

The incorporation of heteroatoms into the structural frameworks of silicate-based materials has brought many interesting structural properties, the most industrially-important of which being probably catalytic activity. Potential applications in catalysis are strongly correlated with the strength of framework acidity, which generally results from a negative charge that is very often induced by the substitution of tetravalent Si atoms by trivalent heteroatoms. The most widespread trivalent heteroatom or active center is by far the aluminum Al, but many others such as B, Ga,  $\text{Fe}^{(\text{III})}$  have been extensively used. Their numbers, locations, and the local structure around them are among the key elements that govern their acidity and, in combination with their morphologies, the overall activity of silicate-based solid catalysts. The presence of heteroatoms in otherwise molecularly-ordered silicate framework modifies the local structure by generating local structural disorder. In particular, the variation in size of heteroatoms in contrast to the Si atoms is expected to alter the local bonding geometry, and the charge deficit associated with the substitution of  $\text{Si}^{4+}$  by  $\text{M}^{3+}$  cations must be compensated somehow by the presence nearby of positively-charged species ( $\text{H}^+$ , metal-earth or alkaline-earth cation, organic cation) which will also contribute to modifying the local structural environment. These environments correspond to local

## *Introduction*

disruptions of the periodicity and symmetry of the three-dimensional structure, and contribute to a local compositional and geometric disorder.

From a materials point of view, controlling the location of heteroatoms and if possible the structure around them in these kinds of materials is crucial, because this opens the way to a control of both the reactivity and the selectivity of the active sites. A simple illustration of this is that the activity of acid sites in molecularly disordered (e.g. mesoporous) silicas is often considerably lower than for the same active sites incorporated in molecularly ordered silicates such as zeolites.<sup>1</sup> Obtaining and establishing the distributions of heteroatoms in silicates and their impact on the materials properties, however, has been and continues to be a major challenge for materials science from both a synthesis and characterization point of view. The preferential incorporation of a given type of heteroatom into a single crystallographic site, in particular, appears to be an extremely difficult task. The available results reveal a near-random<sup>2</sup> or poorly preferential<sup>3</sup> incorporation of heteroatoms. When large enough single crystals are available, reliable refinements of the site occupancies can be obtained for some heteroatoms,<sup>2,4</sup> but substitutions levels remain particularly challenging to establish for others, such as for Al,<sup>5</sup> particularly when single-crystal diffraction is impractical and/or the degree of crystallinity is insufficient. Powder X-ray diffraction primarily probes the long-range molecular order, and may easily be used to obtain unit cell parameters, space groups, and in many cases even accurate atomic positions for the ideal long-range structure, but is not or poorly sensitive to local structures lacking long-range 3D crystallinity. Thus, and despite a huge amount of work, many uncertainties remain regarding the comprehensive understanding of heteroatom distributions and their local structural implications in otherwise molecular-ordered silicate frameworks. Because it can be used to probe ordered as well as disordered environments at the local level, solid-state Nuclear Magnetic Resonance (NMR) spectroscopy has in principle the capacity to play an important role to solve this difficult question, and this is one of the main objectives of the present thesis.

Several reasons account for the difficulties in achieving preferential incorporation of heteroatoms. The key structural and synthetic parameters that are likely to drive the preferential incorporation onto one site rather than another are still unknown. Furthermore, the available characterization techniques often fail to demonstrate the site specificity. These two problems are of course strongly embedded, because the easiest way to understand which factors drive such a preferential incorporation is to compare situations where it worked (albeit accidentally using a trial-and-error approach) with situations where it did not. For this, however, one has to be able to tell the difference experimentally. While the local structural point of view of solid-state NMR could be used in principle to characterize heteroatom distributions and the local structure around them in silicate materials, limited spectral resolution, combined with multiple potential

## Introduction

local environments that may be generated by Si/M substitutions, so far often led to somewhat ambiguous answers to this difficult question.<sup>6-7</sup>

Fundamentally, the ideal 3-dimensional (3D) structure of almost all (with to our knowledge only one exception<sup>8</sup>) zeolites is composed of only tetrahedral (T) sites connected via bridging O atoms to four other tetrahedral sites, which primarily leads in solid-state <sup>29</sup>Si NMR to sites designated as  $Q^4$  environments. These Si environments are all chemically similar, differing essentially by the Si-O-Si bond angle connecting the TO<sub>4</sub> tetrahedra, and presumably have very similar molecular-level properties, as would have the heteroatoms potentially substituting them. In this context, there appears to be no strong driving force for a preferential incorporation of heteroatoms at certain crystallographic sites in most of these systems. This could be the reason why there has never been (again, to our knowledge) a report of a zeolite existing in a high-silica form, and where Al or other heteroatoms could be incorporated selectively in certain framework sites. In rare cases where a heteroatom occupies a specific zeolite framework site (e.g. three-coordinated B borosilicate zeolite MCM-70<sup>9</sup>, Al in scolecite<sup>5</sup>), this site is occupied exclusively by the heteroatom, while the other sites have a pure Si composition.

In this context, one of the objectives of our work is to find an alternative route for controlling heteroatom distributions in zeolites. A possible way would be to insert the heteroatoms into molecularly-ordered silicate materials containing chemically distinguishable Si environments in their frameworks to promote a clear energy difference between situations where the heteroatom sits into one site or another. This might be the case for layered silicates,<sup>10-11</sup> whose frameworks, while still molecularly-ordered, are less condensed than zeolites and contain ordered tetrahedral sites connected via bridging oxygen atoms to only three other tetrahedral sites, their fourth O atom being a non-bridging oxygen. Si atoms occupying such sites give rise in <sup>29</sup>Si NMR to environments designated as  $Q^3$  <sup>29</sup>Si moieties, and have a signature that is generally well separated from that of their  $Q^4$  sites (which are similar to those contained in zeolites). While  $Q^3$  environments often exist in zeolites, they correspond in that case to defects within their framework or at their surface, but for the remarkable exception of zeolite SSZ-74, which has been shown to contain ordered Si vacancies in its framework.<sup>8</sup> In layered silicates, in contrast to all other zeolites,  $Q^3$  environments are molecularly ordered, and part of the crystal structure.<sup>12-17</sup> Furthermore, these layered silicates form an important class of zeolite precursors. This was repeatedly demonstrated by several research groups, who showed how layered silicates may transform, by condensation of the  $Q^3$  sites of adjacent silicate layers upon calcination, to form a zeolite with a 3D structure strongly related to the 2D structure of the precursor.<sup>13-14,18-19</sup>

## Introduction

Among the large number of existing layered silicates, surfactant-directed layered silicates are excellent model systems to test our ability to control of heteroatom locations, and are potential new precursors of 3D zeolites. This class of self-assembled materials with high degrees of both short-range molecular and long-range mesoscopic order now includes the particularly-interesting nano-structured zeolites designed by Ryoo and co-workers.<sup>20-21</sup> The first historical examples of surfactant-directed layered silicates,<sup>22-23</sup> however, have far simpler (and thinner) structures and also, as a result, far simpler solid-state <sup>29</sup>Si NMR signatures. Their structures (in their pure siliceous form) have recently been solved despite their lack of long-range 3D crystallinity.<sup>24</sup> Tuning the hydrophobicity of the surfactant alkylammonium headgroups (-NMe<sub>3</sub><sup>+</sup> or -NMe<sub>2</sub>Et<sup>+</sup> for example) is used to direct different framework structures, leading to different numbers (none higher than five) of distinct tetrahedral sites. Here we study the incorporation of Al and B heteroatoms into strongly related C<sub>16</sub>H<sub>33</sub>Me<sub>3</sub>N<sup>+</sup>- and C<sub>16</sub>H<sub>33</sub>Me<sub>2</sub>EtN<sup>+</sup>- directed layered silicates.

The main objective of my thesis project has been to shed light on the complicated local compositional and geometric disorder that results from the incorporation of Al and B heteroatoms into the frameworks. This deterioration of the local structural order adds to the intrinsic lack of long-range molecular order that considerably limits the relevance of diffraction methods to investigate the structure of these materials. We thus used experimental solid-state NMR and modeling at the density functional level of theory (DFT) as the main techniques, although in combination with important other techniques, such as XRD and ICP analyzes, to establish the distribution of Al and B atoms in the otherwise molecularly-ordered silicate frameworks and probe the local structure around them.

Before addressing the specific question of the Al and B heteroatoms into the layered silicate materials which are the main focus of this work, one first needs to place these materials into the general context of the mesoporous and lamellar silicates. This will be done in the first chapter of this manuscript (Chapter A), with the objective to establish the influence of heteroatoms on the local structure in other porous materials. Several examples for the substitution of B and Al heteroatoms, in particular, are discussed to determine their incorporation behavior. Previous studies of the synthesis and structure of the surfactant-directed layered silicates that were used during my thesis as model systems to study heteroatom distributions in silicates will be reviewed in this chapter.

Having described the issues regarding porous and lamellar silicate materials that are most relevant to our main objectives on the basis of the existing work, it will be possible to identify the need for experimental and modeling that have the capacity to address the problematic of the distributions and local structures around Al and B heteroatoms incorporated into silicate frameworks. The techniques used

## *Introduction*

in this work will thus be described in Chapter B, with an emphasis on their strengths and limitations in the particular context of the materials which we studied here. The extent of order and disorder associated with the presence of heteroatoms in the frameworks can be measured primarily by solid-state NMR. Hence, this chapter briefly explains the basic theory of solid-state NMR and technical aspects of different experiments that we used in the context of this thesis. It also reviews the basic theory of other complimentary techniques such as DFT calculations, XRD and ICP analysis. Syntheses of materials are of course the primary step to introduce novel materials or to modify the existing materials. Hence, hydrothermal synthesis protocols used to prepare the studied materials are briefly discussed in this chapter.

As our main objective is to investigate the local structures around heteroatoms in the silicate framework, Al and B heteroatoms are incorporated into two strongly related surfactant-directed layered silicate materials. The distributions of Al and B heteroatoms and their consequences on the local structures of these materials are discussed in chapter C and chapter D, respectively. The Si environments in the vicinity of heteroatoms are probed on the basis of spatial proximities and connectivities between Al or B heteroatoms and Si atoms, and of their interactions with the organic-surfactants. NMR parameters are calculated by DFT to support the NMR results. The radically different behaviors upon Al or B incorporation into the different framework structures of two otherwise strongly-related silicates provide key elements to ultimately understand, how heteroatom distributions can be controlled.

Similar methodologies can be extended to the study of heteroatoms substitution in other materials, where they illustrate the large range of distinct scenarios that the presence of heteroatoms can create order or disorder at the local level. This aspect will be discussed in chapter E, through the examples of aluminosilicate clay minerals (montmorillonites) and new calcium borosilicate phase ( $\text{CaB}_{2/3}\text{Si}_{1/3}\text{O}_{8/3}$ ). The important questions that we wished to address in these systems are: (1) the repartition of  $\text{Al}^{3+}/\text{Mg}^{2+}$  and  $\text{Si}^{4+}/\text{Al}^{3+}$  species in the octahedral and tetrahedral layers of montmorillonites, which govern the overall layer charge and thus the cation exchange capacity, (2) the local structure in a new calcium borosilicate phase, whose average long-range structure determined by diffraction pattern appears to contain some extent of compositional and/or geometrical disorder. Again, solid-state NMR imparts the detailed insights of chemical composition and the local structure of these inorganic materials.



---

# **Chapter A**

## ***A literature study of porous and lamellar silicate materials***

---

### **A.1 Introduction**

Porous silicate materials cover many applications in several scientific disciplines. They have played a key role in remarkable innovations in the field of ceramics, glasses, elastomers, metals, polymers, zeolites etc. The use of such materials has then been extended to a vast range of industrial areas, including organic and inorganic chemistry, health, life science... etc. A crucial aspect of porous silicate materials is the understanding of the possible chemical interactions between organic and inorganic entities and their consequences on the molecular structure and properties. This includes not only the physico-chemical properties of individual organic and inorganic phases, but also of the interfaces between them. In particular, the nature (electrostatic, Van-der-Waals or hydrogen bonding) and relative extents of their mutual interactions in the organic-inorganic mesophase are crucial in directing the framework topology. The inorganic part is usually responsible for the materials mechanical strength and (for example) their rheological (deformation of materials under applied force) properties. These systems exist in different forms such as fibers, whiskers, particles, mesh, lamellar materials etc. Their pore size varies from few micrometers to several nanometers, and the availability of such pores depends on the ability to remove the organic template or structure-directing agent without deteriorating the materials architecture. The applicability of such hybrid porous materials depends on several factors, (i) the particle and pore sizes (ii) the degree of flexibility related to the mechanical strength, and importantly (iii) the nature of framework atoms. The last point implies that the framework atoms can control the applicability of hybrid materials through their individual molecular-level properties. Hence the study of these hybrid materials is crucial in material chemistry. In this regards, the present chapter is divided into three main sections.

**Section A.2** focuses on the basic concepts and classifications of hybrid organic-inorganic materials. These materials are classified based on the nature of the interactions at the organic-inorganic interface, and the sizes and shapes of their pores and/or cages, which gives rise to designations such as microporous, mesoporous and lamellar silicates. While the chemical and physical properties of porous

silicate materials might in principle be controlled by fully understanding and controlling both their mesoscopic and molecular structures, their molecular level characterization is in most cases a difficult task. In this context, solid-state NMR technique plays an important role on establishing the local structure, and this section therefore overviews the role of advanced high resolution solid-state NMR technique in material chemistry.

**Section A.3** then reviews the design and structural studies of layered silicate composites, with particular emphasis on the surfactant-directed layered silicates which are the focus of a large part of this thesis. The surfactants play a crucial role in the formation of lamellar structure, where charge densities of the surfactant headgroups are critical for the onset of molecular order. Hence, this section explains the structural behavior on the course of crystallization and relates this behavior to the charge density of different organic surfactants. This section focuses predominantly on the two lamellar materials in whose frameworks the incorporation of Al and B will later be discussed in detail: (i)  $C_{16}H_{33}Me_3N^+$ - and (ii)  $C_{16}H_{33}Me_2EtN^+$ - surfactant-directed layered silicates.

One of the most important fields of application of porous silicate materials is heterogeneous catalysis. The catalytic strength or acidity of a silicate material depends among other things on the nature of its framework atoms. For example, presence of heteroatoms in the silicate framework correlates with the extent of acidic strength, and **section A.4** consequently reviews the importance of heteroatoms in porous silicate materials. The specific siting of heteroatoms is believed to potentially direct or at least influence the efficiency and selectivity of silicate materials for catalysis. Hence, this section describes a few examples of zeolites or related materials showing preferential siting of heteroatoms in the silicate framework. Because our work focused on studying the distribution of Al and B heteroatoms in the literature discussing the incorporation of these two heteroatoms in porous silicate materials are discussed in detail on the basis of a few particularly relevant examples.

## **A.2 Porous silicate materials and solid-state NMR**

### ***A.2.1 Concept and applications of hybrid materials***

The term hybrid material was well known for centuries, which consisting of two constituents such as organic and inorganic phase at nanometer or molecular level. In the ancient days, these materials have been extensively used in the mixture of dyes and paints, especially in the form of organic pigments. In the recent days, much scientific activity has been devoted to understand the concept of hybrid materials. The contemporary attempts have aimed to design new and enhance the performance of existing hybrid organic-inorganic materials. The structural aspects and approaches tailoring their mechanical, physical and chemical properties have been neatly explained in the modern literature of material chemistry.<sup>25-30</sup> A

key limitation in this field is the lack of accurate and precise analytical protocols giving access to the local structure of hybrid materials. This is because of their inherent heterogeneity, dynamics and importantly the multiple types of order and disorder at various length-scales that are define their morphologies. However, in the recent days, improved characterization methods have provided novel insights into their structures and established perspectives for the rational design of novel hybrid materials.<sup>31-34</sup> As a consequence, these materials have drawn the attention of different emerging research areas such as optoelectronics, catalysis and ion conduction as well as in the biological field.

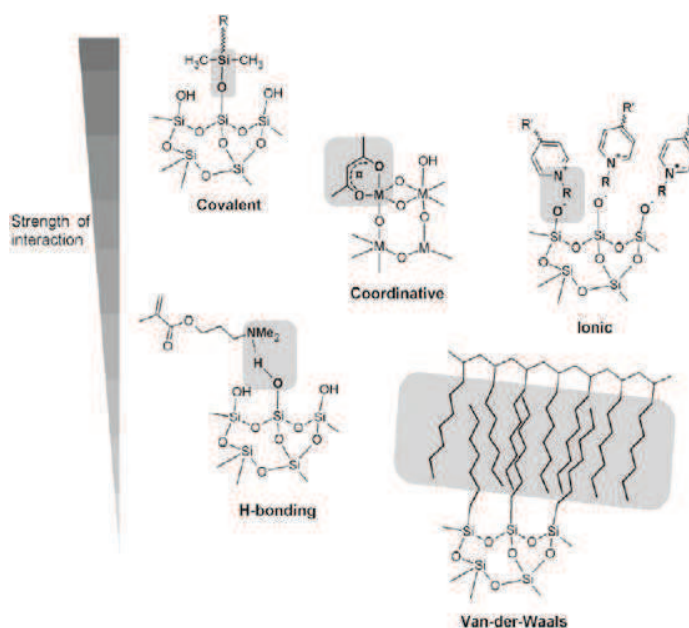


**Figure A.1** [Ref: Kickelbick et.al.<sup>25</sup>] *The strength of interactions at the organic-inorganic interface of hybrid materials.*

Hybrid materials have been classified according to the nature of the chemical interactions at their organic-inorganic interface. As illustrated in Figure A.1, a first class of materials exhibits weak electrostatic interactions between the organic and inorganic entities, with the formation of hydrogen bonds or through weak Van-der-Waals interactions. A second class of materials reveals strong chemical interactions between the two phases, where the inorganic moieties are strongly embedded with the organic entities through covalent bonds. The ionic or coordinate bonds are other types of stronger chemical interactions between the two phases. In summary, as shown in Figure A.1, the strength of chemical interactions between the organic and the inorganic phases of hybrid materials can be ordered in the following sequence: Van-der-Waals interactions < H-bonding < ionic bonding < coordinate bonding < covalent interactions.<sup>25</sup> While covalent bonds tend to form mechanically stronger materials, the weaker

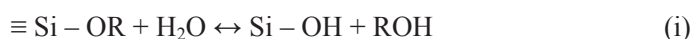
interactions have the advantage of offering greater versatility, with the possibility in particular to remove the organic fraction to open the pore structure.

Combining the properties of the organic and inorganic fractions has led to major developments, for instance in fields such as optoelectronics<sup>35-36</sup>, particularly as molecular sensors, photovoltaic devices and biosensors etc.<sup>35,37-38</sup> It is often desirable to increase the robustness and mechanical strength of the materials by cross linking the guest organic molecules with the host porous inorganic structure, on in the case of lamellar materials, the inorganic layers between them (pillaring<sup>39-40</sup>). This can be done by condensation of silanols (Si-OH) with the organic polymer matrix. As a consequence of the resulting increase of mechanical strength,<sup>41</sup> hybrid materials can then be prepared as monoliths<sup>42-43</sup>, for example. The monolithic materials may be shaped as discs, stacked layers, rolled sheets, sponges, irregular chunks, tubes and cylinders,<sup>44</sup> and are extensively used in chromatography, optics, catalysis, diagnostics, genomics, proteomics, and micro-fluidics, etc. Another example is enzymes immobilization,<sup>45</sup> which could be achieved by cross-linking of silica-based organic-inorganic hybrid materials. Likewise these hybrid materials have been used for multi-functional purposes in many applications.

Many synthetic routes have been studied in order to prepare and functionalize porous silicate materials. This includes the sol-gel method, templating approach, post-synthesis treatments, and, importantly the hydrothermal synthesis of porous materials such as zeolites.

***Sol-gel method:*** The sol-gel method has been applied initially to prepare transparent oxide glasses on hydrolysis of metal alkoxide. Later, this method has been widely employed to synthesize different types of materials<sup>46</sup> such as microporous, mesoporous materials and polymers, etc. The sol-gel method basically exploits the diphasic nature of the synthesis mixture, which contains both solid and liquid phase, and where the sol or solution gradually evolves to form a gel. The metal alkoxides and metal salts are often used as precursors, which undergo various hydrolysis and poly-condensation reactions to form a colloid. The solid phase may adopt a wide range of structural morphologies from discrete colloidal particles to continuous chain-like or strongly interconnected polymer networks.<sup>47-48</sup> While the sol-gel technique has initially been developed to synthesize the glasses and ceramics,<sup>29</sup> its tendency to form glasses is in fact poor,<sup>49</sup> and nowadays the majority of glasses are prepared by quenching process. In the past few decades, the sol-gel method showed an extraordinary output for synthesizing hybrid organic-inorganic materials. This is because organic moieties are in then blended with the inorganic components and may be easily and homogeneously inserted in the structure as a result. A typical sol-gel condensation reaction may be described as follows. The first step (i) is the polymerization of alkoxide silanes in aqueous or gel medium and forming silanols (Si-OH). Secondly (step (ii) or (iii)), successive

condensation reactions of such silanol groups form a network of Si-O-Si connectivities,<sup>50</sup> thereby converting the monomeric reactants to oligomers and then more or less inter-connected polymers to ultimately form the backbone of the final hybrid material.



**Templating approach to the synthesis of porous materials:** The nature of chemical interactions between the organic molecules and inorganic precursors are crucial in developing the pore architecture. The templating process is a particularly important approach for synthesizing mesoporous materials. A medium consisting of micelles of surfactant molecules, (and called the template) is used as a removable scaffold, around which the material can be formed to then create an architecture of channels and cavities, once the organic fraction removed at the end of or after the synthesis.<sup>51</sup> The key property of surfactants in this process is their amphiphilic character, with a chemical structure that contains both a hydrophilic and a hydrophobic part. A well-known example is quaternary ammonium salts with long alkyl chains, such as the cetyltrimethyl ammonium used for the synthesis of the well-known MCM-41 material having a hexagonal arrangement of cylindrical pores. These molecules have a natural tendency to self-assemble in aqueous solution to form a stable micellar structure with the aim of minimizing the energy associated with hydrophilic-hydrophobic interfaces. Figure A.2 shows a few examples of materials prepared from different types of micelle structures using the templating process.

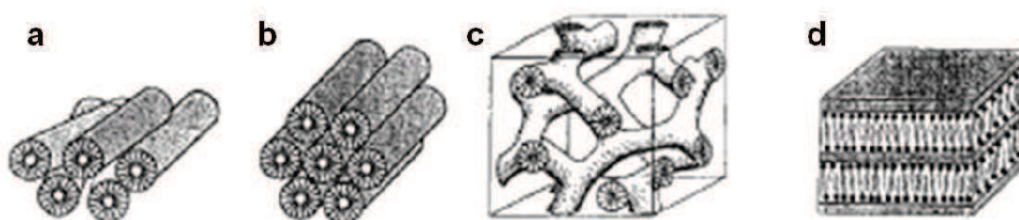


**Figure A.2** Examples of structures formed by templating process, (a) disordered micellar rods, (b) hexagonal-packed micellar rods, (c) three-dimensional structures and (d) lamellar structures.<sup>52-53</sup>

The inorganic precursors condense around the template following the steps described above to form a network that strengthens while the condensation process continues. Template removal can be carried out as a post-synthesis treatment at high temperatures (calcination), during which the architecture of the

inorganic phase will in favorable cases be preserved and sometimes even consolidated due to further framework condensation.

**Post-synthesis treatment:** Functionalization of hybrid materials can also be carried out by post synthetic treatment<sup>54</sup> or secondary synthesis. This method has been used to modify porous silicate materials, and especially mesoporous or zeolite catalysts. Many post-synthesis treatments came to light in the past few decades. One example is the incorporation of Al atoms into the frameworks of porous silicate materials for desired applications. In particular, pore volume of the ordered aluminosilicate mesostructures of the MCM-41 family<sup>55</sup> have been significantly increased by post synthesis hydrothermal treatment. This modifies the Si/Al ratio, however, crystal symmetry remains same even after several post-synthesis treatment. Furthermore, the applicability of ordered mesoporous silica have also been increased by post-synthesis treatment.<sup>56</sup> For example, SBA-15 and MSU-H materials were functionalized by grafting functional groups such as vinyl, epoxide or amine groups that play a variety of roles in many applications.

**Hydrothermal synthesis:** The hydrothermal synthesis is more popular in synthesizing zeolites or related porous silicate materials.<sup>57-60</sup> This is a process in which the crystal forms under high pressure in aqueous medium at relatively high temperature. Normally the steel vessel or autoclaves were used to keep the temperature and pressure constant for prolonged period. A typical hydrothermal synthesis mechanism is shown in the Figure A.3 (example of aluminosilicate zeolites). The precursors (silica and alumina source) were dissolved in H<sub>2</sub>O in alkaline condition (high pH). The continuous stirring of this mixture forms a gel, which is heated at relatively high temperature (100-200°C) in a sealed autoclave, such that the inside pressure increases. At the beginning of hydrothermal synthesis, the mixture remains amorphous, but after some time above the induction period it starts to form crystalline zeolite. Slowly, most of the amorphous reactants turn to the crystalline product.<sup>61</sup>

The main advantages of hydrothermal synthesis in contrast with the other methods are:<sup>62</sup>

- i. the ability to form the crystalline phase which are unstable at melting point,
- ii. crystal growth takes place regardless of the high vapor pressure,
- iii. the chemical composition is controlled,
- iv. large amount of crystals may be produced.

The hydrothermal synthesis method has been used to synthesize the materials that will be discussed in the next chapters.

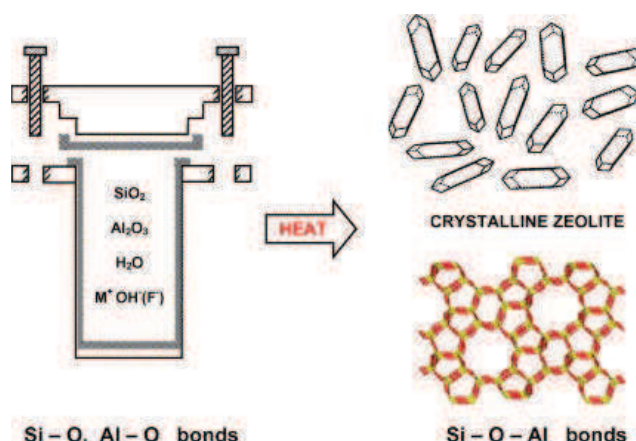


**Figure A.3** [Ref: Cundy et.al.<sup>61</sup>] Mechanism of hydrothermal synthesis of zeolites

## **A.2.2 Solid-state Nuclear Magnetic Resonance (NMR) in material chemistry**

### **A.2.2a Why solid-state NMR spectroscopy in material chemistry?**

The structure of porous silicate materials have been established by using several characterization techniques that are sensitive to different structural features and length scales. This includes lattice and/or pore structure, extent of order and disorder, nature of framework atoms and many other structural features. The experimental techniques that have been employed the most to investigate the structure of these materials are diffraction techniques, electron microscopy and spectroscopic methods.<sup>11</sup> On the other hand, the porosity and surface area of porous materials could be measured by physical gas adsorption techniques.<sup>63</sup> The diffraction technique<sup>64-65</sup> provides essential structural information such as the existence and extent of a long-range-ordered periodic structure, the associated unit cell parameters, and possible space groups. However, complete determination of a new molecularly-ordered structure often requires single crystals with adequate size and quality, which may be particularly difficult to obtain for some zeolites or layered silicates. When single crystals are not available, complementary techniques often provide additional information that is crucial to build structural models and ultimately determine a full structure. Furthermore, the X-ray scattering factors may be too similar between atoms, such as Al and Si. Consequently it fails to provide detailed insights of Si, Al ordering in the zeolite framework but establishes the long range molecular order.

On the other hand, the electron microscopy is an alternative characterization method revealing the structural insights particularly by high-resolution images collected at atomic level. A fundamental reason for the huge success of electron microscopy is that it provides images that they are easy to interpret, as compared to spectral information for example, and which may consequently be used readily by any

scientist independent of its background. These microscopic techniques such as scanning electron microscopy (SEM), transmission electron microscopy (TEM) and electron diffraction method are complimentary to the XRD technique. All these techniques use a beam of energetic electrons to inspect the objects on a very fine scale. The SEM image is a result of electrons reflected by a sample, while TEM image is a result of electrons passing through the sample. Both methods provide topographical, morphological, compositional and crystalline information. However, SEM concentrates on the particle surfaces, while TEM provides the internal details of a sample. The acquired images (TEM) can be assessed by comparing with the calculated images that obtained from lattice parameters of X-ray diffraction. Electron diffraction is another technique which uses electrons to exploit the structural information. This is very similar to XRD but focusing on much smaller particles or regions of a sample. Nowadays, rapid progress of this microscopic technique allows it to play a crucial role in solving the structure of several kinds of silicates and aluminosilicates materials, including zeolites.<sup>8,66-67</sup> However, these methods mainly deal with the long- or medium-range molecular order. It has therefore been a major challenge with the diffraction and microscopic techniques to investigate the local structure, especially in the presence of some degree of structural disorder. In this context several spectroscopic techniques that include vibrational spectroscopy (infrared and Raman), Mossbauer spectroscopy, electrons spin resonance (EPR) spectroscopy and importantly NMR spectroscopy provide important complimentary information to elucidate the molecular-scale structure of porous silicate materials. These techniques establish the structural features at the molecular level by revealing coordination numbers, site symmetries, crystal imperfections, variations in the local order, and also by identifying the impurities. High-resolution solid-state nuclear magnetic resonance (NMR) in particular, has the potential to provide key insights into the local structure of porous silicate materials. The NMR method is primarily sensitive to local molecular-level structure and delivers unique information that may be linked (though often not without effort) to local bonding geometry, conformations, and molecular motions. This section will briefly review the impact of solid-state NMR for the porous and lamellar silicate materials that are the focus of most this thesis work. Technical details of the method will be left for the next chapter (section B.2).

#### ***A.2.2b Study of NMR active nuclei in porous materials***

The solid-state NMR has been widely used to characterize and/or elucidate the structure of silicate-based materials, including a broad range of microporous, mesoporous, lamellar, and mesostructured silicates etc. The main building blocks in the silicate framework of all these materials are SiO<sub>4</sub> tetrahedra. Hence at first view, the local structure could be established by collecting <sup>29</sup>Si and/or <sup>17</sup>O NMR spectra. The <sup>17</sup>O MAS NMR<sup>68-70</sup> provides valuable structural information, but is simply impractical at natural abundance of the NMR active isotope: <sup>17</sup>O, which is only 0.037%. Although one can achieve

high sensitivity with  $^{17}\text{O}$  enrichment, the silicate materials are very sensitive to synthetic conditions and in few cases extremely difficult to synthesize with  $^{17}\text{O}$  enrichment without disrupting the crystal structure. When  $^{17}\text{O}$  enrichment can be successfully achieved,  $^{17}\text{O}$  NMR gives invaluable structural information. Nevertheless,  $^{17}\text{O}$  is a quadrupolar nucleus (spin quantum number,  $I = 5/2$ ) and consequently often exhibits broad second-order quadrupolar line shapes, which may yield poorly resolved and complicated spectra that may be difficult to disentangle to establish the structure. Alternatively the  $^{29}\text{Si}$  NMR has been extensively studied, since, with the spin quantum number of  $1/2$ , the extent of anisotropic interactions is lower in contrast with the quadrupolar nuclei. This leads in favorable cases to sharp NMR signatures that compensate in part for the low natural abundance (4.7%). In molecularly-ordered silicates, these resonances are in principle specific of individual Si crystallographic sites differing for example by their bonding geometries. Furthermore, isotopic  $^{29}\text{Si}$  enrichment allows performing advanced multidimensional solid-state NMR experiments to exploit the specific structural features. In this regards, the group Prof. Bradley Chmelka at UCSB, has been actively involved in adapting the synthesis of zeolites and related hybrid materials to the isotopic enrichment in  $^{29}\text{Si}$  to facilitate solid-state NMR studies.<sup>23,71-72</sup>

Many research groups have been involved in controlling the acidity of porous silicate materials for the desired applications by incorporating several heteroatoms such as Al, B, Ga, Fe, Ti etc into their frameworks. The structural features of these materials could be established by detecting  $^{27}\text{Al}$ ,  $^{11}\text{B}$ ,  $^{69}\text{Ga}$ ,  $^{71}\text{Ga}$ ,  $^{57}\text{Fe}$ ,  $^{47}\text{Ti}$ ,  $^{49}\text{Ti}$  solid-state NMR spectra, although some of these spectra are challenging to acquire and/or interpret. Since, our work is related to Al- and B-containing porous and lamellar materials, we focus here on the information provided by  $^{27}\text{Al}$  and  $^{11}\text{B}$  NMR. The natural abundance of  $^{27}\text{Al}$  nuclei is 100% yielding good sensitivity but its quadrupolar nature gives rise to complex NMR spectra. One can nevertheless see a clear spectral separation between four- and six-coordinated Al atoms in  $^{27}\text{Al}$  MAS NMR spectra. The four-coordinated  $\text{AlO}_4$  present in most of the aluminosilicates zeolites often appeared in the region between +50 to +80 ppm, whereas six-coordinated  $\text{AlO}_6$  species present in particular in layered aluminosilicates such as clays typically appear between -10 and +20 ppm. In a few cases, five-coordinated  $\text{AlO}_5$  have been identified, whose  $^{27}\text{Al}$  isotropic chemical shift range is +30 to +40 ppm.<sup>11</sup>

Boron atoms are another important heteroatom often introduced into the zeolitic framework for specific applications. The coordination state of B atoms in zeolites is normally tetrahedra  $\text{BO}_4$ , while trigonal  $\text{BO}_3$  units often exist in borosilicate glasses or minerals. The NMR-active isotope,  $^{11}\text{B}$ , is also a quadrupolar nucleus having spin quantum number  $3/2$  and a natural abundance of 80.1%. The  $\text{BO}_3$  units exhibit broad resonances with often well-defined second-order quadrupolar line shapes in  $^{11}\text{B}$  NMR spectra, whereas  $\text{BO}_4$  units are often reflected by narrow peaks due to their more spherically-symmetric shape. In contrast with the case of  $^{27}\text{Al}$ , however, the spectral separation between these two different

configurations is found to be small. As a result, sometimes sharp resonance of  $\text{BO}_4$  tetrahedra may overlap with broad contribution of trigonal  $\text{BO}_3$  units, especially in the  $^{11}\text{B}$  spectrum collected at low magnetic field, if the material contains both features. The chemical shift range of  $\text{BO}_4$  and  $\text{BO}_3$  units found to be -4 to +2 ppm and +12 to +25 ppm, respectively, their overlap at low magnetic field being due to the shift associated with the second-order quadrupolar broadening of  $\text{BO}_3$  units, which moves the corresponding peaks into the  $\text{BO}_4$  region.<sup>10</sup>

The framework negative charge introduced by heteroatoms in silicate frameworks is generally compensated by extra-framework cations such as  $\text{Na}^+$ ,  $\text{Ca}^+$  or alkyl ammonium surfactants in the case of mesoporous silica. The role of these cations could be explored by detecting  $^{23}\text{Na}$ ,  $^{43}\text{Ca}$  nuclei. The influence of surfactant molecules on the molecular or pore structure could be probed by performing  $^1\text{H}$ ,  $^{13}\text{C}$  NMR experiments. In addition, strong or weak electrostatic interactions between organic surfactants and inorganic porous materials could be established by advanced multidimensional HETCOR (Heteronuclear correlation) NMR experiments. For complex materials, there may be many difficulties associated with the fine interpretation of NMR measurements of all the nuclei discussed above, especially for  $^{27}\text{Al}$  and  $^{11}\text{B}$  nuclei because of their broad quadrupolar NMR signatures. Nevertheless, advanced NMR techniques exist that can be used to increase resolution or observe only those nuclei that are close in space to another type of NMR-active nuclei, all of which can be combined to obtain, with the help also of other techniques, a clear picture of the local structure of the material.

#### ***A.2.2c Effect of bonding geometries and heteroatoms on $^{29}\text{Si}$ chemical shift***

The great success of NMR crystallography in material chemistry would have not been possible without detailed knowledge of  $^{29}\text{Si}$  NMR chemical shifts. Three major structural features have greater impact on the  $^{29}\text{Si}$  chemical shift distribution: (i) the coordination state of  $^{29}\text{Si}$  sites, (ii) the nature of neighboring crystallographic sites and (iii) bonding geometries around the central Si atom. The coordination state of Si atoms in porous materials is often  $\text{SiO}_4$  tetrahedra, which resonate in the region of -120 to -60 ppm. Rarely,  $\text{SiO}_6$  octahedron was observed for example in stichovite<sup>73</sup> and thaumasite<sup>74</sup> resonating in the region of -191.3 to -179.9 ppm and five coordinate  $\text{SiO}_4\text{F}$  species are often found in zeolites synthesized in fluoride containing media. The coordination state of Si atoms is generally designated by  $Q^n$ , where n refers to the number of Si-O-T (T = four-coordinated Si, Al, B etc) linkages. Each addition of T sites (Si) to the Si atom via O atoms in turn decreases the electronegativity of O atom and causes shift of  $^{29}\text{Si}$  NMR signals to lower frequency. Such effect on  $^{29}\text{Si}$  chemical shift is completely different if the connected T sites are heteroatoms, in which case the central  $^{29}\text{Si}$  is referred to as  $Q^n(m)$  moieties, (m = number of heteroatoms, e.g. B or Al). Especially in the case of aluminosilicates, for each

replacement of Si by an Al atom, a low-field shift of 5 ppm has been observed.<sup>11</sup> This is because the substitution of Al by Si atoms decreases the shielding of the central Si atom.

In the case of boron-containing silicates, the way <sup>29</sup>Si chemical shifts are influenced by B atoms is still unclear. Recently, Nanba *et.al.*<sup>75</sup> anticipated the effect of boron on SiO<sub>4</sub> units by molecular orbital calculations. Upon substitution of B atoms, the isotropic chemical shift of the central Si atom is likely to shift towards higher frequency. On the other hand, Vogels *et.al.*<sup>76</sup> mentioned in the characterization of B-substituted saponites that no significant difference in <sup>29</sup>Si chemical shift would be expected between Q<sup>3</sup>(0B) and Q<sup>3</sup>(1B) species. This is because B atom exhibits stronger electronegativity (2.04) that is close to the Si atom (1.9), in contrast with Al which has a significantly weaker electronegativity (1.61). As a result, the B-O linkage in a B-O-Si sequence is less polar compared to the Al-O bond. Therefore Q<sup>3</sup>(1B) <sup>29</sup>Si sites in saponites are expected to resonate less downfield than Q<sup>3</sup>(1Al) and closer to the Q<sup>3</sup>(0B) moieties. This is evident with the small difference between the chemical shift of Q<sup>3</sup>(0B) and Q<sup>3</sup>(1B) <sup>29</sup>Si sites.

On the other hand, bonding geometries in zeolites and related materials also have a significant contribution to the chemical shifts. Numerous examples in zeolites describe the relationship between <sup>29</sup>Si chemical shift of Q<sup>n</sup> (n = 0, 1, 2 or 3) species and the average of the Si-O-T (T = Si, Al, B etc) bond angle to the n tetrahedral neighbors.<sup>77-79</sup> Engelhardt and Radeglia<sup>80</sup> initially reported the theoretical interpretation of chemical shift and the bond angle. A maximum of 10 ppm shift difference has been observed accounting to the concomitant modification of Si-O-T bond angles. Similar effects have also been noticed in the case of 2:1 clays, layered silicate-based systems,<sup>81</sup> which are basically composed of tetrahedral and octahedral sheets, and which will be discussed in more detail later in this chapter. In such systems, the effects of bond angles on <sup>29</sup>Si chemical shifts should be considered together with the systematic decrease of <sup>29</sup>Si chemical shifts on increasing the total negative charge of the layer by substituting more Si atoms by Al in the tetrahedral layer. Nevertheless, the structural distortions due to the rotation of tetrahedral sheets and the nature of the cationic species within the octahedral layer appear to be the main factors affecting <sup>29</sup>Si chemical shifts in clays. This relationship between the bond angle and chemical shift provides fruitful information regarding the structure of clay minerals and of silicate-based materials in general. Likewise, the Si-O bond length also has an effective correlation with the isotropic <sup>29</sup>Si chemical shift. Down-field shifts (i.e. to higher ppm values) have thus been observed for larger Si-O bond lengths and vice versa. For example, Grimmer *et.al.*<sup>82</sup> reported 1 ppm shift for 1x10<sup>-4</sup> nm Si-O bond length. This is also consistent with semi-empirical calculations. Hence it has been suggested by several studies that Si-O bond length and Si-O-T bond angle are closely related and strongly correlated with <sup>29</sup>Si chemical shift distribution.<sup>83</sup> The effects of the bond angle may thus significantly interfere with the

typical 5 ppm shift generally associated with Si/Al substitution, and which is too often considered systematic.<sup>84</sup>

### ***A.2.3 Classification of Microporous, Mesoporous and Lamellar silicate materials based on the degree of molecular order.***

Porous or lamellar silicate materials have been classified into several groups based on their structural morphology and the extent of molecular order and disorder. Solid-state NMR provides structural insights at the molecular level to make a clear distinction among such silicate materials. The degree of short-range molecular order and disorder is directly reflected in the line widths of 1D <sup>29</sup>Si MAS NMR spectra through chemical shift distributions. In this regards, Massiot and coworkers<sup>85</sup> gathered representative examples of the extents of molecular order and disorder at various length scales in silicate materials, along with their corresponding 1D <sup>29</sup>Si MAS NMR spectra, plotted in Figure A.4 on the same scale to allow direct comparison.

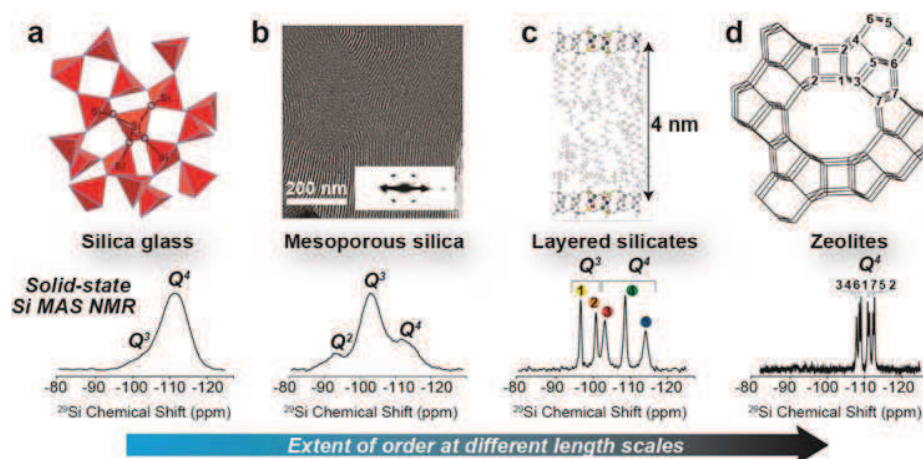


**Figure A.4** [Ref: Massiot et.al.<sup>85</sup>] (a) Amorphous silica glass consisting of a disordered arrangement of SiO<sub>4</sub> tetrahedra and (bottom) corresponding <sup>29</sup>Si spin-echo MAS NMR spectrum. (b) Hexagonal mesoporous silica exhibiting a highly-ordered pore architectures at nanometric length scales as showed in (top) the Transmission electron microscopy (TEM) image, and amorphous silica walls at the molecular level as revealed by (bottom) the <sup>29</sup>S[<sup>1</sup>H] CPMAS NMR spectrum.[Kirmayer et.al.<sup>86</sup>] (c) Cartoon representing in the in-plane view of a surfactant-directed layered silicate consisting of thin (0.8 nm) molecularly-ordered silicate sheets giving rise to five well resolved <sup>29</sup>Si peaks (bottom) in <sup>29</sup>Si[<sup>1</sup>H] CPMAS NMR spectrum. [Hedin et.al.<sup>23</sup>] (d) Highly-ordered silicate framework structure of high-silica zeolite ZSM-12 and (bottom) corresponding <sup>29</sup>Si MAS NMR spectrum showing extremely narrow peaks (courtesy D.H. Brouwer).

In general, glasses are considered as amorphous materials and exhibit a highly disordered network. This amorphous nature is directly reflected by the extent of broadening of  $^{29}\text{Si}$  peaks. As shown in Figure A.4a, the full width at half maximum (FWHM) of  $^{29}\text{Si}$  peaks found to be in the range of 10 ppm. The majority of the Si atoms in such dense silicate frameworks correspond to fully-condensed  $Q^4$  (one Si atoms connected to four other Si atoms via bridging O atom) crystallographic sites, with a small amount of partially-condensed  $Q^3$  Si atoms (one Si atoms connected to three other Si atoms via bridging O atom) also present. Figure A.4b shows the TEM image (top) and  $^{29}\text{Si}$  MAS NMR spectrum (bottom) of mesoporous silica material. This material presents a high degree of long-range order in the hexagonal arrangement of its cylindrical pores, which gives rise to the beautiful fingerprint pattern in the TEM image. However, the silica walls are highly disordered at the molecular level and exhibit broad  $^{29}\text{Si}$  NMR signatures reminiscent of glasses. The three distinct signals observed in the  $^{29}\text{Si}[^1\text{H}]$  CP-MAS NMR spectrum indicate that this mesoporous materials is mainly constituted with  $Q^2$ ,  $Q^3$  and  $Q^4$   $^{29}\text{Si}$  sites, although the contribution of  $Q^4$  sites may underestimated in such a non-quantitative spectrum. Nevertheless, the large number of partially condensed  $Q^3$  and  $Q^2$   $^{29}\text{Si}$  sites directly results from the considerably largest surface area of this type of materials, as compared to glasses.

By extension, the NMR technique is also extremely sensitive to the short-range molecular order. This can be identified by means of sharp  $^{29}\text{Si}$  NMR signatures, as is the case for non-crystalline layered silicates shown in Figure A.4c.<sup>22</sup> In these materials, which will be discussed at length in this manuscript, the 2D silicate layers are separated by long-chain organic surfactants, forming a highly-ordered lamellar structure. In addition, highly molecularly-ordered domains can be seen in HRTEM image<sup>24</sup> within the 2D silicate layers. Such short range molecular order was first detected in the  $^{29}\text{Si}$  MAS NMR spectrum by five well resolved  $^{29}\text{Si}$  peaks. In fact, our current research work has focused on understanding and controlling the molecular composition and structure of new alumino- and boro-silicate materials directly based on these non-crystalline layered silicates. Previous studies focusing on the silicate forms of these materials are reviewed below, in section A.3. Finally, the silicate framework of microporous zeolite materials may reveal highly ordered molecular structure in all three-dimensions. As shown in Figure A.4d, their  $^{29}\text{Si}$  MAS NMR spectra may in favorable cases (high crystallinity, high or pure-silica content) present extremely narrow (FWHM of 0.4 ppm)  $^{29}\text{Si}$  peaks. Much effort has been dedicated to understanding the structural insights of microporous, mesoporous and lamellar silicates, and solid-state NMR provides in many cases valuable information on the often complicated extents of order and disorder that may be present in these rich materials.

### A.3 Layered silicate composites

#### A.3.1 Different types of layered silicates

Layered silicates, also designated as phyllosilicates, consist of two-dimensional frameworks where the main building blocks are  $\text{SiO}_4$  tetrahedra. The interlayer space between the consecutive 2D silicate sheets may typically be filled with cations and/or water molecules. Generally speaking, several kinds of layered silicates exist, which mostly differ by the nature of 2D framework structure and the interlayer species. Here we discuss two distinct categories of layered silicates having distinct framework morphologies. Both types of materials consist of negatively-charged frameworks which are compensated by cations in the inter-layer space. However the molecular origin of these charges are different.

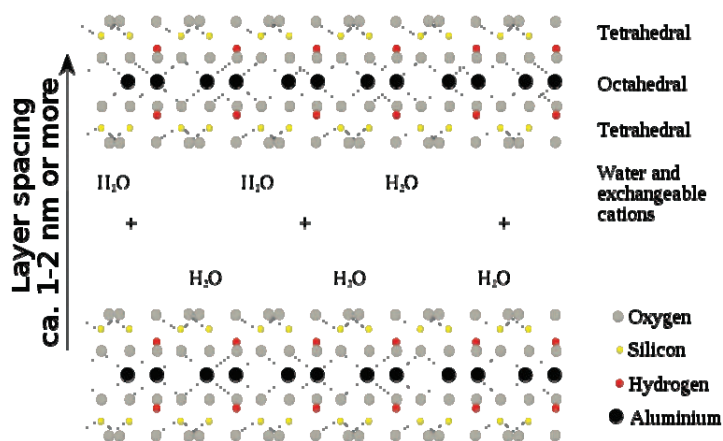


**Figure A.5** [Ref<sup>87</sup>] 2:1 clay minerals (belongs to smectite family: montmorillonites)

The first example is the group of 2:1 clay minerals, also referred to as smectites. Some of these materials are naturally occurring minerals, such as montmorillonites, nontronite and illite group of minerals. While naturally occurring montmorillonites have been largely studied, some important questions remain unresolved regarding their molecular structure. The complexity of the structure, which may undergo a number of atomic substitutions, along with the co-existence in many cases of impurities that are difficult to separate from the main phase poses a challenge for the complete understanding of their structural insights. In this regards, over the past few decades many efforts have been made on to synthesize these materials artificially to better understand and control their crystal structure so as to tune their physico-chemical properties. Figure A.5 depicts the molecular structure of montmorillonites. Each sheet is composed of one octahedral layer sandwiched between two tetrahedral layers (thus the “2:1” designation). The octahedral layer is primarily (or exclusively in synthetic materials) constituted with 6-coordinated Al and Mg atoms while the tetrahedral layers are primarily composed of 4-coordinated Si

atoms, along with a few some four-coordinated Al atoms. Each  $Mg^{2+}$  cation in the octahedral layer and  $Al^{3+}$  cation in the tetrahedral layer contribute to the overall negative charge of the layer, which is compensated by exchangeable cations such as  $Na^+$ ,  $Ca^+$ ,  $K^+$  or  $Mg^+$  ions, generally solvated by water molecules, in the interlayer space. A detailed study of the molecular-scale structure and composition of montmorillonite minerals will be discussed in the chapter E (see section E.2).

Over the past few decades, many efforts have been focusing on improving the quality of microporous and mesoporous materials especially for the industrial applications. While mesoporous materials often contains large pores (2-50 nm), giving access to the larger molecules inside the cavities, the silica walls of such materials exhibit amorphous nature at the molecular level (see figure A.4.b). This significantly reduces the robustness of the materials, limits catalytic reactivity, and makes their structural characterization challenging. It has been particularly challenging to determine the availability of active sites in such amorphous silicate framework. These limitations raise the need to find a different way, in order to achieve crystallinity at both mesoscopic and molecular length scales.

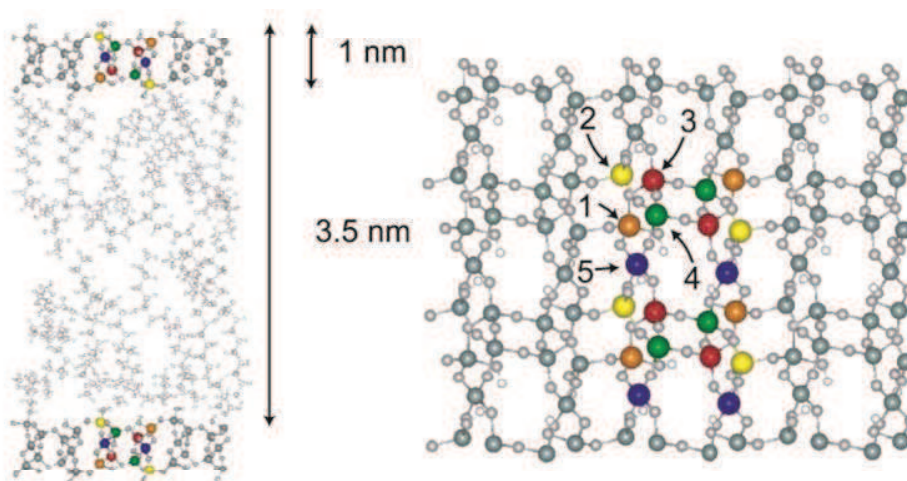


**Figure A.6** [Ref: Hedin et.al.<sup>23</sup>] Schematic representation of surfactant-templated layered silicates

In this context, Chmelka and coworkers<sup>22-23,88</sup> reported the synthesis and characterization of ordered lamellar silicates self-assembled in the presence of alkyl-ammonium surfactant molecules. In contrast to the clays discussed above, the frameworks of these materials are purely siliceous, and the net negative charge comes from incompletely condensed ( $Q^3$ )  $SiO_4$  units associated with non-bridging oxygen atoms. A schematic representation of these surfactant-directed layered silicates (briefly discussed in section A.2.3) is shown in Figure A.6. Here the organic surfactants are the key to obtain molecularly-ordered lamellar structure. They serve at the same time as a template, to control the mesoscopic ordering,

and as a structure-directing agent promoting framework crystallization (as in zeolites) within the silicate sheets. Using the right synthesis conditions, the corresponding materials reveal ordered morphologies at both molecular and mesoscopic lengthscales. One of the objectives of our work was to enhance the framework acidity of surfactant-directed layered silicates by incorporating active sites into their 2D inorganic frameworks. In this context, this section provides a complete description of such surfactant-directed layered silicates, based on the various studies that have been reported since their discovery. These materials were synthesized under hydrothermal condition at 135°C in basic pH (11.5). The charge densities of the alkyl-ammonium surfactant headgroups are the main driving force for both the self-assembly and subsequent onset of molecular order within the silicate framework. Hence, the structural behavior manifested as a function of crystallization time is largely influenced by the charge density of organic surfactants, as will be discussed below. Christiansen *et.al.*<sup>22</sup> and Hedin *et.al.*<sup>23</sup> reported the local structural studies of these 2D silicate materials by advanced solid-state NMR techniques, first principle calculations and XRD experiments. The next section summarizes these results.

### ***A.3.2 Charge density of the structure directing agents in surfactant-directed layered silicates***

Many factors influences on the development of molecular order during the synthesis of surfactant-directed layered silicate materials (SDLS). This primarily includes pH of the gel mixture, temperature, duration of crystallization, and, most importantly, the nature of the surfactant headgroups. In this case the surfactants act not only as a template, but also as structure directing agents (SDA) and their headgroup hydrophobicity is a key aspect in this context. The hydrophilic headgroups strongly interact with the oligomeric silicate species in the gel medium and thereby “directing” the crystallization into a given molecular-scale structure. Christiansen *et.al.*, systematically studied the structure of 2D crystalline silicate sheets considering the effect of charge densities of surfactant headgroups. Crystallization time (defined as the time after which no significant evolution of the sample could be observed) was found to increase continuously on decreasing the charge densities of the surfactant headgroups. This was evidenced by synthesizing a series of lamellar silicate-tri-alkylammonium composites with systematic increase of the charge density of the surfactant headgroup, as summarized in Figure A.7.

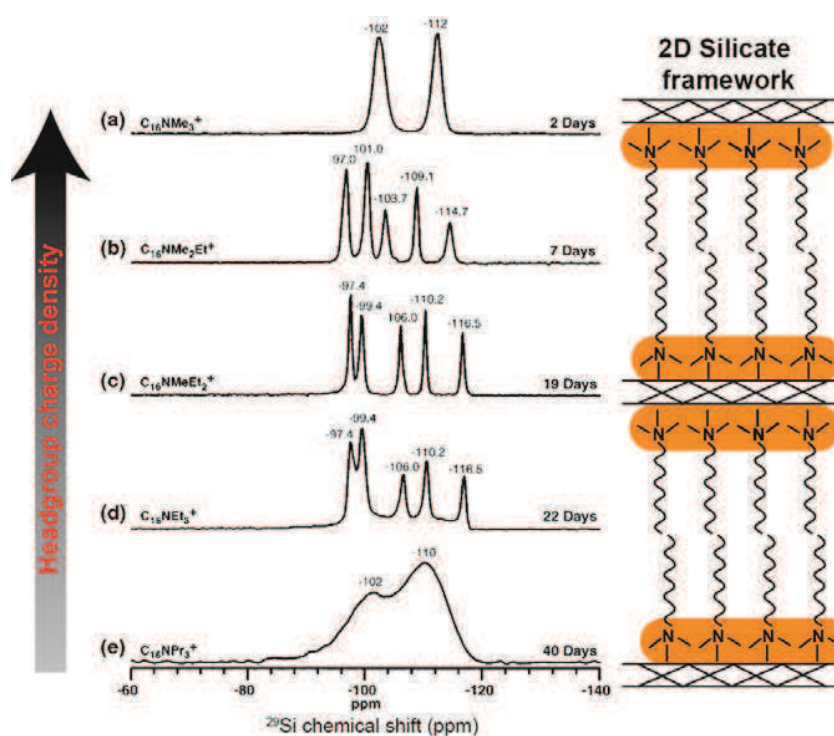


**Figure A.7** [Ref: Christiansen et.al.<sup>22</sup>] <sup>29</sup>Si[<sup>1</sup>H] CP-MAS NMR spectra of non-crystalline layered silicates synthesized under hydrothermal condition at 135°C temperature by using surfactant groups (a) C<sub>16</sub>H<sub>33</sub>Me<sub>3</sub>N (b) C<sub>16</sub>H<sub>33</sub>Me<sub>2</sub>EtN (c) C<sub>16</sub>H<sub>33</sub>MeEt<sub>2</sub>N (d) C<sub>16</sub>H<sub>33</sub>Et<sub>3</sub>N and (e) C<sub>16</sub>H<sub>33</sub>Pr<sub>3</sub>N, respectively. A schematic representation of lamellar silicates (C<sub>16</sub>H<sub>33</sub>Me<sub>3</sub>N surfactant) is shown on right side.

For example, when the surfactant headgroup is trimethyl (-Me<sub>3</sub>), then the associated charge density is relatively high and then it takes 2 days to form a fully molecularly-ordered framework consisting of two distinct crystallographic sites, as illustrated by the two well-resolved <sup>29</sup>Si peaks at -102 and -112 ppm <sup>29</sup>Si MAS solid-state NMR spectrum (Figure A.7a). The structure of this molecularly ordered silicate framework is thought to resemble the structure of octosilicate.<sup>89</sup> The resulting molecular-scale structure is completely different when one methyl group of the surfactant headgroup is replaced by an ethyl group (C<sub>16</sub>H<sub>33</sub>Me<sub>2</sub>EtN<sup>+</sup>- surfactant). As can be seen in Figure A.7b, the <sup>29</sup>Si MAS NMR spectrum of C<sub>16</sub>H<sub>33</sub>Me<sub>2</sub>EtN<sup>+</sup>- surfactant directed layered silicate, which takes 7 days to fully crystallize, shows five well resolved <sup>29</sup>Si peaks. The width of each <sup>29</sup>Si peak is smaller (FWHM 0.8-1.1 ppm) in contrast with those of C<sub>16</sub>H<sub>33</sub>Me<sub>3</sub>N<sup>+</sup>- silicate material (FWHM 2.0 ppm) indicating an even higher degree of molecular order in the framework structure. When the surfactant headgroup is further modified by replacing another methyl by an ethyl group, it then requires 19 days to obtain a lamellar silicate material. Here also, five <sup>29</sup>Si peaks were observed, however, the chemical shift of each <sup>29</sup>Si peak is different from those five <sup>29</sup>Si peaks observed for C<sub>16</sub>H<sub>33</sub>Me<sub>2</sub>EtN<sup>+</sup>-silicate material. Such differed chemical shift distribution points to

their different interactions with the surfactants, the connectivities, and presumably also the silicate framework structures of both materials being the same. It is worth of mentioning that, the lower charge density of the surfactant headgroup requires longer hydrothermal synthesis in spite of its symmetric nature. For instance, when the surfactants contains tri-ethyl group, the presence of broad  $^{29}\text{Si}$  background signal after 22 days of crystallization (Figure A.7d) indicates that this crystallization is still incomplete. Finally, in the case of tri-propyl headgroups, even after 40 days crystallization, the material exhibits an amorphous nature (Figure A.7e), the interactions between the headgroup and the silicate moieties being too weak in this case to induce framework crystallization. All these results strongly suggest that the charge density of the surfactant headgroup (along may be with their symmetry) critically influence on the crystallization process.

### ***A.3.3 $\text{C}_{16}\text{H}_{33}\text{Me}_3\text{N}^+$ - and $\text{C}_{16}\text{H}_{33}\text{Me}_2\text{EtN}^+$ - layered silicate composites***

In the rest of this manuscript we shall focus essentially on  $\text{C}_{16}\text{H}_{33}\text{Me}_3\text{N}^+$ - and  $\text{C}_{16}\text{H}_{33}\text{Me}_2\text{EtN}^+$ -silicate materials, which are the fastest to crystallize. Christiansen *et.al.* studied the preliminary stages of the formation on these materials using a combination of XRD,  $^{29}\text{Si}$  NMR and FTIR spectroscopy and I summarize their results here. The diffraction technique is the principal characterization method used to examine the long-range molecular (at wide angles) and mesoscopic (at small angles) order. For example, the  $\text{C}_{16}\text{H}_{33}\text{Me}_3\text{N}^+$ - layered silicate, after 1 day hydrothermal synthesis, the silicate structure is found to be amorphous at the molecular level as revealed by XRD, solid-state NMR and also Infrared (IR) data, as shown in Figure A.8.1. Such molecular disorder is reflected in the  $^{29}\text{Si}$  MAS NMR spectrum (Figure A.8.1b) by three broad peaks at -90, -100 and -109 ppm attributed to  $Q^2$ ,  $Q^3$  and  $Q^4$  species, and in the FTIR spectrum (Figure A.8.1c) by a broad absorption band characteristic of amorphous silica.<sup>90</sup> The presence of  $100$  reflections at 3.26 nm and weak  $200$  reflections at 1.76 nm nevertheless point to the poorly-ordered lamellar mesoscopic structure.

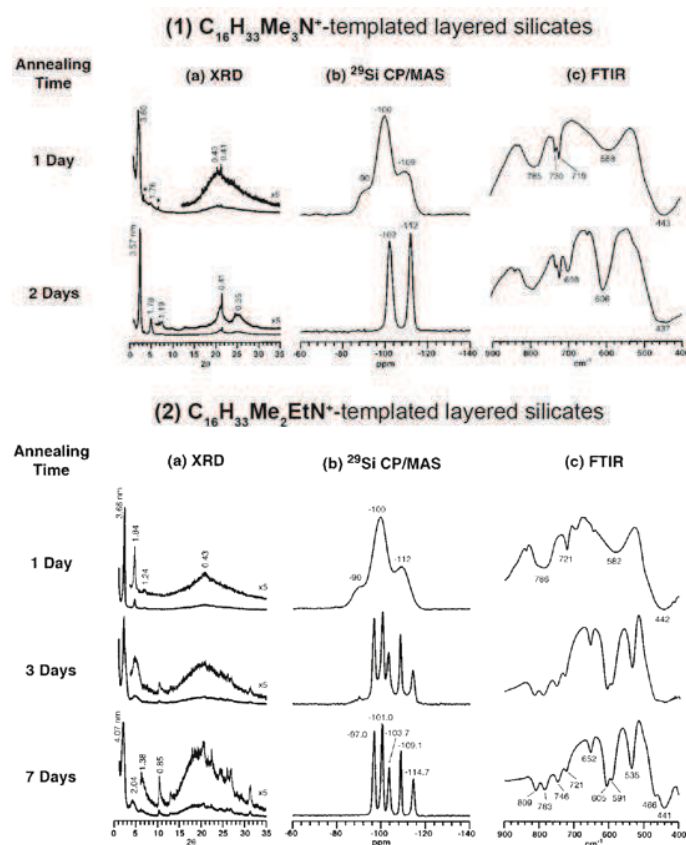


**Figure A.8** [Ref: Christiansen *et.al.*<sup>22</sup>] The (a) XRD, (b)  $^{29}\text{Si}$  CP-MAS NMR and (c) FTIR spectra of  $\text{C}_{16}\text{H}_{33}\text{Me}_3\text{N}^+$ - (Fig.C.2.1, 1 and 2 days) and  $\text{C}_{16}\text{H}_{33}\text{Me}_2\text{EtN}^+$ - layered silicates (Fig.C.2.2, 1, 3 and 7 days), respectively.

Extending the hydrothermal synthesis to 2 days in identical synthesis condition, leads to a well molecularly and mesoscopically ordered layered silicate composite. As showed in the Figure A.8.1a (2 days), the low angle 100, 200 and 300 reflections observed at 3.57, 1.78 and 1.19 nm, respectively points to the mesoscopic lamellar order and small reflections at wide angle observed at 0.41 and 0.35 nm attest to the presence of the molecular ordering in the silicate framework. The two well resolved  $^{29}\text{Si}$  peaks at -102 and -112 ppm observed in the  $^{29}\text{Si}$  MAS NMR spectrum, which could be attributed to  $Q^3$  and  $Q^4$   $^{29}\text{Si}$  moieties, respectively, confirm considerably increased degree of local molecular order. In addition, the FTIR spectrum (A.8.1c, 2 days) shows two well-defined bands at 606 and 698  $\text{cm}^{-1}$ , which have been assigned in other synthetic silicate materials to double-four-membered (D4R) and six-membered rings, respectively.<sup>91-92</sup> The molecular order remains the same when the hydrothermal synthesis time is extending beyond two 2 days.

On the other hand, slight assymetry and globally lower charge density of the  $C_{16}H_{33}Me_2EtN^+$ -surfactant headgroup results in a completely different molecular-scale structure and crystallization behavior. At the beginning of hydrothermal synthesis (Figure A.8.2 1day), the molecular arrangement is again disordered, as is evident with diffraction, IR and NMR spectroscopic data, despite the presence of lamellar mesoscopic order.

The structure appears to be considerably more ordered after a prolonged hydrothermal synthesis of 3 days, and the crystallization then continues until it is complete after 7 days of crystallization. This is demonstrated by  $^{29}Si$  CP-MAS NMR spectrum (Fig.A.8.2b), where five well resolved peaks reveal highly molecularly-ordered network. The line width of these five narrow peaks at -97.0, -101.0, -103.7, -109.1 and -114.7 ppm is less than 1 ppm that confirms at the local level the crystalline like structure. Few reflections at wide angle XRD spectrum (Fig.A.8.2a) for both 3 and 7 days silicate material, further supports the conclusion drawn by  $^{29}Si$  solid-state NMR spectrum. The small number of these wide-angle reflections and their broadening nevertheless indicate that the degree of long-range molecular order is poor. Thus the order observed in 1D  $^{29}Si$  NMR is only short range. In addition, the FTIR spectrum of  $C_{16}H_{33}Me_2EtN^+$ -silicate material shows vibrational bands at 535, 605 and 652  $cm^{-1}$  points to the five, six and four-membered rings, respectively.

#### ***A.3.4 Local structure by multi-dimensional NMR experiments.***

The two-dimensioinal (2D) surfactant-directed layered silicates shows highly molecularly-ordered local domains but lack long-range three-dimensional (3D) crystallinity. This is due to the presence between the silicate sheets of the flexible organic surfactants that causes the layers to be uniaxially stacked with tranversely isotropic orientations, which breaks the periodicity of atomic positions from one layer to another. All the studies reviewed so far provides only the basic information pointing to the long-range molecular order and the role of surfactants influencing the local structure.

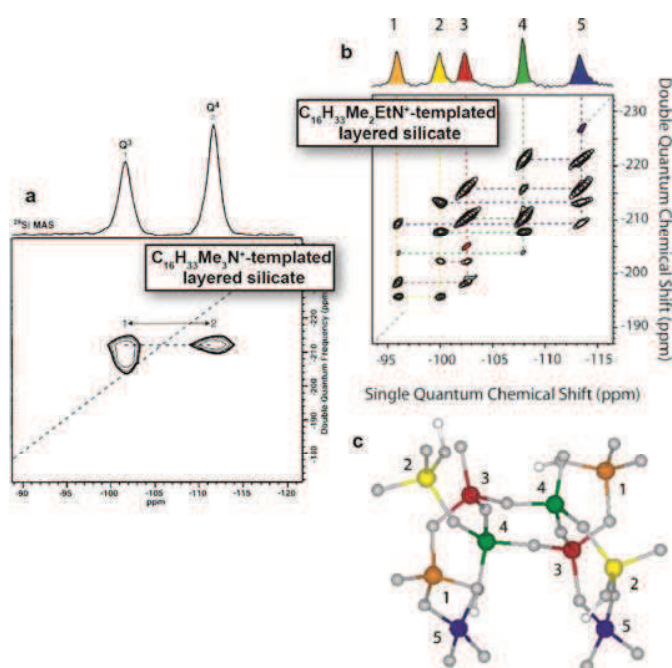


**Figure A.9** [Ref: Christiansen et.al.<sup>22</sup> and Hedin et.al.<sup>23</sup>] (a) The 2D  $^{29}\text{Si}$  [ $^{29}\text{Si}$ ] refocused INADEQUATE NMR spectrum of  $\text{C}_{16}\text{H}_{33}\text{Me}_3\text{N}^+$ - layered silicate material (b) The 2D  $^{29}\text{Si}$  [ $^{29}\text{Si}$ ] DQ recoupling NMR spectrum of  $\text{C}_{16}\text{H}_{33}\text{Me}_2\text{EtN}^+$ - layered silicate material. The color of each  $^{29}\text{Si}$  peak corresponds to the respective Si sites as showed in the model (c) of  $\text{C}_{16}\text{H}_{33}\text{Me}_2\text{EtN}^+$ - layered silicates. The quantitative  $^{29}\text{Si}$  MAS NMR spectra were showed at the top of each 2D spectrum.

The next step is to get insights onto the molecular-scale structure of the layers by establishing the connectivities and/or spatial proximities between Si atoms. Advanced multi-dimensional NMR experiments are crucial to determine such molecular interactions. Of particular interest in this case are experiments which probe the existence of connectivities (via bridging O atoms) between Si atoms.<sup>71</sup> Figure A.9a presents an example of such experiment collected for the  $\text{C}_{16}\text{H}_{33}\text{Me}_3\text{N}^+$ - layered silicate material. The details on how such an experiment was collected are beyond the scope of this chapter, and the interested reader is invited to look into the corresponding article.<sup>23</sup> The principle of this type of experiments will be briefly presented in Chapter B (section B.2.4). The through-bond-mediated spectrum of Figure A.9a shows two strong correlations between the  $Q^3$  and  $Q^4$   $^{29}\text{Si}$  signals, which establish that  $Q^3$  and  $Q^4$   $^{29}\text{Si}$  sites are connected to each other via bridging oxygen atom. The layered structure in this material is believed to be isostructural to the framework structure of crystalline octosilicate RUB-18 ( $(\text{Na}_8[\text{Si}_{32}\text{O}_{64}(\text{OH})_8]32\text{H}_2\text{O})^{89}$ ), where the  $Q^3$  and  $Q^4$   $^{29}\text{Si}$  sites are designated as sites T2 and T1, respectively. If this is true then each  $Q^3$   $^{29}\text{Si}$  site should be connected to two  $Q^4$  and one  $Q^3$   $^{29}\text{Si}$  sites, whereas each  $Q^4$   $^{29}\text{Si}$  site should be connected to two  $Q^4$  and two  $Q^3$   $^{29}\text{Si}$  sites (See Table A.1). The

absence of  $Q^3$ - $Q^3$  and  $Q^4$ - $Q^4$  correlation peaks in this spectrum, while apparently in contradiction with such a connectivity pattern, may in fact be explained by a property of the  $J$  coupling interactions, whose effects are known to vanish for two sites with identical chemical shifts. Observing such auto-correlation peaks in  $J$ -mediated NMR experiments is often challenging and sometimes impossible. Nevertheless, we establish in Chapter D (**section D.2.3**) that such connectivities in fact exist in this material and that the connectivity pattern is indeed identical to that of octosilicate.

**Table A.1 List of  $^{29}\text{Si}$ -O- $^{29}\text{Si}$  connectivities established for  $\text{C}_{16}\text{H}_{33}\text{Me}_2\text{EtN}^+$ - and  $\text{C}_{16}\text{H}_{33}\text{Me}_3\text{N}^+$ -layered silicate materials.**

Material model	Silicon sites	$^{29}\text{Si}$ chemical Shift	Connectivities
$\text{C}_4\text{H}_9\text{Me}_2\text{EtN}^+$ - layered silicate	Si1	-96.7	Si2, Si3 and Si5
	Si2	-100.7	Si1, Si4 and Si5
	Si3	-103.3	Si1, Si4, Si4 and Si5
	Si4	-108.7	Si2, Si3, Si3 and Si5
	Si5	-114.3	Si1, Si2, Si3 and Si5
$\text{C}_4\text{H}_9\text{Me}_3\text{N}^+$ - layered silicate	T1	-111.5	T1 (x2), T2 (x2)
	T2	-101.5	T1 (x2), T2

The  $^{29}\text{Si}$ -O- $^{29}\text{Si}$  connectivities between the framework Si atoms have also been established by probing the spatial proximities between the Si atoms using 2D correlation experiments probing homonuclear  $^{29}\text{Si}$ - $^{29}\text{Si}$  dipolar couplings. Figure A.9b shows an example of such a spectrum collected for the  $\text{C}_{16}\text{H}_{33}\text{Me}_2\text{EtN}^+$ -layered silicate material (again, the principle of such experiments will be summarized in Chapter B, and the interested reader should look into the corresponding article).<sup>23</sup> In contrast with the experiment described above, the later probes not only the connected Si atoms (which are necessarily also close in space) but also the non-connected nearby Si atoms via their (comparably weaker) dipolar couplings. Pairs of correlation peaks at the same frequency in the vertical dimension of the 2D spectrum correspond to pairs of  $^{29}\text{Si}$  nuclei that are close in space, stronger intensity typically pointing to connected Si atoms. The  $^{29}\text{Si}$ -O- $^{29}\text{Si}$  connectivities of the corresponding layered silicate material first reported in ref<sup>22</sup> and then further confirmed in later work<sup>71</sup> are listed in Table A.1. An example of plausible structural model in accordance with the molecular connectivities was postulated in ref.<sup>23</sup> and is shown in Figure A.9c.

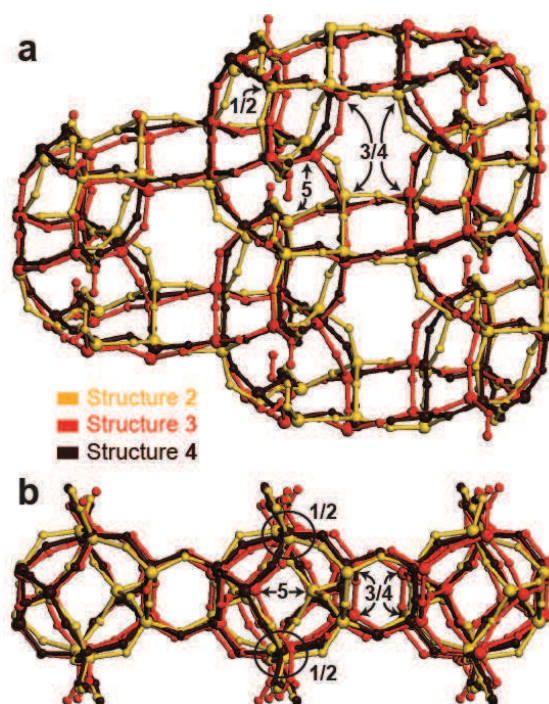


**Figure A.10** [Ref: Brouwer *et.al.*<sup>24</sup>] Superimposition of three candidate structure of  $C_{16}H_{33}Me_2EtN^+$ -directed layered silicate material shown in yellow (structure 2), red (structure 3) and brown (structure 4) color viewed from the top (a) and the side (b).

While this model structure shown in Figure A.9c was fully compatible with all the data available at that time, it was later shown not to precisely correspond to the actual framework structure. Brouwer *et.al.*<sup>24</sup> very recently reported the complete structure determination of the  $C_{16}H_{33}Me_2EtN^+$ -directed layered silicate, using a new protocol combining the results of XRD, solid-state NMR and DFT calculations to build, refine, and validate framework structural models using a comprehensive search across all possible structures. The final candidate structures were ultimately validated on the basis of their lattice energies, and the comparisons of calculated and experimental  $^{29}Si$  isotropic chemical shifts and  $^2J(^{29}Si-O-^{29}Si)$  couplings. Excellent agreement between all experimental and theoretical constraints suggested that three closely related structures referred to as structures number 2, 3, and 4 in ref. 24, and shown in yellow, red, and brown in Figure A.10, respectively, represent equally valid representation of the (unique) actual framework structure, within the limits of the modeling. In chapter C and D, these three candidate structures are considered for all our DFT calculations to study the local structure around of Al and B heteroatoms incorporated into their frameworks.

## **A.4 Heteroatoms in porous silicate materials and their importance**

### **A.4.1 Distribution of heteroatoms in zeolites and related materials**

It is well known that the acidities and thus the catalytic activity of porous materials are expected to correlate with the availability and accessibility (pore size, particle size and diffusion limitation) of active sites within the silicate framework. For example, most of the zeolites are aluminosilicates, which contain ample amounts of Al atoms that are responsible for the catalytic activity. The catalytic activity of these materials depends on several parameters, which mainly includes (i) the size of the cages and cavities, (ii) the nature of charge compensating species, (iii) the nature of framework atoms and (iv) particle sizes and morphologies etc. The arrangements of the tetrahedral sites (primarily SiO<sub>4</sub>) corresponding to the building units of these materials result in a wide range of molecular and/or pore architectures. Such pores may include a wide range of channels and cavities, and are the central point of attention for many industrial applications. In the absence of heteroatoms generating acidity, however, these frameworks are rather inert. The heteroatoms or active sites are mainly responsible for the framework acidities, and the catalytic properties can be tailored with the different acidic strength of distinct heteroatoms. For instance, the Si(OH)M species where M = Al, Fe, Ga and B, contributes to the framework acidities in the order: Al>Fe≈Ga>B.<sup>93-96</sup> Hence, these active sites have been extensively studied in the field of microporous and mesoporous materials. Furthermore, the distributions of these heteroatoms in the silicate framework directly or indirectly influence the materials activity and selectivity, but it may also affect their crystal structure and lattice parameters. The catalytic performance is closely interlinked with the coordination state of the heteroatoms.<sup>97</sup> For example four- or six-coordinated Al atoms implicates different ring structure in aluminum-containing zeolites. Hence efforts have been made to synthesize industrially efficient materials by considering all the factors that influence the heteroatoms distribution in the silicate framework.

There are good reasons to believe that the placement of heteroatoms alters the local structure of silicate framework and generates disorder. This is particularly true when there is a substantial difference in size between heteroatoms and the framework Si atoms. The presence of heteroatoms breaks, at the local level, the symmetry and periodicity of the three dimensional structure of zeolites. As a result the distribution of heteroatoms alters the local environment by generating compositional and geometric local disorder. The local modification driven by such heteroatoms have been observed in many systems, for example in beta zeolites.<sup>98</sup> On the other hand, the pore architecture of the zeolites or related materials is largely influenced by these active sites.<sup>99</sup> For example, Al in ZSM-5<sup>100</sup>, ZSM-11<sup>101</sup> and Theta-1<sup>102</sup> and Fe in ZSM-5<sup>103</sup> revealed particularly by non-empirical quantum chemical calculations. In most cases, however the incorporated heteroatoms represent local defects that have little impact on the average long-

range structure as probed by diffraction technique, even though they are suspect to modify the local structure. Thus, while the isomorphic substitution of framework Si atoms by heteroatoms is among the most important features accounting for the function of zeolites and related materials, it has been and continues to be a major challenge to establish the distribution and/or preferential incorporation of heteroatoms into their structure. On the other hand, the zeolite frameworks, which primarily consist of geometrically different, but chemically similar crystallographic sites (only fully condensed T sites, or  $Q^4$  sites) often suggest a near-random distribution of active sites. Very few zeolites have been successfully prepared with a specific substitution of certain crystallographic Si sites by heteroatoms such as Al or B, as will be discussed in the following section.

The isomorphic substitution of heteroatoms in a specific crystallographic site may be an important potential way to the control of the physico-chemical properties of porous materials. Even a partially preferential substitution may be sufficient to change their physico-chemical properties. However, there are currently no experimental techniques to unambiguously establish the distributions of heteroatoms such as Al or B within silicate frameworks. Before addressing the problem of the preferential incorporation of heteroatoms at certain crystallographic sites, however, one must first discuss the parameters that make it possible at all to substitute Si atoms by others in silicate frameworks, independent of the location of these sites.

The incorporation of heteratoms in the silicate framework could be achieved generally by two synthetic routes: (1) direct incorporation of heteroatoms under hydrothermal conditions during the synthesis and (2) post-synthetic treatments of zeolites to insert the desired heteroatoms.<sup>104</sup> In 1952, Goldsmith reported for the first time the isomorphous substitution of Ge into thomsonite material. After that, many research groups<sup>93,97</sup> have been and continue to be actively involved on this issue. Several factors controlling, influencing, and/or promoting substitution of heteroatoms, particularly in zeolites, were well explained by Ione and Vostrikova,<sup>105</sup> and also reported by Fricke *et.al.*,<sup>106</sup> as follows. (1) The ratio of radii of the framework atoms strongly impacts on the substitution of heteroatoms. The favored value of  $\Delta r/r$  is  $\leq 0.15$ , where  $r$  is the radius of atom to be replaced by another and  $\Delta r$  is the difference of the radii between those two atoms. (2) The coordination state of framework atoms play a significant role, the larger atoms easily replace the smaller atoms if the replacement leads to a decrease in the coordination state of larger atoms. (3) The electronegativity ratio and ionization potentials of exchanging atoms also have great contribution to the substitution. (4) The substitution of heteroatoms could be favored as long as the framework atoms keep the same long range electrostatic interactions. (5) Substitution also occurs when the charges of the exchanged atoms differed by 1, 2 or 3 units. (6) The exchanging atoms should not chemically react with each other. On the other hand, Pauling *et.al.*<sup>107</sup> described in the 1960's a criterion

where the isomorphic substitution derived from crystal chemistry and geometric considerations. Zeolite frameworks usually contain packages of negatively charged oxygen anions ( $O^{2-}$ ). The defected region apparently establishes the tetrahedral and octahedral vacancies. Thus, Pauling describes that, if  $\rho = r_{Me}/r_{O^{2-}} = 0.214-0.4$  ( $r_{Me}$  = radius of cation,  $r_{O^{2-}}$  = radius O atom), the cation will choose the location of tetrahedral sites or octahedral sites if  $\rho = 0.4-0.6$ .<sup>106</sup> Later, Deka *et.al.*<sup>108</sup> reported the influence of isomorphous substitution of active sites on the acidity of zeolites based on the charge density of hydrogen bond, bond length of bridging hydroxyl groups and their vibrational frequencies by using both Hartree–Fock and density functional theory calculations.

#### **A.4.2 Boron heteroatoms in porous silicate materials**

An important part of this manuscript is dedicated to the incorporation of Al and B heteroatoms in non-crystalline layered silicates. Hence this section focuses more specifically on the importance of Al and B atoms and their structural features upon insertion into the silicate framework. Boron is an important candidate heteroatom for the substitution into porous silicate materials. The weaker acidity of B atoms in contrast with the other heteroatoms (Al, Fe, Ga) offers the possibility to modulate the catalytic properties for those reactions that demand mild acidic catalysts.<sup>109-110</sup> Taramasso *et.al.*<sup>111</sup> reported for the first time the synthesis of B containing zeolites, which are sometimes referred to as boralites, in 1980. These B-zeolites may be more selective for certain catalytic reactions, as reported by Hoelderich *et.al.*<sup>112</sup> For example B-ZSM-5 was found to be more efficient and selective than Fe-ZSM-5 (MFI framework topology) in the conversion of 2-phenylpropanol to 1-phenylpropan-2-one. The weak acidity of B-zeolites, particularly the B-pentasil zeolite, plays a significant role during the conversion of acetals to enol ethers, as well as from methyl benzene and methanol to olefins. Vetrivel *et. al.*<sup>113</sup> described the possibility of substitution of B atoms at different framework sites in ZSM-5 zeolite structure by using semiempirical quantum chemical MNDO (modified neglect of diatomic overlap) approach. These calculations on the other hand suggest that the Lewis acidity of B-ZSM-5 is stronger than the Bronsted acidity in contrast with the Al-ZSM-5. This may be due to the larger electronegativity of B (2.0) than Al (1.6). The electron density of the bridging oxygen atoms is drastically reduced upon B incorporation in contrast with Al substitution, which further decreases the framework Bronsted acidity. The site preference for B atoms in the silicate framework is completely different in contrast with the other heteroatoms due to the smaller atomic size. As a consequence, it distorts the structure to the extent that diameter of the straight and sinusoidal channels considerably decreases, for example in B-ZSM-5.<sup>113</sup> As the concentration of B atoms increases, this generates a large amount of strain in the zeolitic framework which thus loses its stability. This explains why obtaining high Si/B ratios is still challenging, and also why the Si/B ratio of the product is always less than the precursor's. Moreover, the extent of B atoms incorporation may also

depend on the number of organic ions present inside the cages. The size of the organic ions also strongly influences the degree of B atoms incorporation. Another important feature is the acidic strength of all the incorporated B atoms was found to be uniform and completely independent of the site preferences.<sup>113</sup> Another important feature of borosilicate zeolites is that they can be post-synthetically modified by isomorphic substitution of B atoms by Al to prepare aluminosilicate zeolites (e.g., large-pore zeolites SSZ-24 and SSZ-31) that have not been possible to otherwise synthesize directly.<sup>114</sup>

As discussed earlier, two-dimensional layered silicates may often be precursors of 3D zeolites. These materials contain both fully condensed ( $Q^4$ ) and partially-condensed ( $Q^3$ ) crystallographic sites, which could be exploited to achieve preferential incorporation of heteroatoms. Many attempts were made to incorporate B atoms into layered silicate frameworks. Initially Millini and coworkers showed the substitution of B atoms into layered silicate ERB-1.<sup>115</sup> After calcination at 270°C, yields 3D microporous structure of MWW type material. Schwieger *et.al.*<sup>116</sup> reported the isomorphous substitution of B into the layered silicates which are identified as hectorite types, magadiite and kenyaite types. One step forward, recently Komura *et.al.*<sup>117</sup> reported the synthesis of layered borosilicate B-PLS-1 from layered silicate H-LDS. The dehydration-condensation of B-PLS-1 layered silicate at 550°C then forms CDS-1 zeolite exhibiting CDO topology. While substitution of B atoms in the above mentioned materials were studied systematically, none of them discussed the distribution or location of B atoms (preferential or random incorporation) in the silicate framework.

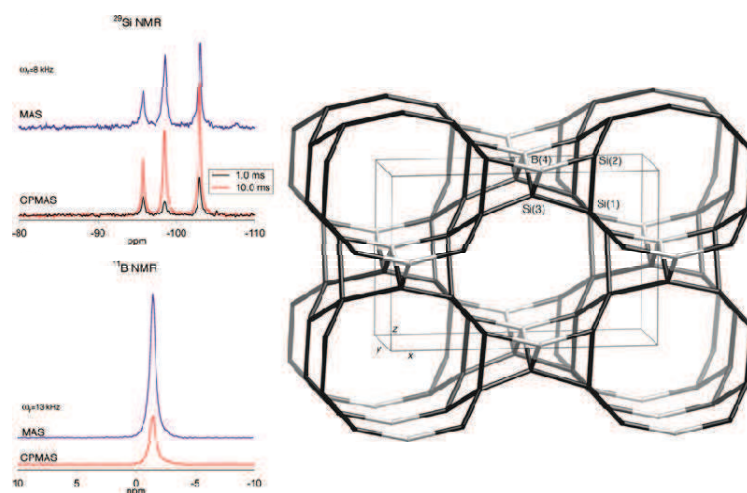


**Figure A.11** [Ref: Xie *et.al.*<sup>9</sup>]  $^{29}\text{Si}$  and  $^{11}\text{B}$  MAS NMR spectra of MCM-70 borosilicate zeolite (left). Crystal structure of MCM-70 (right).

Recently, Xie *et.al.*<sup>9</sup> reported that B atoms are fully incorporated at a specific crystallographic site in borosilicate zeolite MCM-70. Here the framework represents four crystallographic sites, three of which

are occupied exclusively by Si atoms and the fourth one is purely occupied by B atoms. This is well established by synchrotron powder diffraction data and  $^{29}\text{Si}$  and  $^{11}\text{B}$  MAS NMR data. As shown in the Figure A.11, it is clear from  $^{29}\text{Si}$  MAS NMR spectra (showing three  $^{29}\text{Si}$  peaks) that the framework contains only three distinct Si crystallographic sites. The well resolved  $^{29}\text{Si}$  signals further indicates the signature of non-random distribution of B in the sample, which was suggested earlier by Dorset *et.al.*<sup>118</sup> The  $^{11}\text{B}$  MAS NMR spectra shows single sharp peak at -1.47 ppm, consistent with the signature of 4-coordinated B atoms. The combination of all these data with the Rietveld refinement conducted on high-quality synchrotron X-ray diffraction data established that one of the four crystallographic sites is fully occupied by B atoms in MCM-70 material, the other three sites being exclusively occupied by Si atoms, which explains the perfectly ordered local environments observed by  $^{29}\text{Si}$  and  $^{11}\text{B}$  solid-state NMR. There is no evidence (to our knowledge) for the existence of a form of MCM-70 material (MVY framework topology<sup>119</sup>) with less B in the framework (no signature of Si/B disorder at the B crystallographic site), which indicates that framework B atoms cannot be considered as local defects in this case.

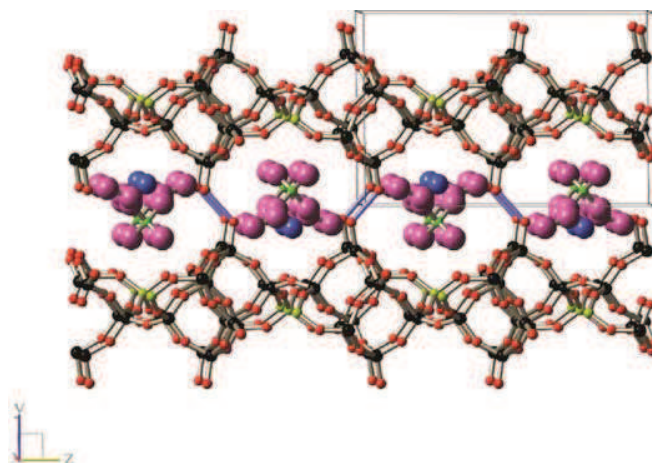


**Figure A.12** [Ref: Grünewald-Lüke *et.al.*<sup>120</sup>] Model of B-RUB-39 showing the specific location of T-site for B in the silicate layer (T-atom in green).

Grünewald-Lüke *et.al.*<sup>120</sup> also reported the incorporation of a small amount of B atoms into layered silicates and then formation of 3D zeolites by condensation of the layered precursor. They successfully synthesized the layered borosilicate B-RUB-39 in a single step reaction. The condensation of the silicate layers leads to the formation of 3D zeolite B-RUB-41 of RRO framework morphology. Figure A.12 shows the model of B-RUB-39 where B atoms are said to be substituted in a single crystallographic site, although the experimental evidence for this claim is somewhat insufficient from our point of view. These conclusions were primarily based on distance considerations derived from the Rietveld structure refinement of these materials. The crystal structure of B-RUB-39 depicts a slightly shorter d(T-O) bond

length for crystallographic site T5 (1.58 Å) than for the others (around 1.60 Å), which was interpreted as a preferential incorporation of B in Si-5, is the same feature was also observed in the calcined material B-RUB-41. The  $^{11}\text{B}$  and  $^{29}\text{Si}$  MAS NMR measurements are indeed in good agreement with the incorporation of the B atoms in a single crystallographic site, although they can hardly be used to confirm its location.

#### **A.4.3 Aluminum heteroatoms in porous silicate materials**

The frameworks of most of the natural and synthetic zeolites are composed of Si and Al atoms. It is primarily the stronger acidic nature of Al atoms in contrast with the other heteroatoms made Alumino zeolites so popular, and lots of efforts have been made, since many decades to investigate the heteroatom distribution and structural morphologies of Al-containing silicate materials. As for other heteroatoms, the distribution of Al atoms in the silicate framework indeed has direct impacts on the catalytic performance and selectivity. The alumino-zeolites include several classes of materials with different framework topologies such ranging from small cages or channels (e.g., delimited by six Si-member rings) to relatively large pores such as the 16-Si-member ring channels of zeolite ITQ-40.<sup>121</sup> The most widely employed zeolites are probably the ones having MFI types of frameworks, with their 3D network of interconnected 10-member ring channels which facilitates diffusion of guest molecules within the material. The most famous MFI-type zeolite is the aluminosilicate ZSM-5 (Si/Al ratios typically in the range of 5–100 and to infinity, in which case it is generally referred to as the silicalite-1 material), which is invented early in 1967 by Argauer and Landolt.<sup>122</sup>

Dedecek and coworkers<sup>123</sup> reported important work regarding the determination of the distribution of Al atoms in zeolites, and in the ZSM-5 material in particular. The electrostatic and Van der Waals interactions between cationic  $\text{Na}^+$  species, anions ( $\text{Cl}^-$ ,  $\text{NO}_3^-$ ) and hydrophobic  $\text{TPA}^+$  moieties with inorganic species provides insights onto the location of Al atoms. The distribution of Al atoms are establish on the basis of two main principles: (i) the placement of Al atoms in individual framework rings is crucial for the location of protons and metal ions, and (ii) the placement of Al atoms control the accessibility of protons or metal ions for guest molecules.<sup>124</sup> Such methods will consequently be able to make a difference between different groups of T sites based on their exposition to different types of ring structures, rather than between individual T sites, as shown in Figure A.13. On the other hand, Van Bokhoven *et.al.*<sup>125</sup> described a new technique called X-ray standing waves, which opens new promising perspectives for the determination of the specific occupancy of Al atoms in zeolites. The structural features and distribution of framework and extra-framework atoms in zeolites could be specifically derived by collecting the X-ray fluorescence or photoelectrons under the influence of standing waves. The resulting spectrum mainly reveals amplitude and phases of Fourier components yielding different

modulation curves for Al and Si atoms. This distinct behavior of Al and Si atoms has been used to establish their distribution in a simple model zeolite, scolecite, revealing in this case highly ordered location of the all Al atoms within one of the two crystallographic T sites (T1) being purely occupied by Al atoms and the other one (T2) only by Si atoms (similar to the case of B atoms in MCM-70 described above). It is hoped that this technique will in the future be extended to more complex frameworks with unknown Al/Si distributions, the current limitation being that the XSW analysis in such a case requires a higher number of Fourier components to resolve the large number of T-sites, which involves in particular further improvements of the instrumentation.

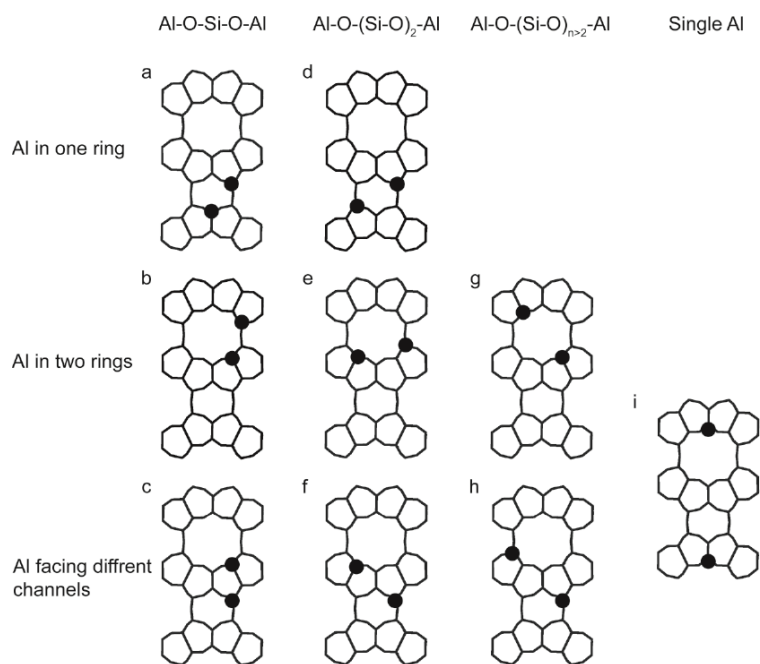


**Figure A.13** [Ref: Dedecek et. al.<sup>124</sup>] Distribution of Al atoms in different ring structures.

Solid-state NMR spectroscopy would seem to have a number of advantages to solve or contribute to solving the issue of Al (or B) heteroatom locations in porous silicates, with its local character, the high sensitivity of a number of NMR parameters to even subtle variations of the local composition and bonding geometry, and the high receptivity and natural abundance of <sup>27</sup>Al (and <sup>11</sup>B) nuclei. Despite these advantages, however, various studies focusing on Al distributions, very few have led to conclusive evidence of a preferential heteroatom distribution. The main limitation in almost all cases is the spectral resolution of the different NMR-active nuclei, which is too low to identify individual crystallographic sites when Al is present in the zeolite frameworks. While <sup>29</sup>Si NMR was used in early studies to establish the Al composition in zeolite frameworks consisting of a single T site, such as zeolite Na-Y,<sup>126</sup> this approach could not be extended to more complicated zeolite frameworks because <sup>29</sup>Si lines then very

rapidly broaden and overlap. Similar limitations apply to  $^{27}\text{Al}$  NMR, where, even by removing the quadrupolar broadening by advanced two-dimensional NMR techniques (so-called multiple-quantum (MQ)-MAS technique<sup>127</sup>), only very few distinct groups of sites (if any) among the total number of T sites present can be resolved in most cases.<sup>7,128-129</sup> This led so far to rather uncertain or ambiguous conclusions about the Aluminum distributions. More recent work by Van Eck, Kentgens and coworkers demonstrated how single-crystal  $^{27}\text{Al}$  NMR could be used to precisely establish Al distributions in zeolites by exploiting a specific NMR set up based microcoils to detect the NMR signal of very small samples.<sup>130</sup> This work, presented in some NMR conferences, has not been published to our knowledge but offers very interesting perspectives in this field.

While several studies suggest a non-random distribution of Al atoms within the framework of some zeolites, only indirect evidence is provided in most cases. Furthermore, controlling the heteroatom location to obtain a site-specific incorporation remains one of the most challenging challenges of materials science despite several decades of intensive research addressing this issue. The few cases where a fully preferential Al or B heteroatom distribution was observed, such as B atoms in MCM-70 zeolite or Al atoms in scolecite, are very peculiar situations where one of the crystallographic sites is fully occupied by the heteroatom, and where the structure does not exist without full occupancy of this site by the heteroatom. The heteroatom cannot in such cases be considered as a local defect, as is the case for vast majority of heteroatom-containing zeolites, lamellar, or porous silicates. In the general case however, the difficulties associated with the experimental determination of heteroatom locations in porous silicate materials are for a large part responsible for the lack of understanding of the synthesis routes capable of controlling their distributions. Another reason is that in zeolites, the ordered three-dimensional silicate framework is composed of chemically equivalent fully-condensed ( $Q^4$ ) sites. As a result the structural behavior of such sites upon heteroatom incorporation is expected to be very similar, leading to near-random or poorly-preferential distributions. Layered silicates such as those studied in this work are an interesting alternative as zeolite precursors in this respect, since their ordered structures are composed of chemically distinct  $Q^3$  and  $Q^4$  crystallographic sites. While incompletely-condensed  $Q^3$  sites may be present in zeolites, they correspond to (presumably) randomly distributed defects, in most cases, with the one exception of SSZ-74 zeolite, which has been shown to contain ordered Si vacancies, associated with ordered  $Q^3$  sites around it.<sup>8</sup>

## **A.5 Conclusion**

Porous silicate materials are industrially well known as solid acid catalysts. The applicability of these materials depends, among other things, on their porosity and extent of crystallinity. They are generally classified in the literature in three main categories: microporous, mesoporous, and lamellar

silicates. Because these materials share the same main building units in the form of  $\text{SiO}_4$  tetrahedra, they exhibit some similarities in their molecular-level properties, but also some remarkable differences. One of the most important examples of such differences is the stronger activities of the acid heteroatom sites incorporated in molecularly-ordered microporous frameworks as compared to the same type of sites incorporated in the molecularly-disordered frameworks of mesoporous silicas. While the positions of these tremendously important heteroatom sites within molecularly-ordered silicate frameworks could be established in a few cases where crystal sizes were large enough to perform single-crystal diffraction measurements, this remains an extremely challenging problem for the large majority of silicate-based materials. In this context, high-resolution solid-state NMR provides structural information at the molecular level that may be used to establish the local structure in both ordered and disordered materials.

Layered silicates are an important class of solid catalysts and of zeolite precursors, owing to their ability to transform in favorable cases into 3D zeolites. The surfactant-directed layered silicates which are the focus of the major part of this work, in particular, are among the first historical examples of materials that combine molecular-level order within their silicate sheets and mesoscopic (lamellar) order typical of surfactant-templated silica materials. They represent ideal model systems to study the local structures around heteroatoms incorporated in silicate-based catalysts.

---

# **Chapter B**

## **Methods and Materials**

---

### **B.1 Introduction**

The deep understanding of porous silicate materials at various length scales would not have been possible unless the input of novel characterization methods. This chapter is centered on the principles of experimental techniques, theoretical and synthesis aspects that are used to establish the distribution of heteroatoms in surfactant-directed layered silicates. In this respect, all experimental methods and synthesis criteria will be described in three main sections. Solid-state nuclear magnetic resonance (NMR) is the principal experimental technique employed here to investigate the local structure around the heteroatoms, and will be discussed in section **B.2**. This mainly includes a brief discussion of the basic principles of solid-state NMR and of the multi-dimensional NMR pulse sequences that are used to characterize the materials. On the other hand, the characterization of advanced materials by solid-state NMR alone is rarely sufficient to obtain a complete picture of the systems. Therefore, other experimental techniques such as, diffraction methods, Inductively Coupled Plasma (ICP) analyses and quantum chemical calculations have also been considered to characterize the layered silicates studied in this work. The principle of all these methods will be briefly explained in section **B.3**. Furthermore, synthesis of studied materials will be discussed in section **B.4**. This section focuses more specifically on the insertion of heteroatoms such as Al and B atoms into 2D silicate framework of non-crystalline layered silicate materials.

### **B.2. Measuring or Exploiting solid-state NMR interactions**

#### **B.2.1 NMR interactions in solids**

The nuclear spin  $I$  is the intrinsic quantum property of the atomic nucleus. These are very mobile in the solution state due to the molecular motion but rigid in the solid form and consequently present in many different orientations. As a result, each spin experiences local magnetic field that differs from the external magnetic field  $B_0$ , and depends on the orientation of its local environment with respect to the latter. Furthermore, nuclear interactions between the spins also depend on their relative orientations. The magnetic field around each nucleus and the resultant electronic cloud interacts with that of their neighboring nuclei. Such interactions between the nuclear spins correspond to internal spin interactions

and may be related either to spatial proximities (dipole-dipole interactions) or through bonding connectivities (indirect spin-spin or  $J$ -coupling interaction) between the atoms. In contrast, purely magnetic interactions between the nuclear spins with the external magnetic field are designated as the external spin interactions. The sum of both internal and external spin Hamiltonian gives total NMR hamiltonian ( $\hat{H}$ ) and could be written as,<sup>131</sup>

$$\hat{H}_{\text{total}} = \hat{H}_{\text{external}} + \hat{H}_{\text{internal}} \quad (\text{B.1})$$

Generally two kinds of external spin Hamiltonian or magnetic interactions are involved in an NMR experiment. Firstly, all nuclear spins interact with strong static magnetic field ( $B_0$ ), and secondly, smaller transverse pulsed radio-frequency fields ( $B_{\text{RF}}$ ) are applied to generate desired transition between the Zeeman energy levels of the nuclear spins. The internal spin Hamiltonian, on the other hand, depends on the NMR parameters of a number of nuclei, each nucleus experiencing the magnetic influence of neighboring nuclei. All these spin interactions makes the system extremely complex, with a resultant internal spin Hamiltonian that can be written as:

$$\hat{H}_{\text{internal}} = \hat{H}_{\text{CSA}} + \hat{H}_{\text{D}} + \hat{H}_{\text{J}} + \hat{H}_{\text{CQ}} + \hat{H}_{\text{others}} \quad (\text{B.2})$$

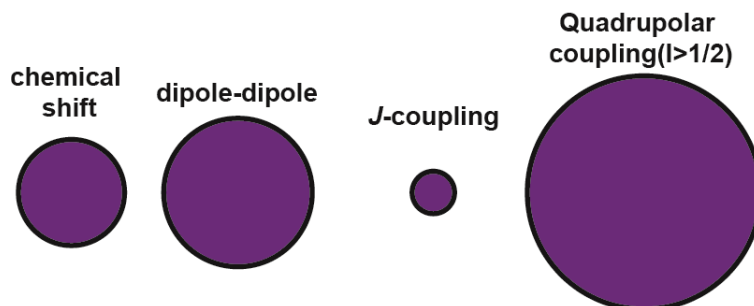


**Figure B.1** Relative magnitudes of NMR inteactions in solids.

In this formula,  $\hat{H}_{\text{CSA}}$  refers to the chemical shift anisotropy,  $\hat{H}_{\text{D}}$  to the dipole-dipole (also called direct spin-spin or dipolar) interactions,  $\hat{H}_{\text{J}}$  to the indirect spin-spin interactions (whose isotropic part is better known as scalar coupling),  $\hat{H}_{\text{CQ}}$  designates the quadrupolar interactions and  $\hat{H}_{\text{others}}$  includes some other interactions such as hyperfine Hamiltonian if the spin system is paramagnetic. Figure B.1 pictures the relative strength of the different contributions to the NMR Hamiltonian in solids. For nuclei with a spin quantum number  $I > \frac{1}{2}$  (quadrupolar nuclei), one can expect a strong interaction between the nucleus and the surrounding electric field gradient (of the order of several MHz), in addition to the magnetic field. This is the quadrupolar interaction, which often causes dramatic broadening of solid-state NMR spectra. This interaction is absent for spin  $\frac{1}{2}$  nuclei, and the NMR anisotropies are comparatively smaller as a

result than for quadrupolar nuclei. The second largest anisotropy is generally the dipole-dipole interactions (typically tens of kHz), after which comes the chemical shift anisotropies (typically  $10^3$  to  $10^4$  Hz), and, last the  $J$ -coupling interaction, which typically ranges between a few Hz to a few hundreds of Hz.

**Dipole-dipole interactions (D):** Each nuclear spin is associated with a magnetic moment, which interacts with the nearby nuclear spins. These spatial interactions may occur between nuclear spins of the same (homonuclear case) or of different kinds (heteronuclear case). Such spatial or direct spin-spin interactions are measured in terms of dipolar couplings (D). The dipolar Hamiltonian between nuclear spins I and S is given by,

$$\hat{H}_{IS} = -d(3\cos^2\theta - 1)I_zS_z \quad (\text{B.3})$$

Here,  $\theta$  is the angle between the external magnetic field and vector joining two nuclear spins, and  $d$  is the dipolar coupling constant,  $d = -\frac{\mu_0}{4\pi} \frac{\gamma_I \gamma_S \hbar}{r_{IS}^3}$  (in Hz) (B.4)

Where  $\mu_0 = 4\pi * 10^{-7} \text{ Hm}^{-1}$  is the permeability of free space,  $r_{IS}$  is the distance between the two nuclear spins (in metres),  $\gamma_I$  and  $\gamma_S$  are the magnetogyric ratios ( $\text{rad s}^{-1}$ ), and  $I_z$  and  $S_z$  are the  $z$ -components of two nuclear spins I and S, respectively. The dipolar interactions are typically averaged out due to isotropic reorientations of the molecules on timescales that are considerably faster than the NMR measurement ( $10^{-8}$  to  $10^{-9}$  s), but they are very strong in the NMR spectra of solids collected under static conditions. The orientation dependence of the dipolar interaction with respect to the external magnetic field is given by  $(3\cos^2\theta - 1)$  term of the dipolar Hamiltonian in equation B.3. In a polycrystalline sample, the spins are oriented in all possible directions with equal probabilities<sup>132</sup> and as a result resonates at different NMR frequencies. The resulting spectrum is a powder pattern, which for a system of two nuclear spins is called Pake<sup>133</sup> pattern, as shown in Figure B.2.

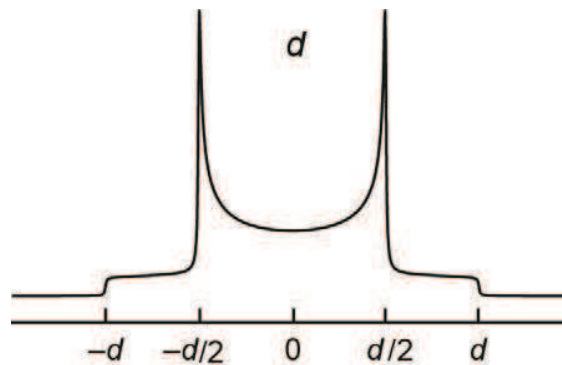


**Figure B.2** [Ref: Laws et.al.<sup>132</sup>] Dipolar Pake doublet in solids

**Chemical shift anisotropy (CSA):** The external magnetic field  $B_0$  causes the electrons to circulate, and this current generates in turn an additional magnetic field that adds or subtracts (i.e. “shielding”) the external magnetic field. The CSA reflects the fact that the electronic cloud around the spins may not always be spherically symmetric, causing differed orientation of electronic cloud with respect to  $B_0$  to yield very different NMR frequencies. The resulting magnetic field experienced by the desired nucleus is typically in the order of  $1 \times 10^6$  times smaller than  $B_0$ , which is nevertheless large enough to make in favorable conditions (for example in a liquid) clear distinction between different nuclear spins of a given type on the basis of their different local environments. The CSA varies linearly with the external magnetic field and is given in units of parts per million. The strengths of CSA interactions typically range between 10 ppm for light atoms with a relatively symmetric environment ( $^{29}\text{Si}$   $Q^4$  sites, for example) to 1000 ppm for heavier nuclei. The local magnetic field experienced by the nuclei is the sum of the applied magnetic field ( $B_0$ ) and induced magnetic field ( $B_{CS}$ ), which is given by,

$$B_{\text{Local}} = B_0 + B_{CS} \Rightarrow (1 + \sigma) B_0 \quad (\text{B.5})$$

where,  $\sigma$  is the chemical shielding tensor that determines the orientation dependence of chemical shielding interactions. The isotropic part of  $\sigma$  can be written as,

$$\sigma_{\text{iso}} = \frac{1}{3} (\sigma_{xx} + \sigma_{yy} + \sigma_{zz}) \quad (\text{B.6})$$

The total chemical shift Hamiltonian is given by,

$$\hat{H}_{CS} = -\hbar\omega_0\sigma_{\text{iso}} I_z - \frac{1}{2} \hbar\omega_0\delta_{CS} ((3 \cos^2\beta - 1) + \eta_{CS} \sin\beta^2 \cos 2\alpha) \quad (\text{B.7})$$

Where  $\omega_0 = -\gamma B_0 (1 + \sigma_{\text{iso}})$  is the isotropic chemical shift,  $\alpha$  and  $\beta$  are the Euler angles between  $B_0$  and principal axis system (PAS). The anisotropic terms  $\delta_{CSA}$  and the asymmetry  $\eta_{CS}$  can be written as,

$$\delta_{CSA} = \sigma_{zz} - \sigma_{\text{iso}} \quad (\text{B.8})$$

$$\eta_{CS} = (\sigma_{yy} - \sigma_{xx}) / \delta_{CS} \quad (\text{B.9})$$

While only the isotropic part contributes to the frequencies in liquid-state NMR spectra, which makes it possible to distinguish a number of even slightly different chemical environments, the CSA gives rise in solids under static conditions to broad powder patterns that will cause chemically different sites to dramatically overlap with each other.

**Scalar (or indirect spin-spin) couplings (J):** The bonding interactions between the nuclear spins through electrons give rise to an interaction called indirect spin-spin couplings or scalar couplings (although this

designation should be in principle be restricted to the isotropic contribution to this interaction) or  $J$  couplings. These through-bond interactions are most often intramolecular, but can also be inter-molecular in the case of hydrogen bonds, for example. In an isotropic spin system (in the liquid state, or in solids under magic-angle spinning, see below), the  $J$ -couplings are independent of the orientation and provide direct information on the molecular structure by establishing the connectivities. The magnitude of  $J$ -couplings is generally considerably smaller than the dipolar and CSA interactions in solids, but they can nevertheless be exploited under certain conditions. The isotropic part of the  $J$ -coupling Hamiltonian between the two nuclear spins I and S can be written as,

$$\hat{H}_J = 2\pi J_{IS} I_z S_z \quad (\text{B.10})$$

Where  $J_{IS}$  is the scalar couplings between the nuclear spins I and S. We note that the anisotropic part of this interaction can also be measured in some cases, but this is beyond the scope of this work.

**Quadrupolar couplings (CQ):**

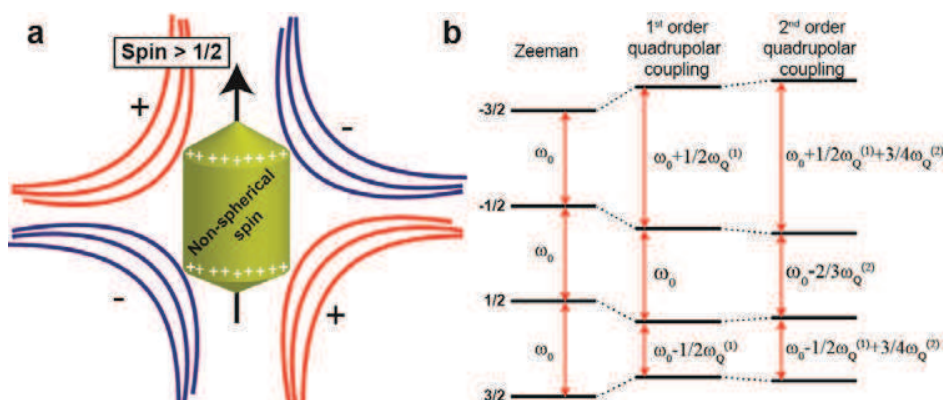


**Figure B.3** (a) Interaction of non-spherical nuclei ( $spin > 1/2$ ) with the electric field gradient (EFG), (b) Energy level diagram of spin-3/2 system in presence of Zeeman field, first order and second order quadrupolar interaction.

The quadrupolar nuclei ( $I > 1/2$ ) possess non-spherical charge distribution giving rise to an electric quadrupole moment.<sup>132</sup> In the presence of an external magnetic field the quadrupole moment of the nuclear spin interacts with the electric field gradient (EFG) that is generated by surrounding electrons, as shown in Figure B.3a. For a nuclear spin I, there will be  $2I+1$  spin states and  $2I$  possible transitions. The quadrupolar interactions ( $\hat{H}_Q$ ) is larger than all other NMR anisotropic interactions and is determined by two terms: the 1<sup>st</sup> and 2<sup>nd</sup> order quadrupolar coupling Hamiltonians,

$$\hat{H}_Q = \hat{H}_Q^{(1)} + \hat{H}_Q^{(2)} \quad (\text{B.11})$$

## Methods and Materials

The first order quadrupolar coupling is given by,

$$\omega_Q^{(1)} = \frac{3eqeQ}{2I(2I-1)\hbar} \quad (\text{B.12})$$

Where,  $e$  is the electron charge,  $eq$  is the  $z$  component of the EFG and  $Q$  is the nuclear quadrupole moment. The SI unit of  $\omega_Q$  is given by  $\text{rad}\cdot\text{s}^{-1}$ . As showed in the Figure B.2b, the energy level diagram of spin-3/2 nuclei reveals three transitions,  $-3/2$  to  $-1/2$ ,  $-1/2$  to  $1/2$  and  $1/2$  to  $3/2$ . Here, central transition from  $-1/2$  to  $1/2$  is unaffected by the 1<sup>st</sup> order quadrupolar Hamiltonian. But, the satellite transitions  $-3/2$  to  $-1/2$  and  $1/2$  to  $3/2$  are altered by an amount that is proportional to the 1<sup>st</sup> order quadrupolar coupling constant ( $\omega_Q^{(1)}$ ). This is again reflected for powdered samples by extremely broad NMR powder patterns. The 2<sup>nd</sup> order quadrupolar hamiltonian  $H_Q^{(2)}$  possess coupling constant  $\omega_Q^{(2)}$ , given by,

$$\omega_Q^{(2)} = (\omega_Q^{(1)})^2/2\omega_0 \quad (\text{B.13})$$

which interestingly scales down with the magnetic field, in contrast with the CSA interaction, for example.

### B.2.2 Principle of 1D and 2D NMR spectroscopy

The physical properties of nuclear spin are the basis for the NMR spectroscopy. In general, the spinning nuclei possess angular momentum  $P$  and the charge. The motion of this charge results to an associated magnetic moment, which is given by

$$\mu = \gamma P \quad (\text{B.14})$$

Where,  $\gamma$  is the magnetogyric ratio and found to be constant for any given nuclei.

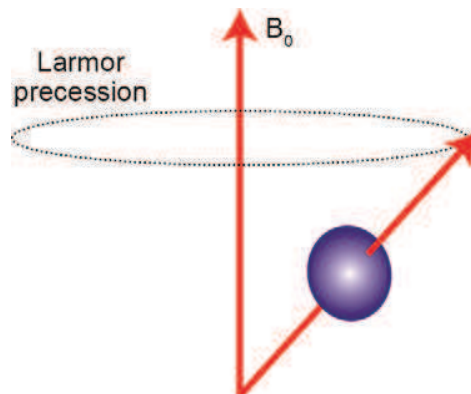


**Figure B.4** Schematic representation of larmor precession at static magnetic field.

In the presence of external magnetic field, the nuclear spins exhibits two orientations (for spin  $\frac{1}{2}$  nuclei, for example): parallel (the  $\alpha$  state) or anti-parallel (the  $\beta$  state) to the magnetic field. The effect of static magnetic field on the nuclear spins (in classical terms) generates a circular motion called precession around  $\mathbf{B}_0$  (Fig. B.4). The rate of precession, described in terms of angular velocity, is called the Larmor frequency of the nucleus. The direction of the precession is directly related to the sign of the magnetogyric ratio. The resonance happens when the nucleus changes its state by absorbing the quantum energy of applied electromagnetic radiation. This happens when frequency of the applied perturbation matches the larmor frequency, which then fulfills the resonance condition. The corresponding energy is given by,

$$\Delta E = h\nu = h\gamma B_0/2\pi \quad (\text{B.15})$$

where  $h$  is the Planck's constant. On the other hand, the  $\alpha$  and  $\beta$  spin states have slightly different energies, and their relative populations at thermal equilibrium are governed by the Boltzmann's distribution law,

$$N_\alpha/N_\beta = e^{\Delta E/k_B T} \quad (\text{B.16})$$

Where  $N_{\alpha,\beta}$  represents the number of nuclei in the  $\alpha$  and  $\beta$  states,  $k_B$  the Boltzmann constant and  $T$  is the temperature. This small difference in population generates a fraction of bulk-magnetization along the Z-axis (the direction of  $\mathbf{B}_0$ ). A radio frequency (RF) irradiation applied perpendicular to the magnetic field along a direction that rotates at or very close to the Larmor frequency (on-resonance irradiation) during an appropriate duration may flip all or part of this magnetization to the transverse plane. This magnetization then freely evolves for certain duration under the effect of the local molecular interactions and the corresponding signal can be detected as an electric current induced in the coil previously used to generate the RF excitation, in the form of Free Induction Decay (FID). This time domain signal  $S(t_2)$  or FID is converted into frequency domain  $S(\omega_2)$  by Fourier Transformation (FT).

$$S(t_2) \xrightarrow{FT} S(\omega_2) \quad (\text{B.17})$$

The 1D NMR spectrum<sup>134</sup> is a plot of signal intensity (y-axis) versus resonating frequency of nuclei (x-axis). In many cases, one or even several 1D NMR spectra may not be sufficient to fully characterize the molecular or local structure since many chemical and/or spectral features may overlap in the spectra, making it difficult to disentangle individual contributions. This can often be solved by detecting an NMR signal in a second dimension.

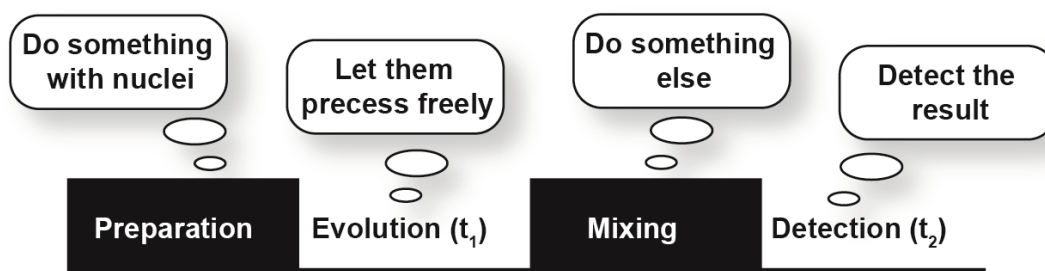


**Figure B.5** Schematic general representation of 2D NMR method

Appropriately-chosen two-dimensional (2D) NMR spectra may provide more detailed information on the molecular structure than the combination of individual 1D NMR spectra. 2D NMR experiments generally consist of 4 steps: the preparation, evolution ( $t_1$ ), mixing and detection ( $t_2$ ) periods, as shown in Figure B.5. During the preparation period, a set of RF pulses generates magnetization coherences, and this part also includes the delays required to let the spins relax to the equilibrium state. Then evolution of the nuclear spins takes place under the desired Hamiltonian, which will give rise to the signal in the so-called indirect dimension. The modulation taking place during this period is not detected directly (via a current induced in the coil) but indirectly (hence the name of the corresponding dimension) via a modulation of the signal detected at the end, as a function of the  $t_1$  evolution time. All spin interactions can be manipulated into observable signal by applying carefully designed series of pulses and/or free-evolution delays during the mixing period. During these, the magnetization is either transformed into a state where it can then evolve under a different Hamiltonian, or transferred to other spins on the basis of their mutual (direct or indirect) spin-spin interactions. Then signal is detected as a function of time during detection period. 2D NMR spectra contain two frequency axes and/or most chemical shift scales. The signal is the result of the Fourier Transform (FT) of free induction decays obtained in both indirect (F1) and direct (F2) dimensions:

$$S(t_1, t_2) \xrightarrow{FT} S(\omega_1, \omega_2) \quad (\text{B.18})$$

Figure B.6 shows the example of a homonuclear correlation NMR experiment, in which the 2D spectrum mainly contains diagonal correlation peaks (A and B) corresponding to cases where the signal evolving during the  $t_1$  and  $t_2$  evolution periods were the same, meaning that the corresponding magnetization was not transferred, or transferred to a site with identical chemical shift. The cross peaks (X) are the result of nuclei that exchanged the magnetization during the mixing time, such that the frequency detected during the  $t_1$  and  $t_2$  evolution periods were different. The presence of such cross peaks is the signature of the existence of a spin-spin interaction that can be used to generate such a magnetization transfer.

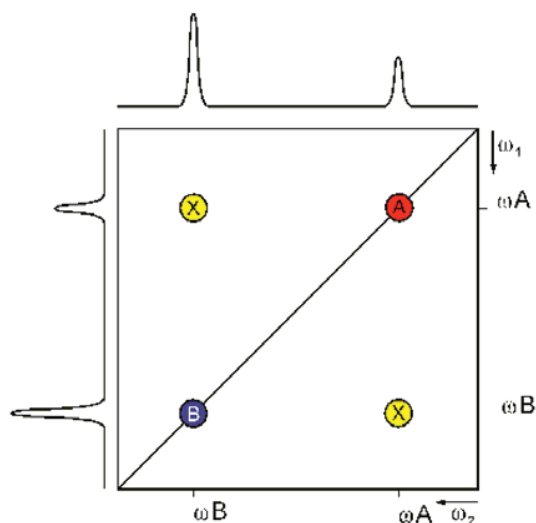


**Figure B.6** [Ref<sup>135</sup>] Schematic representation of a typical 2D NMR spectrum representing in this case a correlation between the same chemical shift information in both dimensions (homonuclear correlation spectrum).

**Transverse dephasing measurements based on spin-echo experiments:** The solid-state NMR spectra are strongly affected by homogeneous and inhomogeneous interactions, which in turn intensify the line broadening. Such interactions could be discriminated and identified by measuring transverse dephasing rates.<sup>136-140</sup> Inhomogeneous contributions to the broadening, which include in particular chemical shift dispersion due to structural disorder, magnetic field inhomogeneities, or bulk magnetic susceptibility, may typically be refocused by a spin echo. This means that the signal decay that occurs during the spin echo is due to the other contributions to the broadening. This may be expressed as follows. The total dephasing rate ( $R_2^*$ ) of the NMR signal directed in a standard experiment is given by:

$$R_2^* = 1/T_2^* \quad (\text{B.23})$$

where  $T_2^*$  is the total transverse dephasing time associated with the observed spectral broadening.  $R_2^*$  may also be written as,

$$R_2^* = R_2'(\text{homogeneous}) + R_2''(\text{inhomogeneous}) \quad (\text{B.24})$$

Where,  $R_2' = 1/T_2'$  is the non-refocusable contribution to the transverse dephasing rate, and  $R_2'' = 1/T_2''$  the refocusable contribution. By definition,  $R_2'$  governs to the signal loss (or dephasing) during a spin echo. This non-refocusable dephasing rate  $R_2'$  includes incoherent contributions due to stochastic processes such as transverse relaxation or chemical exchange (generally slow in rigid solids), and, most relevant here, coherent contributions primarily due to residual dipolar couplings. The latter can in

principle be experimentally modified or even quenched, for example by changing the spinning frequency or the quality of heteronuclear decoupling. This property of the coherent contributions to the homogeneous (or non-refocusable) transverse dephasing time was used in this thesis work to probe the interactions between heteroatoms and nearby protons.

The pulse program shown in Figure B.7 was used to measure the transverse dephasing times  $T_2'$  to be used as a probe of residual dipolar couplings to nearby protons. Hence, the resultant  $T_2'$  values provides structural insights probing respective chemical interactions.

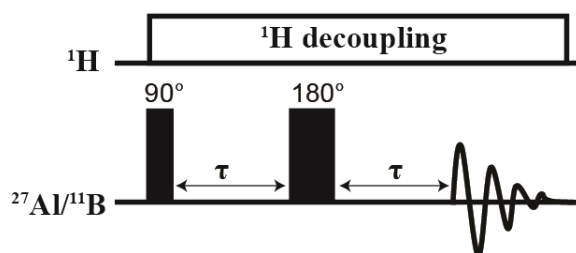


**Figure B.7** Pulse program of spin-echo experiment

The above figure describes the spin-echo pulse programme for  $^{27}\text{Al}$  or  $^{11}\text{B}$  nuclei, with heteronuclear  $^1\text{H}$  decoupling. DFS pulses (not showed in the figure) were applied prior to the excitation in order to enhance the signal. The pulse sequence starts with  $90^\circ$  pulse, which flips the magnetization to the transverse plane (xy plane). Then nuclear spins evolve during the free-evolution period  $\tau$  and are then refocused by a  $180^\circ$  pulse. Parts of the signal that were successfully refocused by the pulse evolve back to their initial phase at the end of the second free evolution period  $\tau$ , whereas non-refocusable parts keep dephasing, resulting in signal loss. The intensity of the NMR signal at the end of the sequence is given by,

$$I(2\tau) = I(0) \exp[-2\tau/T_2'] \quad (\text{B.25})$$

Interactions with nearby protons are probed by playing with the heteronuclear spin decoupling applied during the echo, with non-refocusable transverse dephasing rates that increase dramatically when heteronuclear decoupling is turned off in protonated environments.

### **B.2.3 Sensitivity and resolution enhancement**

The characterization of materials by solid-state NMR is a difficult task. One of the main reasons is their poor sensitivity and resolution due to the large anisotropic interactions. In addition, low natural abundance and low gyromagnetic ratio of NMR active nuclei often leads to poor sensitivity. In the case of quadrupolar nuclei, the large quadrupolar interactions further contributes to the spectral broadening and the resulting lack of resolution. Nevertheless, many technical and methodological improvements have been introduced to increase the sensitivity and/or resolution and obtain NMR spectra that can reveal

important chemical information. The most commonly-used techniques in solid-state NMR are the magic angle spinning (MAS) that averages the dipolar couplings and CSA, the removal of residual dipolar couplings by homo- and heteronuclear decoupling schemes and lastly, the transfer of magnetization from sensitive and abundant nuclei to less sensitive and less-abundant nuclei via cross-polarization. Furthermore, signal enhancement can be achieved especially for half-integer quadrupolar spin systems by using special techniques designed to enhance the initial magnetization, such as the adiabatic frequency sweeps. These techniques and methodologies are briefly described in this section.

**Magic angle spinning (MAS):** In 1950 Andrew<sup>141</sup> and Lowe<sup>142</sup> came up with new ideas to average the dipolar and CSA interactions. They demonstrated the possibility of obtaining a solid-state NMR spectrum similar to solution-state spectra by spinning the sample at magic angle that correspond to angle between the rotor and external magnetic field ( $54.74^\circ$ ), as shown in the Figure B.8a. The dipolar coupling and CSA Hamiltonians both contain a  $3\cos^2\theta-1$  term that reduces to zero for  $\theta = 54.74^\circ$ , where  $\theta$  is the angle between  $B_0$  and rotor axis. Hence, fast magic angle spinning (MAS) averages the dipolar couplings and chemical shift anisotropy to their isotropic value (zero for the dipole-dipole interactions and the isotropic chemical shift for the CSA), which considerably increases the resolution (and as a result the signal to noise) of the spectrum.

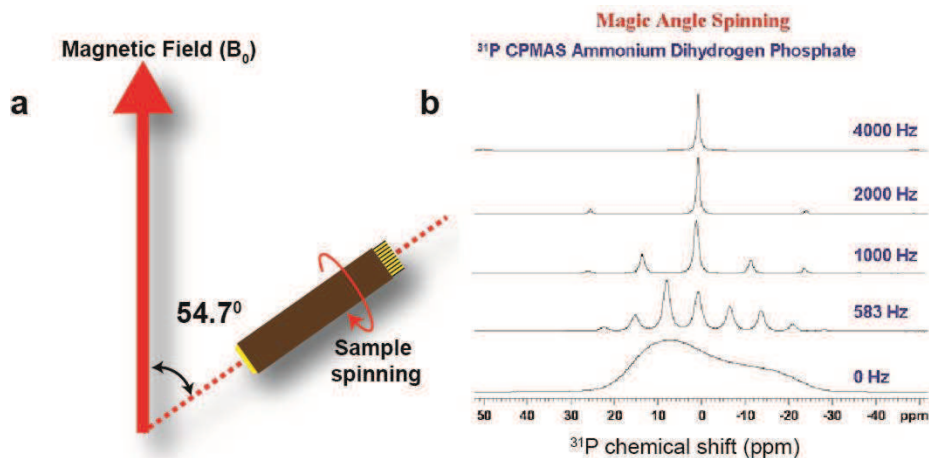


**Figure B.8** (a) Magic angle spinning (MAS) of the sample rotor with respect to the external magnetic field ( $B_0$ ) (b)  $^{31}\text{P}$  NMR spectra with respect to magic angle spinning [Ref<sup>143</sup>].

As illustrated in Figure B.8, if the spinning frequency is less than CSA then the isotropic lines with small intensity are observed on both side of the central (i.e. isotropic) peak at distances equal to multiples of the spinning frequency. These are called spinning side bands, and their envelope is often used to measure CSA tensor. Technically speaking, the maximum spinning speed attainable is inversely

## *Methods and Materials*

proportional to the rotor dimension. Nowadays, advanced NMR probes are available, in which we 0.75 mm rotors can be spun up to 110 kHz (Nishiyama *et.al.*). Incomplete averaging of the dipolar interactions by the magic-angle spinning will typically result instead in a broadening of the central and spinning side bands, which will decrease with increasing spinning speeds. For example, as shown in Figure B.8b, static  $^{31}\text{P}$  NMR spectrum of ammonium dihydrogen phosphate is relatively broad reflecting dominated CSA and dipolar contribution. At spinning speed 583 Hz, it partially averages the CSA that results several spinning side bands. The separation between two peaks is 583 Hz. Increasing the spinning speed to 1 kHz reduces the residual dipole-dipole interactions, which yields considerably narrower central peak and side bands than at 583 Hz. In addition, the number of sidebands reduces, which further increases the signal of the remaining bands (the integral is kept constant). At higher spinning speeds the sensitivity and resolution of the isotropic peak keep increasing to the point where a single sharp NMR peak associated with the one crystallographic P site of this material is observed.

***MAS of quadrupolar nuclei:*** Quadrupolar interactions contain first and second order anisotropic terms. First order terms can in principle be averaged to zero by MAS, but in practice their magnitude is such (typically several MHz) that satellite transition only split in a wide number of sidebands spreading over hundreds or thousands of ppm. However, the second order terms are only scaled down but not averaged out with MAS. This can be articulated in terms of zeroth-, second- and fourth-order Legendre polynomial,  $P_n(\cos\theta)$ , where  $P_0(\cos\theta) = 0$ .

$$P_2(\cos\theta) = (3\cos^2\theta - 1) \quad (\text{B.19})$$

$$P_4(\cos\theta) = (35\cos^4\theta - 30\cos^2\theta + 3) \quad (\text{B.20})$$

the averaged 2<sup>nd</sup> order quadrupolar term can then be written as,

$$(\omega_Q^{(2)})_{\text{rot}} = A_0 + A_2 P_2(\cos\beta) + A_4 P_4(\cos\beta) \quad (\text{B.21})$$

Where  $\beta$  is the angle between the magnetic field and rotor axis,  $A_2$  and  $A_4$  are the functions of  $\omega_Q$ ,  $\omega_0$  and  $\eta$  is the orientation of the EFG tensor with respect to the rotor axis.

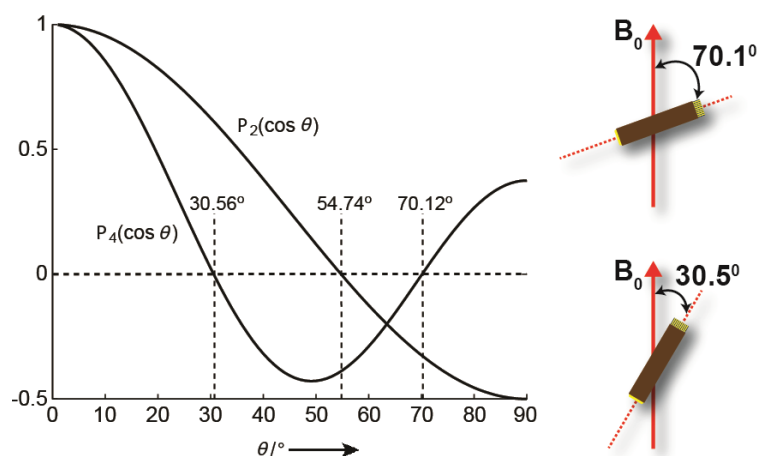


**Figure B.9** [Ref: Sun *et.al.*<sup>144</sup>] Plot showing second and fourth order Legendre polynomials as a function of  $\theta$ , while  $P_2 \cos \theta = 0$  at magic angle  $54.74^\circ$  and  $P_4 \cos \theta = 0$  at angle  $30.56^\circ$  and  $70.12^\circ$ .

As illustrated in Figure B.9, the rotor axis orientations that would cause the second-order quadrupolar interaction to vanish are different from the magic angle, which causes the first-order interaction to vanish. Hence, the only solution to completely average down the quadrupolar interaction is a double rotation around two different axis. Technical solutions actually exist, with double-rotation NMR probes,<sup>145-147</sup> but these are so challenging to design (and sometimes to operate) that very few have been commercialized. NMR spectroscopists usually work instead directly with the second-order quadrupolar powder pattern, which provides important NMR information, and/or use advanced methodologies such as the multiple-quantum MAS (MQ-MAS) 2D experiment,<sup>148</sup> which have been designed to remove the second-order quadrupolar broadening in the indirect dimension.

The line shape of NMR spectrum of quadrupolar nuclei (e.g.  $^{27}\text{Al}$ ) reveals the quadrupolar coupling constant and asymmetry parameter, as shown in Figure B.10. Here,  $^{27}\text{Al}$  spectra are simulated at different quadrupolar coupling constant by fixing isotropic chemical shift to 55 ppm (typical of 4 coordinated Al atoms) and asymmetry parameter to 0, and at different asymmetry parameter by fixing isotropic chemical shift again to 55 ppm and quadrupolar coupling constant to 2 MHz. At magic angle spinning,  $^{27}\text{Al}$  spectra are relatively sharper associated with different quadrupolar line shape at different condition, whereas at static condition the spectra are broad and unresolved.

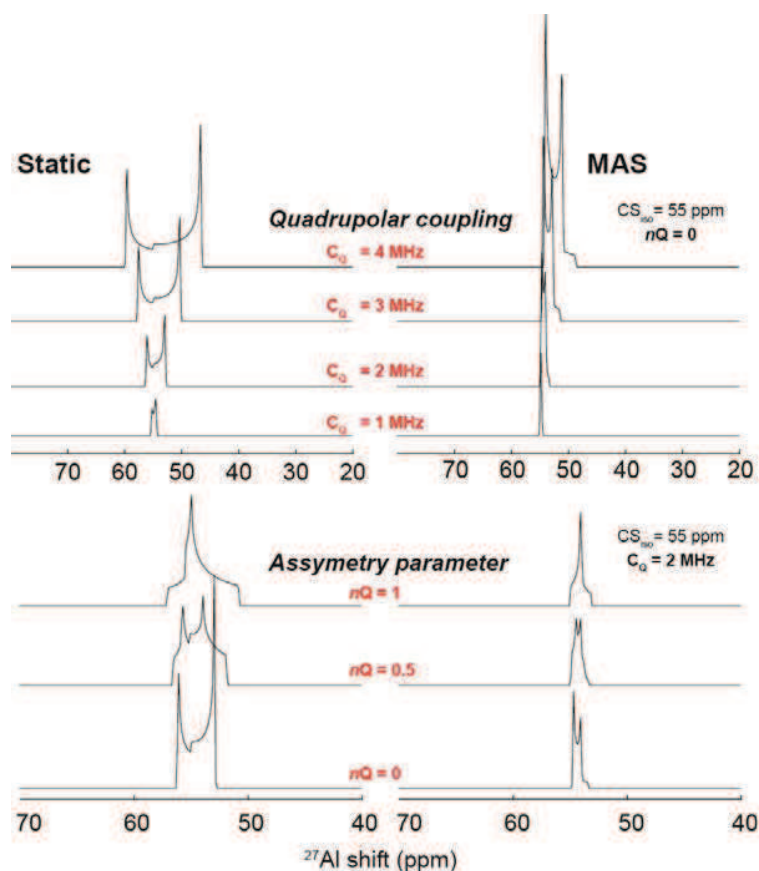


**Figure B.10**  $^{27}\text{Al}$  NMR spectra were simulated by using Dmfit program at static and magic angle spinning (MAS) condition, which shows variability in line shapes and distribution at different quadrupolar coupling constant and asymmetry parameter. The simulation was done by considering the magnetic field at 17.6 T.

**Heteronuclear decoupling:** Another important technique implemented in NMR spectroscopy to improve the sensitivity and resolution of NMR spectra is heteronuclear spin decoupling. The chemical features revealed by broad NMR signatures in the solid-state NMR spectrum often dominated by heteronuclear dipolar couplings. This is particularly seen in the protonated solids, while exploiting isotropic chemical shift of nucleus for example  $X = {}^{13}\text{C}$ ,  ${}^{29}\text{Si}$  or  ${}^{31}\text{P}$ , which are strongly coupled by  ${}^1\text{H}$  dipolar interaction. As a result, X nucleus experiences a strong  ${}^1\text{H}$ -X heteronuclear dipolar interaction, which is reflected by broad NMR peaks. However, these interactions could be averaged to obtain narrow lines by means of two approaches. First approach is averaging the dipolar interactions by spinning the sample at magic angle, which is called magic angle spinning. The second approach is eliminating the  ${}^1\text{H}$  interactions on X nucleus by manipulating the  ${}^1\text{H}$  spins in such a way that, over the time, there effect on X nucleus is averaged to zero. This is called heteronuclear  ${}^1\text{H}$  spin decoupling. The  ${}^1\text{H}$  spins parallel to the  $B_0$  (spin up)

produces a shift in the resonance frequency of a nucleus X and the  $^1\text{H}$  spins anti-parallel to  $B_0$  (spin down) also produces shift, which is opposite to the former. Then by applying RF pulses constantly on the  $^1\text{H}$  channel, rotates the spin up and spin down state and averages heteronuclear dipolar couplings between  $^1\text{H}$  and X nucleus. Thus it averages the  $^1\text{H}$  magnetic moment to zero and presents narrow peaks in X spectrum. This is called continuous-wave (CW) spin decoupling. In the recent days efforts have been made on to develop new efficient  $^1\text{H}$  heteronuclear spin decoupling techniques. This mainly includes TPPM,<sup>149</sup> SPINAL64,<sup>150</sup> eCM<sup>151</sup> and XiX<sup>152</sup> etc.

**Cross-polarization:** The gyromagnetic ratio of NMR active nuclei and their natural abundance both contributes to the sensitivity of solid-state NMR spectra. For example, the rare nuclei (with low natural abundance) such as  $^{13}\text{C}$  or  $^{29}\text{Si}$  require long experimental times to collect a decent NMR spectrum. This is mainly because of (i) low gyromagnetic ratio, (ii) low natural abundance and (iii) long longitudinal  $T_1$  relaxation rates which usually demand long recycling delays. One experimental approach that provided a breakthrough for enhancing the signal of such rare nuclei is the cross-polarisation (CP)<sup>153</sup> technique. The basic principle of the CP experiment is to transfer the magnetization from abundant nuclei with high gyromagnetic ratio (typically  $^1\text{H}$  or  $^{19}\text{F}$ ) to rare nuclei such as  $^{13}\text{C}$  or  $^{29}\text{Si}$  through dipolar couplings. The pulse sequence of CP technique is showed in Figure B.11.

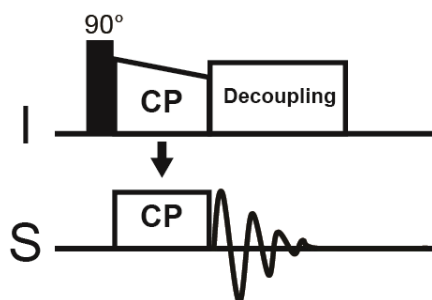


**Figure B.11** Cross-polarisation pulse sequence with a ramp amplitude shape on the  $^1\text{H}$  channel.

In a CP experiment, the repetition rate between each scan is limited by the  $T_1$  of the abundant nuclei (spin I), which, in the case of protons, for example, is often considerably smaller than that of rare nuclei (S). A  $90^\circ$  pulse on the I channel flips the magnetization to the transverse plane, after which it is locked in the transverse plane by applying a long pulse along its direction. Magnetization transfer is achieved by applying at the same time another long pulse on the S channel with pulse field strengths on the I and S channels matching the Hartmann-Hahn condition.<sup>154</sup> The signal, coming from the I spins may then be detected on the dilute S spins channel. The Hartmann-Hahn condition for a static solid is given by,

$$\omega_{\text{RF}}^{\text{I}} = \omega_{\text{RF}}^{\text{S}} \Rightarrow \gamma_{\text{I}} B_{\text{RF}}^{\text{I}} = \gamma_{\text{S}} B_{\text{RF}}^{\text{S}} \quad (\text{B.22})$$

where  $\gamma_I$  and  $\gamma_S$  are the gyromagnetic ratios of I and S spins and  $B_{rf}^I$  and  $B_{rf}^S$  are the RF field strength applied on each channel. While the maximum CP gain per scan is a factor of  $\gamma_I/\gamma_S$ , the overall improvement in signal to noise for a given experimental time can be considerably higher than this if the longitudinal relaxation time of the I spins is fast, as is often the case for protons. Several improvements to the original CP technique using constant-amplitude irradiation on both channels have been introduced. The Figure B.11 presents the pulse programme of ramped-CP,<sup>155</sup> where the amplitude of the contact pulse on either I or S spins is steadily increased to broaden the relevant Hartmann-Hahn condition. Another approach is the adiabatic passage through Hartmann-Hahn condition. A significant signal enhancement could be observed by using adiabatic shape under fast MAS. In the present work, we used adiabatic shapes for transferring the magnetization from  $^1\text{H}$  to  $^{29}\text{Si}$  nuclei and ramped-CP for the  $^1\text{H}$  to  $^{27}\text{Al}$  or  $^{11}\text{B}$  (quadrupolar) nuclei. The CP condition between spin  $1/2$  and quadrupolar nuclei requires fulfilling some other specifications, which will be discussed in the respective chapters.

***Double Frequency Sweep (DFS) for quadrupolar nuclei:***

Most of the heteroatoms responsible for the catalytic activities and acidities in porous silicate materials are quadrupolar nuclei, for example  $^{27}\text{Al}$ ,  $^{11}\text{B}$  etc. Moreover, about 2/3 of the NMR-active nuclei in the periodic table have a spin quantum number  $>1/2$ . Many of these nuclei give rise to large quadrupolar couplings and are often associated with poor sensitivity due to low natural abundance, low gyromagnetic ratio, and/or large quadrupolar interactions. In this context, an alternative approach has been proposed to increase the intensity of the signal of half-integer quadrupolar nuclei (integer-spin quadrupolar nuclei are often trickier to manipulate, but fortunately also much less numerous). This is achieved by increasing the populations of the central  $-1/2 \rightarrow 1/2$  transition by manipulating the satellite transitions using pulses whose carrier frequency is swept adiabatically across the frequency range of the satellite transitions (but without touching the central one). Pulse shapes include hyperbolic secant pulses (HS), frequency-swept fast-amplitude modulated pulses (SF FAM) and widely-used double frequency sweep (DFS) technique. The Boltzmann distribution law gives the population difference of the  $(2I+1)$  energy levels at room temperature. By saturating or inverting the populations of the satellite transitions, one can in principle increase the population difference between the  $-1/2$  and  $1/2$  energy levels and hence increase the central transition signal.<sup>156-159</sup> The DFS preparation method used in this work, which works under both MAS and static condition. It is characterized by a cosine-modulated amplitude that splits the frequency-swept region onto both sides of the spectrum to excite the satellite-transition region as a whole. The group of Kentgens<sup>158</sup> reported that by using DFS as a preparation period, the maximal signal enhancement that can be achieved is a factor of 2 for spin  $3/2$  and 3 for spin  $5/2$  nuclei. While these theoretical factors are often approached for large quadrupolar interactions, little improvement can be obtained for symmetric

environments associated with smaller quadrupolar interactions, such as four-coordinated B sites. Here, we used double frequency sweep (DFS) preparation period for most 1D and 2D NMR experiments using  $^{11}\text{B}$  (3/2) or  $^{27}\text{Al}$  (5/2) excitation (though not for quantitative experiments).

#### **B.2.4 Through-bond solid-state NMR spectroscopy**

The ability to probe bonding interactions and spatial proximities between the nuclear spins have strongly contributed to making NMR spectroscopy a popular characterization technique. The bonding information is often a necessary step to determine the molecular structure. In liquid state, where anisotropies are averaged by rapid tumbling of nuclear spins, the only remaining NMR interactions are  $J$ -couplings. These  $J$ -couplings reveal the connectivities between the identical or different nuclei. Scalar couplings may also be used to transfer spin polarisation from nuclei with large Boltzmann population difference and/or fast relaxation delays to the desired nuclei possessing lower Boltzmann population difference via  $J$ -mediated coherence transfer echoes. This approach called Inensitive Nuclei Enhanced by Polarisation Transfer (INEPT) is the primary building block of the vast majority of pulse sequences in liquid-state NMR.

However in solids, as mentioned before, the dominating anisotropies such as CSA and dipolar couplings or quadrupolar couplings often prevent measuring or exploiting the smaller  $J$ -couplings directly. Nevertheless, nowadays the use of fast MAS and efficient heteronuclear decoupling techniques in solid-state NMR suppress these interactions and makes it possible to investigate such weak bonding interactions. The measurement of small  $J$ -couplings, particularly in disordered solids, has dragged much attention. In the early 1980's researchers implemented  $J$ -mediated transfer experiments in solid-state. Many research later reported the combination of experiments designed for liquids, such as the COSY or INADEQUATE- experiments with the CP technique to establish homonuclear bonding interactions in inorganic rigid solids, amorphous glasses,  $^{29}\text{Si}$  enriched and natural abundance zeolites etc.<sup>136,160-164</sup> This was then extended to through-bond heteronuclear correlation experiments such as 2D INEPT, multiple-quantum correlation experiments, especially the MAS- $J$ -HMQC<sup>165</sup> revealing the connectivities between dissimilar atoms including quadrupolar nuclei ( $^{27}\text{Al}$ ,  $^{11}\text{B}$  etc), which largely contributed to the success of solid-state NMR, especially in the field of zeolites.<sup>166</sup>

***Z-filtered refocused INADEQUATE:*** Lesage and coworkers<sup>136</sup> successfully adapted the liquid-state NMR experiment referred as refocused INADEQUATE to probe homonuclear connectivities in disordered solids. The local structures of a wide range of isotopically-enriched or natural-abundance materials have been better understood with the help of the refocused INADEQUATE method.<sup>167-170</sup> As shown in Figure B.12, the pulse sequence first starts with  $^1\text{H}$ -X CP sequence transferring the

magnetization from protons to the rare nuclei. Then the first spin-echo creates anti-phase coherences via  $J$ -coupling evolution. The first  $90^\circ$  pulse converts these antiphase coherences into double quantum (DQ) coherences between the coupled spins. The evolution of DQ coherence takes place during the indirect evolution period and then transformed back to the antiphase terms on applying the second  $90^\circ$  pulse. Finally these antiphase terms are converted into detectable in-phase terms during second spin-echo ( $\tau$ ) for detection. A pair of coupled spins gives rise to two correlations at the individual frequencies in the direct (horizontal) dimension and at the sum of the individual frequencies in the indirect dimension. One predicts maximum efficiency for a spin-echo delay  $\tau = 1/(4J)$  in the limit of isolated spin pairs.

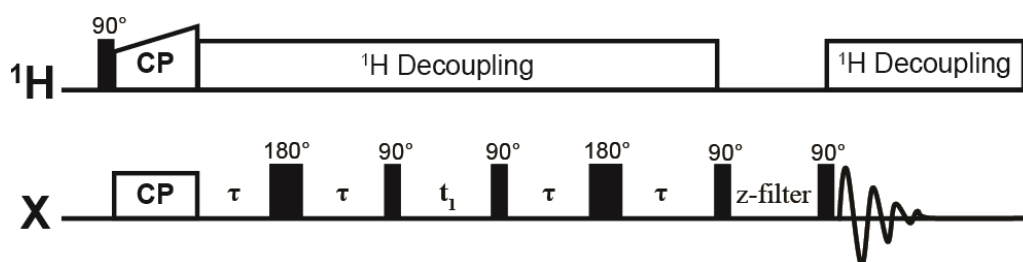


**Figure B.12** Pulse program of *z*-filtered refocused INADEQUATE experiment

The main reason for inserting the *z*-filter before acquiring the signal is to remove unexpected anti-phase dispersive contributions arising from multi-spin effects.<sup>171-172</sup> During the whole INADEQUATE sequence and acquisition, heteronuclear  $^1\text{H}$  decoupling has been included to remove the proton dipolar interactions. The higher the decoupling, the weaker the loss of signal due to transverse dephasing during the coherence transfer echoes, and the higher the 2D signal to noise.<sup>140,173</sup> As explained earlier, our objective is to determine the effects of heteroatoms on siliceous framework of surfactant-directed layered silicates. To do so, one must first establish the framework Si-O-Si connectivities in the absence of heteroatoms. The  $^{29}\text{Si}$ -O- $^{29}\text{Si}$  connectivities of the surfactant-directed layered silicate described in the most part of this work have been examined in detail on the basis of such INADEQUATE or refocused INADEQUATE experiments.<sup>22-24,71,174</sup> Here, we reproduced this experiment for the same samples containing Al and B heteroatoms incorporated within their silicate frameworks to identify their effects on neighboring Si environment (see chapters C and D).

***J*-mediated Heteronuclear Multiple Quantum Correlation (HMQC) experiment:** Through-bond correlation experiments such as the HSQC (Heteronuclear Single-Quantum Correlation) and the HMQC (Heteronuclear Multiple-Quantum Correlation) experiments reveal the bonding between chemically distinct atoms. These  $J$ -mediated heteronuclear correlation experiments were also introduced for liquid-state NMR, to probe for example the connectivities between  $^1\text{H}$  and  $^{13}\text{C}$  nuclei, and then adapted by

Lesage *et.al.*<sup>165</sup> for solid-state NMR by combining them with magic-angle spinning and efficient heteronuclear decoupling schemes. Afterwards, this sequence has been utilized to establish heteronuclear connectivities in disordered inorganic solids, glasses, zeolites etc. Within the Al or B containing layered silicates used in this work, it is crucial to probe the connectivities between Al or B with Si atoms to then probe the local structure around these heteroatoms. Figure B.13 represents the pulse sequence of the  $^{11}\text{B}/^{27}\text{Al}$  [ $^{29}\text{Si}$ ]  $J$ -HMQC with heteronuclear  $^1\text{H}$  decoupling.

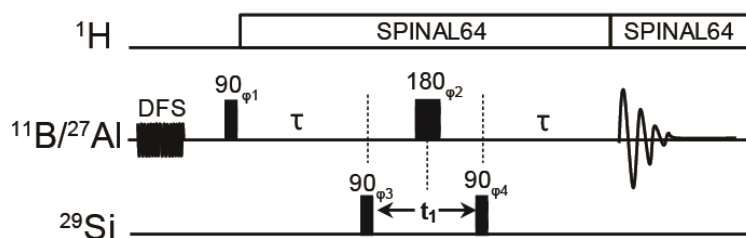


**Figure B.13** Pulse program of  $^{11}\text{B}/^{27}\text{Al}$  [ $^{29}\text{Si}$ ]  $J$ -mediated HMQC with DFS preparation and heteronuclear  $^1\text{H}$  decoupling.

The pulse programme starts with a DFS pulse (see B.2.2) on the  $^{27}\text{Al}$  or  $^{11}\text{B}$  channel, in order to increase the initial magnetization (applicable only to quadrupolar nuclei e.g.  $^{11}\text{B}/^{27}\text{Al}$ ). The first  $90^\circ$  pulse on  $^{11}\text{B}$  or  $^{27}\text{Al}$  flips the magnetization to the transverse plane. Then the in-phase coherences are transformed into the anti-phase coherences during first evolution period  $\tau$ , which are then converted into heteronuclear multiple-quantum coherences by the second  $90^\circ$  pulse on the  $^{29}\text{Si}$  channel. These DQ coherences should in principle evolve at the sum of the individual chemical shifts (here  $^{29}\text{Si}$  and  $^{11}\text{B}$  or  $^{27}\text{Al}$ ) during indirect dimension  $t_1$ , but, the evolution under  $^{11}\text{B}$  or  $^{27}\text{Al}$  chemical shifts is refocused by applying a  $180^\circ$  pulse on the  $^{11}\text{B}$  or  $^{27}\text{Al}$  channel in the center of the  $t_1$  evolution period, such that these terms evolve only under the  $^{29}\text{Si}$  chemical shifts in the indirect dimension. These heteronuclear DQ coherences are transforming back into antiphase coherences by another  $90^\circ$  pulse on the  $^{29}\text{Si}$  channel, which are then converted back to the detectable in-phase terms during  $2^{\text{nd}}$   $\tau$  period. Here the magnetization transfer is mediated by heteronuclear  $^{11}\text{B}\text{-O-}^{29}\text{Si}$  or  $^{27}\text{Al}\text{-O-}^{29}\text{Si}$   $J$ -couplings and  $^{11}\text{B}$  or  $^{27}\text{Al}$  signal is detected in the direct dimension ( $t_2$ ). The 2D MAS- $J$ -HMQC spectrum shows the correlations exclusively of Si atoms (F1 or indirect dimension) which are connected to B or Al atoms (F2 or direct dimension). As for most  $J$ -mediated NMR experiments in the solid-state, using efficient heteronuclear  $^1\text{H}$  decoupling (such as SPINAL 64) to prevent or slow down signal dephasing during the free evolution delays  $\tau$  is the key to the success of this experiments.

### B.2.5 Probing homo- and heteronuclear spatial proximities

Dipolar couplings are among the main anisotropic interactions responsible for the broadening of solid-state NMR spectra, and it is often mandatory to use magic-angle spinning to remove these as well as other anisotropic interactions. However, these dipolar couplings provide very important chemical information on internuclear proximities or even distances. In this context, many techniques were developed to reintroduce the dipolar couplings at desired times of NMR pulse sequences. The main goal of these recoupling techniques is to selectively reintroduce homonuclear or heteronuclear spin-spin interactions, but not other spin interactions. This section briefly explains the homo- and heteronuclear recoupling techniques establishing spatial proximities via dipolar couplings in solids.

**Homonuclear recoupling sequences (SR26<sub>4</sub><sup>11</sup>):** The internuclear proximities or distances between atoms of the same type could be selectively probed by applying symmetry-based recoupling techniques.<sup>175-179</sup> Among the various recoupling methods that may be used to reintroduce the dipolar couplings, two important groups are the CN<sub>n</sub><sup>v</sup> and RN<sub>n</sub><sup>v</sup> type sequences.<sup>180-181</sup> Both consist in rotor synchronized symmetry-based recoupling pulses which are applied to excite and reconvert double-quantum coherences between the spins. Here, we used RN<sub>n</sub><sup>v</sup> recoupling sequences, and more specifically SR26<sub>4</sub><sup>11</sup>, to reintroduce homonuclear dipolar couplings between <sup>29</sup>Si species in surfactant-directed layered silicates. Many advantages of SR26<sub>4</sub><sup>11</sup> sequence over other recoupling sequences made it very popular to determine the structure of many ordered and disordered silicates. First, this sequence is very robust to reintroduce weak homonuclear dipolar couplings even for systems with large CSA interactions. The scaling factor is strong enough to measure the weak dipolar interactions. Finally, the relation between the MAS and RF field strength required for the recoupling process is compatible with typical probe limitations under suitable MAS frequencies. The super-cycled SR26<sub>4</sub><sup>11</sup> is given by<sup>182</sup>,

$$SRN_n^v = (RN_n^v)_0 (RN_n^{-v})_0 (RN_n^v)_\pi (RN_n^{-v})_\pi \quad (\text{B.26})$$

where,  $N = 26$ ,  $n = 4$  and  $v = 11$  and  $RN_n^v$  is given by,

$$RN_n^v = [R_\Phi R'_{-\Phi}]^{N/2} \quad (\text{B.27})$$

Here,  $R$  is a composite  $\pi$  pulse that flips the magnetization by  $\pm\pi$  about  $\Phi$  and  $R'$  is derived from  $R$  by changing the signs of all phases. The overall RF phase shifts of  $R$  is denoted by  $\phi$  and is given by,

$$\Phi = \pi v/N \quad (\text{B.28})$$

The recoupling RF field strength is related to the number of rotor periods defining the length of a complete recoupling cycle. One  $RN_n^v$  sequence occupies exactly  $n$  rotor periods, and the RF field should

thus be  $N/n$  times the spinning frequency. In the  $SR26_4^{11}$  sequence, for instance, the nutation frequency of the recoupling RF field should be set to 6.5 times the spinning frequency. For example, if the spinning frequency is 4.6 kHz, then the recoupling RF field should be around 30 kHz. On the other hand, RF field strength for heteronuclear  $^1H$  decoupling should be 3 times than the recoupling RF field to avoid interferences between the recoupling and the decoupling.<sup>183</sup>

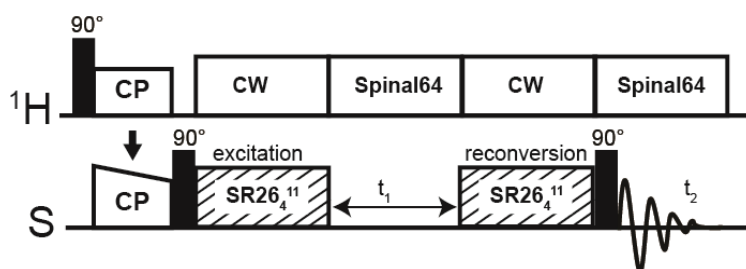


**Figure B.14** Pulse program of homonuclear symmetry based DQ recoupling experiment.

The pulse program (Fig. 14) starts with a basic CP sequence transferring magnetization from  $^1H$  to S spins. Then, first  $90^\circ$  pulse on S spins flips the magnetization back to z axis. Then, the first  $SR26_4^{11}$  recoupling block excites the DQ coherences during  $\tau$ , which evolve during  $t_1$  to then be reconverted to longitudinal magnetization by the second  $SR26_4^{11}$  recoupling block of same duration  $\tau$ . The last  $90^\circ$  pulse flips the magnetization back to the transverse plane for detection. Heteronuclear CW  $^1H$  decoupling is used during recoupling (again to avoid interferences between decoupling and recoupling), and SPINAL64  $^1H$  decoupling is used during acquisition in both direct and indirect dimensions. The dipolar-coupled spin pairs yield pairs of correlation peaks at their individual frequencies in the direct (horizontal) dimension and at the sum of their individual frequencies in the DQ dimension. This is identical to the expected signature of  $J$ -coupled spin pairs in the refocused INADEQUATE experiment, and these experiments can be described as  $J$ -mediated and dipolar-mediated double-quantum single-quantum (DQ-SQ) experiments, respectively.

**2D Heteronuclear correlation experiment (HETCOR):** The simplest possible way of probing spatial proximities between two distinct types of nuclei in solids is to use the HETCOR experiment, which is simply the 2D version of the basic CP experiment. As shown in Figure B.15, after 1<sup>st</sup>  $90^\circ$  pulse, I spins evolves during  $t_1$  before transferring the magnetization to S spins. Then S spins are detected in the direct dimension after cross-polarisation. In most of the cases I spin correspond to protons, while the S spins generally correspond to the rare nuclei  $^{13}C$ ,  $^{29}Si$ , but 2D HETCOR experiments are also compatible with quadrupolar nuclei<sup>184-185</sup> used as either I or S spins.

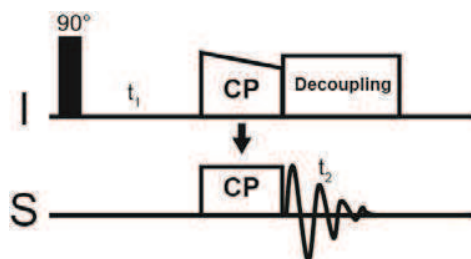


**Figure B.15** 2D HETCOR (heteronuclear correlation) pulse programme

For example,  $^{11}\text{B}[^1\text{H}]$  and  $^{27}\text{Al}[^1\text{H}]$  2D HETCOR experiments have been extensively studied. In addition,  $^{27}\text{Al}$ - $^{29}\text{Si}$  correlation based on HETCOR experiments have been reported.<sup>186</sup> Heteronuclear  $^1\text{H}$  decoupling is employed during acquisition in order to improve the resolution and sensitivity. However, in some complex systems or  $^1\text{H}$  rich samples, the homonuclear  $^1\text{H}$  dipolar couplings may considerably deteriorate the resolution in the indirect dimension. Nevertheless, many homonuclear decoupling techniques such as eDUMBO<sup>139</sup>, FSLG<sup>187</sup> has been used to sort this problem. Very fast spinning (nowadays up to 110 kHz) is another option, although it may be limited by small sample volumes. See chapters C and D for more details on  $^{27}\text{Al}[^1\text{H}]$  or  $^{11}\text{B}[^1\text{H}]$  HETCOR experiments that were employed to investigate the charge compensation mechanisms associated with the heteroatoms incorporated in surfactant-directed layered silicates.

**Heteronuclear recoupling sequences ( $R4_1^2$ ):** Probing heteronuclear proximities for instance between  $^{11}\text{B}$  or  $^{27}\text{Al}$  and  $^{29}\text{Si}$  species is necessary to derive the local interactions for example in heteroatoms-containing surfactant-directed layered silicate materials. Several recoupling techniques have been introduced so far, in order to reintroduce heteronuclear dipolar couplings, which primarily include rotary-resonance recoupling<sup>188</sup> techniques. Then, symmetry-based heteronuclear recoupling techniques were employed, which follow similar principles as the homonuclear recoupling techniques described in the previous section. Recently, Brinkmann and coworkers<sup>189</sup> measured OH distances by probing heteronuclear dipolar couplings between O and H atoms by using the  $\text{SR}4_1^2$  symmetry-based recoupling sequence, which belongs to the  $RN_n^v$ <sup>181</sup> recoupling group. Later, Hu and coworkers<sup>190</sup> showed the advantage of such recoupling techniques for investigating heteronuclear spatial proximities through dipolar-mediated HMQC-type experiments. Figure B.16 shows the pulse sequence of the dipolar-mediated HMQC. According to Levitt's symmetry-based analytical calculations, the RF field strength for  $\text{SR}4_1^2$  recoupling sequence should be twice the spinning frequency,  $\nu_I = 2\nu_R$ .

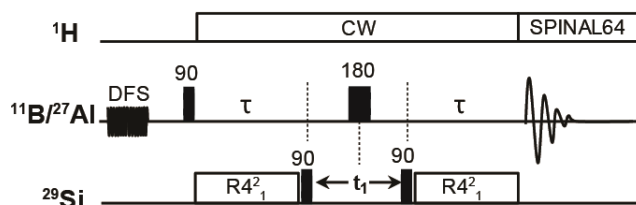


**Figure B.16** Pulse programme of  $^{11}\text{B}/^{27}\text{Al}$  [ $^{29}\text{Si}$ ] dipolar-mediated HMQC with DFS and heteronuclear  $^1\text{H}$  decoupling.

The principle of this experiment is very similar to  $J$ -HMQC (see section B.2.3 for pulse program details), but the multiple-quantum coherences are generated through dipolar couplings owing to the recoupling pulse trains applied during the two  $\tau$  delays, rather than under the effect of  $J$ -couplings. DFS pulses have also been used here, in order to increase the sensitivity. The heteronuclear  $^1\text{H}$  CW decoupling was employed during recoupling to remove the interferences of  $^1\text{H}$  dipolar couplings, and SPINAL 64 was applied during acquisition to maximize the spectral resolution.

### B.3 Other Experimental and Computational Methods

#### B.3.1 X-ray Diffraction (XRD)

X-ray Diffraction is a characterization technique that was adopted to investigate crystal structure of materials with different morphologies or forms, such as single crystals, polycrystalline powders, thin films... etc. The lattice structures of crystalline materials are associated with the regular repetition of atomic planes across long distances. When an X-ray beam strikes this material and interacts with the atoms of the planes, part of the beam is transmitted, absorbed by the sample, refracted and scattered and part of it is diffracted. The angle between the incident and the diffracted beams are related to the distance information between the planes of atoms constituting the lattice structure by the Bragg's diffraction law:

$$n\lambda = 2d\sin\theta \quad (\text{B.29})$$

where,  $n$  is an integer,  $\lambda$  is the wavelength of X-ray beam ( $\lambda_{\text{CuK}\alpha} = 1.5418 \text{ \AA}$  applied here),  $d$  is the distance between the adjacent planes ( $d$ -spacings) and  $\theta$  is the incident angle. While single-crystal diffraction is probably the most powerful technique to determine the molecular structure of a crystalline solid, powder diffraction, although considerably less powerful is nevertheless tremendously important in material science. The two main XRD characterization methods: wide-angle (WAXS) and small-angle X-ray (SAXS) scattering were employed to investigate the lattice and lamellar structure of surfactant-directed layered boro- and aluminosilicates, studied in this work. The reflections in the Wide-angle X-ray scattering (WAXS) usually appear in the region of  $5^\circ$  to  $50^\circ$   $2\theta$ . This is often used in zeolite chemistry to identify crystalline structures of zeolites, determining the small  $d$ -spacing structures ranging from 10 to 2

Å. In layered silicate materials, WAXS experiments provide information relative to the unit cell dimension and symmetry within the layer planes. Small-angle X-ray scattering (SAXS), from  $2\theta \approx 0^\circ$  to  $10^\circ$ , is suitable to characterize long-range mesoscopic ordering characteristic of the pore or layer architecture, as it characterizes larger  $d$ -spacings (often from 1 to 15 nm). Different mesostructured materials (e.g., lamellar, hexagonal, cubic) may be readily identified and distinguished based on SAXS data.

### **B.3.2 ICP analysis**

Quantitative analyses of inorganic ordered-disordered materials could be done by Inductively Coupled Plasma (ICP) method. The basic principle of ICP analyses is to heat the sample in a plasma temperature (6000K – 10000K). Such high temperature could be reached when time varying electric current is passed through the coil, which is placed in the region of rarefield (noble) gas, for example argon. The sample at high temperature produces the light. The amount of light emitted from the sample is directly proportional to relative proportion of individual atomic substituent. The same procedure is repeated for standard solutions without altering other parameters. The concentration of each element is determined by comparing the intensity of light emitted from the sample with respect to the intensity of light from the standard solution. All samples should be in aqueous solution for the analysis. Most of the inorganic solid-materials are not easily dissolved in organic solvents or weak acids. Hence, these solid-materials were dissolved in concentrated strong acids, for instance hydrofluoric acid (HF) or nitric acid (HNO<sub>3</sub>). ICP analyses are generally able to determine atomic concentrations ranging from 0.005 parts-per-million (PPM,  $10^{-6}$ ) up to 1000 PPM.

### **B.3.3 Quantum Chemical Calculations**

Despite the large improvement that solid-state NMR spectroscopy have undergone in the last decades, spectral characterization can rapidly become complex for solid materials exhibiting a large number of non-equivalent sites, as in the case of crystalline zeolites, or amorphous materials. This becomes even more challenging for quadrupolar nuclei, where NMR peaks are broadened by the quadrupolar interaction. The best way to overcome these problems is to use molecular modeling in combination with the experiments. In particular, by using quantum chemical approaches, it is possible to calculate NMR parameters,<sup>191</sup> i.e. the electric field gradients and the chemical shifts tensors, and then to simulate the NMR spectra. While early quantum chemical techniques were devoted to study the magnetic properties of the isolated molecules, recent techniques nowadays allow the treatment of extended systems by exploiting the translational symmetry inherent to crystals. The first technique in this regards was the Linear Augmented Plane Wave (LAPW) approach, which allow the calculation of electric field gradients

(EFG). Later, other methods have appeared based on the plane wave – pseudopotential approach such as the Gauge Including Projected Augmented Wave (GIPAW) and other methods allowing the calculations of NMR chemical shifts<sup>192-193</sup> and  $J$ -couplings for crystalline systems. Here we used the CASTEP<sup>194-195</sup> code to model our layered structure, and the GIPAW<sup>192-193</sup> method implemented in this code to calculate NMR parameters. CASTEP is a code based on Density Functional Theory (DFT) that uses a plane-wave approach, with the pseudopotential approximation, and periodic boundary conditions. The detailed technical aspects of these methods will be discussed in the following sections.

### What is Density Functional Theory (DFT)?

DFT is a quantum mechanical modeling method used in physics and chemistry to investigate the electronic structure (principally the ground state) of many-body systems, particularly atoms, molecules, and the condensed phases. One should know the basic principle of quantum mechanics for better understand the principle DFT calculations. The behavior of a system consisting of  $N$  electrons and  $M$  nuclei, which could be anticipated by solving the Schrödinger equation,

$$\hat{H}\Psi = E\Psi \quad (\text{B.30})$$

Where,  $\hat{H}$  is the Hamiltonian operator corresponding to the total energy of the system,  $\Psi$  is the wave function depending on nuclear and electronic coordinates, and  $E$  is the total energy of the studied system. In its detailed form,  $\hat{H}$  can be written as follows (in atomic units):

$$\hat{H} = -\frac{1}{2} \sum_i^N \nabla_i^2 - \frac{1}{2} \sum_A^M \frac{1}{M_A} \nabla_A^2 - \sum_i^N \sum_A^M \frac{Z_A}{\vec{r}_{iA}} + \frac{1}{2} \sum_i^N \sum_{j \neq i}^N \frac{1}{\vec{r}_{ij}} + \frac{1}{2} \sum_A^M \sum_{B \neq A}^M \frac{Z_A Z_B}{\vec{R}_{AB}}$$

The first two terms of the Hamiltonian operator represent the kinetic energy part and correspond

respectively to the electronic ( $-\frac{1}{2} \sum_i^N \nabla_i^2$ ) and nuclear ( $-\frac{1}{2} \sum_A^M \frac{1}{M_A} \nabla_A^2$ ) kinetic energy. The three

remaining terms represent the potential energy of the system and correspond respectively to the electron-

nuclear attraction ( $\sum_i^N \sum_A^M \frac{Z_A}{\vec{r}_{iA}}$ ), the electron-electron repulsion ( $\frac{1}{2} \sum_i^N \sum_{j \neq i}^N \frac{1}{\vec{r}_{ij}}$ ) and the nuclear-nuclear

repulsion ( $\frac{1}{2} \sum_A^M \sum_{B \neq A}^M \frac{Z_A Z_B}{\vec{R}_{AB}}$ ).

Since equation (B.30) is a multivariable (depends on  $N$  electronic and  $M$  nuclear variables), its resolution is very complicated. This led to the use of approximations. The first and most famous one is the Born-Oppenheimer approximation, which makes the separation between electronic and nuclear degrees of freedom. This is due to higher mass of the nuclei in comparison with that of electrons. Even so, solving the resulting “electronic” Schrödinger equation remains very complicated, because of its many-

body nature resulting from the fact that the electronic degrees of freedom are coupled to each other. Many other methods came through at this stage to overcome the complexity of the electronic Schrödinger equation, providing several approximations to solve it. Among these the Hartree-Fock<sup>196-197</sup> used to be a rather popular method, but it is time consuming and fails to describe systems with strong electron correlation effects. Accounting for such effects is possible with the so-called post-Hartree-Fock approaches, whose computational cost is nevertheless often prohibitive. In all of these methods, the main objective is to determine the wave function  $\Psi$ .

Another approach was to consider the “electronic charge density”  $\rho$  as the fundamental variable instead of considering the wave function  $\Psi$ . In fact, as the electronic density is an observable depending only on three coordinates  $(x, y, z)$  – (or more precisely on four coordinates if we consider the electronic spin coordinate), – its determination is much easier than determining the wave function. Once the electronic density of the studied system is known, its wave function could be easily determined since  $\rho(\vec{r}) = |\Psi|^2$ . This is the principle of the Density Functional Theory, which was introduced by Hohenberg, Kohn and Sham<sup>198</sup> during the sixties, who demonstrated that all the energetic part of the Hamiltonian operator could be written as “functional” of the electronic density:  $E[\rho(\vec{r})]$ . Note that the term “functional” is equivalent to the familiar one “function” used in mathematics, where the only difference is that the “function” associate a number to another number ( $x \xrightarrow{f(x)} y$ ), while a “functional” associate a function to a number ( $f(x) \xrightarrow{F[f(x)]} y$ ). In the DFT formalism, the energy is a **functional** of the electronic density, which is a **function** of the Cartesian coordinates  $x, y, z$ .

In the Kohn-Sham formulation of the density functional theory, the many-body electronic Schrödinger equation of a system of  $N$  electrons could be separated into  $N$  equations involving single-particle wave functions ( $\varphi_i(\mathbf{r})$ ).

$$-\left(\hbar^2/2m_e\right) \nabla^2 \varphi_i(\mathbf{r}) + v_{\text{eff}}(\mathbf{r}) \varphi_i(\mathbf{r}) = \varepsilon_i \varphi_i(\mathbf{r}) \quad (\text{B } 31)$$

Where,  $v_{\text{eff}}(\mathbf{r})$  represents the Kohn-Sham potential which is a functional of the electronic density and is composed of the following terms:

(i) the external potential:  $V_{\text{ext}}(\mathbf{r})$  corresponding to the electrons-nuclei interaction,

(ii) the Hartree potential:  $V_{\text{H}}[\rho(\mathbf{r})] = \int d\mathbf{r}' \frac{\rho(\mathbf{r}')}{|\mathbf{r}-\mathbf{r}'|}$  corresponding to the coulombic electron-electron repulsion), and

(iii) the Exchange-Correlation potential:  $V_{\text{xc}}$ , which contains electron-electron interactions terms out of the coulombic interaction, related to the quantum nature of electrons.  $v_{\text{eff}}(\mathbf{r})$  could be written as :

$$v_{\text{eff}}(\mathbf{r}) = V_{\text{ext}}(\mathbf{r}) + V_{\text{H}}[\rho(\mathbf{r})] + V_{\text{xc}}[\rho(\mathbf{r})] \quad (\text{B } 32)$$

All the terms of equation B.32 can be determined precisely, except the Exchange-Correlation potential term ( $V_{xc}$ ), which is unknown and contains the most critical part of the electron physics. Hence, a physical approximation is necessary to represent  $V_{xc}$  term as accurately as possible. In this context, many attempts have been made to find the most suitable and universal approximations, and this field is still progressing until now. The ideal goal is to find the most accurate expression for the exchange correlation term, without being time consuming. The best known families of exchange correlation functional (listed from the oldest to the most recent) are LDA for Local Density Approximation, GGA for Generalized Gradient Approximation and the Hybrid functionals. In our calculations (geometry optimizations and NMR calculations) we used the Perdew, Burke and Ernzerhof (PBE)<sup>199</sup> method which belongs to the GGA family.

***Periodic boundary condition and plane wave approach:*** The large number of electrons present in an extended system makes impractical to model the system by quantum computation methods. Nevertheless, by considering the inherent translational symmetry of the crystalline systems, Bloch proposed a theory to solve such complicated systems. The basic principle of this theory is to consider only the crystallographic unit cell under periodic boundary condition instead of making calculation on an infinite system. Hence the wave function in equation B.31 could be exemplified by summation of periodic functions over the reciprocal lattice vectors  $k$ . For numerical implementation, these periodic functions should be represented by a set of basis function. While there are many possible choices, amongst the simplest way (in a mathematical point of view) is to expand these periodic functions in terms of plane waves. One of the main advantages of the plane wave-based DFT calculations is that the quality of the basis is adjusted by a single parameter: the kinetic cutoff energy  $E_{cut}$ .

***Pseudopotential approximation:*** The modeling of extended systems could be time consuming even by using the periodic boundary conditions depending on the number of atoms, and consequently the number of electrons, of their unit cells. One way to overcome this problem is to consider explicitly only the valence electrons during calculation, and to keep the core electrons frozen. also, the core-valence interactions are replaced by an effective potential, the “pseudopotential”. This approximation is justified by the fact that the core electrons do not play any important role in the interactions between atoms in contrast to the valence electrons. Due to this approximation, the valence wave functions could be approximated by pseudo-wave functions having a less complicated form in the core region (near to the nucleus), and thus could be represented by a much smaller number of plane waves, making the calculation faster. Although the pseudopotential approximation is very useful to perform electronic structure calculation and optimize crystal structures, it is not able to perform calculations of NMR parameters. This

is because these parameters strongly depend on the electronic density close to the nucleus, which is not precisely represented by the approximated “pseudo-wave functions”. Face to this problem, the PAW (Projector Augmented Wave) and the GIPAW (Gauge Including Projector Augmented Wave) methods have been invented.

**Computation of NMR parameters:** One important parameter in NMR is the Electric Field Gradient (EFG) tensor, especially observed for quadrupolar nuclei (spin  $I > 1/2$ ). In fact, EFG tensor is used to calculate the quadrupolar coupling  $C_Q$  and asymmetry parameter  $\eta_Q$ . The calculation of EFG tensor is straightforward. However, it could not be done using the pseudopotential approximation. In fact, EFG depends only on the charge density ( $\rho$ ) near to the nucleus. As explained above, the valence pseudo-wave functions used in the pseudopotential approximation have a simple form in the core region, preventing them to correctly describe the charge density ( $\rho$ ) in this region. The PAW method brings a solution to this problem by introducing some mathematical corrections to the valence “pseudo”-wave functions. This method introduces a linear transformation that uses predefined functions, i.e. the projectors, to map the valence “pseudo”-wave function onto the corresponding “all-electron” wave functions. This procedure is fast and hence the calculation of EFG tensor is very short (few seconds for a system of  $\approx 100$  atoms using 64 processors).

Another important parameter in NMR is the shielding tensor. The latter is defined as the response of any system to an external uniform magnetic field. In fact, when a sample is placed in a uniform magnetic field, an electric current ( $j(r)$ ) is induced in the material producing a non-uniform induced magnetic field ( $B_{in}$ ) (as explained in the section B.2.1) given by the Biot-Savart law as :

$$B_{in}(r) = \frac{\mu_0}{4\pi} \int d^3r' j(r') \times \frac{r-r'}{|r-r'|^3} \quad (\text{B } 33)$$

The shielding tensor is defined as, the ratio between the induced magnetic field  $B_{in}$  and the external field:

$$B_{in}(r) = -\sigma(r) B_{ext} \quad (\text{B } 34)$$

To calculate the shielding tensor, one needs to determine  $B_{in}$ , and so, needs to calculate the induced electronic current  $j(r)$ . Unfortunately, the PAW method is not sufficient to do this. An improvement of this method was made by Mauri *et. al.*<sup>192-193</sup> known as GIPAW method that allows calculations of electronic current  $j(r)$ . It is important to note that the calculation of the shielding tensor is much time consuming than that of the EFG (approximately one day for a system of  $\approx 100$  atoms using 64 processors).

The GIPAW method determines only the shielding tensor for the studied sample. In contrast, experiments typically measure the change in shielding relative to a reference standard – what we called the chemical shift ( $\delta$ ).

$$\delta = -[\sigma - \sigma_{ref}]$$

The shielding of the reference standard ( $\sigma_{\text{ref}}$ ) could be obtained by performing a calculation on the standard compound itself. However, it is often not convenient to do this procedure, because of the errors on NMR parameters that DFT calculations could induce. Such errors may be compensated by calculating chemical shifts on the basis of series of computations performed on model crystalline systems of known structures. Correlation plots between experimental isotropic chemical shifts and calculated isotropic chemical shielding were then plotted for an appropriate series of reference compounds that comprises large domain of chemical shifts for each type of nuclei. A series of compounds used in our work for the calibration of  $^{29}\text{Si}$ ,  $^{11}\text{B}$ , and  $^{27}\text{Al}$  isotropic chemical shifts on the basis of the corresponding isotropic shielding calculated by DFT are listed in Table B.1. The corresponding correlations plots are shown in Figure B.17. Their corresponding equations are:  $\delta_{\text{iso}}$  (ppm) =  $-1.004 \sigma_{\text{iso}} + 95.3$  for  $^{11}\text{B}$ ,  $\delta_{\text{iso}}$  (ppm) =  $-0.920 \sigma_{\text{iso}} + 288.5$  for  $^{29}\text{Si}$ , and  $\delta_{\text{iso}}$  (ppm) =  $-0.977 \sigma_{\text{iso}} + 541.9$  for  $^{27}\text{Al}$ . The deviation of the slopes from -1 in all these three correlation plots highlights the importance to use a series of reference compounds to calculate chemical shifts, rather than using only one compound.

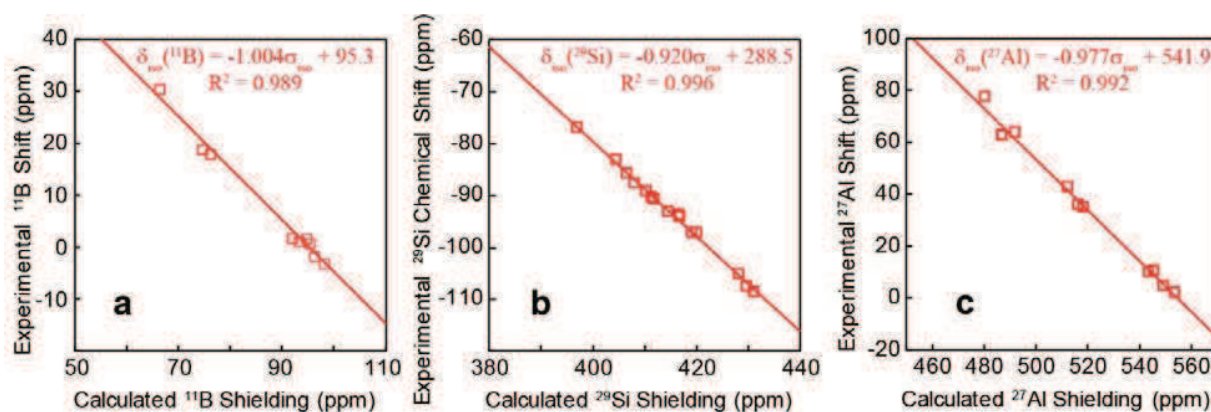


**Figure B.17** Correlation plots of (a)  $^{29}\text{Si}$ , (b)  $^{11}\text{B}$  and (c)  $^{27}\text{Al}$ , between experimental isotropic chemical shifts and isotropic shielding calculated by DFT for the series of reference crystals of known structures listed in Table B.1.

**Table B.1. Calculated shielding ( $\sigma_{\text{iso}}$ ) and experimental chemical shifts ( $\delta_{\text{iso}}$ ) of reference silicates of known crystal structures.**

Nucleus	Compound, formula	References	Site #	Experimental shift (ppm)	Calculated shielding (ppm)
<sup>11</sup> B	Reedmegnerite NaBSi <sub>3</sub> O <sub>8</sub>	200	1	-1.9	96.31
	Datolite CaBSiO <sub>4</sub> (OH)	200	1	1.0	93.38
	Danburite CaB <sub>2</sub> Si <sub>2</sub> O <sub>8</sub>	200	1	0.7	95.45
	BN cubic	200	1	1.6	94.80
	BN hexagonal	200	1	30.4	66.40
	diomignite Li <sub>2</sub> B <sub>2</sub> O <sub>7</sub>	200	1	17.9	76.22
	dilithium tetraborate		2	1.7	92.04
	BPO <sub>4</sub>	200	1	-3.3	98.23
<sup>29</sup> Si	Sassolite B(OH) <sub>3</sub>	200	1	18.8	74.70
	albite NaAlSi <sub>3</sub> O <sub>8</sub>	200	3	-105	428.0
			2	-97	419.0
			1	-93	414.4
	datolite CaBSiO <sub>4</sub> (OH)	201	1	-83	404.4
	danburite CaB <sub>2</sub> Si <sub>2</sub> O <sub>8</sub>	201	1	-89	410.1
	Pyrophyllite	200	1	-94	416.7
	Si <sub>4</sub> Al <sub>2</sub> O <sub>10</sub> (OH) <sub>2</sub>				
	Talc Si <sub>4</sub> Mg <sub>3</sub> O <sub>10</sub> (OH) <sub>2</sub>	200	1	-97	420.0
	Na <sub>2</sub> SiO <sub>3</sub>	201	1	-76.8	396.9
	α-Na <sub>2</sub> Si <sub>2</sub> O <sub>5</sub>	202	1	-93.6	416.5
	β-Na <sub>2</sub> Si <sub>2</sub> O <sub>5</sub>	202	1	-85.6	406.5
			2	-87.5	408.0
	δ-Na <sub>2</sub> Si <sub>2</sub> O <sub>5</sub>	203	1	-90.6	411.7
		2	-90.2	411.2	
<sup>27</sup> Al	Berlinite AlPO <sub>4</sub>	204	1	42.9	512
	YAlO <sub>3</sub>	205	1	10.7	545.31
	Y <sub>3</sub> Al <sub>5</sub> O <sub>12</sub>	205	1	77.5	480.04
			2	2.1	553.33
	Sillimanite Al <sub>2</sub> SiO <sub>5</sub>	206	1	63.9	491.72
			2	4.7	549.07
	Al <sub>2</sub> Ge <sub>2</sub> O <sub>7</sub>	206	1	36	516.15
	Andalusite Al <sub>2</sub> SiO <sub>5</sub>	207	1	35	518.21
			2	10	543.34
	Low albite NaAlSi <sub>3</sub> O <sub>8</sub>	208	1	62.7	486.69
Albite NaAlSi <sub>3</sub> O <sub>8</sub>	208	1	63	486.7	

## B.4 Syntheses of Materials

Majority of the porous silicate materials such as zeolites, lamellar silicates etc were synthesized under hydrothermal condition, since it has more advantages over other synthesis methods (See section A.2.1, Hydrothermal synthesis for more details). In this work, we use hydrothermal synthesis method to prepare Al- and B-containing surfactant-directed layered silicates. Syntheses protocols of all the studied materials are given below.

### B.4.1 Syntheses of surfactant-directed layered silicates

The typical synthesis procedure of surfactant-directed layered silicates follows the work by Christiansen et al.<sup>22</sup> and given as follows. The molar compositions are given by: 1.0 SiO<sub>2</sub>: 0.7 surfactant: 0.7 tetra-methyl-ammonium hydroxide (TMAOH): 113.4 H<sub>2</sub>O: 9.9 methanol (CH<sub>3</sub>OH). Firstly, the surfactant was dissolved in H<sub>2</sub>O by stirring the mixture for few minutes, after which TMAOH and CH<sub>3</sub>OH were added drop by drop. This mixture was stirred continuously for 30 minutes and then solid silica source (Cabosil, hydrolyzed for 7 days) or liquid silica source TMOS (tetra-methoxy ortho silicate) was added. The solution was stirred again for 2 hours, after which the pH was lowered to *ca.* 11.5 by adding concentrated hydrogen bromide (HBr) if needed. The mixture is stirred for another 2 hours and finally transferred into a Teflon-lined Parr reaction vessel that was well sealed and placed into an oven at 135 °C for 7 days. After 7 days (for C<sub>16</sub>H<sub>33</sub>Me<sub>2</sub>EtN<sup>+</sup>-) or 2 days (for C<sub>16</sub>H<sub>33</sub>Me<sub>3</sub>N<sup>+</sup>-) of hydrothermal reaction, the vessel was cooled to room temperature. The precipitates were subsequently filtered and excess of surfactants and solvents were washed using deionized water. The washed precipitates were dried at 90 °C overnight for other characterization.

### B.4.2 Hydrothermal Synthesis of heteroatoms-containing surfactant-directed layered silicates

**Syntheses of surfactant-directed layered Aluminosilicates:** Surfactant-directed aluminosilicates were synthesized using the following molar compositions: 1.0 SiO<sub>2</sub>: x NaAlO<sub>2</sub>: 0.7 TMAOH: 113.4 H<sub>2</sub>O: 9.9 CH<sub>3</sub>OH: 0.7 surfactants (either C<sub>16</sub>NMe<sub>3</sub>Br or C<sub>16</sub>NMe<sub>2</sub>EtBr), where x is 0.1 and 0.04 for C<sub>16</sub>N<sup>+</sup>Me<sub>3</sub>- (i.e., Si/Al = 10) and C<sub>16</sub>N<sup>+</sup>Me<sub>2</sub>Et-directed aluminosilicates (i.e., Si/Al = 25), respectively. In a typical synthesis, C<sub>16</sub>NMe<sub>3</sub>Br or C<sub>16</sub>NMe<sub>2</sub>EtBr surfactants were dissolved in deionized water, after which TMAOH and CH<sub>3</sub>OH were added. The solution was stirred for 30 min, after which the silica precursors (either *a*SiO<sub>2</sub> or <sup>29</sup>SiO<sub>2</sub>) were added and the reaction media stirred at room temperature for 7 and 21 days in the case of *a*SiO<sub>2</sub> and <sup>29</sup>SiO<sub>2</sub>, respectively. Then NaAlO<sub>2</sub> were added and the solution was stirred for another 2 h, which was transferred into a Teflon-lined ParrTM 4745 stainless-steel reactor, well-sealed, and heated at 135 °C under static conditions for 2 and 7 days for C<sub>16</sub>N<sup>+</sup>Me<sub>3</sub>- and C<sub>16</sub>N<sup>+</sup>Me<sub>2</sub>Et-directed aluminosilicates, respectively. After the hydrothermal treatment, the as-synthesized surfactant-directed

aluminosilicates were collected by vacuum filtration, washed using excess deionized water, and dried in the oven at 90 °C overnight.

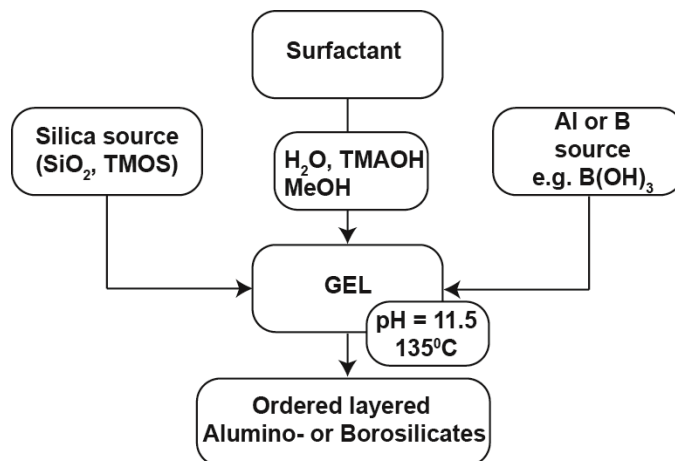


**Figure B.18** Flow chart of hydrothermal synthesis of heteroatom-containing surfactant-directed layered silicates.

**Syntheses of surfactant-directed layered Borosilicates ( $C_{16}H_{33}NEtMe_2Br$ ):** The molar composition to synthesize  $C_{16}H_{33}NMe_2Et$ -directed layered borosilicates is given by: 1.0  $SiO_2$ :  $x B_2O_3$ : 0.7 surfactant: 0.7 tetra-methyl-ammonium hydroxide (TMAOH): 113.4  $H_2O$ : 9.9 methanol ( $CH_3OH$ ), where  $x$  is the starting Si/B ratio (5-10). As showed in the figure B.18, the synthesis procedure is similar to the siliceous surfactant-directed layered silicates. After stirring the mixture for 2 hours, boron source was added, which in turn lowers the pH by 0.2-0.4. Then pH was further lowered to 11.5 by adding concentrated hydrogen bromide (HBr) if needed. The mixture is stirred for another 2 hours and finally transferred into a Teflon-lined Parr reaction vessel that was well sealed and placed into an oven at 135 °C for 7 days. After 7 days (for  $C_{16}H_{33}Me_2EtN^+$ -) or 2 days (for  $C_{16}H_{33}Me_3N^+$ -) of hydrothermal reaction, the vessel was cooled to room temperature. The rest of the procedure is same, as explained in section B.4.1.

**$^{29}Si$  enrichment of surfactant-directed layered borosilicates:** All the above mentioned surfactant-directed layered silicates were synthesized with  $^{29}Si$  enrichment in order to investigate the local structure by advanced multi-dimensional NMR experiments. The synthesis procedure is similar to those synthesized with natural abundance  $^{29}Si$  source as precursors. Initially the enriched solid silica source ( $^{29}SiO_2$ ) was hydrolyzed in TMAOH solution at 90°C for 19 days. This may have been due to Cabosil ( $SiO_2$ ) appears to be less condensed than  $^{29}SiO_2$ . With the same amount of Cabosil and  $^{29}SiO_2$  (e.g., 100 mg), it often takes longer to dissolve  $^{29}SiO_2$ . The mixture was then cooled to room temperature and recondensed by adding concentrated HBr drop by drop. The mixture was centrifuged several times with deionized water

to let precipitate settle down at the bottom. The hydrolyzed  $^{29}\text{SiO}_2$  was filtered using Whatmann filter paper then kept in oven at  $90^\circ\text{C}$  for overnight. Then  $^{29}\text{SiO}_2$  was cooled to room temperature and used for the actual synthesis. The hydrothermal synthesis of surfactant-directed layered borosilicates with  $^{29}\text{Si}$  enrichment is same as explained for the sample with  $^{29}\text{Si}$  natural abundance.

#### **B.4.3 Synthesis of Montmorillonites**

The natural montmorillonite (Na-MMT) originates from the Newcastle formation (cretaceous), Crook County, Wyoming. Sodium exchanges were performed by immersing the clay into a 1 M solution of sodium chloride. The cation exchange was completed by washing and centrifuging five times with dilute saline solutions. Samples were finally washed with distilled–deionized water and transferred into dialysis tubes to clean the clays by removing chloride anions on the external surface of the samples and then dried at room temperature. The synthetic Na-exchanged montmorillonite (Na-S-MMT) was prepared as described in reference.<sup>209</sup> The samples were dried by heating the sample at  $100^\circ\text{C}$  under vacuum ( $p = 15\text{ mmHg}$ ) during 2 h in a Schlenk flask, which was then filled with Argon and transferred into an argon-containing glove box for NMR rotor filling.

#### **B.4.4 Synthesis of new calcium borosilicate phase**

A new calcium borosilicate phase was synthesized using  $\text{CaCO}_3$  (99.95%, Alfa Aesar),  $\text{SiO}_2$  (99.99%, Saint-Gobain), and  $\text{B}_2\text{O}_3$  (99.99%, Alfa Aesar). The hygroscopic  $\text{B}_2\text{O}_3$  precursor was previously dried, and the starting oxides were weighted in a glove box under argon atmosphere to avoid moisture contamination. Glass melting was performed in platinum crucibles at different high temperatures ranging from  $1200$  to  $1500^\circ\text{C}$  depending on the targeted composition. Samples were kept at this temperature for 2 h and subsequently quenched to room temperature.

**B.5 Conclusions:** Solid-state NMR is the main characterization technique employed in our studies to investigate the local structure around heteroatoms in non-crystalline layered silicates. Several NMR anisotropic interactions make the NMR spectrum broader and reduce their relevance to exploit the local structure. Nevertheless, many methodological developments have made it possible to reach high sensitivity and resolution and thus provide precise structural information. Multi-dimensional NMR experiments play an important role, for example by establish the spatial proximities and connectivities between different atoms via dipolar and  $J$ -couplings, which opens the way to investigations of the order and disorder around heteroatoms incorporated into silicate frameworks. In addition, other experimental methods such as XRD, ICP analysis and quantum chemical calculations provide additional information, which emphasize the results of solid-state NMR. Synthesis of these novel materials with  $^{29}\text{Si}$  enrichment

### *Methods and Materials*

is crucial in our studies because the natural abundance of  $^{29}\text{Si}$  is 4.7%, and hence performing multi-dimensional NMR experiments is extremely difficult. Hydrothermal synthesis of these materials with  $^{29}\text{Si}$  enrichment has thus far been challenging. In spite of many complications, however, these materials were successfully synthesized with 99%  $^{29}\text{Si}$  isotopic enrichment.

---

## **Chapter C**

# ***Structural study at the local level around Al heteroatoms in surfactant-directed layered silicates***

---

### **C.1 Introduction**

We saw in chapter A that much research efforts have been focusing on improving the quality of a wide range of micro- and mesoporous materials for different industrial applications. Few limitations associated with for example in mesoporous materials has motivated researchers to think in a different way, in order to achieve crystallinity at both mesoscopic and molecular length scales. The alkyl-ammonium surfactant-directed layered silicates<sup>22-23,88</sup> introduced in the previous chapter are among the examples of such materials. The availability of chemically distinguished crystallographic  $Q^3$  and  $Q^4$  Si sites in their layered silicate frameworks intuitively suggests that it might be possible to better control the sitting of catalytically active heteroatoms incorporated into their frameworks than in zeolites whose frameworks generally consists (in the absence of defects) of only fully condensed  $Q^4$  Si sites. In this chapter we discuss the incorporation of Aluminum, one of the most important and most studied active site, as it endorses stronger acidic natures, in two strongly related  $C_{16}H_{33}Me_3N^+$ - and  $C_{16}H_{33}Me_2EtN^+$ -directed layered silicates

**Section C.2** covers the synthesis aspects and the evolution of long- and short-range ordering characterized by small angle and wide angle XRD as a function of Al loading. **Sections C.3 and C.4** explore the local structure upon Al incorporation on  $C_{16}H_{33}Me_3N^+$ - and  $C_{16}H_{33}Me_2EtN^+$ -directed layered silicates, respectively, using 1D  $^{27}Al$  and  $^{29}Si$  MAS NMR studies, and by probing the influence of incorporated Al atoms on neighboring Si environments by means of spatial and bonding interactions between  $^{29}Si$  and  $^{27}Al$  nuclei. The surfactants that play a central role in directing the molecular order also have strong interaction with the incorporated Al atoms, which are characterized through  $^1H$  and  $^{27}Al$

proximities. DFT calculations were conducted on structural models to calculate NMR parameters in order to support the experimental values.

## C.2 Placement of Al heteroatoms in surfactant-directed layered silicates

The catalytic activity of aluminosilicates is strongly related to the number of incorporated Al atoms. As discussed in the previous chapter non-crystalline  $C_{16}H_{33}Me_3N^+$ - and  $C_{16}H_{33}Me_2EtN^+$ -directed layered silicate exhibit molecularly-ordered 2D crystalline silicate sheets separated by long chain organic surfactants. As illustrated in the Figure C.1, we seek to incorporate Al heteroatom by substituting Si sites into the lamellar silicate framework. While this is expected to perturb the short range molecular order within the silicate framework, the mesoscopic order is unaffected. This is well demonstrated by diffraction studies conducted for  $C_{16}H_{33}Me_3N^+$ - and  $C_{16}H_{33}Me_2EtN^+$ -layered aluminosilicates synthesized with different Al loadings.

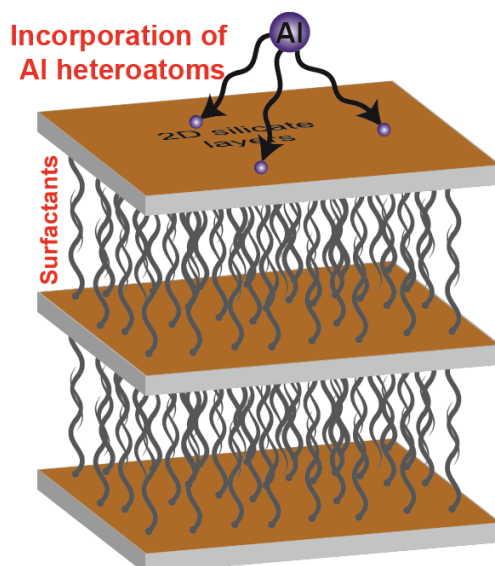


**Figure C.1** Cartoon showing the incorporation of Al heteroatoms into molecularly ordered two-dimensional silicate framework separated by long chain organic surfactants.

As shown in the Figure C.2, the powder X-ray pattern of  $C_{16}H_{33}Me_3N^+$ -layered silicates (pink) shows strong reflection at small angle that corresponds to 1.69 nm d-spacing. This reflection depicts the mesoscopic order. In addition, 0.42 and 0.35 nm d-spacings reveal the limited extent of long-range molecular order within the silicate framework. Interestingly, upon Al incorporation with  $Si/Al \approx 73$  ( $Si/Al$  ratio was measured by ICP analysis), the XRD spectrum (blue) shows small-angle reflections at the same positions that have been observed for the siliceous layered silicates. Even at  $Si/Al \approx 35$  (red) and 15

(black), the small-angle reflections exhibits identical  $2\theta$  values. This indicates that the mesoscopic order remains unaltered even at higher Al loading. Nevertheless a few additional reflections at wide angles suggest that Al incorporation may affect (and seemingly increase for Si/Al=15) the intra-sheet molecular order and causes a loss of global symmetry, especially at high Al loading. These additional reflections in the XRD pattern are however, insufficient to precisely describe the modifications of the local structure resulting from the Al incorporation.

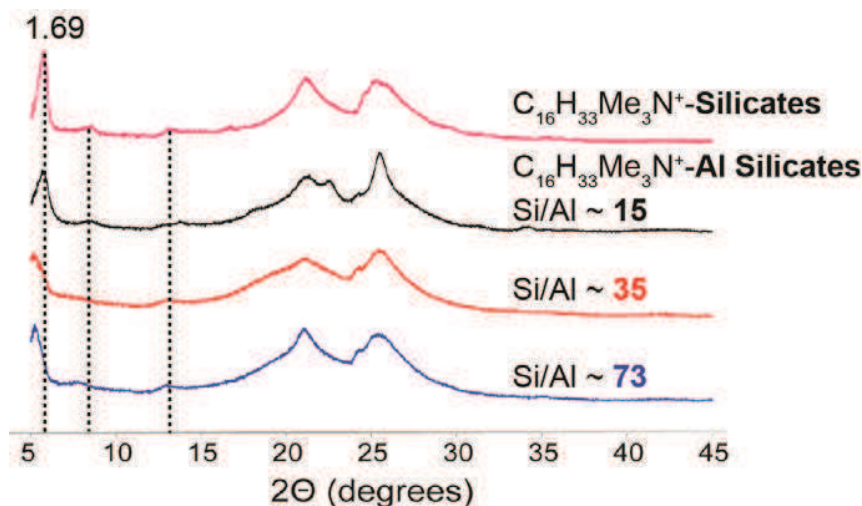


**Figure C.2** XRD spectrum of siliceous  $C_{16}H_{33}Me_3N^+$ -layered silicates (pink) and  $C_{16}H_{33}Me_3N^+$ -layered aluminosilicates with different Si/Al (73 - blue, 35 - red and 15 - black) ratio.

The same situation is observed in the case of  $C_{16}H_{33}Me_2EtN^+$ -layered aluminosilicates. Strong reflections at small angle (not shown) depict the lamellar structure of surfactant-directed layered silicates, and indicate that the mesoscopic order remains same even at the highest Al loadings (for example, Si/Al  $\approx$  25). Here, the intra-sheet molecular order also remains same, since small reflections at wide angle XRD spectra (Figure C.3) of  $C_{16}H_{33}Me_2EtN^+$ -layered aluminosilicates (with different Al loading, Si/Al = 100, 40 and 25 indicated by red, black and blue colors, respectively) remain unaltered even for the sample with high Al content. In principle, the Al incorporation deteriorates the molecular order by generating compositional and local geometric disorder within the first few coordination spheres of the Al. However, diffraction studies are typically unable to reveal such local disorder, a fortiori given the lack of 3D crystallinity of these materials. This could be probed on the other hand by high-resolution solid-state NMR technique.

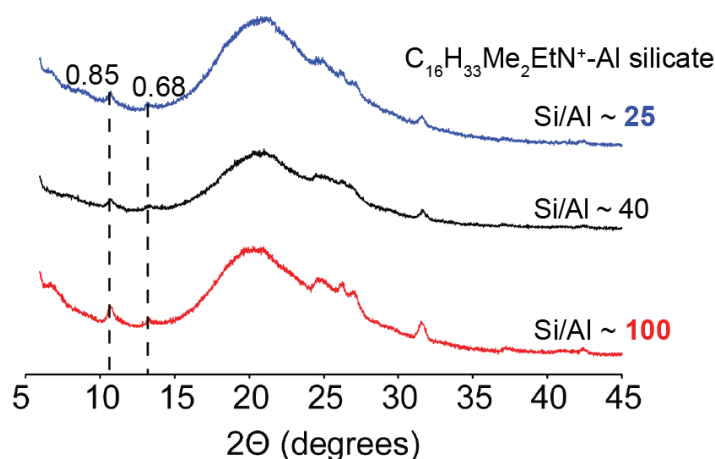


**Figure C.3** XRD spectra of  $C_{16}H_{33}Me_2EtN^+$ -layered aluminosilicates with different Si/Al (100, 40 and 25) ratio.

### C.3 Distribution of Al heteroatoms in $C_{16}H_{33}Me_2EtN^+$ -directed layered silicate

#### C.3.1 Probing influence of Al atoms on the local structure

In the present section we mainly discuss the consequences of Al incorporation on neighboring  $^{29}Si$  environment in  $C_{16}H_{33}Me_2EtN^+$ -directed layered aluminosilicate. The local structure around the Al atoms in the two-dimensional (2D) silicate framework can be identified primarily by 1D  $^{29}Si$  and  $^{27}Al$  MAS NMR measurements. The NMR experiments were collected for the samples synthesized at natural abundance  $^{29}Si$  (4.7%). As shown in the Figure C.4a, the  $^{29}Si[{}^1H]$  CP-MAS NMR spectrum presents five well resolved  $^{29}Si$  peaks at -96.8, -100.7, -103.4, -108.8 and -114.5 ppm labeled as Si1, Si2, Si3, Si4 and Si5, respectively (from left to right). The  $^{29}Si$  sites, Si1 and Si2 have been attributed to incompletely condensed  $Q^3$  and Si3, Si4 and Si5 to fully condensed  $Q^4$   $^{29}Si$  sites. The chemical shifts and line broadenings (FWHM) of all the five  $^{29}Si$  signals are similar to those observed in the corresponding siliceous material.<sup>22</sup> This indicates that the silicate structure remains globally the same even after Al incorporation. However, a broadening at the bottom of  $^{29}Si$  [ ${}^1H$ ] CP-MAS NMR spectrum suggests that the silicate framework may be altered or distorted near the Al region, while the rest of the structure remains unaltered. Several structural features related to the intrinsic property of the incorporated heteroatoms possibly justify the deterioration of molecular order around the Al atoms. First, the presence of an Al atom next to a silicon atom is known to modify the  $^{29}Si$  shift of the latter, with a global difference of 5 ppm between a  $Q^n$  and  $Q^n(1Al)$  unit. Second, the slight differences of atomic sizes between Al and Si atoms is expected to give rise to local structural distortion upon Al incorporation, caused by variation of bond lengths and Si-O-Al bond angles. Finally, the negative charge introduced by the substitution of  $Si^{4+}$

by an  $\text{Al}^{3+}$  cation must be compensated somehow, either by the presence of an additional  $\text{H}^+$  (Bronsted acid site, Al-OH, SiOH moieties) or a cationic surfactant molecule. This also is expected to change the local environment and can cause broadening of the  $^{29}\text{Si}$  NMR spectrum. Hence it is very clear from  $^{29}\text{Si}$  MAS NMR spectrum that the well resolved  $^{29}\text{Si}$  peaks pointing to the well defined ordered silicate structure in the Al free region, contrast with additional broadened  $^{29}\text{Si}$  contribution, which indicate that the local structure is largely affected around the Al atoms.

The local structural environment of Al atoms was probed by direct detection of  $^{27}\text{Al}$  nuclei. For example, as shown in the Figure C.4b the  $^{27}\text{Al}$  echo-MAS NMR spectrum contain a single broad  $^{27}\text{Al}$  peak centered at 53.4 ppm appeared in the region of four-coordinated Al atoms. In addition, the  $^{27}\text{Al}$  echo-MAS NMR spectrum confirms the absence of six-coordinated  $^{27}\text{Al}$  entities, which are supposed to appear in the region of 0-30 ppm. Six-coordinated Al atoms have been considered as extra-framework atoms except in few zeolites. The line width (FWHM) of the corresponding  $^{27}\text{Al}$  peak is  $\approx 10$  ppm, which is quite large in contrast with the  $^{29}\text{Si}$  peaks. Two main factors may contribute to the  $^{27}\text{Al}$  spectral broadening: (i) distribution of  $^{27}\text{Al}$  chemical shifts and (ii) second-order quadrupolar couplings due to anisotropic electric field gradients around the quadrupolar ( $I = 5/2$ )  $^{27}\text{Al}$  nuclei. Nevertheless, four-coordinated Al atoms in the silicate framework may be nearly isotropic environments, in which case the latter effect would be small. The  $^{27}\text{Al}$  NMR spectrum was collected at high magnetic field (17.6 T), which reduces the 2<sup>nd</sup> order quadrupolar interactions (which scale down with the square of the magnetic field) but even at 11.7 T (spectrum not shown) there is little evidence of such a broadening. Thus the  $^{27}\text{Al}$  peak reveals primarily the distribution of  $^{27}\text{Al}$  chemical shift which may be an indication that Al atoms may be incorporated at different crystallographic sites rather than preferentially in one.

The extent of molecular order in the silicate framework can also be established by probing the spatial or bonding interactions between Si atoms. For example, the 2D  $^{29}\text{Si}$  double quantum-single quantum (DQ-SQ) recoupling NMR measurements provide local structural insights by establishing spatial proximities. The homonuclear  $^{29}\text{Si}$ - $^{29}\text{Si}$  dipolar couplings were reintroduced by applying symmetry based SR26<sub>4</sub><sup>11</sup> recoupling pulses.<sup>181-182</sup> The correlation peaks in the 2D spectrum reveals the signature of spatially coupled  $^{29}\text{Si}$  spin pairs. The availability of NMR active  $^{29}\text{Si}$  nuclei in the sample at natural abundance  $^{29}\text{Si}$  is only 4.7%, which limits the sensitivity and receptivity of the NMR spectrum. As a result, the  $^{29}\text{Si}$  enrichment is crucial to determine the desired  $^{29}\text{Si}$ -O- $^{29}\text{Si}$  connectivities or  $^{29}\text{Si}$ - $^{29}\text{Si}$  proximities (see chapter B for synthesis details). The  $\text{C}_{16}\text{H}_{33}\text{Me}_2\text{EtN}^+$ -surfactant directed layered aluminosilicate was successfully synthesized with  $^{29}\text{Si}$  enrichment, and the corresponding 2D  $^{29}\text{Si}$  DQ-SQ recoupling NMR spectrum is shown in Figure C.4c.

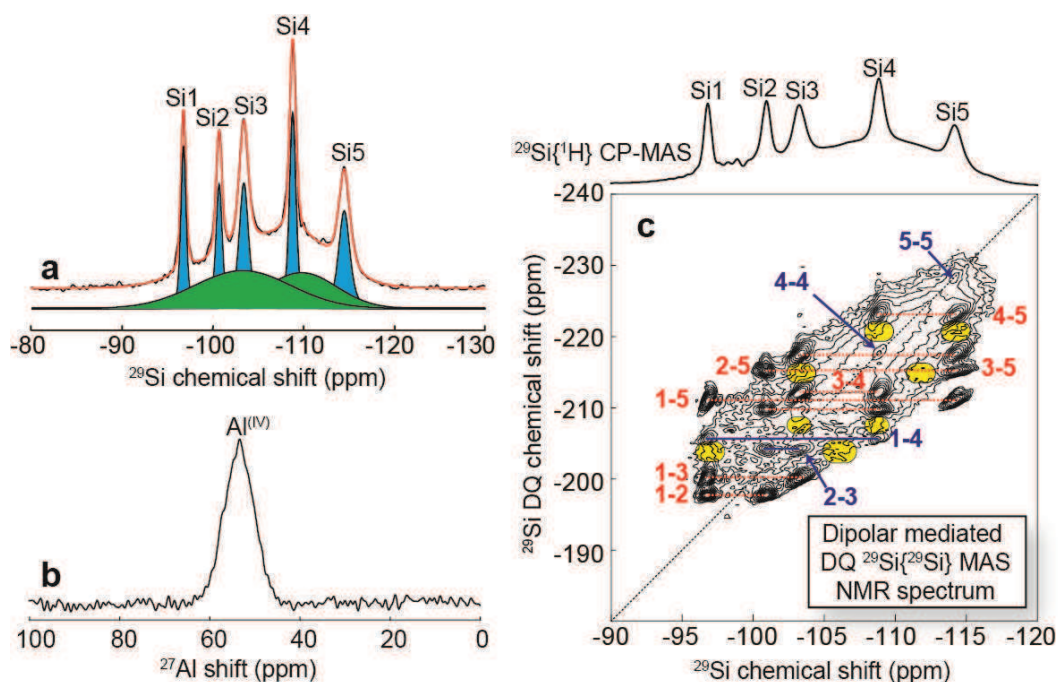


**Figure C.4** (a)  $^{29}\text{Si}\{^1\text{H}\}$  CP-MAS (black) (b) and  $^{27}\text{Al}$  echo-MAS NMR spectrum of  $\text{C}_{16}\text{H}_{33}\text{Me}_2\text{EtN}^+$ -surfactant directed layered aluminosilicate ( $\text{Si}/\text{Al} = 40$ ) for the sample at natural abundance  $^{29}\text{Si}$  collected at a magnetic field of 9.4 T and 17.6 T, respectively. The  $^{29}\text{Si}\{^1\text{H}\}$  CP-MAS spectrum is fitted by Dmfit program<sup>210</sup>, where red dotted line is the simulated spectrum, peaks in blue color signifies the  $^{29}\text{Si}$  features in the Al free region and green region points to the  $^{29}\text{Si}$  features around the incorporated Al atom. (c) Dipolar-mediated  $^{29}\text{Si}$  DQ-SQ recoupling NMR spectrum of  $^{29}\text{Si}$  enriched  $\text{C}_{16}\text{H}_{33}\text{Me}_2\text{EtN}^+$ -surfactant directed layered aluminosilicate ( $\text{Si}/\text{Al} = 70$ ) collected at a magnetic field of 7.0 T with a spinning frequency of 4.6 kHz. Yellow region in the spectrum points to the  $^{29}\text{Si}$ -O- $^{29}\text{Si}$  connectivities of Si atoms in Al free region and Si atoms around incorporated Al atom.

The recoupling duration was set to a short duration of 3.5 ms, which ensures that the spectrum will be largely dominated by contributions from spatial interactions between connected Si atoms (typically located at ca. 3 Å from each other). Long-range interactions between non-bonded Si atoms should give rise in comparison to considerably smaller contributions. This is particularly true with  $^{29}\text{Si}$  enrichment where dipolar truncation will cause further attenuation of such long-range contacts. The 2D spectrum shows strong correlations (marked with red labels) revealing the identical features of those obtained for the siliceous layered silicates (See chapter A, Figure A.9). The weak correlations (blue lines) corresponds to the weak dipolar interactions, which are specific of proximities between non-connected  $^{29}\text{Si}$  pairs Si1-Si4, Si2-Si3, Si4-Si4, Si5-Si5...etc. A large spectral broadening in the 2D spectrum was observed in the region of both  $Q^3$  and  $Q^4$   $^{29}\text{Si}$  sites. This is consistent with the broadening observed at the

1D  $^{29}\text{Si}[^1\text{H}]$  CP-MAS NMR spectrum (showed at the top of the 2D spectrum) and suggests that part of the silicate framework seems to be highly disordered upon Al incorporation. This is a first indication that Al heteroatoms may be not incorporated in a single crystallographic site, in which case one might reasonably expect to see a set of resolved correlation peaks. One interesting observation is that Si atoms in the disordered region around Al atoms have large interaction with the Si atoms of the Al free-region. This is evidenced by  $^{29}\text{Si}$ -O- $^{29}\text{Si}$  correlation peaks that are expected to observe in the highlighted yellow region. Likewise, there are many contributions of ordered and disorderd  $^{29}\text{Si}$ -O- $^{29}\text{Si}$  connectivities or  $^{29}\text{Si}$ - $^{29}\text{Si}$  proximities revealed in the 2D spectrum, however it is difficult to exploit precisely such contributions in the presence of large spectral broadening. All the experimental evidence discussed above indicate that Al atoms were indeed incorporated in the layered silicate framework. However, the location of Al atoms in the 2D silicate framework has not been established. Hence, further experimental analysis were required to establish the distribution of Al atoms and the resulting local modifications of the 2D crystalline framework. Further elements to answer this different questions were obtained selectively by probing the bonding and through-space interactions between the Al and Si atoms.

### ***C.3.2 Multi-dimensional solid-state NMR probing the heteronuclear spatial interactions***

The extent of disorder as a result of Al atoms incorporation in the silicate framework could be determined by probing spatial interactions between the Si and Al atoms. For example, 2D dipolar mediated HMQC NMR investigates the influence of Al atoms on the neighboring Si environment. Over the past few decades, few examples of such heteronuclear  $^{29}\text{Si}$ - $^{27}\text{Al}$  NMR correlation measurements were reported to exploit the proximities and connectivities between Si and Al atoms in zeolites, for example.<sup>211-215</sup> In the dipolar mediated NMR experiments, the heteronuclear  $^{27}\text{Al}$ - $^{29}\text{Si}$  dipolar couplings are selectively reintroduced through various mechanism. In the current studies, we used  $R4^2_1$  symmetry-based dipolar recoupling scheme.<sup>189-190,216</sup> The 2D  $^{27}\text{Al}[^{29}\text{Si}]$  dipolar-mediated HMQC spectrum of  $\text{C}_{16}\text{H}_{33}\text{Me}_2\text{EtN}^+$ -surfactant directed layered aluminosilicate (natural abundance  $^{29}\text{Si}$ ) shown in the Figure C.5 shows a broad correlation revealing the signatue of spatially coupled  $^{29}\text{Si}$ - $^{27}\text{Al}$  entities.

It is typically challenging to perform such NMR experiment for aluminosilicate materials at natural abundance  $^{29}\text{Si}$ , since the availability of NMR isotopic  $^{29}\text{Si}$  is only 4.7%. Moreover, the availability of incorporated Al atoms in the sample described here is very low with a Si/Al ratio of 40. Nevertheless a 2D  $^{27}\text{Al}[^{29}\text{Si}]$  dipolar-mediated HMQC NMR spectrum was successfully recorded, albeit with a limited signal to noise and a rather long experimental time of 3 days. This opens the possibility of exploiting the structural features of heteroatom-containing zeolites or other related materials at molecular level using the excellent efficiency of this type of correlation experiment.

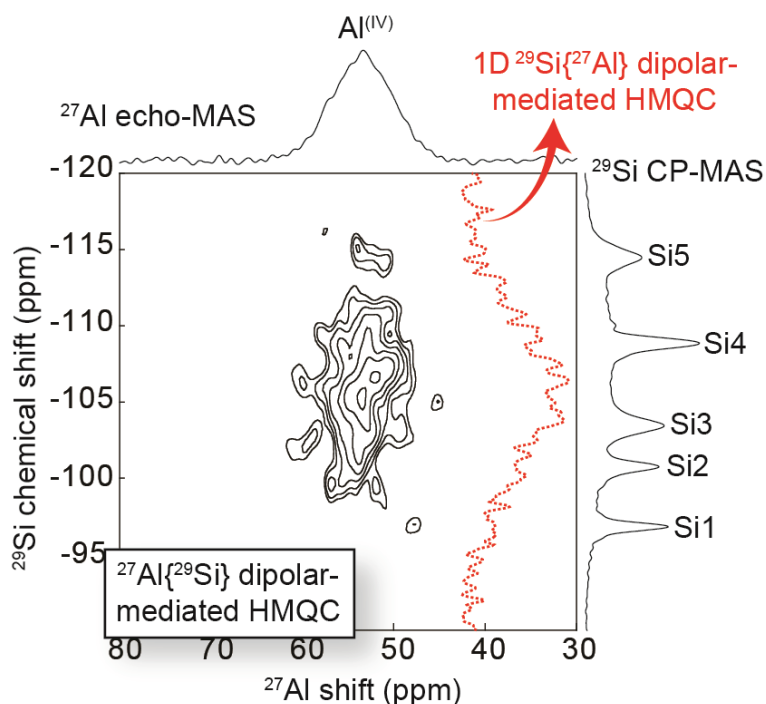


**Figure C.5** 2D  $^{27}\text{Al}\{^{29}\text{Si}\}$  dipolar-mediated HMQC NMR spectrum of  $\text{C}_{16}\text{H}_{33}\text{Me}_2\text{EtN}^+$ -surfactant directed layered aluminosilicate ( $^{29}\text{Si}$  natural abundance,  $\text{Si}/\text{Al} = 40$ ) collected at a magnetic field of 17.6 T by spinning the sample at 7.5 kHz. The  $^{27}\text{Al}$  and  $^{29}\text{Si}$  spectrum showed on top and right of the 2D spectrum, respectively are similar to those shown in Figure C.4a and C.4b, respectively. The red dotted spectrum in the horizontal dimension is the 1D dipolar-mediated  $^{29}\text{Si}\{^{27}\text{Al}\}$  CP-HMQC spectrum collected at a magnetic field of 17.6 T.

The 2D spectrum shows a broad correlation in the indirect ( $^{29}\text{Si}$ ) dimension correlated with single broad  $^{27}\text{Al}$  peak in the direct dimension, which indicates that incorporated Al atoms are closely surrounded by Si atoms from (most likely) the layered silicate framework. The recoupling duration was set to 5.2 ms to maximize signal to noise. This duration was found (from model aluminosilicate systems) to probe predominantly the spatial proximities between the Al and Si atoms, but also to a minor extent of non-connected nearby Si atoms. Hence, it is difficult to establish the specific location or distribution of Al atoms with the evidence of this 2D HMQC spectrum only. This suggests again that Al atoms may be randomly incorporated and has no specific location in the silicate framework. The red spectrum shown in the horizontal dimension is the 1D dipolar-mediated  $^{29}\text{Si}\{^{27}\text{Al}\}$  CP-HMQC spectrum of the same material collected at 17.6 T. Here, the magnetization is transferred from  $^1\text{H}$  to  $^{29}\text{Si}$  nuclei via cross-polarisation and then HMQC sequence implemented to probe the  $^{29}\text{Si}$ - $^{27}\text{Al}$  spatial interaction. The  $^{29}\text{Si}$  signal (detected in the direct dimension) depicts the signature of spatially coupled  $^{29}\text{Si}$ - $^{27}\text{Al}$  spin pairs. The collection of a

$^{27}\text{Al}$  dimension is not required because the sample contains only one type of four-coordinated Al atoms. In this spectrum also the broad  $^{29}\text{Si}$  contribution reveals the disorderness around the Al atoms. It is nevertheless remarkable that the distribution of  $^{29}\text{Si}$  signal associated with the surroundings of the incorporated Al is particularly broad, indicating a wide range of local structural environments around them. Furthermore, this peak is centered around -105 or -106 ppm, a region typically characteristic of  $Q^4(1\text{Al})$  environments, with little or no intensity in the  $Q^3(1\text{Al})$  region (-95 ppm). The absence of correlations in the  $Q^3(1\text{Al})$  region suggests that local modification happens upon Al incorporation, since whatever the Si site substituted with an Al atoms, one expects in principle one or two  $Q^3$  neighbors which become  $Q^3(1\text{Al})$  upon Si/Al substitution. However, high sensitivity would be required to more accurately analyze such observations, which brought us to synthesize the material with 99%  $^{29}\text{Si}$  isotopic enrichment.

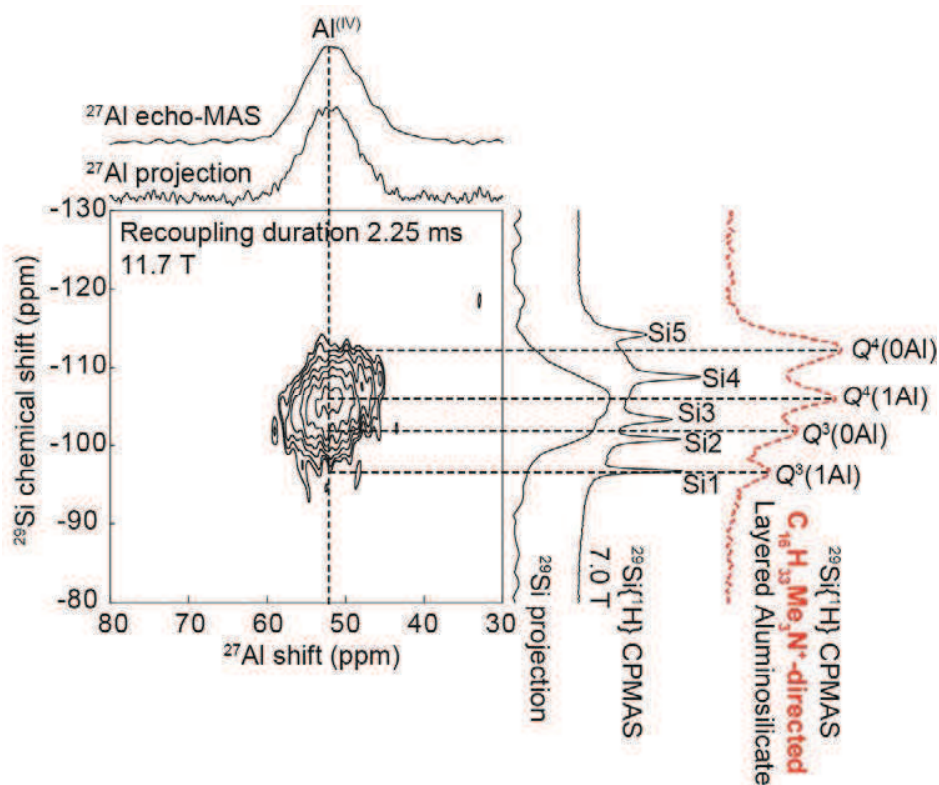


**Figure C.6** [Courtesy: Ming-Feng Hsieh] 2D  $^{27}\text{Al}[^{29}\text{Si}]$  dipolar-mediated HMQC NMR spectrum of  $^{29}\text{Si}$  enriched  $\text{C}_{16}\text{H}_{33}\text{Me}_2\text{EtN}^+$ -surfactant directed layered aluminosilicate ( $\text{Si}/\text{Al} = 70$ ) collected at a magnetic field of 11.7T, at 8 kHz MAS. The  $^{27}\text{Al}$  echo-MAS and  $^{29}\text{Si}[^1\text{H}]$  CP-MAS NMR spectrum and the corresponding projections are showed at the top and right of the 2D spectrum, respectively.

### *Aluminum-containing surfactant-directed layered silicates*

As explained earlier, the  $C_{16}H_{33}Me_2EtN^+$ -surfactant directed layered aluminosilicate with  $^{29}Si$  enrichment and Si/Al ratio of 70 has been synthesized successfully in spite of many complications. The  $^{27}Al$  echo-MAS and  $^{29}Si[{}^1H]$  CP-MAS NMR spectrum of  $^{29}Si$  enriched material is almost similar to the spectra of layered aluminosilicate at natural abundance  $^{29}Si$ , as shown in the Figure C.4. This indicates that the local environment around Al atoms remains same regardless of  $^{29}Si$  enrichment.

As shown in the Figure C.6,  $^{27}Al[{}^{29}Si]$  dipolar-mediated HMQC NMR spectrum was collected at a magnetic field of 11.7T by spinning the sample at 8 kHz. Here also, a broad correlation is observed corresponding to  $Q^4(1Al)$  and there appears to be little  $Q^3(1Al)$  or none of these  $^{29}Si$  sites in the indirect dimension with respect to a single broad signal corresponding to four-coordinated Al atom centered at 52 ppm. The  $^{27}Al$ - $^{29}Si$  heteronuclear dipolar couplings were reintroduced at the recoupling duration of 2.25 ms. Hence, the correlations are expected to reveal almost exclusively the signature of  $^{27}Al$ -O- $^{29}Si$  connectivities. Nevertheless, small contributions from non-connected  $^{29}Si$  species cannot be completely excluded. A broad correlation is observed in the  $^{29}Si$  dimension from -112 to -98 ppm, while in the  $^{27}Al$  dimension, the line width still remains as broad as observed in the 1D  $^{27}Al$  MAS spectrum (See the  $^{27}Al$  and  $^{29}Si$  projection). It is difficult to exploit the distribution of  $^{29}Si$  features from the broad correlation in the 2D spectrum. Hence, the broad distribution of chemical shift in both  $^{29}Si$  and  $^{27}Al$  dimension suggests that Al atoms are randomly incorporated at several distinct tetrahedral sites in the 2D silicate framework rather than specifically in one crystallographic site.

The  $^{29}Si$  chemical shift is known to be strongly influenced by the incorporated Al atoms, which displace the  $^{29}Si$  resonances of connected  $^{29}Si$  sites by 5 ppm per Al neighbor to higher frequencies, as was established for several aluminosilicate zeolites.<sup>10</sup> This is however a general trend, and there may be individual cases where the effect of an Al atom on the  $^{29}Si$  chemical shift of connected Si may be different since it depends on the Si-O-Al bond angle and bond length. The expected ranges of  $Q^4$ ,  $Q^4(1Al)$ ,  $Q^3$  and  $Q^3(1Al)$  are expected to be centered around -110, -105 -100 and -95 ppm, respectively. This infact beautifully illustrated by the  $^{29}Si$  MAS NMR spectra of the  $C_{16}H_{33}Me_3N^+$ -surfactant aluminosilicates (to be discussed at length in section C.4), an example of which (Si/Al = 15) is shown in red to the right of Figure C.6. The absence of contribution in the region of  $^{29}Si$   $Q^3(1Al)$  at -95 ppm for the  $C_{16}H_{33}Me_2EtN^+$ -directed aluminosilicate suggests the local modification or molecular rearrangement of the structure upon Al incorporation, such that the Al atoms connects with only  $Q^4$   $^{29}Si$  neighbors. Indeed, we know from the Si-O-Si connectivities established before that whatever the Al incorporation site(s), it should always have at least one  $Q^3(1Al)$  Si neighbors unless the framework was subject to a profound local structural rearrangement, with an increased extent of framework condensation around Al atoms. This is possible if

the neighboring  $Q^3$  Si cross-link with another  $Q^3$  Si species to make them  $Q^4$  Si moieties, in which case only  $Q^4(1Al)$  species would be obtained.

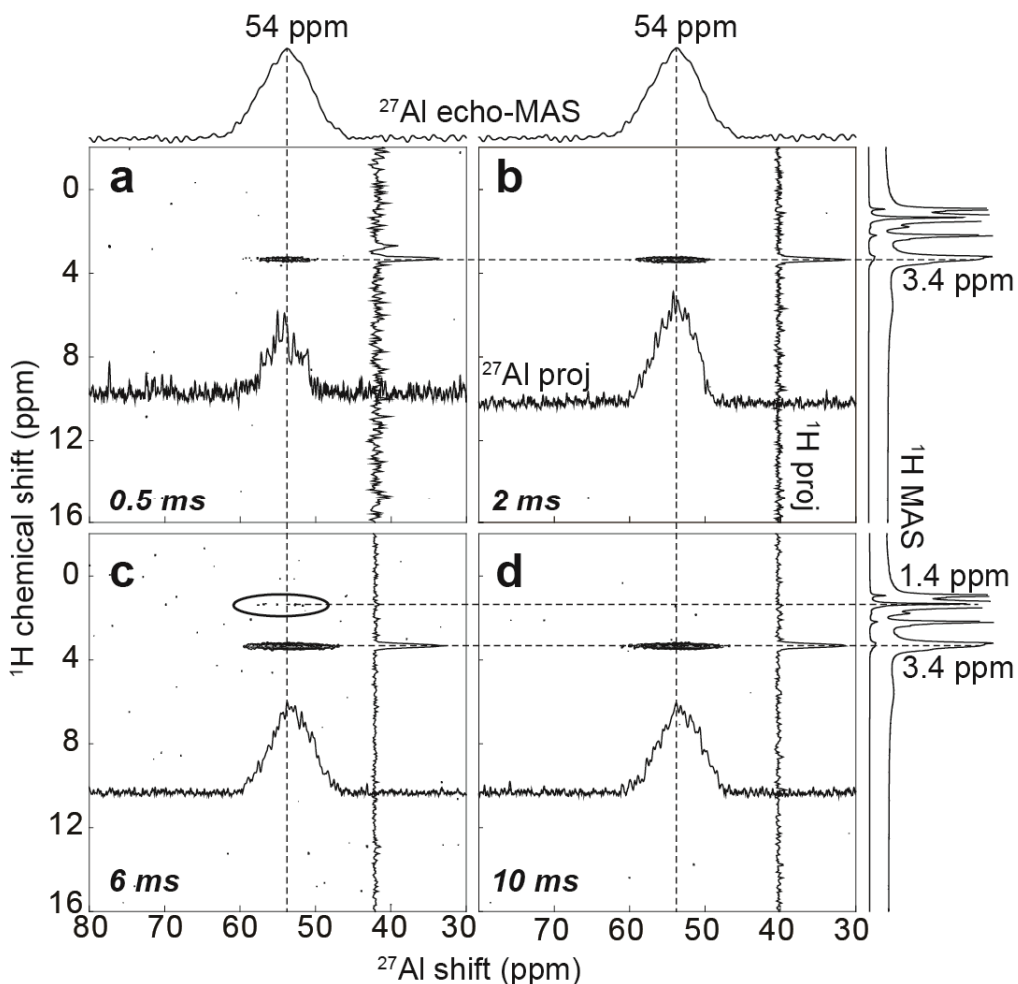


**Figure C.7** 2D  $^{27}Al[{}^1H]$  HETCOR NMR spectrum of  $C_{16}H_{33}Me_2EtN^+$ -surfactant directed layered aluminosilicate (natural abundance  $^{29}Si$ ,  $Si/Al = 40$ ) collected at a magnetic field of 20T by spinning the sample at 18 kHz with contact time (a) 0.5 ms, (b) 2 ms, (c) 6 ms and (d) 10 ms.

There are many ways in this respect to establish the associated molecular rearrangement. Primarily, the nature of incorporated Al atoms could be determined by establishing the spatial proximities between  $^{27}Al$  and nearby  ${}^1H$  moieties by collecting  $^{27}Al[{}^1H]$  HETCOR NMR spectrum, to probe the influence of the Al incorporation at the organic-inorganic interface. Figure C.7 represents the  $^{27}Al[{}^1H]$  HETCOR NMR spectrum of  $C_{16}H_{33}Me_2EtN^+$ -surfactant directed layered aluminosilicate acquired with contact times ranging from 0.5 (a) and 10 ms (d), at a magnetic field of 20.0 T by spinning the sample at the MAS rate of 18 kHz. The long contact times are used to probe the long range contacts

between  $^{27}\text{Al}$  and  $^1\text{H}$  species of the surfactant molecules in particular. Whereas short contact times are expected to reveal even small amounts of strongly coupled protons as would be found in Al-OH or Al-OH-Si species. All the 2D spectra in Figure C.7 exhibits a strong correlation peak at 3.4 ppm in the  $^1\text{H}$  dimension with respect to a single four-coordinated  $^{27}\text{Al}$  peak centered at 54 ppm, which are unambiguously assigned to  $^1\text{H}$  of the alkyl-ammonium surfactant headgroup. A small additional contribution observed at 1.4 ppm in the  $^1\text{H}$  dimension with respect to  $\text{Al}^{(\text{IV})}$  for the case with 6 ms contact time could be assigned to the  $\alpha\text{-CH}_2$  group of the alkyl-ammonium surfactant chain. There is no other contribution observed in the  $^1\text{H}$  dimension which confirms especially the absence of hydroxyl groups such as Al-OH, Si-OH or Al-OH-Si the Bronsted acid sites commonly found in zeolites that could have been expected to compensate the negative charge introduced by incorporated Al atoms. This negative charge must thus be compensated by only positively-charged alkyl-ammonium surfactants, which is consistent with the strong correlation peak observed at 3.4 ppm in the  $^1\text{H}$  dimension. This further supports the previous hypothesis that structural rearrangement may happen upon Al incorporation, since condensation of two  $\text{Si-O}^-$  to form an  $\text{Si-O-Si}$  or one  $\text{Al-O}^-$  and one  $\text{Si-O}^-$  to form an  $\text{Al-O-Si}$  would result in a loss of two negative charges, making the compensation of the Al negative charge unnecessary. In order to confirm all these hypotheses DFT calculations were conducted on aluminosilicate models considering surfactants as charge compensating entities, and also, given the complications inherent to the modelling of such non-bonding interactions between the framework and highly mobile surfactant molecules, on simpler models using protonated SiOH groups instead.

### ***C.3.3 DFT calculations of Al-containing $\text{C}_{16}\text{H}_{33}\text{Me}_2\text{EtN}^+$ - directed layered silicates***

The NMR parameters of Al-containing non-crystalline layered silicates have been calculated by first principle calculations and compared to the experimental values. The agreement between the experimental and calculated values allows to evaluate the different structural constraints. Advanced structure-determination protocols designed to overcome the absence of long-range 3D crystallinity of these materials were applied to the  $\text{C}_{16}\text{H}_{33}\text{Me}_2\text{EtN}^+$  - directed layered silicate material, and, led to the identification of three possible (and possibly co-existing) candidate structural models<sup>24</sup> (named structures 2, 3 and 4). All the three models were considered in our calculations, with one Al atom then successively substituting one of the possible crystallographic Si sites. The silicate framework of each of these models is composed of a unit cell with 10 Si sites (related two by two by symmetry). Smaller chain  $\text{C}_4\text{H}_9\text{Me}_2\text{EtN}^+$  surfactant molecules were included in the inter-layer space for all of the model structures to mimic the charge-compensating surfactant molecules (to have computational time).

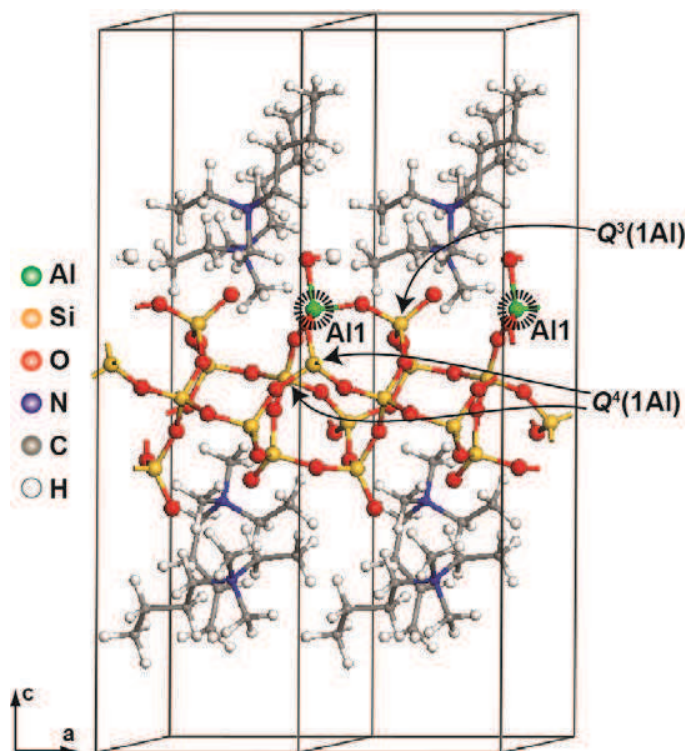


**Figure C.8** Structural model of  $C_4H_9Me_2EtN^+$ -directed layered aluminosilicate optimized by using planewave-based DFT. The Al is substituted into one of the Si1 ( $Q^3$ ) among the 10 T-sites present in the unit cell of candidate structure 2. The Al incorporation introduces an additional charge, which is compensated by adding proton directly on Al in  $Q^3$  sites. The black lines delimitate the unit cell.

One of the Si atoms out of 10 in the unit cell of  $C_4H_9Me_2EtN^+$ -directed layered aluminosilicate model has been replaced by an Al atom. Geometry optimizations were then conducted on these model structures to calculate NMR parameters. Likewise, the calculations were performed separately for all the three candidate structures by successively placing one Al atom into each  $^{29}Si$  sites, Si1, Si2, Si3, Si4 and Si5. The Si/Al substitution introduces a negative charge, which is compensated by a H atom added either to the directly-attached non-bridging O to form a Al-O-H moiety if Al is in  $Q^3$  site or on the non-bridging oxygen of one of the connected  $Q^3$  Si atom if Al is in a  $Q^4$  site. Figure C.8 represents the layered aluminosilicate model for the case where Al atoms are substituted into Si1  $^{29}Si$  site and H atom is added directly to Al via O atom. It has been shown from  $^{27}Al[{}^1H]$  HETCOR NMR spectrum (Figure C.7) that there is no hydroxyl groups at the organic-inorganic interface, but the unit cell was found too small to add an additional surfactant molecule for charge compensation. The  $^{29}Si$  chemical shifts are then calculated and plotted against the experimental values, as shown in the Figure C.9a. The symbols such as open

triangle and circle in the plot refers to Si(1Al) and Si(0Al) species, respectively. The colors of the symbols denote the different type of crystallographic  $^{29}\text{Si}$  sites.

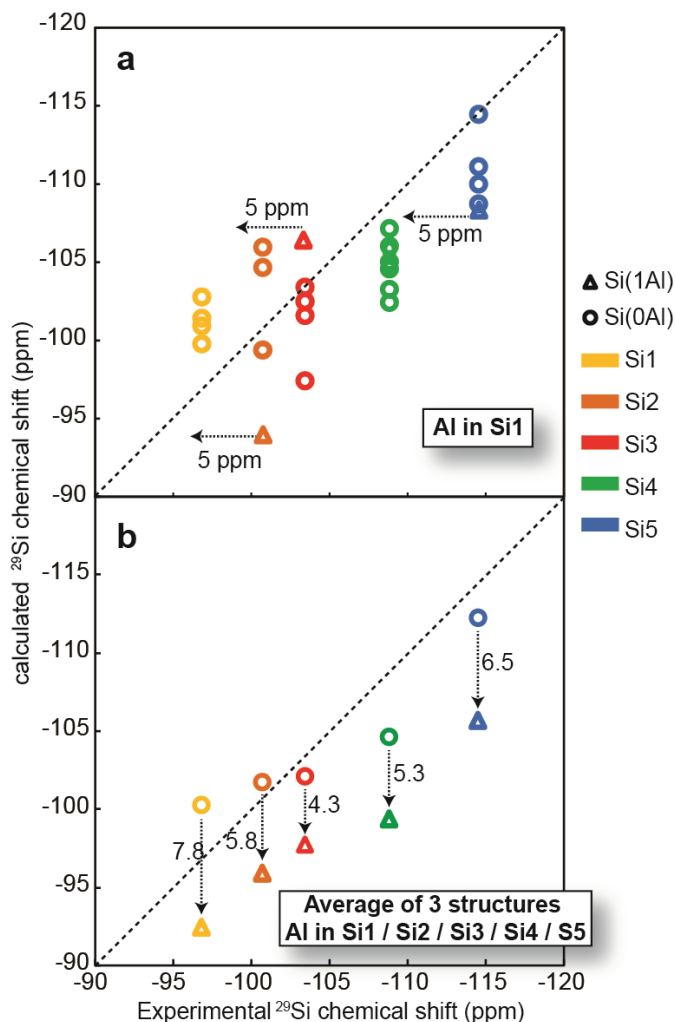


**Figure C.9** Plot of calculated vs experimental  $^{29}\text{Si}$  chemical shift of  $\text{C}_{16}\text{H}_{33}\text{Me}_2\text{EtN}^+$ - directed layered aluminosilicate, while the DFT calculations were conducted on three plane-wave optimized structural models, (a) when Al in Si1 crystallographic site (b) average  $^{29}\text{Si}$  chemical shift considering Al substitution in each crystallographic sites. The color of symbols triangle (Si(0Al)) and circle (Si(1Al)) in the plots represents different types of crystallographic sites such as Si1 (yellow), Si2(orange), Si3(red), Si4(green) and Si5(blue).

As explained earlier, the Al atoms have stronger influence on the neighboring  $^{29}\text{Si}$  species, which is reflected by a global displacement of  $^{29}\text{Si}$  chemical shift to higher frequency. In zeolites and other related silicate materials a 5 ppm shift has been observed for each addition of Al atom. The calculated  $^{29}\text{Si}$

chemical shifts show a large distribution of values for each crystallographic  $^{29}\text{Si}$  site, independent on their connectivity with Al atom (open circles). This is mainly because all the DFT calculations describe a static structure. As a result, each Si atom in these models sees only one of many possible positions and orientations of the surrounding alkyl-ammonium surfactant head groups. In contrast, in the real materials at ambient temperature, these head-group motions are dynamically averaged (at the timescale of  $^{29}\text{Si}$  NMR experiments, i.e.  $10^{-8}$  s), as established previously for the siliceous  $\text{C}_{16}\text{H}_{33}\text{Me}_2\text{EtN}^+$  - layered silicate.<sup>174</sup> This averages the most part of the distribution of  $^{29}\text{Si}$  chemical shifts and lead for each site to a single frequency. At temperature of  $0^\circ\text{C}$  or lower, however, the  $^{29}\text{Si}$  line widths broaden considerably (to the point where they largely overlap) because the distribution of surfactant headgroups orientations and positions, where motions are now too slow to be averaged, generate a distribution of  $^{29}\text{Si}$  chemical shifts. [See section D.4.2 for more details] The same thing happens with calculated  $^{29}\text{Si}$  chemical shifts, which are thus poorly reliable because they depend too much on the local energy minimization in which the nearby surfactant are found. Nevertheless, the  $^{29}\text{Si}$  chemical shifts calculations corroborate the influence of Al atoms on neighboring  $^{29}\text{Si}$  environment, which is reflected by the similar trend of shifting to higher frequency.

The average  $^{29}\text{Si}$  chemical shifts calculated for all the three candidate structures considering the Al atoms substituted into each crystallographic site is plotted against the experimental values, as shown in the Figure C.9b. Very interestingly, the average calculated  $^{29}\text{Si}$  chemical shift of Si(1Al) is 5.9 ppm higher than that of the Si(0Al) species. Thus, the displacement of  $^{29}\text{Si}$  chemical shift to higher frequency confirmed by calculations strongly supports the influence of Al atoms on its first  $^{29}\text{Si}$  neighbors. It could be suggested that the DFT calculations are robust to exploit the extent of chemical interactions with the neighboring environment. However, the large distributions of  $^{29}\text{Si}$  chemical shifts calculated for static models are only of limited relevance and should be considered with much caution. Hence, all the NMR experimental and calculated results suggest that Al atoms are randomly incorporated into different crystallographic sites.

## C.4 Distribution of Al heteroatoms in $C_{16}H_{33}Me_3N^+$ -directed layered silicate

### C.4.1 Local structure by 1D NMR methods

While the long-range lamellar organization of  $C_{16}H_{33}Me_3N^+$ -directed layered silicates is identical to the  $C_{16}H_{33}Me_2EtN^+$ -directed layered silicates, their short-range ordered molecular-scale structure is different, and the consequences of Al incorporation on neighboring  $^{29}Si$  environment also found to be entirely different. The structure of siliceous  $C_{16}H_{33}Me_3N^+$ -directed layered silicates resembles the structure of octosilicates.<sup>89</sup> Recently, Xia and co-workers<sup>217</sup> reported Al incorporation in layered silicates with structural features that are identical to the  $C_{16}H_{33}Me_3N^+$ -directed layered silicates. However, synthesis conditions and the precursors were slightly different from our studied materials. Particularly, the surfactant was cetyltrimethyl ammonium hydroxide (CTAOH), which led to a crystallization time of 24 days instead of 2 for our materials. They have also demonstrated the incorporation of Al heteroatoms into lamellar silicates with different Al loading. The main characterization methods are XRD and 1D solid-state NMR. The  $^{29}Si$  peaks observed for the layered silicates reported by Xia and co-workers reveals the significant modifications of the local structure on increasing the Al content. The interpretations were however based on incorrect assignments of the  $^{29}Si$  NMR data, which will be discussed and revised later in the present section.

A series of  $C_{16}H_{33}Me_3N^+$ -directed layered aluminosilicates were synthesized as a function of Al loading with Si/Al ratio of 73, 30 and 15 (measured by ICP) using CTAB as precursor. As demonstrated for the other material in section C.3.1, 1D  $^{29}Si$  and  $^{27}Al$  MAS NMR measurements provides the preliminary insights into the local structure. As can be seen from Figure C.10, the  $^{29}Si$  [ $^1H$ ] CP-MAS NMR spectra (Si/Al = 73, 35 and 15 as shown in Fig C.10b, c and d, respectively) presents additional  $^{29}Si$  peaks on increasing the Al loading in contrast to their siliceous analog (Fig C.10.a). The distribution of  $^{29}Si$  chemical shift indicates the signature of local modification caused by Al incorporation. All three samples with Si/Al = 73, 30 and 15 were prepared at natural  $^{29}Si$  abundance (4.7%). For the sample with Si/Al = 73, the  $^{29}Si$  [ $^1H$ ] CP-MAS NMR spectrum shows two intense peaks at -102 and -112 ppm, which could be attributed to incompletely condensed  $Q^3(0Al)$  and fully condensed  $Q^4(0Al)$   $^{29}Si$  sites, respectively. The intensity of  $Q^4$   $^{29}Si$  site is slightly larger than the  $Q^3$   $^{29}Si$  site suggests that the Al goes into  $Q^3$  sites and/or that the framework undergoes a local increase of polymerization upon Al incorporation, as discussed for the  $Me_2Et$  material. The weak peak at -107 ppm could be attributed to the  $Q^4(1Al)$  moieties. This is consistent with the displacement of  $^{29}Si$  chemical shift by 5 ppm to higher frequency. In addition, a very small peak observed at -95 ppm, which could be attributed undoubtedly to  $Q^3(1Al)$  moieties. The intensity of the additional  $^{29}Si$  peaks found to be weak in contrast to  $Q^3$  and  $Q^4$   $^{29}Si$

peaks, which is in good agreement with the low Al loading (Si/Al = 73). This indicates that the extent of structural modification is directly proportional to the amount of Al loading.

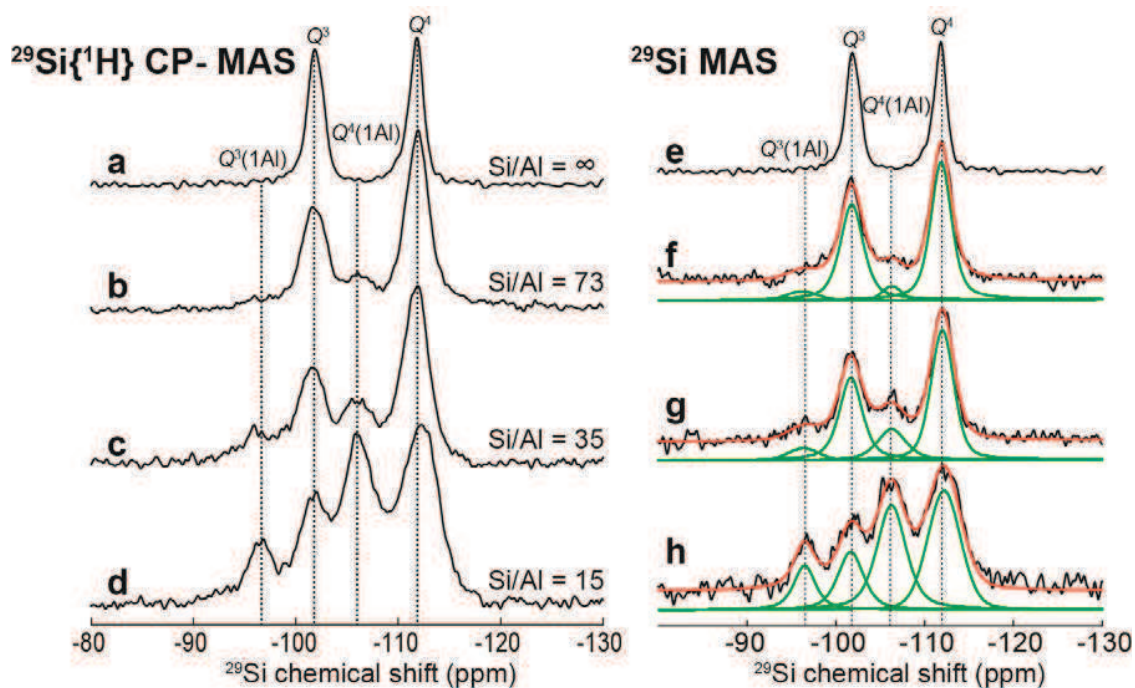


**Figure C.10** 1D  $^{29}\text{Si}\{^1\text{H}\}$  CP-MAS (b, c and d) and quantitative  $^{29}\text{Si}$  MAS (f, g and h) NMR spectra of  $\text{C}_{16}\text{H}_{33}\text{Me}_3\text{N}^+$ -surfactant directed layered aluminosilicate ( $^{29}\text{Si}$  natural abundance) with the Si/Al ratio of (b, f) 73, (c, g) 35 and (e, h) 15 collected at a magnetic field of 9.4 T by spinning the sample at a MAS rate of 10 kHz. The red spectra represents the simulated model of each  $^{29}\text{Si}$  MAS NMR spectra (fitted by Dmfit program). The individual peaks of simulated spectra are shown in green lines. (a, b)  $^{29}\text{Si}\{^1\text{H}\}$  CP-MAS of siliceous  $\text{C}_{16}\text{H}_{33}\text{Me}_3\text{N}^+$ -surfactant directed material collected at a magnetic field of 11.7T.

The relative intensity of  $Q^3$  and  $Q^4$   $^{29}\text{Si}$  peaks gradually decreases on increasing the Al loading with Si/Al = 30 and 15, while the intensity increases for  $^{29}\text{Si}$  peaks  $Q^4(1\text{Al})$  and  $Q^3(1\text{Al})$  species. This points to the availability of increased number of  $Q^n(1\text{Al})$  species (where  $n=3$  or  $4$ ) consistent with the increased Al loading. The relative intensities of all four  $^{29}\text{Si}$  peaks for different Al loadings were measured by collecting  $^{29}\text{Si}$  quantitative NMR spectra with a recycling delay of 500 seconds. The spectra were simulated by using the Dmfit program<sup>210</sup> (Figure C.10f, g and h), using both the quantitative  $^{29}\text{Si}$  MAS NMR spectra and the  $^{29}\text{Si}\{^1\text{H}\}$  CP-MAS NMR spectra to get stronger constraints on the line widths, position and shape (Gaussian/Lorentzian contributions). The relative intensities of  $^{29}\text{Si}$  peaks measured as a function of Al loading are used to determine the probability of Al incorporation in  $Q^3$  or  $Q^4$   $^{29}\text{Si}$  sites (see section C.4.4).

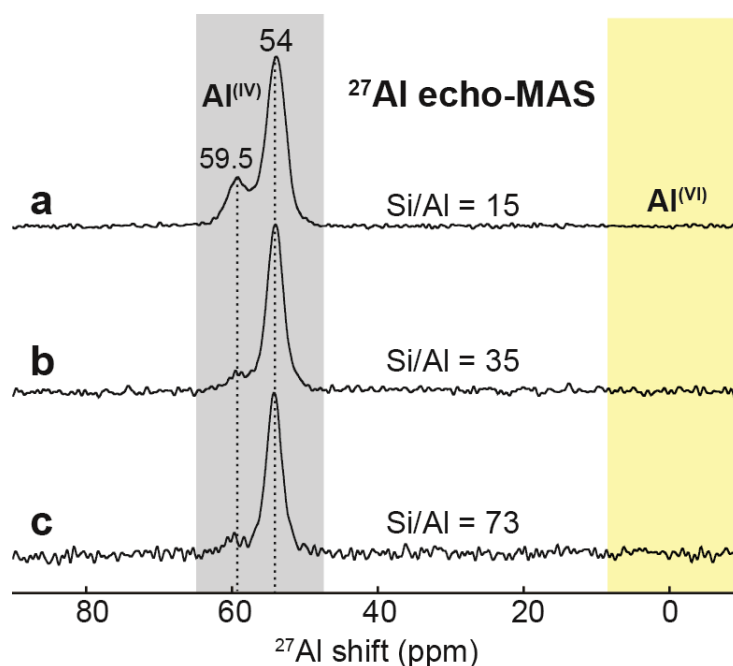


**Figure C.11**  $^{27}\text{Al}$  echo-MAS NMR spectra of  $\text{C}_{16}\text{H}_{33}\text{Me}_3\text{N}^+$ -directed layered aluminosilicate ( $^{29}\text{Si}$  natural abundance) with Si/Al ratio of (a) 15, (b) 35 and (c) 73, collected at a magnetic field of 20.0 T by spinning the sample at 18 kHz MAS.

The  $^{27}\text{Al}$  echo-MAS NMR spectra of  $\text{C}_{16}\text{H}_{33}\text{Me}_3\text{N}^+$ -directed layered aluminosilicate shown in the Figure C.11 (collected at identical experimental condition for all Si/Al ratios) reveal the nature of Al atoms in 2D silicate framework. Primarily, they confirm the presence in the samples of four-coordinated Al and the absence of six-coordinated Al atoms in the sample, which has to appear in the region of 0 ppm (yellow region). The increased substitution of Al atoms is further identified by their increased signal to noise due to a higher intensity of the dominant  $^{27}\text{Al}$  peak. Nevertheless, a smaller peak is observed at 59 ppm for all samples, but its intensity relative to the dominant peak at 54 ppm is highest with Si/Al = 15. This could be attributed to four-coordinated Al atoms that belong to an extra-aluminosilicate phase or impurity. This impurity is probably a small amount of zeolite which could also explain the extra XRD reflection observed for this material. Hence, it could be suggested that Al loading should be limited to the Si/Al > 15 in order to achieve pure surfactant-directed layered aluminosilicate phase. The clear separation between the  $^{27}\text{Al}$  peaks at 54 and 59 ppm will make it possible to draw some conclusions on the layered aluminosilicate phase without interferences from this additional phase. This is potentially true when probing the spatial proximities and bonding connectivities between Al and Si or H atoms, to be discussed below.

## C.4.2 Al heteroatom distribution by multi-dimensional NMR experiments

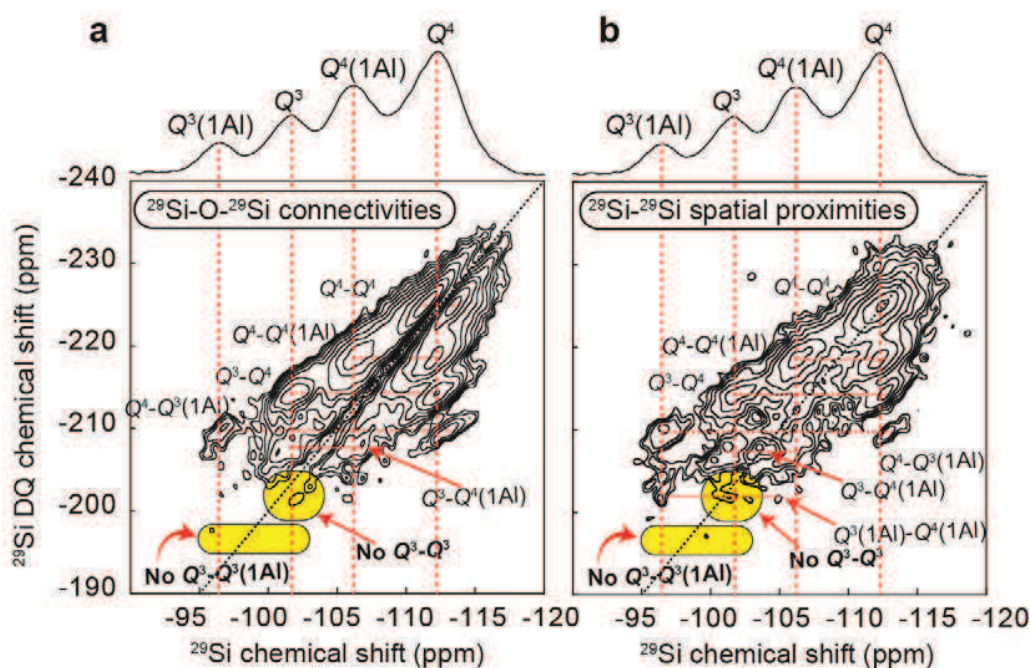


**Figure C.12** 2D (a)  $^{29}\text{Si}[^{29}\text{Si}]$  refocused INADEQUATE and (b)  $^{29}\text{Si}$  DQ recoupling NMR spectrum of  $^{29}\text{Si}$  enriched  $\text{C}_{16}\text{H}_{33}\text{Me}_3\text{N}^+$ -surfactant directed layered aluminosilicate ( $\text{Si}/\text{Al} = 10$  starting ratio) collected at a magnetic field of 7.0 T with spinning frequency of 10 and 4.6 kHz, respectively.

Al incorporation is expected to alter in several distinct ways the local structure of the otherwise molecularly-ordered silicate framework. Such changes at the local level have been established initially by probing the connectivities and spatial proximities between framework Si atoms via  $^{29}\text{Si}$ -O- $^{29}\text{Si}$   $^2J$ - and  $^{29}\text{Si}$ - $^{29}\text{Si}$  dipolar couplings, respectively. The poor sensitivity of the NMR spectrum at natural  $^{29}\text{Si}$  abundance limits the extent depth to which proximities and connectivities between  $^{29}\text{Si}$  and  $^{29}\text{Si}$  or  $^{27}\text{Al}$  species can be probed. In this context, the  $\text{C}_{16}\text{H}_{33}\text{Me}_3\text{N}^+$ -directed layered silicate material was successfully synthesized with 100%  $^{29}\text{Si}$  isotopic enrichment. Figure C.12a illustrates how correlated peaks in the 2D  $^{29}\text{Si}[^{29}\text{Si}]$  refocused-INADEQUATE NMR spectrum of  $^{29}\text{Si}$  enriched  $\text{C}_{16}\text{H}_{33}\text{Me}_3\text{N}^+$ -directed layered aluminosilicate ( $\text{Si}/\text{Al} = 10$  starting ratio) reveal the signature of  $^{29}\text{Si}$ -O- $^{29}\text{Si}$  connectivities between  $Q^n(1\text{Al})$  and  $Q^n(0\text{Al})$  species. Here also, the 1D  $^{29}\text{Si}[^1\text{H}]$  CP-MAS NMR spectrum (shown on top of the 2D spectrum) shows four  $^{29}\text{Si}$  peaks. The 2D spectrum shows a strong correlation peak among  $Q^4$  peaks. This peak is cut in its center by a ridge along the 2:1 diagonal, which is due to the cancellation of the effects of the  $J$ -coupling for two sites with identical chemical shifts. This  $Q^4$ - $Q^4$  and  $Q^3$ - $Q^4$  cross-peaks are identical to those found in the pure-silicate material<sup>22</sup> (also observed in the borosilicate, see Figure D.4a). One would also expect a  $Q^3$ - $Q^3$  connectivity (see connectivity Table A.1),

but these appear to become much less probable with the decreased number of  $Q^3$  sites upon Al incorporation (highlighted in yellow).

The  $Q^4(1Al)$  peak, which is (by definition) characteristic of the first T-shell around the incorporated Al atoms appears to be connected to both  $Q^3$  and  $Q^4$  sites, which again is expected from the connectivities established in the pure-silicate analog. Finally the  $Q^3(1Al)$  moieties appear to be connected only to  $Q^4$  moieties that are furthermore shifted with respect to the main  $Q^4$  signal, indicating a slight change of the local structure around these sites. The absence of  $Q^3(1Al)-Q^3$  signal (highlighted in yellow), given that each  $Q^3$  Si is connected to another  $Q^3$  in the pure-silicate analog, suggests that the Al giving rise to these  $Q^3(1Al)$  sites are in fact incorporated in the connected  $Q^3$  site. Similar information is obtained by probing the spatial proximities between Si atoms via  $^{29}\text{Si}-^{29}\text{Si}$  dipolar couplings, as demonstrated in the Figure C.12b. The 2D  $^{29}\text{Si}$  DQ-SQ dipolar-recoupling NMR spectrum collected at shorter recoupling duration 3.5 ms particularly probes primarily the short-range proximities between connected Si atoms. Thus, almost all the correlation peaks that appear in the  $^{29}\text{Si}[^{29}\text{Si}]$  DQ-SQ refocused INADEQUATE NMR spectrum (Fig C.12a) have also been observed in the dipolar-mediated DQ-SQ NMR spectrum (Fig C.12b). The advantage of this spectrum is that cross peak intensity does not vanish on the DQ-SQ spectrum diagonal (a feature that is intrinsic to  $J$  couplings), which makes it very complementary to the refocused INADEQUATE experiment. For example, a strong correlation is observed between  $Q^4$   $^{29}\text{Si}$  moieties which confirms such probability to be connected. This strongly contrast with the absence (as in the refocussed INADEQUATE) of  $Q^3-Q^3$  cancellations, which were expected. This, along with the decreasing  $Q^3$  intensity for increasing Al content point to the structural modifications that occur upon Al incorporation. Further experimental and theoretical evidence are required to clarify the nature and extent of these structural modifications.

The 2D  $^{27}\text{Al}[^1\text{H}]$  HETCOR NMR spectra of  $\text{C}_{16}\text{H}_{33}\text{Me}_3\text{N}^+$ - directed layered aluminosilicate were collected for the sample with both  $^{29}\text{Si}$  enrichment (Figure C.13a, contact time = 0.5 ms) and at natural abundance  $^{29}\text{Si}$  (Figure C.13b, contact time = 6 ms). The spectra were acquired at high magnetic field (20.0 T) in order (i) to improve the resolution in the  $^1\text{H}$  dimension, (ii) to average the second-order quadrupolar coupling and thus to improve the resolution also in the  $^{27}\text{Al}$  dimension. As shown in the Figure C.13a, the 1D  $^{27}\text{Al}$  echo-MAS NMR spectrum of the  $^{29}\text{Si}$ -enriched material is identical to that of the natural  $^{29}\text{Si}$  abundance analog (Fig C.13b). The only difference between the two  $^{27}\text{Al}$  NMR spectra is the slightly larger broadening due to residual  $^{27}\text{Al}-^{29}\text{Si}$  couplings which, with  $^{29}\text{Si}$ -enrichment, form a dense network of coupled spins that are harder to average by the MAS alone. The same peak at 59.3 ppm for both materials points either to two distinct types of incorporated Al or to the existence of extra-phase or impurities in the sample. We shall see that the latter possibility is more likely. The  $^1\text{H}$  MAS NMR

spectrum (in black) and the corresponding projections are shown in the vertical dimension. As can be seen in the Figure C.13a, a strong correlation is observed between the signal corresponding to four-coordinated Al atoms at 53.9 ppm and surfactant headgroup (tri-methyl group) at 3.5 ppm. Seemingly there is no signature of other protons interacting with the incorporated Al atoms. The short contact time of 0.2 ms used here to probe the interactions between  $^{27}\text{Al}$  and  $^1\text{H}$  species is expected to preferentially reveal strongly coupled  $^{27}\text{Al}$ - $^1\text{H}$  pairs as would exist in AlOH or Al-(OH)-Si moieties. In addition, even with longer contact time at 6 ms (Figure C.13b), still there is no signature of protons other than the surfactant headgroups (3.5 ppm) and alkyl chain (new peak at 1.4 ppm). This indicates that no Si-OH, Al-OH, Al-(OH)-Si moieties or even  $\text{H}_2\text{O}$  molecules are present around the incorporated Al atoms. Thus, as already established for the  $\text{C}_{16}\text{H}_{33}\text{Me}_2\text{EtN}^+$  aluminosilicates, the negative charge introduced by the incorporated Al atoms are compensated only by the positively-charged alkyl-ammonium surfactants. This establishes in particular the absence of bronsted acid sites in the sample similar to the case observed in  $\text{C}_{16}\text{H}_{33}\text{Me}_2\text{EtN}^+$ -surfactant directed layered aluminosilicate. Furthermore, a weak correlation is observed at 60 ppm owing to the extra-aluminosilicate phase with respect to tri-methyl surfactant headgroup at 3.5 ppm in the  $^1\text{H}$  dimension (Figure C.13a) indicating that these Al atoms, whether they are also located within the layered silicate framework or in an impurity, are also interacting with the surfactant headgroups.

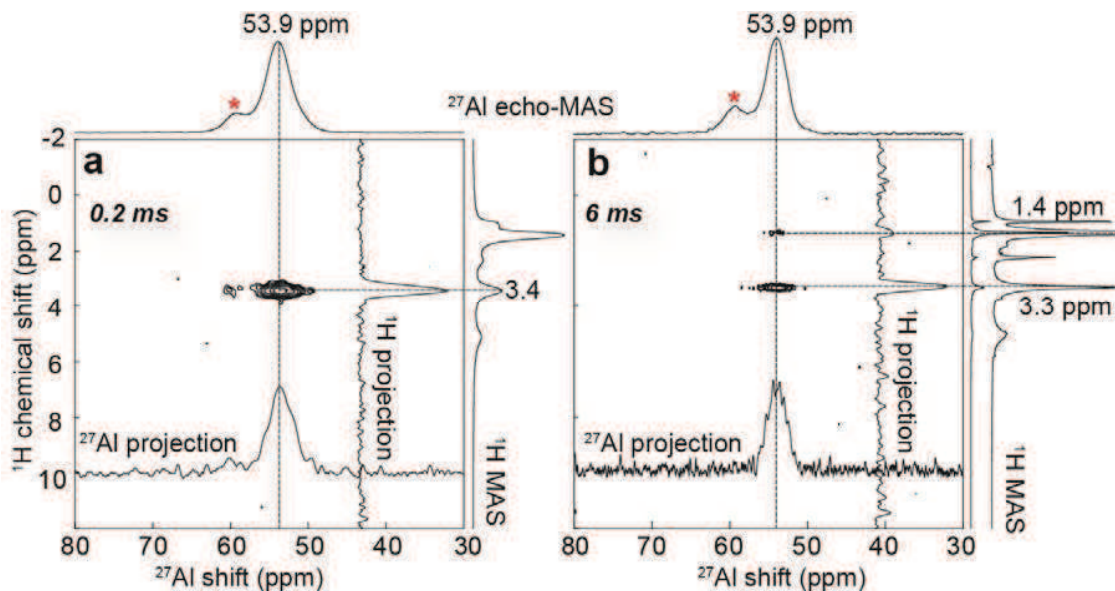


**Figure C.13** 2D  $^{27}\text{Al}[^1\text{H}]$  HETCOR NMR spectra of  $\text{C}_{16}\text{H}_{33}\text{Me}_3\text{N}^+$ -surfactant directed layered aluminosilicate synthesized (a) with  $^{29}\text{Si}$  enrichment and (b) at natural abundance  $^{29}\text{Si}$ . Both spectra were collected at a magnetic field of 20.0T by spinning the sample at 10 kHz and 18 kHz, contact time of 0.2

*ms and 6 ms, respectively. The 1D  $^{27}\text{Al}$  echo-MAS and  $^1\text{H}$  MAS spectrum and the corresponding projections are shown at the top and right of each 2D spectrum, respectively.*

Another important type of solid-state NMR experiment to probe the local structure around the Al atoms is  $^{29}\text{Si}$ - $^{27}\text{Al}$  dipolar- and  $J$ -mediated HMQC, as discussed in the section C.3.2. In this context, Figure C.14 shows 2D  $^{29}\text{Si}$ - $^{27}\text{Al}$  dipolar- and  $J$ -mediated<sup>165</sup> HMQC NMR spectrum, collected at different magnetic field for the  $\text{C}_{16}\text{H}_{33}\text{Me}_2\text{EtN}^+$  layered aluminosilicate. In addition, the  $J$ -mediated HMQC was performed in two different ways at high magnetic field (20.0T): (i) the classical way, which consists of exciting and detecting  $^{27}\text{Al}$  nuclei which have the double interest of relaxing faster than  $^{29}\text{Si}$  nuclei and having a higher magnetogyric ration, providing higher signal, (ii) a more unusual way by first building up signal on  $^{29}\text{Si}$  nuclei using a  $^1\text{H}$ - $^{29}\text{Si}$  CP and then recoupling  $^{27}\text{Al}$  nuclei to finally detect  $^{29}\text{Si}$  signal. All these 2D spectra provide the same structural information despite differences in the transfer mechanism of pulse sequence. As can be seen in the Figure C.14b, a strong correlation is observed between the signals  $\text{Al}^{(\text{IV})}$  at 53.9 ppm and  $Q^4(1\text{Al})$  at -107 ppm. In addition, a weak correlation is observed between the peaks  $\text{Al}^{(\text{IV})}$  at 53.9 ppm and  $Q^3(1\text{Al})$  at -97 ppm. This indicates the connectivity between both  $Q^4$  and  $Q^3$   $^{29}\text{Si}$  sites and the four-coordinated Al atoms at 53.9 ppm. The spectrum shown in Figure C.14c collected at magnetic field 20 T provides the same  $^{27}\text{Al}$ -O- $^{29}\text{Si}$  connectivity information however it gives better resolution than the previous one. Thus it is in good agreement with the presence of  $Q^4(1\text{Al})$  and  $Q^3(1\text{Al})$  crystallographic sites in the sample, as proposed previously based on 1D  $^{29}\text{Si}[^1\text{H}]$  CP-MAS NMR spectrum. On the other hand, the dipolar-mediated HMQC (Figure C.14a) exhibits correlation peaks similar to the  $J$ -mediated HMQC (Figure C.14b). In addition, it shows the contribution of non-connected nearby  $^{29}\text{Si}$  species ( $Q^3$  at -102 and  $Q^4$  at -102 ppm). Firstly, this interpretation confirms that Al heteroatoms are indeed incorporated into the layered silicate framework.

Interesting feature in all the spectra shown in Figure C.14 is the presence of an additional correlation peak at 51 ppm ( $^{27}\text{Al}$  dimension) with respect to  $Q^4(1\text{Al})$   $^{29}\text{Si}$  species at -110 ppm. This correlation peak is the signature of  $Q^4(1\text{Al})$  Si showing a drastic change in the shift values in both  $^{29}\text{Si}$  and  $^{27}\text{Al}$  dimension, in which their local structure seems to be completely different from the dominating  $Q^4(1\text{Al})$   $^{29}\text{Si}$  species which is observed at -107 ppm. As explained earlier, Al incorporation has strong influence on the local structure in such a way that the layered structure is polymerized by making new connectivities between  $Q^3$  or  $Q^4$   $^{29}\text{Si}$  sites. A small part of such polymerized network with large modification in the local structure accounts to this correlation peak.

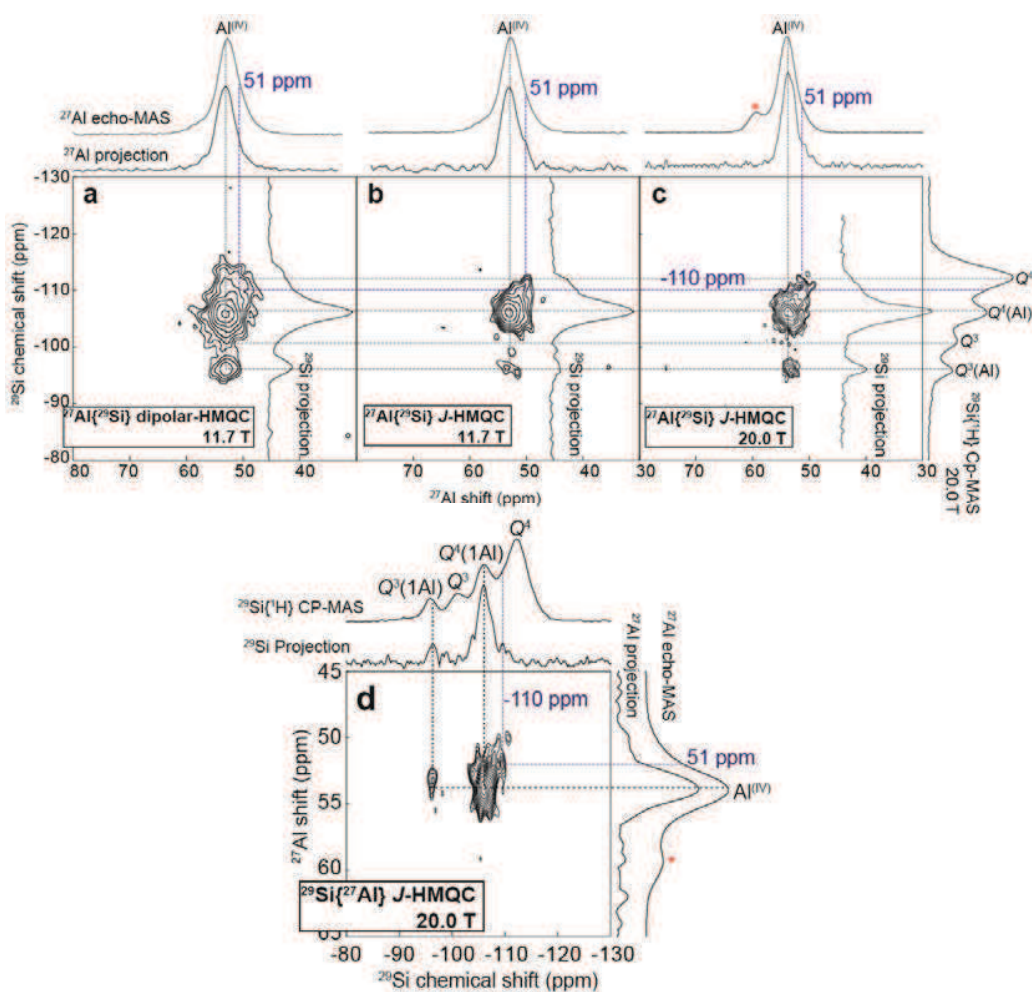


**Figure C.14** The 2D  $^{27}\text{Al}[^{29}\text{Si}]$  (a) dipolar- (b) J-mediated HMQC NMR spectrum of  $^{29}\text{Si}$  enriched  $\text{C}_{16}\text{H}_{33}\text{Me}_3\text{N}^+$ -surfactant directed layered aluminosilicate ( $\text{Si}/\text{Al} = 10$  starting ratio) collected at a MAS of 8 kHz and at a magnetic field of 11.7 T. The  $^{29}\text{Si}[^1\text{H}]$  CP-MAS NMR spectrum showed in the vertical dimension (far right) was collected at a magnetic field of 20.0 T. (c) 2D  $^{27}\text{Al}[^{29}\text{Si}]$  and (d)  $^{29}\text{Si}[^{27}\text{Al}]$  CP-J-mediated HMQC NMR spectrum collected at a magnetic field of 20T by spinning the sample at 14 kHz. For  $^{29}\text{Si}[^{27}\text{Al}]$  CP-HMQC, the magnetization was transferred from  $^1\text{H}$  to  $^{29}\text{Si}$  via cross-polarisation at the beginning of HMQC sequence. The  $^{29}\text{Si}[^1\text{H}]$  CP-MAS and  $^{27}\text{Al}$  echo-MAS NMR spectra are shown in the respective dimension. The red star (\*) points to the impurities or the extra-aluminosilicate phase.

This is further evidenced by probing the heteronuclear connectivities between  $^{29}\text{Si}$  and  $^{27}\text{Al}$  species, where the  $^{29}\text{Si}$  nuclei were detected in the direct dimension and  $^{27}\text{Al}$  nuclei were detected in the indirect dimension (Figure C.14d). The signal enhancement was achieved by transferring magnetization from  $^1\text{H}$  to  $^{29}\text{Si}$  nuclei. Here also, a similar features of  $\text{Q}^3(1\text{Al})$  and  $\text{Q}^4(1\text{Al})$  has been identified. In all the spectra shown in Figure C.14, there is no signature of weak peak at 60 ppm (red star in  $^{27}\text{Al}$  echo-MAS)

that interacts with any of the  $^{29}\text{Si}$  sites. This indicates that these four-coordinated Al atoms belong to an external impurity rather than to Al atoms incorporated into another framework site. The large variation in the intensity of the correlation peaks corresponding to  $Q^4(1\text{Al})$  and  $Q^3(1\text{Al})$  species and especially the reduced intensity corresponding to  $Q^3(1\text{Al})$  species already observed in the 1D spectra suggests that structural rearrangement undeniably takes place upon Al incorporation, which seems to promote framework condensation around it, as already suggested for the  $\text{C}_{16}\text{H}_{33}\text{Me}_2\text{EtN}^+$  layered aluminosilicate material. First principle calculations further provide elements to complete the picture of such consequences of the Al incorporation.

#### C.4.3 DFT modeling of Al-containing $\text{C}_{16}\text{H}_{33}\text{Me}_3\text{N}^+$ - directed layered silicates

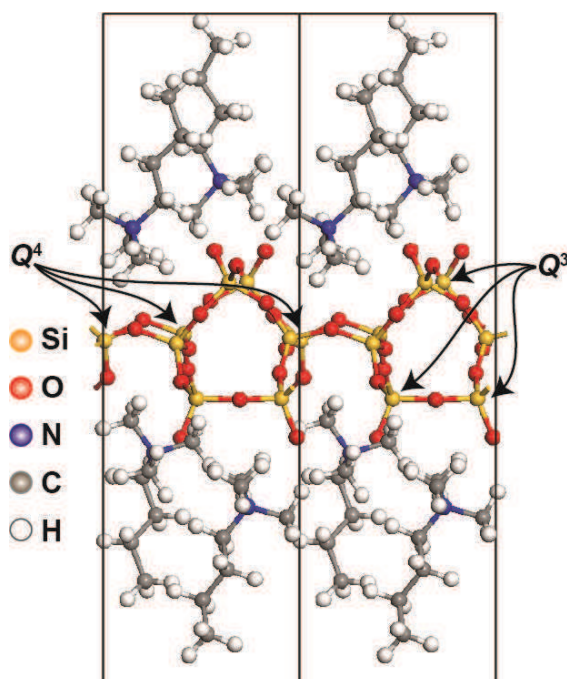


**Figure C.15** Example of DFT optimized model of the  $\text{C}_{16}\text{H}_{33}\text{Me}_3\text{N}^+$  - directed layered silicate material. Each unit cell consists of 8 T sites and the negative charge is balanced by adding  $\text{C}_4\text{H}_9\text{Me}_3\text{N}^+$  molecules to mimic the longer chain of  $\text{C}_{16}\text{H}_{33}\text{Me}_3\text{N}^+$  - surfactants and to have calculation time.

Plane-wave based DFT calculations were conducted on various models designated to capture the local structure(s) around incorporated Al heteroatoms in the  $\text{C}_{16}\text{H}_{33}\text{Me}_3\text{N}^+$  - directed layered aluminosilicate material and to probe the extent of structural rearrangement upon Al incorporation hypothesized based on solid-state NMR measurements. The  $\text{C}_{16}\text{H}_{33}\text{Me}_3\text{N}^+$  - layered framework silicate structure was taken from the reported structure of octosilicate<sup>89</sup>, which is composed of 32 tetrahedral Si sites per unit cell with a 16-fold symmetry (2 inequivalent T sites  $T_1$  and  $T_2$  or here  $Q^4$  and  $Q^3$   $^{29}\text{Si}$  sites, respectively). Our models consists of a single layer of octosilicate per unit cell, with an inter-layer space

(*c* parameter) adjusted to fit charge-compensating alkylammonium molecules between them. Small  $C_4H_9Me_3N^+$  molecules were included in the inter-layer space for all the model structures to mimic the charge-compensating surfactant molecules having longer  $C_{16}H_{33}$  alkyl chains in the real material. An example of such DFT-optimized  $C_4H_9Me_3N^+$  - directed layered silicate model is shown in Figure C.15. Series of geometry optimizations were then conducted on models based on the same initial structure, but with one of the Si atoms replaced by an Al atom.

Several possibilities were considered to balance the framework negative charge introduced upon Al heteroatoms incorporation. Primarily, the negative charge was compensated by adding  $H^+$  species for a few aluminosilicate models. However, these models are not discussed in this chapter, since solid-state NMR measurements suggests that there is no  $H^+$  involved in the charge compensation (Figure C.13). Hence, structural models containing only alkyl-ammonium surfactants as charge compensating agents are taken into account. Furthermore, solid-state NMR measurements strongly suggest that structural rearrangement with a local increase in framework condensation may happen upon Al atom incorporation. Hence, in the studied models, as illustrated in the Figure C.16, pairs of  $Q^3$  Si (or Al) sites with non-bridging oxygen atoms pointing to each other's were made to condense by replacing these two O atoms by a single O atom located midway between the two tetrahedral sites before optimization. Since two negative charges are removed in the process, the charge neutrality of the cell (containing one Al atom) is now simply obtained by removing one surfactant molecule. Table C.1 summarizes the main features, including the size of the supercell used for this model (in numbers of the basic cell containing 8 Si atoms), the number of each distinct types  $Q^n(mAl)$  of Si sites, the number of surfactant molecules, and the Si/Al ratio.

**Table C.1 Number of  $Q^n$  and  $Q^n(1Al)$  species and surfactant molecules added for layered aluminosilicate models shown in Figure C.16.**

Model	Supercell	Si/Al ratio(ICP)	Number of crystallographic Si sites				Total number of surfactants
			$Q^3$	$Q^4$	$Q^3(1Al)$	$Q^4(1Al)$	
Pure-silicate	1x1x1	$\infty$	16	16	0	0	16
(i)	1x2x1	73	10	12	2	6	14
(ii)	1x2x1	35	10	12	2	6	14
(iii)	2x2x1	15	12	15	0	4	13

Three distinct scenarios of structural rearrangements are discussed in this section: incorporation of an Al atom

- (i) in place of a  $Q^3$   $^{29}Si$  site where one cross linking was made between the Al itself and the neighboring  $Q^3$   $^{29}Si$  site (Figure C.16b),

- (ii) in substitution of a  $Q^4$   $^{29}\text{Si}$  site with one cross linking made between one of the connected  $Q^3$  Si neighbors with another  $Q^3$   $^{29}\text{Si}$  site (Figure C.16c), and
- (iii) in place of a  $Q^4$   $^{29}\text{Si}$  site, with two cross-linkings made between two neighboring  $Q^3$  and nearby  $Q^3$   $^{29}\text{Si}$  sites (Figure C.16d).

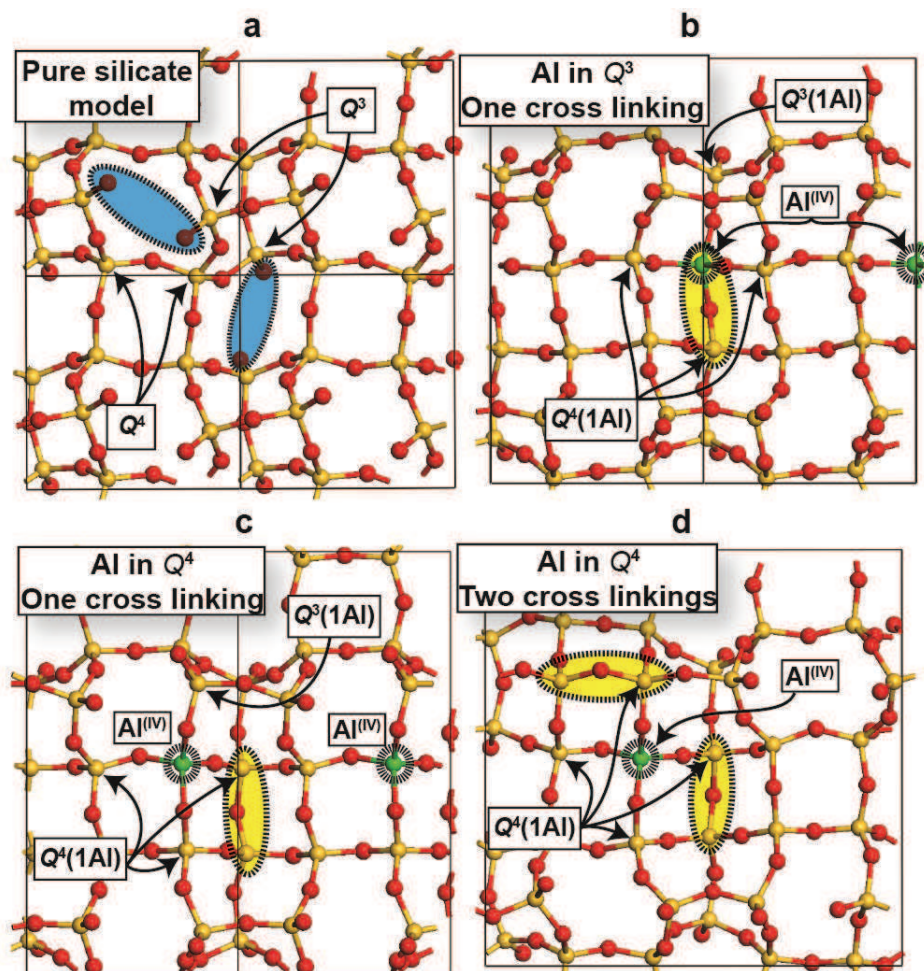


**Figure C.16** Optimized  $\text{C}_4\text{H}_9\text{Me}_3\text{N}^+$ -directed layered aluminosilicate models used to calculate NMR parameters on considering the structural rearrangement upon Al incorporation. (a) Siliceous  $\text{C}_4\text{H}_9\text{Me}_3\text{N}^+$ -layered silicate mode. (b) Model with Al atom substituted into  $Q^3$   $^{29}\text{Si}$  sites where the Al atoms cross link with neighboring  $Q^3$   $^{29}\text{Si}$  site. (c) Al atom substituted into  $Q^4$   $^{29}\text{Si}$  sites where one  $Q^3$  becomes  $Q^4(1\text{Al})$  by cross linking with another  $Q^3$   $^{29}\text{Si}$  sites via O atom. (d) Al atoms substituted into  $Q^4$   $^{29}\text{Si}$  sites where both  $Q^3$  sites become  $Q^4(1\text{Al})$  by cross linking with neighboring  $Q^3$   $^{29}\text{Si}$  sites via O atom. All the structural models are shown in top view with the surfactant molecules hidden for clarity. Solid lines delimitate the supercell used for each model.

### *Aluminum-containing surfactant-directed layered silicates*

The regions potentially concerned by the cross linking process between  $Q^3$   $^{29}\text{Si}$  sites is shown in the blue shaded region of the pure silicate  $\text{C}_4\text{H}_9\text{Me}_3\text{N}^+$ - model (Figure C.16a, viewed from the top with hidden surfactants). For the models with one cross linking, one surfactant per supercell was removed as compared to the pure-silicate model, whereas for those with two cross linkings three surfactants per unit cell must be removed to balance the framework negative charge. The models shown in Figure C.16 were all obtained after geometry optimizations of these structural models. Because the rearrangements associated with the cross linking(s) can affect a relatively large number of atoms, different supercell sizes were used for cases where no, one, or two such cross-linkings were considered. Very interestingly, no Si-O-Si or Al-O-Si bond breaking was observed during the course of these optimizations, which shows the successful convergence of the molecular-scale structure to some stable local energy minima. This supports the concept of the local condensation of the framework in the vicinity of the incorporated Al atom that was hypothesized on the basis of solid-state NMR measurements.

The  $^{29}\text{Si}$  chemical shifts calculated for all these optimized models were unfortunately not relevant to compare with the experimental values. This is because, as mentioned for the  $\text{C}_{16}\text{H}_{33}\text{Me}_2\text{EtN}^+$  layered aluminosilicate material, the calculations were conducted at 0 K on a static configuration, in which case each framework Si site “sees” one of many possible orientations and positions of nearby organic surfactants, which yields large distributions of  $^{29}\text{Si}$  chemical shifts for each type of Si site in the framework. However, in reality, the surfactants are mobile enough at room temperature for these distributions of  $^{29}\text{Si}$  chemical shifts to be dynamically averaged, which gives a single relatively sharp NMR signal from each  $^{29}\text{Si}$  site. Thus  $^{27}\text{Al}$  chemical shifts were calculated for all the structural models shown in the Figure C.16, and the calculated values lie between 61 and 66 ppm, as compared to an experimental shift of 54 ppm (at 20.0 T). Among the various reasons that can explain possible errors on the calculated  $^{27}\text{Al}$  chemical shift, the first is that they also are calculated for static models of a very dynamic system. From a theoretical point of view, the strongest evidence supporting the structural modification upon Al incorporation is the convergence of aluminosilicate models (Figure C.16b, c and d) after geometrical optimization. It indicates that the framework is able to bend such as to accommodate for structural rearrangements without which the experimental NMR data cannot be explained.

#### ***C.4.4 Quantification of framework T sites: experimental and theoretical approach***

All 1D and 2D NMR experiments and DFT calculations conducted on the  $\text{C}_{16}\text{H}_{33}\text{Me}_3\text{N}^+$ -aluminosilicate material concur to suggest that a local polymerization of the silicate framework occurs upon Al incorporation. The nature ( $Q^3$  or  $Q^4$ ) of the Si sites that the Al atoms replace should be reflected in the relative populations of the different types  $Q^n(m\text{Al})$  of  $^{29}\text{Si}$  signals measured in quantitative MAS

experiments, which may be recorded as a function of the Al loading. On the other hand, these populations can be calculated theoretically by considering the probabilities of Al atom incorporation in  $Q^3$  or  $Q^4$  sites, and whether cross-linking occurs or not between nearby  $Q^3$  sites. Comparisons between the experimental (NMR) and calculated populations are thus expected provide information regarding the validity of the different scenarios that can be considered. These experimental and theoretical populations of Si sites (in percentage) are plotted against the number of Al atoms (per 100 Si atoms) in the Figure C.17. The relative populations of Si sites as a function of Al loading extracted from  $^{29}\text{Si}$  quantitative NMR experiments (Fig C.10) are first plotted in Figure C.17a against number of Al atoms. The calculated Si/Al ratios of the models that are discussed in the Figure C.17 are reported in the Table C.2. It is important to notice that we used Si/Al ratios measured by NMR based on the total populations of  $Q^n(1\text{Al})$  and of  $Q^n$  (there was no detectable amount of  $Q^n(1\text{Al})$ ), all of which are very well resolved in the quantitative 1D  $^{29}\text{Si}$  spectrum and whose assignments were unambiguously confirmed by the  $J$ -mediated  $^{29}\text{Si}$ - $^{27}\text{Al}$  correlation experiments. We believe that these populations provide the most direct measure of the Si/Al ratio within the layered aluminosilicate framework of interest. The main limitation of this method is uncertainty in the ratio between the number of  $n[Q^n(1\text{Al})]$  of  $Q^n(1\text{Al})$  species and the number of Al atoms  $n(\text{Al})$ , which lies somewhere between 3 and 4 depending on whether the Al atoms are located in  $Q^3$  sites (with 3 Si neighbors) or  $Q^4$  sites (with 4 Si neighbors). It is quite remarkable that the Si/Al ratios measured with this method are all very different (by a factor close to 2) from the ratios measured by ICP analyzes, a discrepancy that we do not clearly understand yet, but that is under investigation.

**Table C.2 Si/Al ratio calculated theoretically based on the  $^{29}\text{Si}$  quantitative NMR measurement.**

Starting synthesis Si/Al ratio	Relative Population (%)				Measured Si/Al ratios				
	$Q^3(1\text{Al})$	$Q^3$	$Q^4(1\text{Al})$	$Q^4$	ICP	NMR <sup>(a)</sup>			
						Al in $Q^4$ or $Q^3\text{Si}^{(b)}$	Al in $Q^3\text{Si}^{(c)}$	Al in $Q^4$ or $Q^3\text{Si}^{(d)}$	Al in $Q^4\text{Si}^{(e)}$
$\infty$	0	50	0	50	$\infty$	$\infty$	$\infty$	$\infty$	$\infty$
50	4.1	40.5	3.9	51.4	73	49.2	37.4	49	49
25	5	32.8	14.9	47.3	35	20.1	15.1	19.1	19.1
10	11.2	16.6	34	38.2	15	8.9	6.6	7.9	7.9

<sup>(a)</sup>  $n(\text{Si})/n(\text{Al}) = a \cdot (n[Q^n(1\text{Al})] + n[Q^n]) / (n[Q^n(1\text{Al})])$  with  $3 \leq a \leq 4$ .

<sup>(b)</sup> Assuming Al has 4 Si neighbors irrespective of its incorporation in substitution of a framework  $Q^3$  or  $Q^4$  Si sites (meaning in the former case that an Al incorporated in a  $Q^3$  site systematically condenses with a nearby  $Q^3$  Si to become an Al in  $Q^4$ ).

<sup>(c)</sup> Assuming Al has 3 Si neighbors (incorporation in substitution of a framework  $Q^3$  Si)

<sup>(d)</sup> All Al in  $Q^3$  or  $Q^4$  Si sites with one cross-linking (Fig C16.b and c).

<sup>(e)</sup> All Al in  $Q^4$  Si sites with two cross-linkings (Fig C16.d).

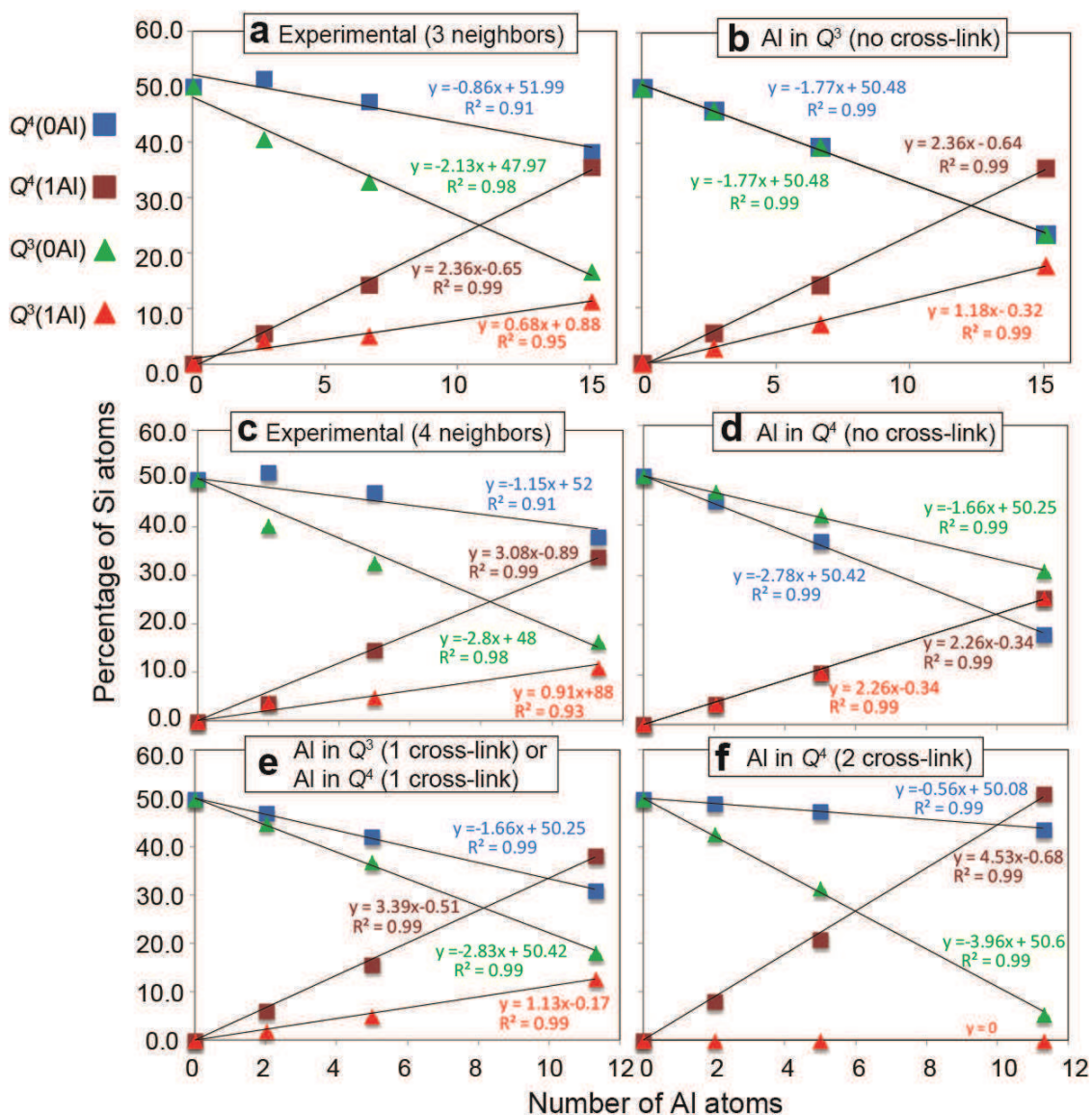


**Figure C.17** Plot of Si atoms in percentage (population) v/s number of Al atoms. Experimental data extracted from <sup>29</sup>Si quantitative NMR spectra shown in Figure C.10, assuming that Al atoms are surrounded by (a) 3 Si neighbors and (c) 4 Si neighbors. (b, d, e and f). Theoretically calculated values by considering Al atoms incorporated into (b) Q<sup>3</sup> and (d) Q<sup>4</sup> Si sites with no additional cross-linking of neighboring Q<sup>3</sup> sites. (e) Al atoms incorporated into Q<sup>3</sup> or Q<sup>4</sup> Si sites with one cross-linking of neighboring Q<sup>3</sup> sites. In both cases, for each Al incorporation two Q<sup>4</sup> and three Q<sup>3</sup> are destroyed that forms three Q<sup>4</sup>(1Al) and one Q<sup>3</sup>(1Al). (f) Al atoms incorporated into Q<sup>4</sup> Si sites considering two cross-linking of Q<sup>3</sup> Si sites where one Q<sup>4</sup> and four Q<sup>3</sup> are destroyed forming four Q<sup>4</sup>(1Al) and none Q<sup>3</sup>(1Al). T sites are represented in different colors: Q<sup>4</sup> – square in blue, Q<sup>4</sup>(1Al) – square in brown, Q<sup>3</sup> – triangle in green and Q<sup>3</sup>(1Al) – triangle in red.

Several possibilities of Al siting are considered in terms of their location and degree of polymerization between nearby  $Q^3$  Si sites (including possibly with the Al itself). Firstly, all Al atoms in substitution of only  $Q^3$  and  $Q^4$  sites without any structural deformation are considered, as shown in the Figure C.17b and d, respectively. In these cases, number of  $Q^3(1Al)$  and  $Q^3$  are systematically overestimated and  $Q^4(1Al)$  and  $Q^4$  are underestimated, which indicates that the aluminosilicate framework is locally more polymerized than the pure-silicate framework, and that the possibility of cross-linking  $Q^3$  sites upon Al incorporation should be considered. In the second scenario, all Al atoms are substituted either into a  $Q^3$  or a  $Q^4$  site, in the former case the Al condenses with a neighboring  $Q^3$  Si site (Fig C.16b), and in the latter case the cross-linking occurs between a  $Q^3$  Si site connected to the Al atom and a neighboring  $Q^3$  Si site (Fig C.16c). Both cases are identical from the point of view of the different Si-site populations, since for Al atom incorporated, two  $Q^4$  and three  $Q^3$  disappear to form three  $Q^4(1Al)$  and one  $Q^3(1Al)$ , and the Al atom is found in a  $Q^4$  environment. The relative populations of framework T sites for these two models are then plotted in Figure C.17e against number of Al atoms per 100 Si atoms (using the Si/Al ratios calculated from NMR data by taking into account that the Al atoms all have 4 Si neighbors in this scenario). A considerably better agreement between the theoretical (Fig C.17e) and experimental (Fig C.17c) values as compared to the cases where no cross-linking (Fig C.17b, d) is considered, which confirms again that a local polymerization of the framework very often (if not systematically) occurs upon incorporation of an Al atom. Furthermore, Al incorporation in  $Q^4$  Si sites with two-cross linkings were also considered, as shown the Figure C.17f. However, the absence in this case of  $Q^3(1Al)$  and a large difference in the population of other Si sites with respect to the experimental data suggest that this case is not particularly representative of the behaviour in this series of aluminosilicate samples.

In summary, even though the simple models with one cross-linking do not entirely capture the experimental data, suggesting that further refinements of the models might be considered, they nevertheless drastically improve the results as compared to the case where no further condensation of the framework occurs upon Al incorporation. These results further support the analyses of the data collected for the other material, where the poor resolution of the  $^{29}\text{Si}$  signals around the incorporated Al did not allow such a thorough quantitative analysis, but where the absence of detectable  $Q^3(1Al)$  signals indicated a similar increase, locally, in the degree of framework polymerization. Such rearrangements of the framework are furthermore expected to considerably affect the  $^{29}\text{Si}$  chemical shifts of nearby  $^{29}\text{Si}$  atoms, which explains at least in part the broad distribution of  $^{29}\text{Si}$  shifts observed in the vicinity of the incorporated Al for the  $\text{C}_{16}\text{H}_{33}\text{Me}_2\text{EtN}^+$ - directed layered aluminosilicates.

### **C.5 Conclusions:**

Al heteroatoms were successfully incorporated into the otherwise molecularly-ordered silicate frameworks of two strongly related,  $C_{16}H_{33}Me_2EtN^+$ - and  $C_{16}H_{33}Me_3N^+$ - directed layered silicates. The substitution of Si by Al heteroatoms largely affects the neighboring  $^{29}Si$  environments. This is well understood by the combination of multi-dimensional solid-state NMR measurements and quantum chemical calculations. In the case of  $C_{16}H_{33}Me_2EtN^+$ - directed layered aluminosilicates, the Al atoms seem to be incorporated in a non-specific way into several crystallographic sites. This is primarily suggested by large chemical shift distribution of  $^{29}Si$  and  $^{27}Al$  frequencies observed in the through-bond or through-space mediated  $^{27}Al$ - $^{29}Si$  correlation spectra, consistent with the large number of possible chemical environments that such non-specific Al incorporation might generate. Most importantly, these 2D  $^{27}Al$ - $^{29}Si$  correlation NMR experiments reveal in both materials the absence or reduced intensity of  $Q^3$  or  $Q^3(1Al)$  species. This ultimately suggests that major structural rearrangements happen upon Al incorporation in such a way that the Al atoms connects with only  $Q^4$   $^{29}Si$  sites. This is further confirmed by DFT calculation modelling and, in the case of the  $C_{16}H_{33}Me_3N^+$ - aluminosilicate material where various types of  $Q^n(mAl)$  Si moieties are resolved and may be quantified for different amounts of incorporated Al, by probability calculations. When  $Q^3(1Al)$  Si atoms in various structural models of both materials are manually connected with neighboring  $Q^3$   $^{29}Si$  sites to make them  $Q^4(1Al)$  and  $Q^4$  sites, subsequent geometry optimizations indicate that the layers have the capacity to bend such as to accommodate for the new Si-O-Si (or Al-O-Si) connectivities while retaining the proper tetrahedral geometries of both  $SiO_4$  and  $AlO_4$  sites. On the other hand, the  $^{27}Al[{}^1H]$  HETCOR confirms the absence of bronsted acidic sites in the sample, as there is no such Al-OH species reflected in the spectrum. This is another indication of the local rearrangements that are concomittant with the Al heteroatom incorporation, where the framework negative charge associated with the Al atoms may be fully compensated without using further addition of alkylammonim surfactants molecules.

*Aluminum-containing surfactant-directed layered silicates*

---

## Chapter D

# *Probing the local structure upon boron incorporation in non-crystalline layered silicates*

---

### D.1 Introduction

Increasing the catalytic performance of porous or lamellar silicate materials is of significant importance in zeolite chemistry. It is well known that the nature of framework atoms, especially the active sites, or heteroatoms, majorly contributes to the increased catalytic activities. Many parameters have to be considered in order to control the catalytic activities and acidities. The incorporation of different kinds of heteroatoms (Al, B, Fe, Ga etc) in several classes of porous materials, particularly in zeolites, was reviewed in chapter A. Chapter C describe the incorporation of aluminum heteroatoms in the ordered silicate frameworks of two strongly related surfactant-directed layered silicates and the modification of their local structure as a result. In the present chapter, we focus on the incorporation of B heteroatoms into frameworks of same lamellar silicate materials. Until now a clear knowledge of site specific distribution of heteroatoms in porous silicate materials is still somewhat unclear (recall chapter A). To this respect our main objectives are, (i) to incorporate B heteratoms into two-dimensional (2D) non-crystalline layered silicates and (ii) to establish the distribution of B heteroatoms in the silicate framework. This chapter is divided into three main sections.

**Section D.2** will focus on the standard synthesis and characterization aspects on boron containing non-crystalline layered silicates. It includes XRD, ICP analysis and one-dimensional (1D)  $^{11}\text{B}$  and  $^{29}\text{Si}$  MAS NMR spectra revealing the effect of B atoms on neighboring Si environment. **Section D.3** is centered on  $\text{C}_{16}\text{H}_{33}\text{Me}_3\text{N}^+$  - directed layered borosilicate, and try to establish the distribution of B atoms. Here, advanced multidimensional solid-state NMR experiments and computational methods were employed to examine the structural behavior upon B incorporation. In particular, the spatial proximities and connectivities between B and Si atoms were probed via heteronuclear  $^{11}\text{B}$ - $^{29}\text{Si}$  dipolar- and  $^{11}\text{B}$ -O- $^{29}\text{Si}$   $J$ -couplings, respectively, and allow determining the boron distribution in the silicate framework. A

similar experimental approach was adopted to investigate the B distribution in  $C_{16}H_{33}Me_2EtN^+$  - directed layered borosilicate, as will be explained in **section D.4**.

## **D.2 Incorporation of boron heteroatoms into surfactant-directed layered silicates**

### ***D.2.1 Hydrothermal synthesis, ICP and XRD analysis***

A typical hydrothermal synthesis of surfactant-directed layered borosilicates follows the same steps that used to synthesize siliceous surfactant-directed layered silicates reported by Christiansen *et.al.*<sup>218</sup> See section **B.4.2** for synthesis details and chemical composition of the precursors. These materials were synthesized primarily with natural abundance  $^{29}Si$  (4.7%) and TMOS (tetra-methoxy-orthosilicate) or Cabosil as Si source. As is discussed below, the B contents in these materials remain low, which severely limitates the ability of solid-state NMR to provide detailed information on the local structure around B atoms. Therefore, it is necessary to prepare these materials with  $^{29}Si$  isotopic enrichment. This ultimately enables to conduct advanced multi-dimensional NMR experiments shedding light onto the B distribution in the molecularly-ordered silicate framework. However, the hydrothermal synthesis of silicate materials with  $^{29}Si$  enrichment has thus far been challenging. Lack of previous expertise on synthesizing zeolites or related porous materials with  $^{29}Si$  enrichment makes synthesis so complicated. However, in the present case, the dense  $^{29}SiO_2$  is dissolved in basic condition to produce  $SiO_4$  species and then recondensed prior to use in actual hydrothermal synthesis. These kinds of modifications in synthesis criterion lead to obtain desired material. Surfactant-directed layered silicate materials and the corresponding analog of heteroatoms (Al or B) incorporation is routinely synthesized with  $^{29}Si$  enrichment, which is one of the major achievements in this project. The amount of incorporated B atoms is quantified by Inductively Coupled Plasma (ICP) analysis. The Si/B is 60 for natural abundance and 70 for  $^{29}Si$  enrichment of  $C_{16}H_{33}Me_2EtN^+$  - directed layered borosilicate. While for the  $C_{16}H_{33}Me_3N^+$  - directed layered borosilicate material, the Si/B ratio found to be 100 and 140 for the sample with natural  $^{29}Si$  abundance and  $^{29}Si$  enrichment, respectively.

The XRD patterns of both materials are showed in Figure D.1. The reflections at (a) small and (b) wide angle XRD spectra of (in blue)  $C_{16}H_{33}Me_3N^+$  - and (in red)  $C_{16}H_{33}Me_2EtN^+$  - directed layered borosilicate found to be identical to the corresponding siliceous layered silicates<sup>22</sup> and also the Al-containing surfactant-directed layered silicates (See section C.2). This indicates that the molecularly ordered structure remains the same in average, despite the possible occasional substitution of some framework silicon sites by boron atoms. Furthermore, it suggests that the extent of deterioration would be limited up to the first or even the second Si neighbors.

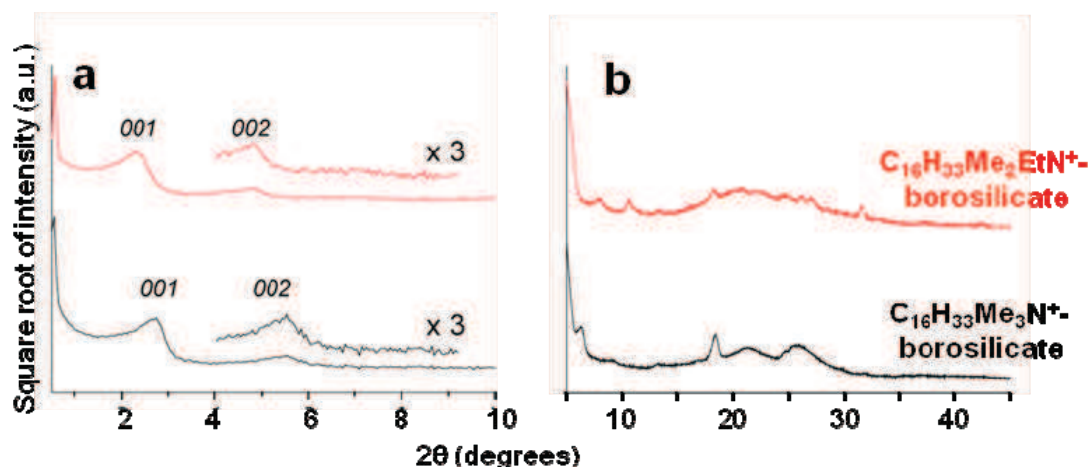


**Figure D.1** (a) Small and (b) wide angle XRD patterns of (black)  $C_{16}H_{33}Me_3N^+$  - and (red)  $C_{16}H_{33}Me_2EtN^+$  - directed layered borosilicate (at natural abundance  $^{29}Si$ ).

#### D.2.2 Effect of B on neighboring $^{29}Si$ environment based on 1D MAS NMR

The main features of the molecular-level structures of surfactant-directed layered borosilicates are primarily revealed in one-dimensional NMR experiments. The  $^{29}Si$  and  $^{11}B$  MAS NMR spectra of  $C_{16}H_{33}Me_3N^+$  - directed layered borosilicate are shown in Figure D.2a and b, respectively. The  $^{29}Si$  [ $^1H$ ] CP-MAS NMR spectrum (Fig D.2a) shows the same two well-resolved peaks at -101.5 and -111.5 ppm as observed in the pure-silicate form of this material<sup>22</sup>, and corresponding to  $Q^3$  and  $Q^4$   $^{29}Si$  moieties. The layered framework of this material is isostructural to crystalline octosilicate RUB-18 ( $Na_8[Si_{32}O_{64}(OH)_8]32H_2O$ ),<sup>89</sup> where these two sites correspond to crystallographic sites  $T_2$  and  $T_1$ , respectively. Here we labeled Si1 and Si2 to designate these two environments in the layered borosilicate material. The presence of boron in this material is revealed by the  $^{11}B$  echo-MAS spectrum (Fig. D.2b), which shows three sharp signals at -0.9, -1.9 and -2.5 ppm indicating the existence of three distinct four-coordinated boron ( $B^{IV}$ ) environments (B1, B2 and B3). This is in apparent contradiction with the existence of only two distinct tetrahedral sites (Si1 and Si2) within the silicate framework and reveals that the B incorporation affects the local structure in several distinct ways, which we seek to understand. While  $^{11}B$  is a quadrupolar nucleus (nuclear spin  $I = 3/2$ ), no significant broadening due to second-order quadrupolar interaction can be observed here, consistent with the nearly isotropic symmetry of  $BO_4$  environments.

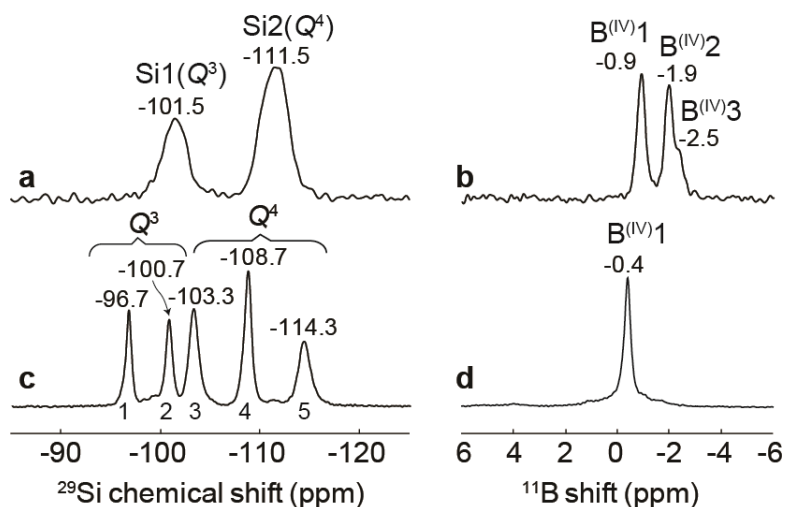


**Figure D.2** Solid-state (left)  $^{29}\text{Si}$  [ $^1\text{H}$ ] CP-MAS and (right)  $^{11}\text{B}$  echo-MAS NMR spectra of layered borosilicates directed by (a-b)  $\text{C}_{16}\text{H}_{33}\text{Me}_3\text{N}^+$  and (c-d)  $\text{C}_{16}\text{H}_{33}\text{Me}_2\text{EtN}^+$  surfactant molecules. All these spectra were collected on samples prepared at natural  $^{29}\text{Si}$  abundance (4.7%). All experiments were performed at a magnetic field of 17.6 T.

On the other hand, a strongly-related material prepared in identical conditions with a slightly more hydrophobic surfactant, forms a distinct framework with markedly different boron-incorporation behavior. As Christiansen *et.al*<sup>22</sup> and Hedin *et.al*<sup>23</sup> reported for pure-silicate systems, using  $\text{C}_{16}\text{H}_{33}\text{Me}_2\text{EtN}^+$ ,  $\text{Br}^-$  as the structure-directing agent yields a similarly short-range ordered lamellar material which essentially differs from the  $\text{C}_{16}\text{H}_{33}\text{Me}_3\text{N}^+$  - directing layered silicate material by the presence of five distinct tetrahedral sites. This is also the case for the material synthesized in the presence of boron, as illustrated in the  $^{29}\text{Si}$ [ $^1\text{H}$ ] CP-MAS spectrum of Figure D.2c, with  $^{29}\text{Si}$  peak positions of  $Q^3$  (-96.7 and -100.7 ppm) and  $Q^4$  (-103.3, -108.7 and -114.3 ppm) sites identical to those reported for the pure-silicate form.<sup>22-23</sup> Again, the presence of boron is established by the  $^{11}\text{B}$  echo-MAS spectrum of Figure D.2d, which shows a single peak at -0.4 ppm that can be assigned to a well-defined four-coordinated  $\text{B}^{(\text{IV})}$  environment. The observation of a single  $^{11}\text{B}$  peak is in marked contrast with the presence of five distinct tetrahedral sites in the framework of the  $\text{C}_{16}\text{H}_{33}\text{Me}_2\text{EtN}^+$ - directed layered borosilicate. This single  $^{11}\text{B}$  peak (0.25 ppm, fwhm) is furthermore narrower than each individual  $^{11}\text{B}$  peak observed for the  $\text{C}_{16}\text{H}_{33}\text{Me}_3\text{N}^+$  - directed layered borosilicate (0.3 to 0.4 ppm, fwhm, Fig. D.2b). Its width is also substantially smaller than the range of  $^{11}\text{B}$  shifts observed for  $\text{B}^{(\text{IV})}$  environments in the borosilicates studied here and others with related alkyl-ammonium structure-directing agents<sup>120</sup> (from -3 to 0 ppm). Such a narrow distribution of chemical environments strongly indicates that B atoms are

incorporated in a single well-defined tetrahedral site, and that the local structure around them is the same throughout the sample.

**Table D 1. Perturbation range induced by the B atoms.**

Materials	Si/B	Perturbation range (Å)	Number of neighbors	% of <sup>29</sup> Si signal affected
C <sub>16</sub> H <sub>33</sub> Me <sub>3</sub> N <sup>+</sup> -directed layered borosilicate	100	4	3.5	3.5
		5	10	10.0
		6	13.5	13.5
		7	16.5	16.5
		8	28	28
C <sub>16</sub> H <sub>33</sub> Me <sub>2</sub> EtN <sup>+</sup> -directed layered borosilicate	70	4	3.9	6.5
		5	9.3	15.5
		6	14.2	23.7
		7	18.7	31.2
		8	29.3	48.8

While the presence of four-coordinated boron was established for both materials from 1D <sup>11</sup>B NMR, it is remarkable that the <sup>29</sup>Si 1D NMR spectra are essentially identical to the ones obtained for the corresponding pure-silicate forms.<sup>22</sup> The presence of boron at tetrahedral sites within either framework should give rise to modifications of the <sup>29</sup>Si frequencies of nearby Si atoms due to the different valence of B<sup>3+</sup> as compared to Si<sup>4+</sup> cations and to local distortions of the framework to accommodate for the smaller size of B. The absence of visible contributions in the <sup>29</sup>Si 1D NMR spectra from such modified environments could suggest that the boron is not incorporated within the layered silicate framework. Nevertheless, these contributions could simply be negligible with respect to the dominant contributions from boron-free domains (i.e. <sup>29</sup>Si nuclei located too far from incorporated B to be sensitive to its direct or indirect effects) because of the small amount of B present in both samples. In the case of the C<sub>16</sub>H<sub>33</sub>Me<sub>2</sub>EtN<sup>+</sup> - directed layered borosilicate, as shown in Table D.1, with a Si/B ratio of 70 and all boron being considered incorporated in the framework, the first neighbors correspond to 5 to 7% of the total amount of Si (depending on whether the B occupies a Q<sup>3</sup> or a Q<sup>4</sup> site), while the first two neighboring spheres represent as much as 17 to 23 % of the total Si, which would no longer be a negligible contribution to the <sup>29</sup>Si NMR spectrum. An important implication of this observation is that, in the hypothesis that the B atoms are indeed incorporated in the framework, the effects of the Si to B substitution on nearby <sup>29</sup>Si shifts are necessarily strongly localized, and probably restricted to the first tetrahedral neighbors since the <sup>29</sup>Si spectra would otherwise be significantly affected. In the case of the C<sub>16</sub>H<sub>33</sub>Me<sub>3</sub>N<sup>+</sup> - directed layered borosilicate with a higher Si/B ratio of 100, the combination of the first and second tetrahedral neighbors represents only 5 to 10% of the total Si amount, so the presence of the boron within the framework could remain undetectable even if its effects extended further than the first connected neighbors.

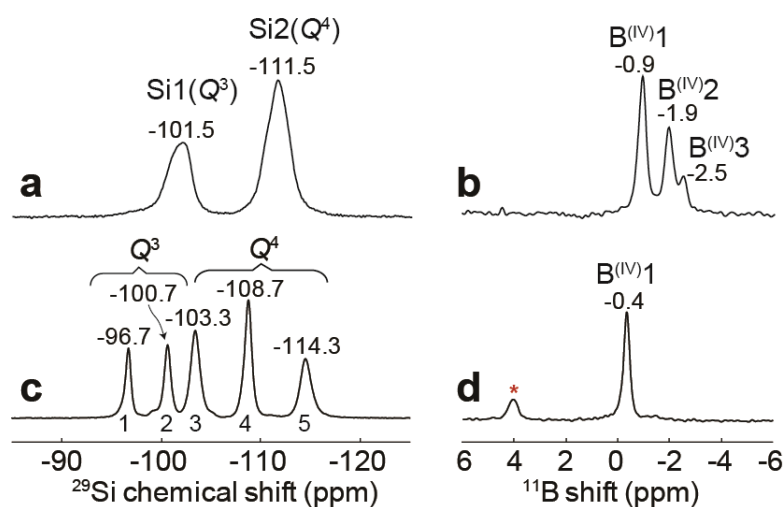


**Figure D.3.** Solid-state (left)  $^{29}\text{Si}[^1\text{H}]$  CP-MAS and (right)  $^{11}\text{B}$  echo-MAS NMR spectra of layered borosilicates directed by (a-b)  $\text{C}_{16}\text{H}_{33}\text{Me}_3\text{N}^+$  and (c-d)  $\text{C}_{16}\text{H}_{33}\text{Me}_2\text{EtN}^+$  surfactant molecules prepared with ca. 100%  $^{29}\text{Si}$  isotopic enrichment. All experiments were collected at a magnetic field of 17.6 T. Red stars point to the impurities or unidentified  $^{11}\text{B}$  moieties.

In the specific case of the materials studied here, and because the boron contents are so low, data of higher quality could be obtained on a sample prepared with isotopic enrichment in  $^{29}\text{Si}$ . The 1D  $^{29}\text{Si}$  and  $^{11}\text{B}$  spectra of the  $^{29}\text{Si}$ -enriched  $\text{C}_{16}\text{H}_{33}\text{Me}_3\text{N}^+$  - and  $\text{C}_{16}\text{H}_{33}\text{Me}_2\text{EtN}^+$  - directed layered borosilicate materials with measured Si/B ratio of 140 and 70 are shown in Figure D.3(a, b) and (c, d), respectively. The 1D spectra collected on  $\text{C}_{16}\text{H}_{33}\text{Me}_3\text{N}^+$ - directed layered borosilicate (Fig D.3a, b) are essentially similar to the spectra collected for the natural abundance sample (Fig. D.2a, b). In light of the  $^{11}\text{B}$  peak assignments discussed above, slight differences in the relative intensities of the main  $^{11}\text{B}$  peaks with respect to the natural-abundance sample may correspond to small differences in the distributions of B within the two crystallographic sites Si1 and Si2, which suggests that fine tuning of the synthesis conditions could possibly impact this distribution. The 1D spectra collected on  $\text{C}_{16}\text{H}_{33}\text{Me}_2\text{EtN}^+$ -directed layered borosilicate prepared with isotopic enrichment in  $^{29}\text{Si}$  (Fig D.3c, d) indicate that this sample is primarily made of a phase identical to the corresponding material prepared at natural abundance (Fig. D.2c, d) with an additional  $^{11}\text{B}$  signal contribution at 4 ppm that can be assigned to a secondary phase (marked with an asterisk). The presence of this secondary phase reflects the difficulty of adapting the syntheses of these materials to the  $^{29}\text{Si}$ -enriched silicon source.

### D.2.3 Establishing local structure by Probing $^{29}\text{Si}$ -O- $^{29}\text{Si}$ connectivities

The structure of  $\text{C}_{16}\text{H}_{33}\text{Me}_2\text{EtN}^+$  - directed layered silicate materials have been solved in their pure siliceous form<sup>24</sup> and structure of  $\text{C}_{16}\text{H}_{33}\text{Me}_3\text{N}^+$  - directed layered silicate is assumed to be similar to the octosilicate RUB18 structure.<sup>89</sup> An important piece of information is provided by  $^{29}\text{Si}$  [ $^{29}\text{Si}$ ] refocused

INADEQUATE NMR measurements, which probe the bonding interactions between framework  $^{29}\text{Si}$  moieties via homonuclear  $^{29}\text{Si-O-}^{29}\text{Si}$   $J$ -couplings. Such  $^{29}\text{Si-O-}^{29}\text{Si}$  connectivities in siliceous layered silicates were first reported by Christiansen *et.al.*<sup>22</sup> and Hedin *et.al.*<sup>23</sup> The local environments around the incorporated B may not be the same in the B-containing non-crystalline layered silicates. This also has greater impact on the Si-O-Si connectivities and thus the corresponding local disorder. To investigate such ambiguities with respect to local disorder upon B incorporation, here we reproduced the  $^{29}\text{Si}[^{29}\text{Si}]$  refocused INQDEQUATE NMR experiment for both  $\text{C}_{16}\text{H}_{33}\text{Me}_3\text{N}^+$  - and  $\text{C}_{16}\text{H}_{33}\text{Me}_2\text{EtN}^+$  - directed layered borosilicate materials (Figure D.4a and b, respectively). In the case of  $\text{C}_{16}\text{H}_{33}\text{Me}_3\text{N}^+$  - directed layered borosilicate, signal corresponding to the  $Q^3$  crystallographic site Si1 is strongly correlated with  $Q^4$  crystallographic site Si2, which indicates that Si1 has two connectivities with Si2  $^{29}\text{Si}$  sites. In these kinds of homonuclear  $J$ -mediated NMR experiments, the absence of intensity along the 2:1 axis (e.g. the “diagonal” in DQ-SQ spectra) points to the fact that the effects of the  $J$ -couplings between two sites of identical chemical shift vanish. Hence the correlations peaks between Si2-Si2 and Si1-Si1 appeared to be splitted on both sides of the diagonal. Their presence nevertheless establishes the existence of Si1-O-Si1 and Si2-O-Si2 connectivity. However, there is no additional contribution observed in the 2D spectrum driven by the effect of incorporated B atoms. This may be due to the extent of B incorporation is extremely small ( $\text{Si/B} = 140$ ), so that their effect is negligible to shown up in the following 2D  $^{29}\text{Si-O-}^{29}\text{Si}$  correlation spectrum. (See table C.1 for Si-Si connectivities)

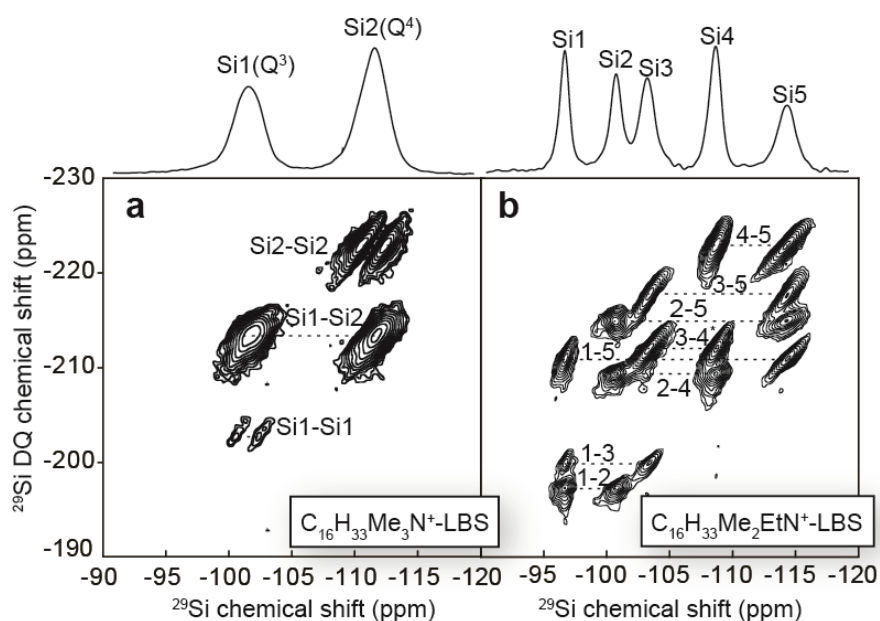


**Figure D.4**  $^{29}\text{Si} [^{29}\text{Si}]$  refocused INADEQUATE experiments collected for (a)  $\text{C}_{16}\text{H}_{33}\text{Me}_3\text{N}^+$  - and (b)  $\text{C}_{16}\text{H}_{33}\text{Me}_2\text{EtN}^+$  - directed layered borosilicate materials prepared with  $^{29}\text{Si}$  enrichment.

**Table D.2 List of Si-O-Si connectivities established for the  $C_{16}H_{33}Me_2EtN^+$ - and  $C_{16}H_{33}Me_3N^+$ -directed layered borosilicates.**

Material model	Silicon sites	$^{29}Si$ chemical Shift	Connectivities
$C_4H_9Me_2EtN^+$ - directed layered borosilicate	Si1	-96.7	Si2, Si3 and Si5
	Si2	-100.7	Si1, Si4 and Si5
	Si3	-103.3	Si1, Si4, Si4 and Si5
	Si4	-108.7	Si2, Si3, Si3 and Si5
	Si5	-114.3	Si1, Si2, Si3 and Si4
$C_4H_9Me_3N^+$ - directed layered borosilicate	Si2	-111.5	Si2 (x2), Si1 (x2)
	Si1	-101.5	Si2 (x2), Si1

A similar situation is observed in the case of  $C_{16}H_{33}Me_2EtN^+$  - directed layered borosilicate. As showed in the figure D.4b (tabulated also in table D.2), the observed correlation peaks are found to be identical to those observed in the case of pure siliceous layered silicates. This confirms that the Si-O-Si connectivities are unaltered upon B incorporation. This may again be due to the small B content in the sample (Si/B = 70). Hence, it is suggested that the effect of B on the local  $^{29}Si$  environment is too small to be detectable despite the resolution gain provided by such 2D NMR spectrum. This means that the local environment of the incorporated B atoms can only be probed if the corresponding atoms can be probed selectively, by somehow eliminating the dominant contributions due to B-free region of these materials.

### D.3 Boron heteroatoms distribution in $C_{16}H_{33}Me_3N^+$ -directed layered borosilicates

In the previous section of this chapter, we mainly discussed the effect of B incorporation on local structure based on 1D  $^{29}Si$  and  $^{11}B$  MAS NMR experiments. While, in the present section, we use advanced solid-state NMR to investigate specifically the direct environment of the incorporated B atoms, independent of the less-interesting regions farther away from its zone of influence. The structural study of  $C_{16}H_{33}Me_3N^+$ -directed layered borosilicates by advanced multidimensional NMR experiments is the center of attention in the present section. The 1D MAS NMR experiments provides the basic information identifying the presence of B in the silicate framework. But it is not sufficient to investigate the specific location of B atoms in certain crystallographic sites. Furthermore, it is very essential to determine the local modifications upon B incorporation. In this context, lots of efforts have been made onto probing the spatial and bonding interactions between the framework Si and B atoms. Initially the siting of B is anticipated by establishing the NMR interactions of incorporated B atoms with the hydrophobic surfactants. This is well supported by measuring the  $^{11}B$  transverse dephasing time ( $T_2'$ ) with surface

proton interactions. This section further explains the advantage of DFT (Density Functional Theory) calculations aiming to investigate the structural modifications observed within the silicate framework. This is achieved by calculating the NMR parameters and then comparing with the experimental values.

### D.3.1 Protons, surfactants, and charge compensation nearby incorporated B heteroatoms

It is reasonable to assume that the two dominant  $^{11}\text{B}$  signals at -0.9 and -1.9 ppm for the  $\text{C}_{16}\text{H}_{33}\text{Me}_3\text{N}^+$ -layered borosilicate might be compared to B incorporated in sites Si1 and Si2, respectively. This hypothesis can be supported by probing their respective interactions with nearby protons. Boron in substitution of Si  $Q^3$  sites are expected to interact much more strongly than boron in substitution of Si  $Q^4$  sites with protons, either because they form B-O-H moieties, or because their non-bridging oxygen strongly interacts with the surfactant head groups or solvent molecules. Here the latter case seems more plausible because the synthesis is conducted in basic conditions. Such a difference may be probed experimentally, for example by measuring transverse dephasing times  $T_2'$  (rate of signal loss during a spin echo) in the presence or absence of heteronuclear  $^1\text{H}$  decoupling.<sup>140,173</sup> The results of such experiments are shown in Figure D.5.

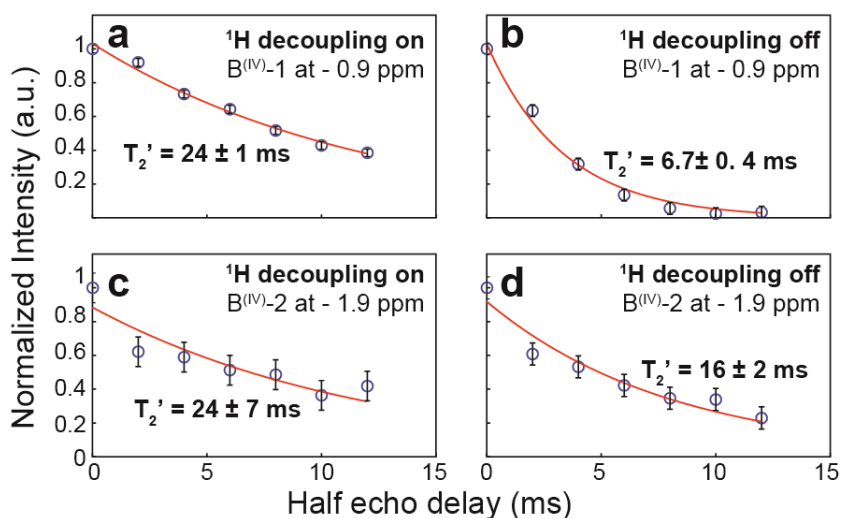


**Figure D.5** Transverse  $^{11}\text{B}$  dephasing time ( $T_2'$ ) measurements conducted (a, c) with and (b, d) without heteronuclear  $^1\text{H}$  decoupling for  $\text{C}_{16}\text{H}_{33}\text{Me}_3\text{N}^+$ -directed layered borosilicates to distinguish between  $Q^3$  and  $Q^4$   $^{11}\text{B}$  environments. While  $Q^3$  sites dephase much more rapidly without than with heteronuclear  $^1\text{H}$  decoupling due to the closer proximity of  $^1\text{H}$ ,  $Q^4$  sites are not strongly affected since their couplings to the protons are weaker.

In the presence of heteronuclear decoupling, identical  $T_2'$  dephasing times ( $24 \pm 1$  and  $24 \pm 7$ , respectively) were measured for both  $^{11}\text{B}$  sites B1 (-0.9 ppm) and B2 (-1.9 ppm) because all interactions

to protons are averaged out, independent of the nature of the B site. The lack of sensibility and resolution limited the reliability of data collected for site B3 (-2.5 ppm). In contrast, in the absence of decoupling, heteronuclear dipole-dipole interactions between the  $^{11}\text{B}$  nucleus and nearby  $^1\text{H}$  nuclei may not be entirely averaged out, and the dephasing times may thus vary as a function of the strength of these interactions. We indeed observe a strong difference between the  $T_2'$  dephasing times of  $^{11}\text{B}$  peaks B1 at -0.9 ppm ( $T_2' = 6.7 \pm 0.4$  ms) and B2 at -1.9 ppm ( $T_2' = 16 \pm 2$  ms). This clearly indicates that the B moieties corresponding to the peak at -0.9 ppm interact more strongly with protons than the other, and can thus be assigned to a boron in a  $Q^3$  site (presumably site Si1), the peak at -1.9 ppm corresponding to a boron in a  $Q^4$  site (presumably site Si2). The similar chemical shifts of the  $^{11}\text{B}$  sites B2 and B3 suggest that the latter most likely also corresponds to B atoms incorporated in a  $Q^4$  site, but of a slightly different type.

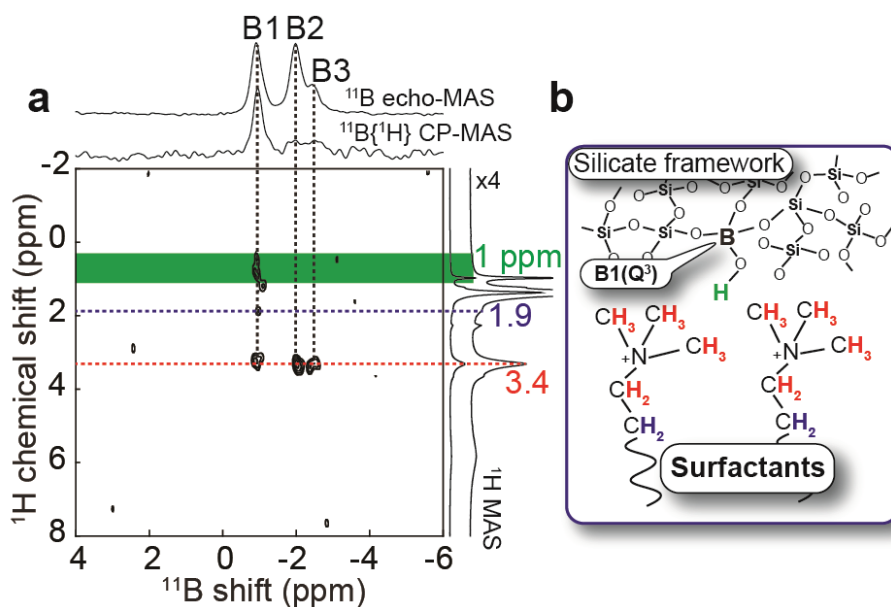


**Figure D.6** (a) Solid-state  $^{11}\text{B}$  [ $^1\text{H}$ ] NMR HETCOR spectra (acquired at 17.6T) of  $\text{C}_{16}\text{H}_{33}\text{Me}_3\text{N}^+$ -directed layered borosilicate (at natural  $^{29}\text{Si}$  abundance), which establishes proximities between the incorporated  $^{11}\text{B}$  and the neighboring  $^1\text{H}$  species. The corresponding  $^{11}\text{B}$  echo-MAS and  $^{11}\text{B}$  [ $^1\text{H}$ ] CP-MAS NMR spectra are shown on top, and the  $^1\text{H}$  MAS NMR spectrum is shown on the right side of the 2D spectrum. The colors of the horizontal lines in the 2D spectra point to the surfactant and surface  $^1\text{H}$  environments of the corresponding color in cartoon shown on the right side (b).

The local environments or molecular moieties that are responsible for such interactions are specific of the incorporated B atoms and are unaffected by the presence of a dominant fraction of B-free regions in this material. Their characterization may shed light on the associated charge-compensation mechanism. The charge deficit resulting from each B/Si substitution must be compensated either by an additional surfactant molecule, by the formation of a Si-OH moiety nearby, or, if B is incorporated in a  $Q^3$

site, of a B-OH moiety. Figure D.6 shows the  $^{11}\text{B}[^1\text{H}]$  HETCOR NMR spectra of the  $\text{C}_{16}\text{H}_{33}\text{Me}_3\text{N}^+$ -directed layered borosilicates. The correlation peaks observed at ca. 3.4 ppm in the  $^1\text{H}$  dimension for all three  $^{11}\text{B}$  sites correspond to surfactant headgroup N-CH<sub>3</sub> and/or N-CH<sub>2</sub> moieties (in red in the associated cartoons). Such correlations point to spatial proximities that are characteristic of the strong electrostatic organic-inorganic interactions playing a key role in the formation of these materials.

Other correlations are also observed between  $^{11}\text{B}$  site B1 at -0.9 ppm which is attributed B in  $Q^3$  sites, and a small  $^1\text{H}$  peak at 1.9 ppm corresponding to the second CH<sub>2</sub> group in the alkyl chain (in blue). The absence of such correlation peaks for  $^{11}\text{B}$  sites B2 and B3 points to the weaker interaction between the latter two and the surfactant, consistent with their assignment to B incorporated in  $Q^4$  sites. Even more interesting is the observation of correlated intensity between the  $^{11}\text{B}$  signal corresponding to B in  $Q^3$  sites and a broader  $^1\text{H}$  signal at ca. 1 ppm (in green). The presence of this 2D correlation peak strongly contrasts with the complete absence of corresponding peak(s) in the  $^1\text{H}$  MAS NMR spectrum or its magnification shown on right of the 2D spectrum. It establishes that these protons are specific of the environment of the B atoms incorporated in  $Q^3$  sites and consequently correspond to a tiny fraction of the total amount of protons present in these materials, given the Si/B ratios of more than 140. They can reasonably be attributed to B-OH moieties, whose correspondingly short  $^1\text{H}$ - $^{11}\text{B}$  distance would be perfectly consistent with the transverse dephasing time measurements discussed above. Such molecular-level insights into the charge compensation mechanism at boron incorporation sites are essential for building structural models describing the possible local structures around these heteroatom sites.

### ***D.3.2 Chemical shift calculations by Density Functional Theory (DFT)***

DFT calculations were conducted on  $\text{C}_{16}\text{H}_{33}\text{Me}_3\text{N}^+$  - directed layered borosilicate material to examine possible local structures around B atoms incorporated into the silicate frameworks and probe the influence of the B on the  $^{29}\text{Si}$  chemical shifts of nearby Si atoms. The  $\text{C}_{16}\text{H}_{33}\text{Me}_3\text{N}^+$  - layered framework silicate structure was taken from the reported structure of octosilicate<sup>89</sup>, which is composed of 32 tetrahedral Si sites per unit cell with a 16-fold symmetry (2 inequivalent T sites T<sub>1</sub> and T<sub>2</sub> corresponding here to sites Si2 and Si1, respectively). In the surfactant-directed analog of octosilicate studied here, adjacent layers are sufficiently far from each other for their positions and orientations to be unrelated and a single layer consequently suffices to describe the structure. Small  $\text{C}_4\text{H}_9\text{Me}_3\text{N}^+$  molecules were included in the inter-layer space for all the model structures to mimic the charge-compensating surfactant molecules having longer  $\text{C}_{16}\text{H}_{33}$  alkyl chains in the real material. The spacing between the layers and the initial positions of the alkylammonium molecules were adjusted manually to avoid contact between periodic images of the surfactants on both sides of the layers. Series of geometry optimizations were then conducted on model structures with one of the Si atoms replaced by a B atom (thereby breaking off the

symmetry). The charge balance was kept by adding a H atom either on the directly-attached non-bridging O to form a B-O-H moiety if B is in  $Q^3$  site or on the non-bridging oxygen of one of the **connected  $Q^3$  Si atom to form Si-OH moiety** if B is in a  $Q^4$  site. Examples of relaxed structures obtained with this approach, with the boron in  $Q^3$  sites, are shown in Figure D.7a, b. These structural models may first be used to interpret the  $^{11}\text{B}$ - $^{29}\text{Si}$  NMR correlation experiments revealing Si-B proximities and Si-O-B connectivities in the corresponding materials.

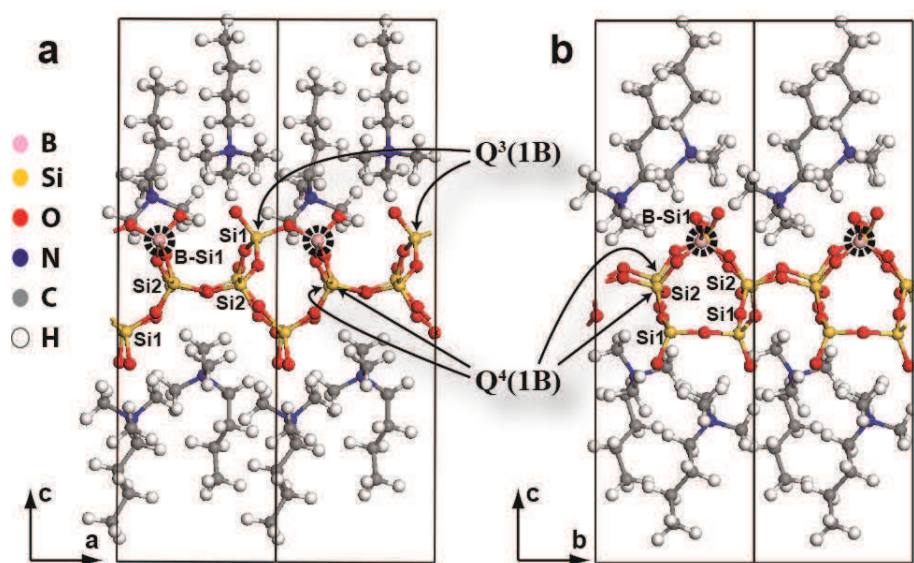


**Figure D.7** Two distinct views of the same structural model used to describe model structures of  $\text{C}_{16}\text{H}_{33}\text{Me}_3\text{N}^+$ -directed layered borosilicates as optimized with planewave-based DFT, using surfactants with shortened  $\text{C}_4$  chains. (a, b)  $\text{C}_4\text{H}_9\text{Me}_3\text{N}^+$ -directed borosilicate model with B incorporated in one site place of a Si1 site ( $Q^3$ ) among the 8 Si sites per unit cell. The additional charge introduced by the substitution is compensated in these particular models by the addition of a proton on the boron in  $Q^3$  site to form a B-OH moiety. The black lines delimitate the unit cell, with two adjacent cells shown in every case.

Calculations of NMR parameters were then conducted on all of the optimized structures, and the results are summarized in Table D3 for the case of  $^{11}\text{B}$  data. Calculated  $^{29}\text{Si}$  chemical shifts show a large distribution of values for each crystallographic site, independent on the connectivity to a B atom. (See section D.4.2 for more details regarding  $^{29}\text{Si}$  chemical shift distribution with the example of  $\text{C}_{16}\text{H}_{33}\text{Me}_2\text{EtN}^+$ -directed layered borosilicate). Hence, here we calculated the  $^{11}\text{B}$  chemical shifts and those seemed to be in good agreement with the experimental values. As already discussed above, the  $^{11}\text{B}$  spectrum shows three peaks, two of which (B2 and B3 sites) may be incorporated in place of  $\text{Si}^2(Q^4)$  sites

and the B1 is located in substitution of Si1 ( $Q^3$ ) sites of the layered silicate framework. This hypothesis is confirmed by DFT calculation results which are reported in Table D.3. Calculations conducted for the  $C_{16}H_{33}Me_3N^+$  - borosilicate models predict different  $^{11}B$  shifts for boron incorporated in the two distinct crystallographic sites (-1.7 to -2.7 ppm for B on site Si2 and -0.1 to -0.7 ppm for B in site Si1). These chemical shift ranges include all experimental  $^{11}B$  peaks attributed to  $Q^3$  sites (B1 at -0.9 ppm) and  $Q^4$  sites (B2 and B3 at -1.9 and -2.5 ppm), respectively, in agreement with the conclusions drawn based on  $^{11}B$  transverse dephasing time measurements above. The  $^{11}B$  chemical shift calculations thus support one hypotheses regarding the incorporation sites of the B. In order to investigate the local modifications that these incorporations induce, multidimensional NMR experiments probing the spatial proximities and connectivities between incorporated B and nearby Si atoms are essential.

**Table D.3** Range of  $^{11}B$  chemical shift values calculated by DFT for  $C_{16}H_{33}Me_3N^+$ -layered borosilicate model structures.

B/Si substitution site	Range of calculated isotropic $^{11}B$ chemical shifts (ppm)	Average isotropic $^{11}B$ chemical shift (ppm)	Experimental $^{11}B$ shift <sup>a</sup> (ppm)
Si2	-2.7 to -1.7	-2.1	-2.5
Si2	-2.7 to -1.7	-2.1	-1.9
Si1	-0.1 to -0.7	-0.4	-0.9

### *D.3.3 Probing spatial proximities and connectivities between B and Si atoms*

The incorporation of B in the  $C_{16}H_{33}Me_3N^+$ -directed layered silicate involves more profound local modifications of the structure. As discussed above, the observation of three  $^{11}B$  NMR peaks cannot be explained by a B/Si substitution at different tetrahedral sites, since there are only two such sites in pure-silicate  $C_{16}H_{33}Me_3N^+$ -layered material. Important information to understand this phenomenon may be obtained by establishing the spatial proximities and connectivities between framework Si and B atoms. In this regards, advanced two-dimensional (2D) correlation NMR experiments probing  $^{11}B$ - $^{29}Si$  proximities and  $^{11}B$ -O- $^{29}Si$  connectivities reveal further incompatibilities between the reference pure-silicate structure and the local environment of some of the  $^{11}B$  moieties.

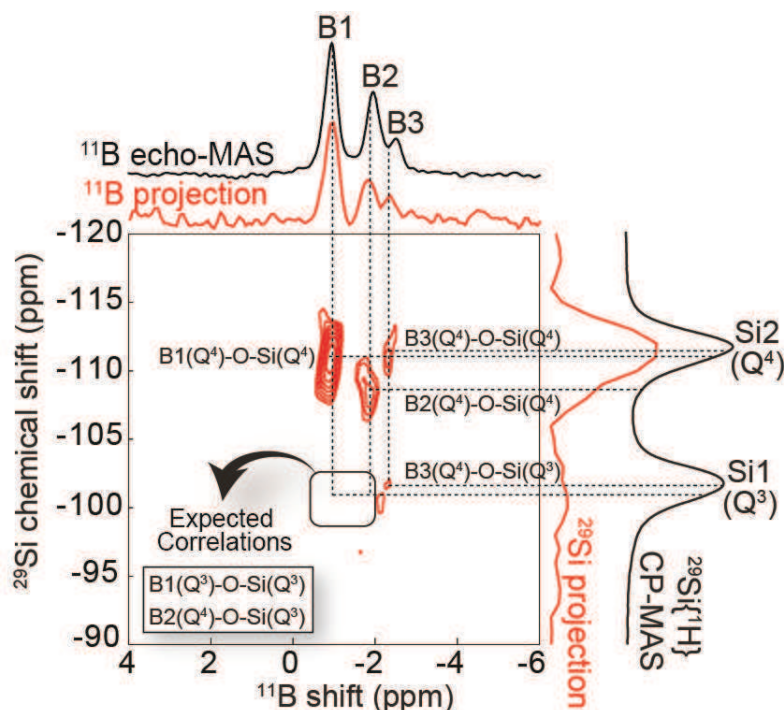


**Figure D.8**  $^{11}\text{B}$  [ $^{29}\text{Si}$ ] solid-state NMR HMQC spectra (acquired at 9.4T) of  $^{29}\text{Si}$ -enriched  $\text{C}_{16}\text{H}_{33}\text{Me}_3\text{N}^+$ -directed layered borosilicate ( $\text{Si}/\text{B} = 140$ ) establishing  $^{29}\text{Si}$ -O- $^{11}\text{B}$  connectivities between the incorporated  $^{11}\text{B}$  and its first  $^{29}\text{Si}$  neighbors.

Figure D.8 shows a 2D  $^2J(^{11}\text{B}\text{-O-}^{29}\text{Si})$ -mediated Heteronuclear Multiple-Quantum Correlation (HMQC)  $^{165}\text{ }^{11}\text{B}[^{29}\text{Si}]$  NMR spectrum collected for a  $\text{C}_{16}\text{H}_{33}\text{Me}_3\text{N}^+$ -directed layered borosilicate prepared with isotopic enrichment in  $^{29}\text{Si}$  (ca. 100%). The  $^{11}\text{B}$  and  $^{29}\text{Si}$  NMR spectra showed in black on top and right of the 2D spectrum, respectively, are the same as in Figure D.3b, a. The red spectra showed on top and right of the 2D spectrum are  $^{11}\text{B}$  and  $^{29}\text{Si}$  NMR projections, respectively. Correlation peaks in the 2D spectrum selectively reveal  $^{29}\text{Si}$  nuclei connected via bridging O atoms to the  $^{11}\text{B}$  nuclei inserted within the framework. Correlated intensity at the  $^{11}\text{B}$  frequency of site B3 (-2.5 ppm in horizontal dimension) and  $^{29}\text{Si}$  frequencies corresponding to both  $Q^4$  and  $Q^3$  regions (-111 and -101 ppm in the vertical dimension, respectively) establish that these  $^{11}\text{B}$  moieties, assigned above to  $^{11}\text{B}$  in  $Q^4$  sites, are connected to both Si1 ( $Q^3$ ) and Si2 ( $Q^4$ ) sites. This is in agreement with the connectivities of the pure-silicate material (based on the structure of iso-structural octosilicate<sup>89</sup>), where every  $Q^4$  site is connected to two  $Q^3$  and two  $Q^4$  Si sites, suggesting that site B3 may be attributed to a  $^{11}\text{B}$  nucleus in substitution of a framework Si  $Q^4$  site Si2.

On the contrary, sites B1 and B2 at -0.9 and -1.9 ppm in the  $^{11}\text{B}$  dimension, assigned above to  $^{11}\text{B}$  in  $Q^3$  and  $Q^4$  environments, respectively, each show a single correlation peak to the  $^{29}\text{Si}$   $Q^4$  region. The

absence of correlations to the  $^{29}\text{Si}$   $Q^3$  region is in strong contradiction with the correlations that would be expected if B atoms were substituted to either a  $Q^3$  or a  $Q^4$  Si atom in the reference pure-silicate structure, since they would each be connected in this case to one or two  $Q^3$  Si atoms, respectively.<sup>89</sup>

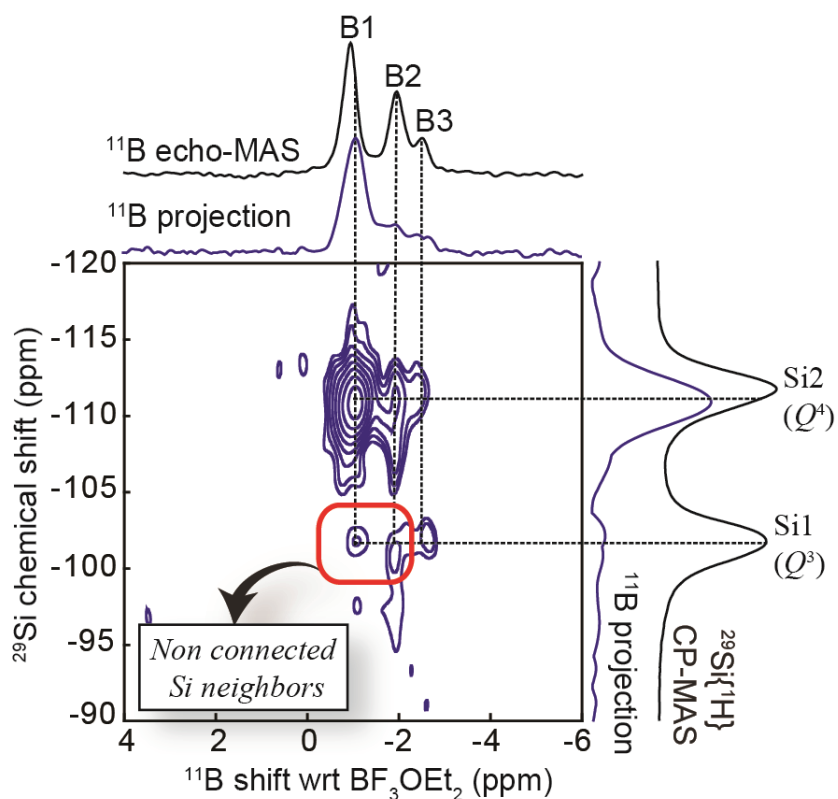


**Figure D.9**  $^{11}\text{B}$  [ $^{29}\text{Si}$ ] solid-state NMR HMQC spectra (acquired at 9.4T) of  $^{29}\text{Si}$ -enriched  $\text{C}_{16}\text{H}_{33}\text{Me}_3\text{N}^+$ -directed layered borosilicate ( $\text{Si}/\text{B} = 140$ ) establishing  $^{29}\text{Si}$ - $^{11}\text{B}$  spatial proximities between the incorporated  $^{11}\text{B}$  and nearby  $^{29}\text{Si}$  species.

This is further confirmed by probing the spatial proximities between B and Si atoms via heteronuclear  $^{11}\text{B}$ - $^{29}\text{Si}$  dipolar couplings. In this context, Figure D.9 shows  $^{11}\text{B}$  [ $^{29}\text{Si}$ ] dipolar-mediated HMQC<sup>190</sup> spectrum of  $^{29}\text{Si}$  enriched  $\text{C}_{16}\text{H}_{33}\text{M}_3\text{N}^+$ -directed material. The  $^{11}\text{B}$  and  $^{29}\text{Si}$  NMR spectra and the corresponding projections (Blue) were showed on top and right of 2D spectrum, respectively. The range of proximities probed between the Si and B atoms depends on the duration of heteronuclear recoupling. With a duration of 5.4 ms as used here, the correlated peaks in the 2D spectrum reveal the signature of non-connected nearby Si atoms around the incorporated B in addition to the contribution from Si-O-B connected atoms. Indeed, all the correlation peaks observed in the  $J$ -mediated experiment (Fig. D.8) are still observed, but additional peaks are now revealed. Specifically, weak correlations between  $^{11}\text{B}$  sites B2 and B1 and Si1  $^{29}\text{Si}$  sites are attributed to the non-connected nearby Si1 environment around the

incorporated B2 and B1 sites. These spectra establish that the local structure around  $^{11}\text{B}$  sites B1 and B2 is modified in such a way that the corresponding B atoms are surrounded exclusively by Si  $Q^4$  sites, reflecting a higher degree of local silicate framework polymerization around these heteroatoms sites, as compared to the pure-silicate regions (see Fig D.4 for Si-O-Si connectivities). This local modification around B1 and B2 sites could be analyzed by DFT calculations.

#### D.3.4 Structural rearrangement upon B incorporation

The structural rearrangement of the silicate framework upon B incorporation is supported by DFT calculations conducted on structural models modified accordingly. For example, the structural model of Figure D.7 was based on a supercell consisting of 1x3x1 cells of a DFT optimized pure-silicate structure, where one Si  $Q^3$  site was substituted by a B atom, with the addition of a proton to compensate the associated charge deficit. The Si  $Q^3$  atom connected to this B/Si substitution site was manually connected to the next nearest Si  $Q^3$  atom by replacing the non-bridging O atoms of the latter two by a single O atom placed at the center of mass of the two Si  $Q^3$  sites. The modification of charge associated with the resulting loss of one O atom was compensated by removing two  $\text{C}_4\text{H}_9\text{Me}_3\text{N}^+$  molecules. The optimized model (Fig D.10b) shows that the use of a sufficiently large supercell makes it possible for the layered framework to bend such as to accommodate for the additional cross-linking and accompanying local structural rearrangements that are necessary to retrieve appropriate tetrahedral  $\text{SiO}_4$  (and  $\text{BO}_4$ ) geometries, in particular. The nature of the B incorporation site ( $Q^3$ ) and the nature of connected Si neighbors ( $Q^4$  only) in this model are fully consistent with all of the experimental data obtained for  $^{11}\text{B}$  site B1. The  $^{11}\text{B}$  chemical shift calculated for this model, reported in Table D.4, is 0.1 ppm, which is in good agreement with the experimental  $^{11}\text{B}$  shift of site B1 (-0.9 ppm).

**Table D.4 Range of  $^{11}\text{B}$  chemical shift values calculated by DFT for  $\text{C}_{16}\text{H}_{33}\text{Me}_3\text{N}^+$ -layered borosilicate model structures with cross linking.**

B/Si substitution site	Range of calculated isotropic $^{11}\text{B}$ chemical shifts (ppm)	Average isotropic $^{11}\text{B}$ chemical shift (ppm)	Experimental $^{11}\text{B}$ shift <sup>a</sup> (ppm)
Si2( $Q^4$ )	-4.0 to -2.2	-3.1	-1.9
Si1( $Q^3$ )	0.1	0.1	-0.9

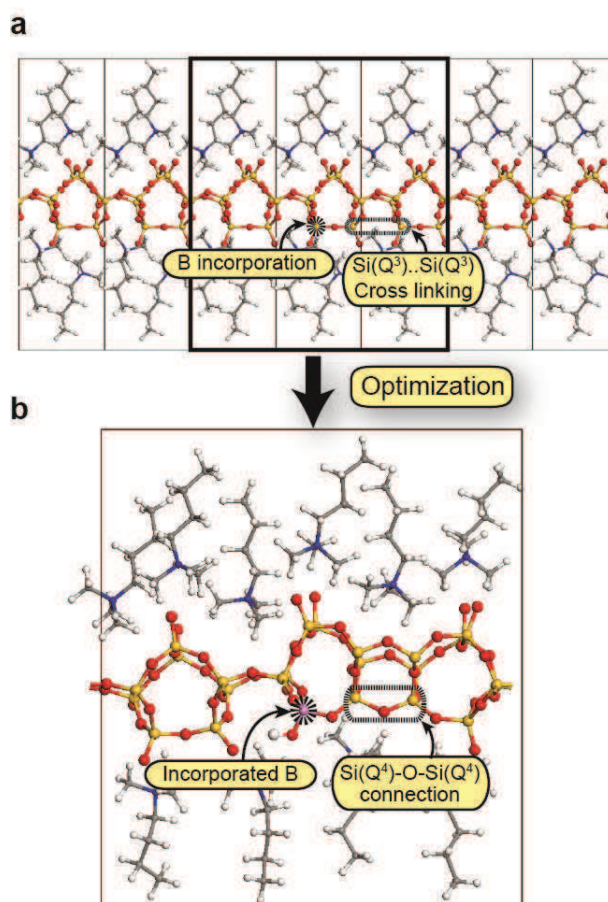


**Figure D.10** (a) DFT-optimized model of the  $C_{16}H_{33}Me_3N^+$ -directed pure-silicate material (featuring multiple cells) pointing the incorporation of B into  $Q^3$  crystallographic site, (b) DFT-optimized model of the  $C_{16}H_{33}Me_3N^+$ -directed layered borosilicate material (single supercell) with B incorporated in a  $Q^3$  site and cross-linking of neighboring Si  $Q^3$  sites with another Si  $Q^3$  sites, as highlighted in yellow.

As shown in Figure D.11a, similar calculation conducted on a model representative of  $^{11}B$  site B2 (*i.e.*, a B atom located in a  $Q^4$  site, and connected exclusively to Si  $Q^4$  sites) is also reported in Table D.4. This model features two additional connectivities involving the two  $Q^3$  sites adjacent to the Boron and which become  $Q^4$  (1B) sites in the optimized structure (Figure D.11b). The  $^{11}B$  chemical shift predicted for this model (-3.1 ppm) is still in reasonable agreement with the experimental shift (Table D.4) of  $^{11}B$  peak B2. Thus it also supports our interpretation that the structure rearranges locally upon boron incorporation because the presence of this heteroatom promotes the condensation of its neighbors. One of our models, with B incorporated in a  $Q^4$  site and only one of the two connected  $Q^3$  Si atoms cross-linked, yielding one  $Q^3$ (1B) site and three  $Q^4$ (1B), may also be considered consistent with the experimental data obtained for B3. However the relative intensities of the two corresponding correlation peaks ( $Q^3$ (1B) and  $Q^4$ (1B)) in Figure D.8 do not suggest a 1:3 population ratio, but rather a 1:1 ratio pointing instead to a

model without additional Si-O-Si cross-linking, as discussed above. Overall, the incorporation of B on silicate framework of  $C_{16}H_{33}Me_3N^+$ -directed material appears to deteriorate the surrounding molecular order by inducing different possible structural rearrangements. However, the polymerization of such silicate species around the incorporated B atom would be limited to the 1<sup>st</sup> and 2<sup>nd</sup> neighbors and the molecular order in the B free region remains identical to the pure-silicate analog.

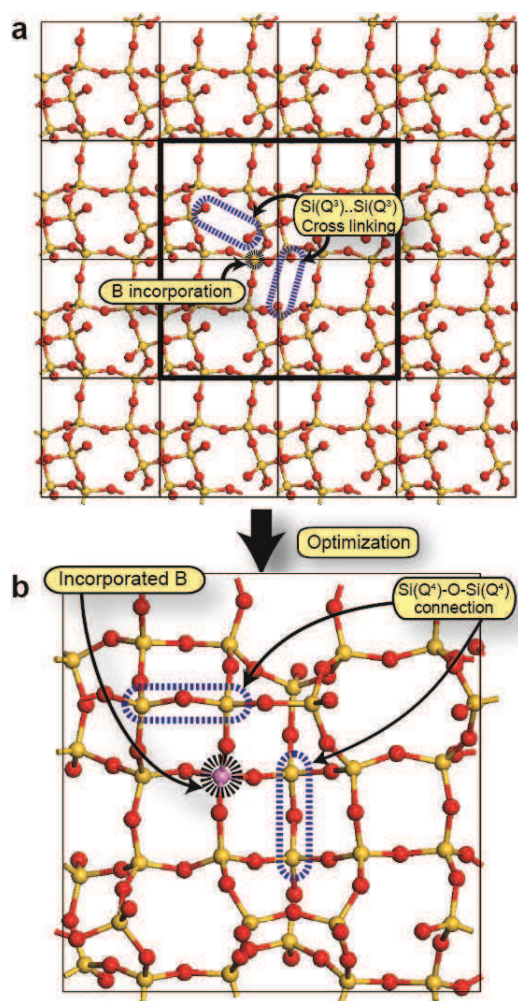


**Figure D.11** (a) DFT-optimized model of the  $C_{16}H_{33}Me_3N^+$ -directed pure-silicate material and (b)  $C_{16}H_{33}Me_3N^+$ -directed borosilicate material (single super cell) with B incorporated in a  $Q^4$  site and two cross-linking of neighboring Si  $Q^3$  sites.

As discussed in the chapter C, similar situation was observed in the substitution of Al heteroatoms in the same material. Structural rearrangement takes place upon Al atoms insertion in the 2D silicate framework to accommodate the local structure relaxation. In the present case, it is clear that, B1 is incorporated into  $Q^3$  and B2 and B3 are incorporated into  $Q^4$  Si sites. However, the substitution of Al atoms whether in  $Q^3$  or  $Q^4$  or both Si sites is somewhat unclear. Nevertheless, solid-state NMR and DFT

calculations strongly support the corresponding changes in the structure (see section C.4). The effect of Al atoms on the local structure is stronger in contrast with the B atoms. This is evidenced by large changes in the structure reflected in the  $^{29}\text{Si}$  MAS NMR (Figure C.10) spectra studied as a function of Al loading. Regardless of the nature of heteroatoms (B or Al), such structural rearrangement observed in the  $\text{C}_{16}\text{H}_{33}\text{Me}_3\text{N}^+$ -directed material indicates that framework topology is very important. Although, similar changes observed in both cases, the resultant framework acidity or catalytic activity is completely different. This is because  $\text{H}^+$  is the charge compensating species that form B-OH moieties in the B-containing material, which is not the case in Al-containing material, where only alkyl-ammonium surfactants balance the framework negative charge.

#### **D.4 Distribution of B heteroatoms in $\text{C}_{16}\text{H}_{33}\text{Me}_2\text{EtN}^+$ -directed layered silicates**

Strongly related surfactant-directed material prepared at same synthesis condition, but similar incorporation of B atoms leads to a very different situation. The main objective is again to incorporate the boron atoms into 2D crystalline silicate framework of  $\text{C}_{16}\text{H}_{33}\text{Me}_2\text{EtN}^+$ -directed layered silicates and to establish the resulting local structure. Many reasons motivated studies of B incorporation in this material in particular: (i) the framework topology of these molecularly-ordered silicates have already been solved in their siliceous<sup>22-23</sup> form, (ii) the availability of chemically distinguished crystallographic sites ( $Q^3$  and  $Q^4$   $^{29}\text{Si}$  sites) allows determining the B location, (iii) some preliminary results have established that these materials form at the preliminary stages of the formation of technologically important nano-porous zeolites designed by Ryoo and co-workers.<sup>20-21</sup> In analogy to the characterization of  $\text{C}_{16}\text{H}_{33}\text{Me}_3\text{N}^+$ -directed layered borosilicate, we followed the same procedure to investigate the siting of B atoms. The  $^{29}\text{Si}$ [ $^1\text{H}$ ] CP-MAS and  $^{11}\text{B}$  echo-MAS NMR spectra of  $\text{C}_{16}\text{H}_{33}\text{Me}_2\text{EtN}^+$ -directed layered borosilicate are shown in the figures D.2 (c,d) and D.3 (c,d) for the samples with natural  $^{29}\text{Si}$  abundance and with 100% isotopic  $^{29}\text{Si}$  enrichment, respectively. These NMR data reveals that boron atoms are substituted into a single crystallographic site (single sharp  $^{11}\text{B}$  peak) and the lamellar structure is unaffected in the boron free region.

##### **D.4.1 H atoms around B heteroatoms**

The  $^{11}\text{B}$   $T_2'$  measurements are similar to the one explained in the section D.3.1. Again the idea is that B  $Q^3$  sites are expected to interact much more strongly with protons than B  $Q^4$  sites. Such interactions are probed by measuring and comparing the  $^{11}\text{B}$  transverse dephasing times  $T_2'$  in the absence and in the presence of heteronuclear decoupling. As showed in the Figure D.12, the  $^{11}\text{B}$   $T_2'$  dephasing times measured for a single  $^{11}\text{B}$  peak of  $\text{C}_{16}\text{H}_{33}\text{Me}_2\text{EtN}^+$ -directed borosilicate in the presence and absence of heteronuclear  $^1\text{H}$  decoupling changed considerably (35 vs. 3.7 ms, respectively). This result should be

compared with similar measurements conducted on the  $C_{16}H_{33}Me_3N^+$ -borosilicate, where a comparable contrast was obtained for the  $^{11}B$  signal which was then attributed to B in substitution of a Si  $Q^3$  site. By comparison turning the decoupling off had little impact for  $^{11}B$  signals attributed to B in a  $Q^4$  site. This strongly suggests that all of the B atoms are incorporated into a  $Q^3$  site in the  $C_{16}H_{33}Me_2EtN^+$ -borosilicate material.

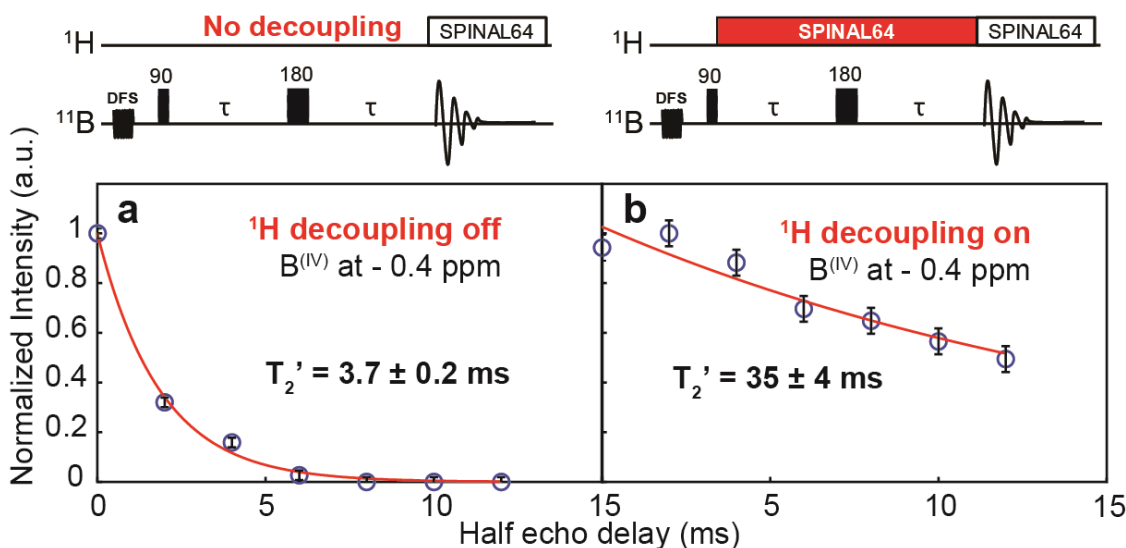


**Figure D.12** Transverse  $^{11}B$  dephasing time ( $T_2'$ ) measurements conducted (a) without and (b) with  $^1H$  decoupling for  $C_{16}H_{33}Me_2EtN^+$ -directed layered borosilicates to distinguish between  $Q^3$  and  $Q^4$   $^{11}B$  environments. Similar to the case of  $C_{16}H_{33}Me_3N^+$ -directed layered borosilicates, the B in  $Q^3$  sites dephase much more rapidly without than with heteronuclear  $^1H$  decoupling due to the closer proximity of  $^1H$ . The respective pulse programs are shown above each plot.

The compensation of the charge deficit associated with the Si to B substitution is investigated by probing the interactions between  $^{11}B$  and  $^1H$  nuclei through  $^{11}B$  [ $^1H$ ] HETCOR NMR measurements as showed in Figure D.13a. The correlation peaks at ca. 3.2 and 3.5 ppm in the 2D spectrum could be attributed to surfactant headgroups N-CH<sub>3</sub> and N-CH<sub>2</sub> signals, respectively, as indicated in the cartoon (red color). A small  $^1H$  peak at 1.9 ppm corresponds to the second CH<sub>2</sub> group in the alkyl chain (in blue). Very interestingly, a correlation peak at ca. 0 ppm ( $^1H$  dimension) with respect to single  $^{11}B$  peak at 0.4 ppm, as indicated in green color, which could possibly attributed to the B-OH moieties (also identified in the case of  $C_{16}H_{33}Me_3N^+$ -directed layered borosilicate at 1 ppm). This is another indication that B has stronger interactions with  $Q^3$  Si sites and suggests B heteroatoms are preferentially incorporated into one of the  $Q^3$  crystallographic sites.

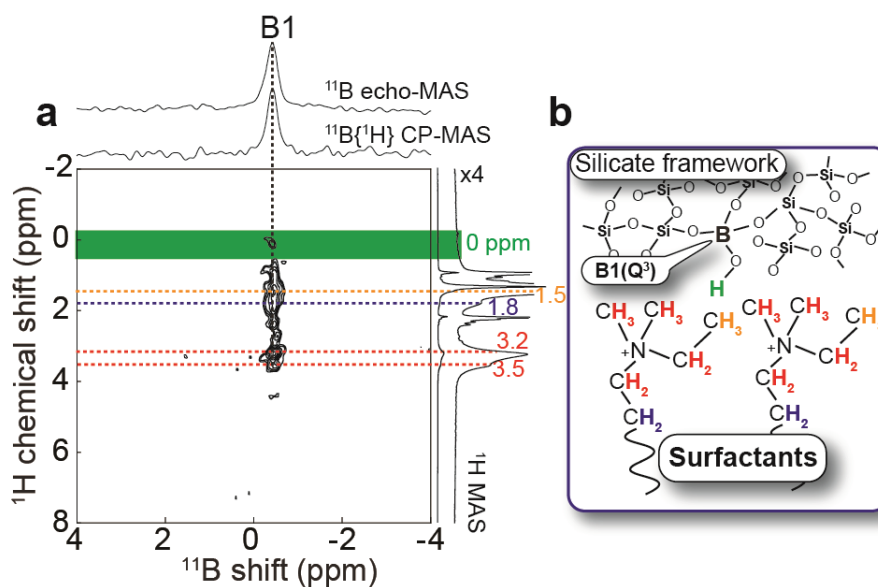


**Figure D.13** Solid-state  $^{11}\text{B}$  [ $^1\text{H}$ ] NMR HETCOR spectrum (acquired at 17.6T) of  $\text{C}_{16}\text{H}_{33}\text{Me}_2\text{EtN}^+$ -directed layered borosilicate (at natural  $^{29}\text{Si}$  abundance). The corresponding  $^{11}\text{B}$  echo-MAS and  $^{11}\text{B}$  [ $^1\text{H}$ ] CP-MAS NMR spectra are shown on top, and the  $^1\text{H}$  MAS spectrum is shown on right of the 2D spectrum. The colors of the horizontal lines in the 2D spectra point to the surfactant and surface  $^1\text{H}$  environments of the corresponding color in cartoon shown on the right side.

#### D.4.2 $^{29}\text{Si}$ and $^{11}\text{B}$ chemical shift calculations by DFT

Advanced structural determination protocols applied to the  $\text{C}_{16}\text{H}_{33}\text{Me}_2\text{EtN}^+$ -directed layered silicate material, led to the identification of three candidate structural models<sup>24</sup> corresponding to equally valid representation of a single framework structure, all of which were considered in our calculations. Each one of these model framework structures of the  $\text{C}_{16}\text{H}_{33}\text{Me}_2\text{EtN}^+$ -directed layered borosilicate material is composed of a unit cell with 10 Si sites (related two by two by symmetry). As for the  $\text{C}_{16}\text{H}_{33}\text{Me}_3\text{N}^+$ -directed layered borosilicate model, here also small  $\text{C}_4\text{H}_9\text{Me}_2\text{EtN}^+$  molecules were included in the inter-layer space for all of the model structures to mimic the charge-compensating surfactant molecules. (See section D.3.2 for further details of model structures). A series of geometry optimizations were then conducted on model structures with one of the ten Si atoms replaced by a B atom. Here also a H atom is added to compensate the charge either on the directly-attached non-bridging O to form a B-O-H moiety if B is in  $Q^3$  site or on the non-bridging oxygen of one of the connected  $Q^3$  Si atom if B is in a  $Q^4$  site. An example of relaxed structure is shown in figure D.14 (a, b) considering that B is located in  $Q^3$  sites.

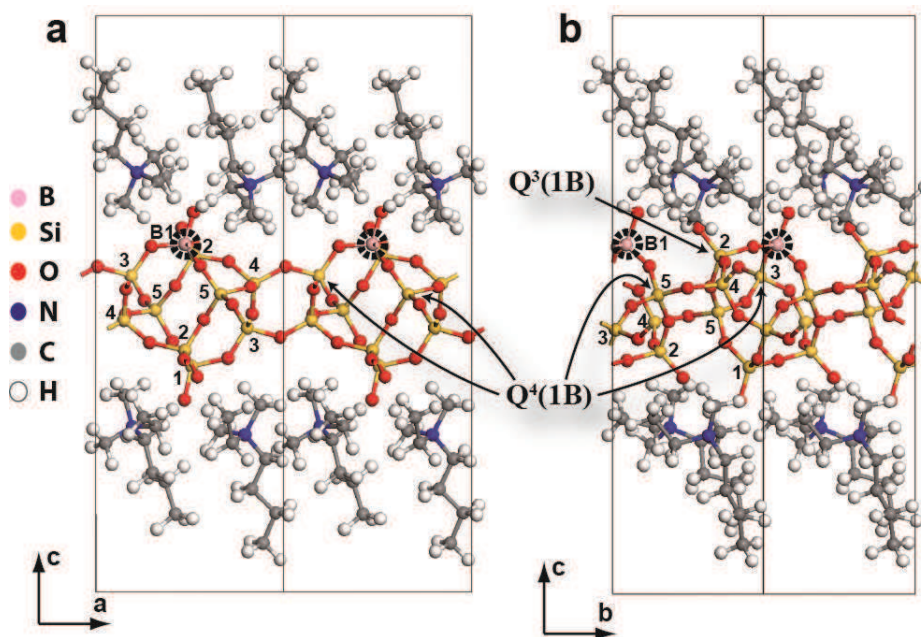


**Figure D.14** Two distinct views of an example of model structure of  $C_{16}H_{33}Me_2EtN^+$ -directed layered borosilicates optimized with planewave-based DFT, using surfactants with shortened  $C_4$  chains. The additional charge introduced by the substitution is compensated in this particular model by the addition of a proton on the boron in  $Q^3$  site to form a BOH unit. The black lines delimitate the unit cell, with two adjacent cells shown along  $a$  and  $b$  directions.

Calculations of NMR parameters were then conducted on all of the optimized structures. Initially  $^{29}Si$  chemical shifts are calculated and plotted with respect to the experimental chemical shift as showed in the Figure D.15. Shown in black above the plots are the corresponding  $^{29}Si[1H]$  CP-MAS NMR spectrum. Open “o” symbols in (a), and (b) correspond to Si atoms that are not connected to a B atom, and whose experimental shifts should correspond (in first approximation) to the dominant  $^{29}Si$  peaks observed experimentally (and identical to pure-silicate materials). Plots (a) and (b) correspond to two distinct situations, with B incorporated either (a) in crystallographic site Si1 or (b) in crystallographic site Si2, with the resulting calculated  $Q^n(1B)$   $^{29}Si$  shifts shown as filled “▲” symbols. Studied models are based on the three candidate structures of the  $C_{16}H_{33}Me_2EtN^+$  - directed layered silicate material and consider in every case all possible B incorporation sites.

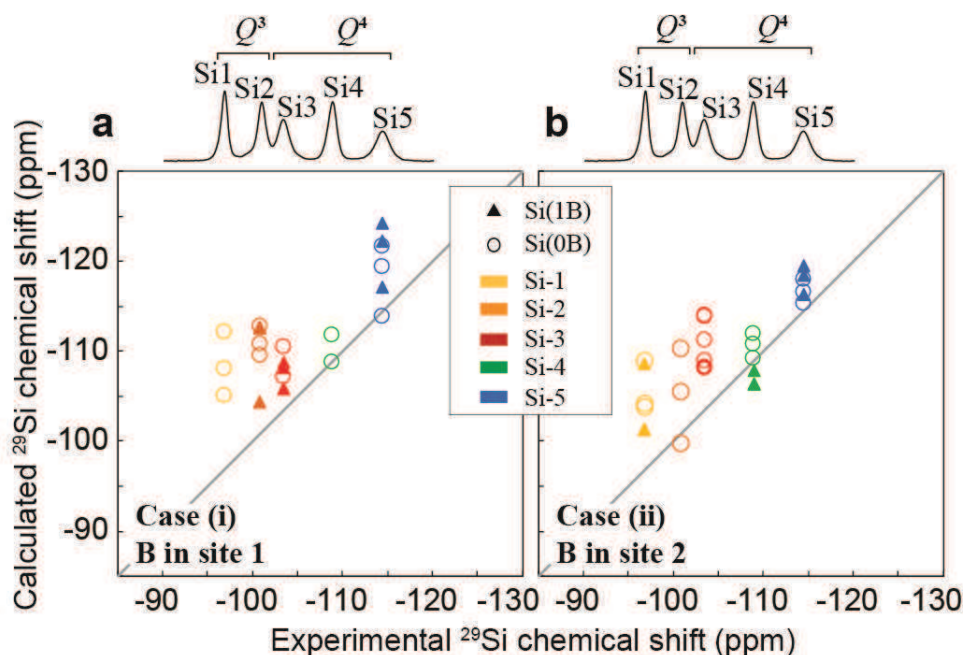


**Figure D.15** Comparisons of experimental  $^{29}\text{Si}$  chemical shifts and isotropic chemical shifts calculated by DFT for all (a, b)  $\text{C}_4\text{H}_9\text{Me}_2\text{EtN}^+$  - directed borosilicate models studied in this work, considering the placement of B in Si1 (case 1) and Si2 (case 2).  $^{29}\text{Si}[\text{H}]$  CP-MAS spectrum shown on top of each plot.

The calculated  $^{29}\text{Si}$  chemical shifts show a large distribution of values for each crystallographic site, independent on the connectivity to a B atom. The main reason for this is that each Si atom in these models sees only one of many possible positions and orientations of the surrounding alkyl-ammonium surfactant head groups, since all the DFT calculations were performed at static condition. In the real materials at ambient temperature, these head-group motions are dynamically averaged (at the timescale of  $^{29}\text{Si}$  NMR experiments, i.e.  $10^{-8}$  s), as established previously for the  $\text{C}_{16}\text{H}_{33}\text{Me}_2\text{EtN}^+$  - layered silicate.<sup>174</sup> At lower temperatures (below ca.  $0^\circ\text{C}$ ) these motions start to freeze and the  $^{29}\text{Si}$  NMR broaden considerably, leading to large spectral overlaps between the signals of the five distinct  $^{29}\text{Si}$  sites. The same situation is observed for the borosilicate analog, which is further confirmed by  $^{29}\text{Si}$  NMR measurements at variable temperature as shown in Figure D.16. A series of  $^{29}\text{Si}$   $[\text{H}]$  CP-MAS NMR spectra collected at different temperature, starting from RT to  $-44^\circ\text{C}$  by steps of  $10^\circ\text{C}$  with 5 kHz spinning frequency (temperature is calibrated using  $\text{PbNO}_3^{219}$ ). At RT ( $20^\circ\text{C}$ ) the  $^{29}\text{Si}$  MAS spectrum shows 5 well resolved peaks. As temperature decreases the resolved peaks becomes broader and broader. Below  $0^\circ\text{C}$ , the resonances of  $^{29}\text{Si}$  sites 2 and 3 overlap with each other and seem like a broad single peak. In this regards, the  $^{29}\text{Si}$  chemical shift may be difficult to consider unless surfactant dynamics are taken into account which is particularly challenging from a modeling point of view. Another alternative is to

consider  $^{11}\text{B}$  chemical shift calculations and compare then with experimental  $^{11}\text{B}$  shift values. Hence the  $^{11}\text{B}$  chemical shift has been calculated for each model as discussed above.

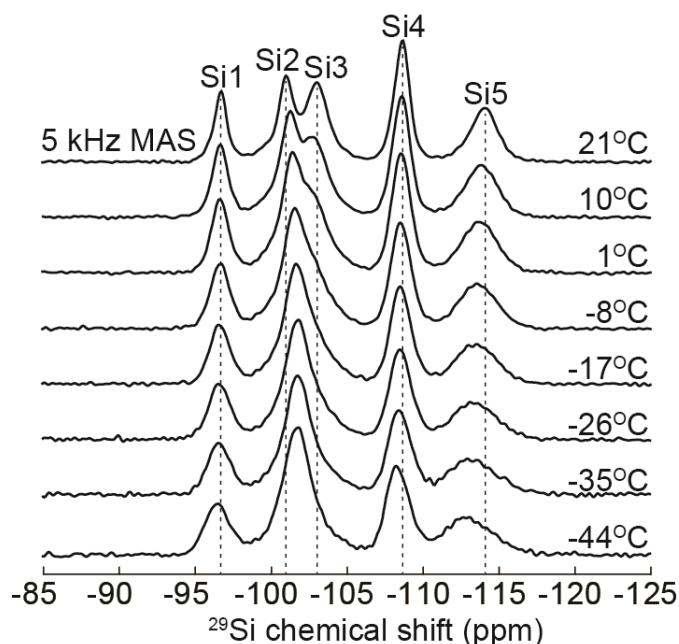


**Figure D.16.**  $^{29}\text{Si}$  [ $^1\text{H}$ ] CP-MAS NMR spectra collected for the increments at temperature from 21 °C to -44 °C at 5 kHz MAS.

The situation is different for calculated  $^{11}\text{B}$  NMR parameters, which can be used in contrast to support and complement experimental data. Calculated  $^{11}\text{B}$  isotropic chemical shifts are reported in Table D.5. The  $^{11}\text{B}$  chemical shifts calculated from our DFT-optimized models are, in average, larger for B in  $Q^3$  site as compared to B in a  $Q^4$  site. In the case of the  $\text{C}_4\text{H}_9\text{Me}_2\text{EtN}^+$  - directed models, these calculated  $^{11}\text{B}$  shifts arrange as a function of the incorporated T site (from one to five) in a similar order as the corresponding experimental  $^{29}\text{Si}$  signals (with the exception of B substituted  $Q^3$  sites Si1 and Si2, for which calculated  $^{11}\text{B}$  values are close). The dispersions of calculated values for B incorporated in a given site tend to be smaller (or are at least not substantially larger) than the differences between two distinct incorporation sites, in contrast to the case of calculated  $^{29}\text{Si}$  chemical shifts. This suggests that the differences observed in average for  $^{11}\text{B}$  chemical shifts are significant. The calculated  $^{11}\text{B}$  chemical shift is typically of the order of 0 to -1 ppm when the B atoms are in substitution of site Si1 and Si2 ( $Q^3$  sites), which is in excellent agreement with the experimental  $^{11}\text{B}$  shift. In contrast, for B atoms in substitution of  $Q^4$  sites Si3, 4 or 5, calculated  $^{11}\text{B}$  shifts are systematically smaller than the experimental  $^{11}\text{B}$  shift. These results thus strongly suggest that the boron atoms are incorporated in one of the two  $Q^3$  sites Si1 or Si2 rather than in a  $Q^4$  site, in agreement with transverse dephasing results.

**Table D.5 Range of  $^{11}\text{B}$  chemical shift values calculated with DFT for  $\text{C}_4\text{H}_9\text{Me}_2\text{EtN}^+$ -layered borosilicate model structures.**

B/Si substitution site	Range of calculated isotropic $^{11}\text{B}$ chemical shifts (ppm)	Average isotropic $^{11}\text{B}$ chemical shift (ppm)	Experimental $^{11}\text{B}$ shift (ppm)
1	-1.1 to -0.8	-1.1	
2	-1.3 to 0.4	-0.5	
3	-2.2 to -1.6	-1.9	-0.4
4	-3.5 to -2.1	-2.8	
5	-4.3 to 2.2	-3.4	

**D.4.3 Probing spatial proximities and connectivities between Si and B atoms**

The influence of B atoms on the local structure could be measured with multi-dimensional solid-state NMR by probing the existence of B-Si spatial proximities or B-O-Si connectivities on the basis of molecular-level  $^{29}\text{Si}$ - $^{11}\text{B}$  dipole-dipole and through-bond-mediated  $^2J(^{29}\text{Si}\text{-O-}^{11}\text{B})$  scalar coupling interactions, as we investigated for the other material (section D.3.3). For example, two-dimensional  $^{11}\text{B}[^{29}\text{Si}]$  NMR correlation spectra exploiting the existence of a through-space dipole-dipole interaction between  $^{29}\text{Si}$  and  $^{11}\text{B}$  nuclei located within a few Å from each other were collected for the  $\text{C}_{16}\text{H}_{33}\text{Me}_2\text{EtN}^+$  - directed layered borosilicate material using Heteronuclear Multiple-Quantum Correlation (HMQC) experiments. These may be used to record two-dimensional spectra in which correlated intensity at a given position points to the presence, at the corresponding frequencies within each individual 1D spectrum, of  $^{29}\text{Si}$  and  $^{11}\text{B}$  nuclei in close proximity to each other. In spite of the small boron content ( $\text{Si/B} = 60$ ) in these materials, such experiments can be collected at natural  $^{29}\text{Si}$  abundance (4.7%), as illustrated in Figure D.17. This opens important perspectives for the wide range of systems in which understanding the local modifications of an otherwise ordered silicate framework upon incorporation of a heteroatom (Al, B, Ga... etc.) is of primary interest to understand and ultimately control, at the molecular level, their physico-chemical properties.

In the 2D spectrum, three correlations are observed in the  $^{29}\text{Si}$  dimension at -99.7, -108.1 and -114.2 ppm with respect to single  $^{11}\text{B}$  peak at -0.4 ppm. Actually this experiment is performed at the recoupling duration of 4.5 ms, which means the observed correlations reveals the signature of both connected ( $^{29}\text{Si}\text{-O-}^{11}\text{B}$ ) and non-connected ( $^{29}\text{Si}\text{-}^{11}\text{B}$ ) species. The intensity of the correlated peaks may vary as it depends on the distances between the incorporated B atoms and the nearby Si atoms. Overall, the signal to noise in this experiment is quite poor (lowest contour level of 45% using strong line broadening) as a result of the combination low  $^{29}\text{Si}$  abundance and B content ( $\text{Si/B} = 60$ ). Hence, it is

necessary to synthesize the corresponding material with 100%  $^{29}\text{Si}$  isotopic enrichment, in order to perform advanced 2D NMR experiments aiming to probe the influence of B atoms on the environments of neighboring Si atoms.

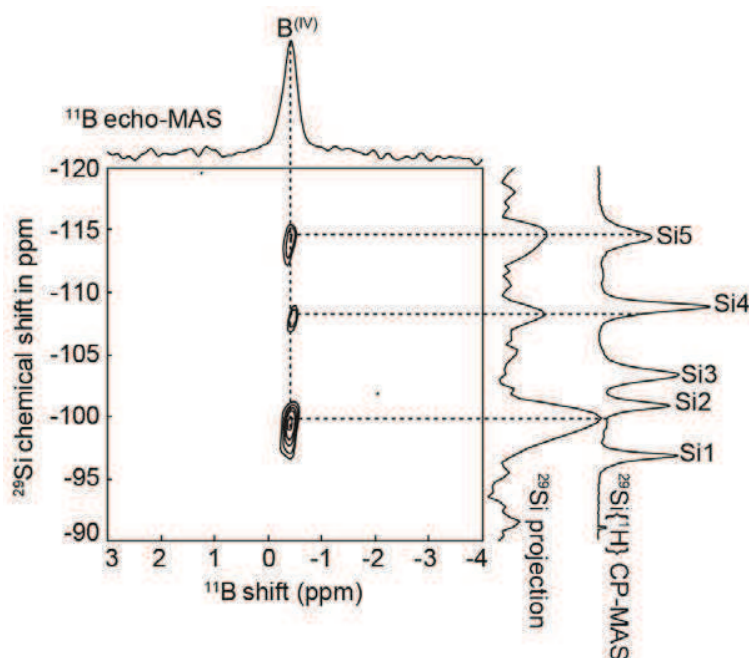


**Figure D.17** Two-dimensional dipolar-mediated  $^{11}\text{B}[^{29}\text{Si}]$  HMQC spectrum of  $\text{C}_{16}\text{H}_{33}\text{Me}_2\text{EtN}^+$ -directed layered borosilicate material synthesized at natural abundance  $^{29}\text{Si}$  ( $\text{Si}/\text{B} = 60$ ). The  $^{11}\text{B}$  echo-MAS spectrum showed on top of the 2D spectrum. The vertical  $^{29}\text{Si}$  NMR projection and the  $^{29}\text{Si}$  [ $^1\text{H}$ ] CP-MAS spectrum (far right) showed on right side. The 2D spectrum was collected at a magnetic field of 17.6 T with MAS frequency of 7 kHz, with recoupling duration of 5.1 ms. 4096 transients were accumulated for each of the 32  $t_1$  increments. Heteronuclear  $^1\text{H}$  decoupling (50 kHz) was applied during both recoupling (CW) and acquisition (SPINAL64).

The sensitivity gain resulting from the isotopic enrichment may be exploited to probe more selectively the atoms located in the direct vicinity of the B atoms incorporated within the silicate framework. This is achieved again by means of a heteronuclear correlation experiment probing through-bond interactions via the scalar  $^2J(^{11}\text{B}-\text{O}-^{29}\text{Si})$  couplings rather than through-space internuclear proximities. Figure D.18 shows for example in red a  $^2J(^{11}\text{B}-\text{O}-^{29}\text{Si})$ -mediated  $^{11}\text{B}[^{29}\text{Si}]$  HMQC spectrum collected on the  $\text{C}_{16}\text{H}_{33}\text{Me}_2\text{EtN}^+$  - directed layered borosilicate prepared with isotopic  $^{29}\text{Si}$  enrichment. Correlation peaks in the corresponding through-bond-mediated 2D NMR spectrum are only due to  $^{29}\text{Si}$  nuclei that are directly connected (via bridging O atoms) to  $^{11}\text{B}$  nuclei. Three  $^{29}\text{Si}$  signals at -98.4, -100.5 and -113.8 ppm are found to correlate with the  $^{11}\text{B}$  peak at -0.4 ppm consistent to our previous conclusions that B was incorporated in  $Q^3$  site and was consequently expected to have three connected Si

neighbors. Their number (three) suggests that the Boron atom has three connected Si neighbors (although the possibility of overlap peaks in the  $^{29}\text{Si}$  dimension cannot be excluded) and is consequently incorporated in a single type of  $Q^3$  site. The small intensity of the cross peak at -0.4 ppm in the  $^{11}\text{B}$  dimension and -100.5 ppm in the  $^{29}\text{Si}$  dimension can be attributed to a smaller  $^2J(^{11}\text{B-O-}^{29}\text{Si})$  coupling magnitude and/or a shorter transverse dephasing rate during coherence transfer echoes for this pair. However, these cross-peaks point to the  $^{29}\text{Si}$   $Q^n(1\text{B})$  environments designating  $Q^n$   $^{29}\text{Si}$  sites directly connected to one B atom. Their small widths in both dimensions (1.0 to 1.6 ppm and 0.3 ppm, FWHM, in  $^{29}\text{Si}$  and  $^{11}\text{B}$  dimensions, respectively) indicate a well-defined local environment of the incorporated B heteroatoms, which are thus presumably located within a well-ordered silicate framework, most probably the surfactant-directed layered silicate framework, which is the only visible signature in the  $^{29}\text{Si}\{^1\text{H}\}$  CP-MAS spectrum (Fig. D.3c).

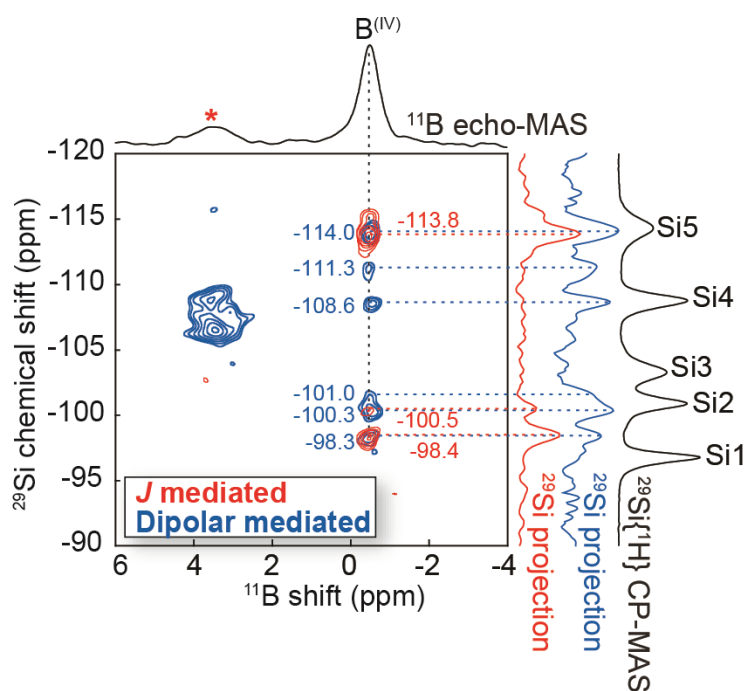


**Figure D.18** Superimposed two-dimensional (in blue) dipolar- and (in red)  $J$ -mediated  $^{11}\text{B}$  [ $^{29}\text{Si}$ ] solid-state NMR HMQC spectra of  $^{29}\text{Si}$ -enriched  $\text{C}_{16}\text{H}_{33}\text{Me}_2\text{EtN}^+$ -directed layered borosilicate ( $\text{Si/B} = 70$ ). Both spectra were collected at 9.4 T. They establish spatial proximities and connectivities (respectively) between  $^{29}\text{Si}$  nuclei of the silicate frameworks and incorporated  $^{11}\text{B}$  nuclei. On the right side of the 2D spectra are (in blue and red) partial  $^{29}\text{Si}$  projections of the region corresponding to the layered borosilicate phase (from 1.0 to -2.0 ppm in the  $^{11}\text{B}$  dimension) and (in black) the  $^{29}\text{Si}\{^1\text{H}\}$  CP-MAS spectrum. The  $^{11}\text{B}$  echo-MAS spectrum is showed on top of the 2D spectrum.

While the through-bond-mediated  $^{11}\text{B}[^{29}\text{Si}]$  correlation experiment probes specially the first neighbors of the incorporated B atoms, the next-nearest neighbors that are sufficiently close in space can in principle be revealed by means of dipolar-mediated experiments. Figure D.18 shows (in blue) the  $^{11}\text{B}[^{29}\text{Si}]$  dipolar-mediated 2D HMQC spectrum collected on the  $^{29}\text{Si}$ -enriched  $\text{C}_{16}\text{H}_{33}\text{Me}_2\text{EtN}^+$  - directed layered borosilicate material. It first shows that the small impurity already observed (at ca. 4 ppm) in the  $^{11}\text{B}$  spectrum of Figure D.3d gives rise to two cross peaks (at ca. -106 and -108 ppm in the  $^{29}\text{Si}$  dimensions) indicating a borosilicate composition. The broadenings of these peaks point to a lesser extent of molecular order as compared to the  $\text{C}_{16}\text{H}_{33}\text{Me}_2\text{EtN}^+$  - directed layered borosilicate phase. The absence of these cross-peaks in the  $J$ -mediated experiment (in red) suggest that the  $^2J(^{11}\text{B}-^{29}\text{Si})$  couplings within this additional phase are small in comparison to the couplings in the borosilicate material of interest. One possible reason for this could be that the boron is strongly depolymerized in this phase, consisting of  $Q^1$  and/or  $Q^2\text{B}^{(\text{IV})}$  moieties, which could explain the position of this  $^{11}\text{B}$  peak (3.8 ppm). It is well-known for  $^2J(^{29}\text{Si}-\text{O}-^{29}\text{Si})$  couplings tend to be smaller when the polymerization degree ( $n$ ) of either  $^{29}\text{Si}$  nucleus decreases.<sup>71,220-221</sup> Most importantly, the signature of this impurity in the 2D HMQC spectrum is clearly separated from that of the phase of interest and consequently does not interfere with its analysis.

More importantly, the dipolar-mediated NMR spectrum (Fig D.18, in blue) shows new correlations in the  $^{29}\text{Si}$  dimension with respect to single  $^{11}\text{B}$  peak at -0.4 ppm, in addition to those already present in the  $J$ -mediated HMQC spectrum (Fig D.18, in red). These additional correlations (at -111.3 and -108.6 ppm and seemingly a shoulder at ca. -101 ppm in the  $^{29}\text{Si}$  dimension) correspond to  $^{29}\text{Si}$  nuclei located in close proximity (less than ca. 5 Å) but not connected to the incorporated  $^{11}\text{B}$  nuclei. Interestingly, the peak at -108.6 ppm and the shoulder at -101 ppm are very close to the frequencies of  $^{29}\text{Si}$  peaks labeled 4 and 2 in the 1D spectrum of Fig. D.3c (-108.7 and -100.7 ppm), which also correspond to sites 4 and 2 in the pure-silicate material (-109.1 and 101.0 ppm).<sup>22</sup> It is thus possible to assign these peaks to  $^{29}\text{Si}$  in sites Si4 and Si2 located close but not connected to the Boron. This demonstrates that the Boron is incorporated in the layered silicate framework rather than in a separate molecularly-ordered phase. It also indicates that the influence of the Si to B substitution on the framework structure is strongly localized, and primarily restricted to the first neighbors of the boron, the second neighbors being largely unaffected, as already suggested above on the basis of 1D  $^{29}\text{Si}$  NMR spectra (Fig D.3c, d).

Some second-nearest Si neighbors of the B are nevertheless perturbed by the distortion necessarily induced to accommodate for the substitution of a Si atom by a smaller B atom, as is illustrated by the peak at -111.3 ppm, which can reasonably be assigned to a  $^{29}\text{Si}$  site Si5 (or even to a Si4) with a slightly modified chemical shift. The observation of narrow  $^{29}\text{Si}$  peaks rather than broad distributions of

$^{29}\text{Si}$  environments in the direct vicinity of the boron shows that the local modification of the framework structure upon B/Si substitution is unique throughout the sample, as already suggested by  $^{11}\text{B}$  1D MAS NMR data. A unique structure modification seems only possible if the boron is always incorporated in the same tetrahedral site, an interpretation that is also supported by the number of  $^{29}\text{Si}$  correlations (three) observed in the through-bond mediated  $^{11}\text{B}[^{29}\text{Si}]$  HMQC spectrum (Fig D.18, in red) at the  $^{11}\text{B}$  frequency of -0.4 ppm.

It is fairly clear in the case of the  $\text{C}_{16}\text{H}_{33}\text{Me}_2\text{EtN}^+$  - borosilicate material that the boron heteroatoms are preferentially incorporated in a single crystallographic site. Hence, the next step is to determine precisely the location of incorporated boron atom (either Si1 or Si2 sites). This can be achieved, in general, by assigning the  $^{29}\text{Si}$  signals of Si-O-B moieties with the previous knowledge of  $^{29}\text{Si}$ -O- $^{29}\text{Si}$  connectivities. These  $^{29}\text{Si}$ -O- $^{29}\text{Si}$  connectivities have been well established for the pure-silicate material,<sup>22,23</sup> and were found identical in the “boron-free” regions (see  $J$ -mediated  $^{29}\text{Si}$ -O- $^{29}\text{Si}$  correlation NMR spectrum, Fig D.4b) of the borosilicate material. Based on our results, boron-free regions, or regions whose  $^{29}\text{Si}$  signals are unaffected by the presence of the boron are defined as Si atoms located away from the first T-shell of the boron.

As already described, the main obstacle for  $^{11}\text{B}$ -O- $^{29}\text{Si}$  assignment is the lack of predefined knowledge of the effect on  $^{29}\text{Si}$  chemical shifts of nearby Si atoms of the Si/B substitution. Such Si atoms are generally referred to as  $Q^n(m\text{B})$ ,  $m$  is the number of incorporated boron atoms. Several studies suggest that it is particularly difficult to establish a general trend for the evolution of the  $^{29}\text{Si}$  shift between  $Q^n(m\text{B})$  and  $Q^n((m-1)\text{B})$  environments in the case of B/Si substitutions (with  $m = 0, 1, \dots, n$  for an arbitrary  $n$  value between 2 and 4).<sup>75</sup> This is in contrast with the case of Al/Si substitutions, where studies of zeolites in particular<sup>222</sup> have been used to establish that one generally expects a 5 ppm shift to low field regions (to the left of the spectrum) between  $Q^n((m-1)\text{Al})$  and  $Q^n(m\text{Al})$   $^{29}\text{Si}$  environments. Such a general trend does not apply in the case of borosilicates. In other words, it is impossible to suggest a clear assignment of the  $Q^n(1\text{B})$  environments generated by the substitution of  $\text{B}^{(\text{IV})}$  atoms on the either of  $Q^3$  Si sites, solely on the basis of  $^{29}\text{Si}$  chemical shifts. Nevertheless, Figure D.19 provides a preliminary analysis of the dependence of  $^{29}\text{Si}$  chemical shifts ( $\Delta\delta_{\text{Si}}$ ) of first nearest  $^{29}\text{Si}$  neighbors upon B incorporation. This Figure depicts the comparison of  $^{29}\text{Si}[^1\text{H}]$  CP-MAS NMR spectrum (in black) and  $^{29}\text{Si}$  projection (in red)  $^{11}\text{B}[^{29}\text{Si}]$   $J$ -mediated. Here we considered two possible cases: (i) B is located in Si2 or (ii) in Si1. Since both are  $Q^3$  sites, one can certainly expect three signals for the first nearest crystallographic sites directly connected to B via bridging oxygen atom.

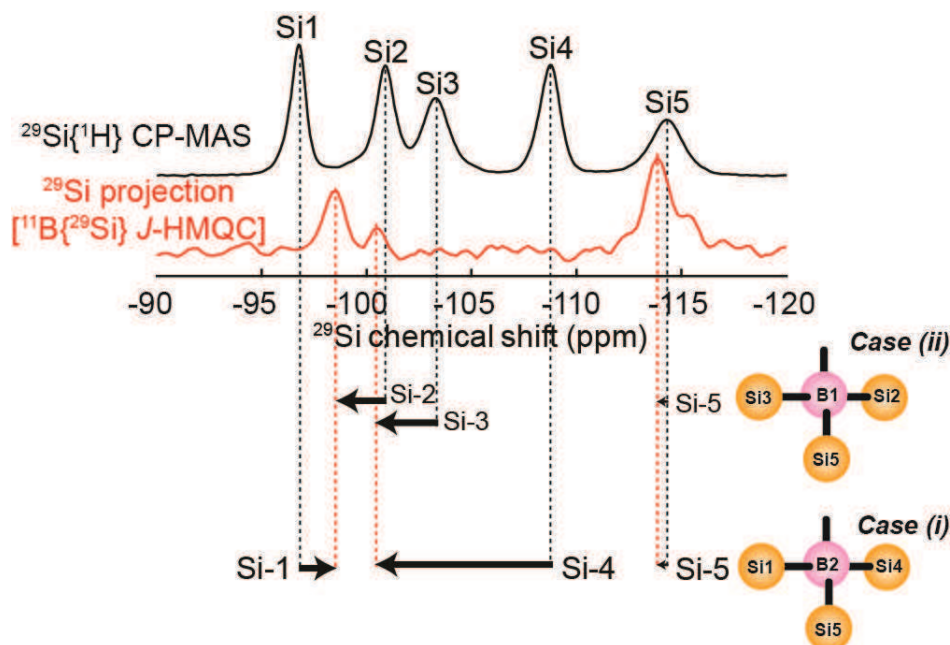


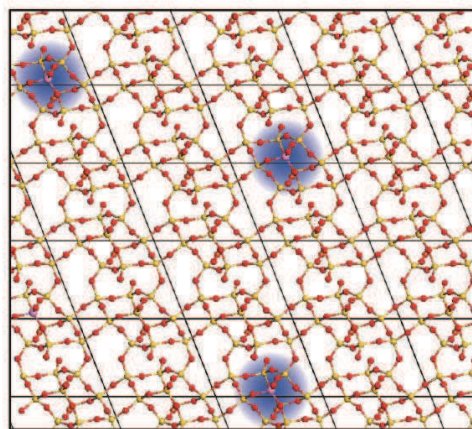
**Figure D.19** Comparison of  $^{29}\text{Si}\{^1\text{H}\}$  CP-MAS (in black) and  $^{29}\text{Si}$  projection of  $^{11}\text{B}\{^{29}\text{Si}\}$  J-mediated HMQC (in red) spectrum of  $^{29}\text{Si}$  enriched  $\text{C}_{16}\text{H}_{33}\text{Me}_2\text{EtN}^+$ -directed layered borosilicate material, where in case (i) B atoms are incorporated into site Si2 and in case (ii) B atoms are incorporated into site Si1 (demonstrated at the bottom of the spectra).

#### Case (i): Incorporation of B into Si2

In this case, the expected  $^{29}\text{Si}$ -O- $^{11}\text{B}$  connectivities are with Si1, Si4 and Si5. The signals at -98.3, -100.3 and -113.8 ppm in the Fig D.19b could be assigned respectively to  $^{29}\text{Si}$  sites Si1, Si4 and Si5. Different effects of Si/B substitution on adjacent  $^{29}\text{Si}$  sites are observed in this case, particularly,  $^{29}\text{Si}$  shifts move in different directions, and by different extents.

#### Case (ii): Incorporation of B into Si1

If we now consider that B is incorporated in substitution of site Si1, the influence of B on neighboring  $^{29}\text{Si}$  environment is different. The  $^{11}\text{B}$ -O- $^{29}\text{Si}$  connectivities are now with Si2, Si3 and Si5 and assigned respectively to peaks at -98.3, -100.3 and -113.8 ppm, as shown in the Fig D.19b. One can clearly see a consistent behavior of all  $^{29}\text{Si}$  chemical shift (all the three peaks are displaced towards left side in contrast to their siliceous analog), which is in agreement with the trend observed upon Al/Si substitution in aluminosilicates. To summarize the entire spectral analysis, the assignments in both the cases strongly indicate that B atoms possibly prefer to locate in Si1 crystallographic sites rather than in Si2 sites.

**D.4.4 Molecularly-ordered defects in the 2D silicate framework**

**Figure D.20** The layered borosilicate model (Fig D.14), where B atoms (light pink) are substituted randomly in the silicate framework. The blue shaded region signifies the perturbation range of incorporated B atoms.

The small line widths observed in both dimensions of the 2D  $^{11}\text{B}$ - $^{29}\text{Si}$  correlation spectra (Fig D.18) reveals that all the B atoms are preferentially incorporated into one of the  $Q^3$  framework Si sites (sites 1 or 2). Particularly, the full width at half-maximum ranging between 1.0 and 1.6 ppm in the  $^{29}\text{Si}$  dimension and 0.3 ppm in the  $^{11}\text{B}$  dimension point to well-defined  $^{29}\text{Si}$  and  $^{11}\text{B}$  environments rather than distributions of local geometries. While the B incorporation presumably takes place at randomly distributed sites Si1 (or Si2) in the otherwise unchanged silicate framework (with respect to the pure-silicate analog), these “defects” appear to be all located within the exact same local structural environment, as if in a specific crystalline site. And yet, as illustrated in the model of Figure D.20, these molecularly-ordered environments lack the periodicity of a true crystal. This is in strong contrast, for example, with the case of borosilicate zeolite MCM-70 (crystal code MVY<sup>223</sup>), having four distinct crystallographic tetrahedral sites, three of which are occupied exclusively by Si atoms, while the fourth is purely occupied by B atoms.<sup>9</sup> In that case, the B site fully belongs to the crystal structure and cannot be described, locally, as a defect. The situation is completely different here because (i) the materials, while molecularly-ordered locally, lack the three-dimensional (or even two-dimensional) periodicity of a crystal, and (ii) the amount of B incorporated is small enough that B incorporation sites are most likely uncorrelated to each other. In spite of such major discrepancies with respect to the definition of a crystal, we predict in light of the remarkably high degree of molecular order around these B incorporation sites, that their molecular-level physico-chemical properties should be the same. This may include catalytic

reactions or the condensation reactions that can transform 2D layered silicates into 3D zeolites or related structures.

## **D.5 Conclusions**

The B heteroatoms are successfully incorporated into the 2D silicate framework of two surfactant-directed layered silicate materials. Advanced high resolution solid-state NMR and computational methods unambiguously establish the distribution of B atoms in the respective non-crystalline layered borosilicates. The B heteroatoms have significant and distinguishable effects on the neighboring Si environment in spite of the small boron loading (Si/B = 60-140). Furthermore, the nature of B siting is entirely different for either material. In the case of  $C_{16}H_{33}Me_3N^+$  - directed layered borosilicate, B atoms are incorporated into several distinct crystallographic sites. The 2D NMR measurements and DFT calculations furthermore strongly indicates that profound structural rearrangement takes place upon B incorporation. This occurs in particular when B occupies  $Q^4$  Si sites, in which case the neighboring  $Q^3$  Si sites condensed with a nearby  $Q^3$  Si site of the same layer, so that the B atoms are connected with only  $Q^4$  Si sites. In the case of  $C_{16}H_{33}Me_2EtN^+$  - directed layered borosilicate, the situation is totally different. Solid-state NMR measurements establish the preferential incorporation of B atoms in a single crystallographic site in this material, without further rearrangement of the framework. The  $^{11}B$  chemical shifts calculated by DFT further supports the NMR results. Another important observation is that the perturbation range around the incorporated B atoms is identical throughout the sample. However, these defected B sites are highly localized though it may lack the periodicity. We thus anticipate from our molecular-level observations that the physico-chemical properties and in particular the reactivities of all of the incorporation sites in this material will be identical.

---

## **Chapter E**

# ***Extension to the study of atomic substitution in other materials***

---

### **E.1 Introduction**

The detailed knowledge of chemical composition and the local molecular arrangement of inorganic materials are crucial to comprehend their physical and chemical properties. In the previous chapters, (C and D) we studied the incorporation of Al and B heteroatoms into two strongly related surfactant-directed layered silicates, with the aim of understanding the mechanism that control the siting and local structural reorganization around these heteroatoms. The structural behavior and local modifications upon these heteroatoms is profoundly different for either material. Such structural insights at molecular level have been determined primarily by solid-state NMR techniques and thereby we successfully established the distribution of heteroatoms in the 2D silicate framework. These sophisticated NMR techniques give a breakthrough to establish the consequences of heteroatoms on the local structure in lamellar materials. In this context, the present chapter focuses on the atomic substitution of heteroatoms in different materials. The main objectives are to establish the local structure around the heteroatoms particularly by solid-state NMR. The two studied materials are completely different from each other. Hence, this chapter is divided into two main segments. The **section E.2** focuses on establishing the chemical compositions of Si, Al and Mg atoms in another type of layered silicates that those studied in the previous chapters: the montmorillonites, which belongs to the so-called smectite clays family. The main objectives are to establish the local structure around the heteroatoms in the tetrahedral and octahedral layers. Furthermore, the relative chemical composition of  $\text{Al}^{3+}/\text{Mg}^{2+}$  and  $\text{Si}^{4+}/\text{Al}^{3+}$  species in the octahedral and tetrahedral layers, respectively have been determined at molecular level by solid-state NMR. The **section E.3** is centered on the study of a new calcium borosilicate phase of chemical composition  $\text{CaSi}_{1/3}\text{B}_{2/3}\text{O}_{8/3}$ . The average long-range structure of this material seems to be disordered but it shows well organized molecular units at local level. Here, the solid-state NMR and DFT calculations were employed to investigate the molecular arrangement at a local level.

## **E.2 Exploiting the local structure of 2:1 clay minerals: Montmorillonites**

The structural investigation of naturally occurring minerals for instance, montmorillonites is extremely difficult. This is because most of the natural montmorillonites contains many impurities. Importantly, the main obstacle from the point of view of solid-state NMR is the presence of paramagnetic and ferromagnetic species (such as FeO and Fe<sub>2</sub>O<sub>3</sub> moieties, respectively) in the material. The paramagnetic species have several effects on NMR spectra (such as, dipolar couplings or relaxation effects) that result in broad NMR features. In such a case, an alternative way to find the structure solution is to study synthesized montmorillonites (for example, iron free) and then comparing the obtained results with the natural montmorillonites. Consequently, the absence of paramagnetic contribution substantially increases the resolution of the NMR spectra and the amount of information that can be obtained. The main objective of the current studies is to establish the local structure and chemical composition of synthetic montmorillonites in contrast with the natural clays, especially by solid-state NMR methods. This includes 1D MAS NMR experiments detecting <sup>29</sup>Si, <sup>27</sup>Al, <sup>25</sup>Mg and <sup>1</sup>H nuclei at higher magnetic field and 2D NMR probing the spatial interactions between Si and Al atoms. The Si/Al<sup>(IV)</sup> molecular ordering in the tetrahedral layer is often studied in the similar kind of layered silicates or clays. The more interesting and remarkable part of the corresponding studies is exploiting the chemical composition of Al<sup>(VI)</sup>/Mg species and the relevant molecular ordering in the octahedral layer. This is accomplished by studying the <sup>25</sup>Mg and <sup>1</sup>H NMR in combination with DFT calculations.

### ***E.2.1 Natural and Synthetic Montmorillonites***

The montmorillonites are hydrous aluminum phyllosilicates belong to the smectite clay minerals. These materials have been extensively studied because of their wide applications, for example, as heterogeneous catalysts, in paints, cosmetics, as rheological control agents, drug delivery systems and geochemical barriers in waste landfills<sup>224-228</sup> and etc. In addition, montmorillonites have large specific surface area which directly impacts on their increased adsorptivities and cation exchange capacities (CEC). The crystalline framework of these materials is composed of a so-called “2:1” layered structure in which an octahedral layer is “sandwiched” between two tetrahedral layers, as shown in the Figure E.1. The AlO<sub>6</sub> and SiO<sub>4</sub> are the principal framework entities in the octahedral and tetrahedral sheets, respectively. The ionic substitution of Mg<sup>2+</sup> for Al<sup>3+</sup> in the octahedral or Al<sup>3+</sup> for Si<sup>4+</sup> in tetrahedral layer are mainly responsible for the overall framework negative charge, which is compensated by cations (Na<sup>+</sup>, Ca<sup>+</sup>, K<sup>+</sup> or Mg<sup>+</sup> etc) in the intra-layer space. Notably, these factors have direct impact on the hydration and swelling properties.<sup>229</sup> On the other hand, the solvated inter-layer water molecules control the extent of chemical interactions of cations with the octahedral or tetrahedral framework entities. Thus cations

have significant solvation in the presence of water molecules resulting in the expansion of interlayer space.<sup>230-232</sup>

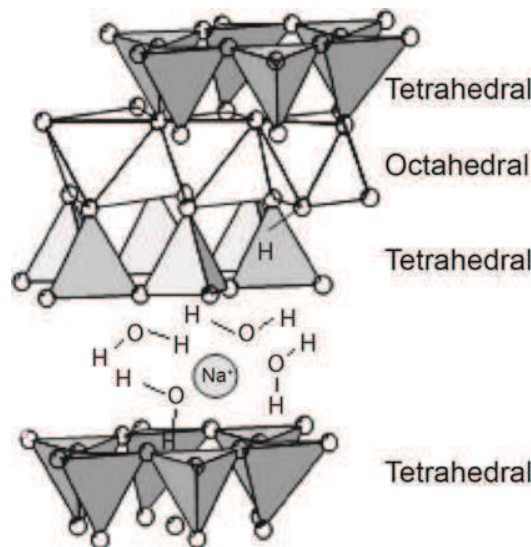


**Figure E.1** [Courtesy: GougeonRD<sup>233</sup>] Schematic representation of Montmorillonites

Despite the clear understanding of the average long-range molecular-scale structure of montmorillonites, understanding the local structure, and in particular the cation distributions within the framework is challenging. Furthermore, the morphological and structural heterogeneity, variable molecular compositions and their relatively small crystal size accounts to the overall complexity. Several characterization techniques have been employed to probe the molecular-scale structure of Na-MMT, such as diffraction techniques or electron microscopy and solid-state NMR. But, limitation associated with lamellar structures, such as stacking disorder, as well as the need for long-range atomic order makes them rather inappropriate to study local environments. In addition, the presence of many impurities and ferromagnetic or paramagnetic species in Na-MMT hinders their characterization using advanced solid-state NMR, a technique that otherwise provides useful information on the local structure around Si and Al atoms in the tetrahedral layer and Al and Mg atoms in the octahedral layer of clay minerals.<sup>81,234-239</sup> Especially, <sup>27</sup>Al and <sup>29</sup>Si NMR experiments<sup>240</sup> reveal the coordination state of Al (tetrahedral or octahedral) and chemical environments of Si, respectively. This ultimately helps to distinguish the local molecular interactions in the octahedral and tetrahedral layers.

An alternative to avoid these limitations is to characterize the synthesized montmorillonites (Na-S-MMT), which are free of paramagnetic species (Na-S-MMT's are synthesized under hydrothermal condition at a temperature of 623K and pressure of 120 MPa. The general molecular formula of Na-S-MMT is given by, (Na<sub>0.68</sub>Mg<sub>0.03</sub>) (Al<sub>3.35</sub>Mg<sub>0.65</sub>) (Si<sub>7.91</sub>Al<sub>0.09</sub>) O<sub>20</sub> (OH<sub>4</sub>)<sup>209</sup>). This allows conducting high-

resolution multi-dimensional NMR experiments probing for example the spatial proximities between Al and Si atoms, which lead to a better understanding their physical chemistry. The  $^1\text{H}$  NMR is another important tool of measuring the chemical interactions at organic-inorganic interface of clay minerals. It may be used to investigate the nature of layered structure at the interface of octahedral and tetrahedral sheets. Alba and coworkers reported for example the sensibility of  $^1\text{H}$  MAS NMR of hydroxyl groups to the different types of octahedral smectite mineral. It captures the extent of variability in their chemical composition.<sup>233,241-244</sup> In the absence of paramagnetic species, higher sensitivity and resolution of the  $^1\text{H}$  NMR spectrum than previously reported could be achieved by collecting the data at higher magnetic field and higher MAS rate. Structural insights into the chemical compositions of Na-MMT can be furthermore derived by studying their synthetic analog (Na-S-MMT material). The  $^{29}\text{Si}$ ,  $^{27}\text{Al}$ ,  $^{25}\text{Mg}$  and  $^1\text{H}$  NMR measurements in combination with DFT calculations provide new insights into the local structure.

### ***E.2.2 Probing the distribution of Al and Si atoms in 2:1 clay minerals***

The Al and Mg are the main framework atoms in the octahedral layer, while the tetrahedral layer is composed of Si and Al atoms. Such differed chemical environments can be identified by detecting  $^{29}\text{Si}$ ,  $^{27}\text{Al}$ ,  $^{25}\text{Mg}$  and  $^1\text{H}$  nuclei. The corresponding 1D quantitative MAS NMR experiments can be used in particular to determine the relative amounts of  $\text{Al}^{3+}/\text{Mg}^{2+}$  and  $\text{Si}^{4+}/\text{Al}^{3+}$  species in the octahedral and tetrahedral layers, respectively. Figure E.2a represents the  $^{29}\text{Si}$  [ $^1\text{H}$ ] CP-MAS NMR spectrum of Na-S-MMT, which reveals the extent of molecular order in the tetrahedral layer. A strong peak at -93.7 ppm can be attributed to  $Q^3$   $^{29}\text{Si}$  species, where the Si atom is connected to three other Si atoms via bridging O atom (basal) within the tetrahedral layer, and to two distinct sites via an “apical” tri-coordinated oxygen atom in the octahedral layer. This is consistent with the  $^{29}\text{Si}$  chemical shift of previously reported values of various Na-MMT, i.e. -94.1 to -93.3 ppm.<sup>81</sup> The extent of molecular order in the layered structure is very sensitive to the presence of Al or Mg atoms in the tetrahedral or octahedral sheets. The charge bearing  $\text{Al}^{(\text{IV})}$  and Mg atoms indeed affect the local structure and may cause geometrical disorder. The resulting deterioration of such molecular order could be identified by  $^{29}\text{Si}$  chemical shift distribution. For instance, the full width at half-maximum (FWHM) of  $^{29}\text{Si}$  peak observed at -93.7 ppm is found to be 3.3 ppm, which indicates a significant distribution of distinct chemical environments at the molecular level and reflects the intrinsic complexity of the montmorillonite local structure.

The additional weak peak at -88.6 ppm could be attributed to the  $Q^3$  (1Al) species (tetrahedral Si site connected to two other tetrahedral Si atoms via bridging oxygen atom and one tetrahedral Al atom, and to the octahedral layer via an apical oxygen atom).<sup>10</sup> The line broadening of the  $^{29}\text{Si}$  peak at -88.6 ppm found to be 3.1 ppm (FWHM), which is almost identical to those observed for  $Q^3$   $^{29}\text{Si}$  sites. This indicates that the extent of local disorder remains same around the Al atoms as in the Al-free regions and

that such  $Q^3(1Al)$  sites belong to the same silicate structure. The  $^{29}Si$  spectrum furthermore reveals the existence of an additional silicate phase reflected by a broad peak centered at -106 ppm, which can thereby be attributed to  $Q^4$  or  $Q^4(1Al)$  species (a Si atom connected to 4 Si atoms or a Si atom connected to 3 Si atoms and one Al atom, respectively). The associated large spectral broadening (FWHM, 13.5 ppm) points to the negligible or poor molecular order in this additional phase. The distinct Si environments could be quantified by means of  $^{29}Si$  echo-MAS NMR spectrum collected with a recycling delay of 1000s, as shown in the Figure E.2b. The spectrum is simulated (dotted lines) by using Dmfit where the chemical shift, line width and line shape of each peak (deconvoluted spectrum, gray lines) were fixed as extracted from the  $^{29}Si[^1H]$  CP-MAS NMR spectrum (Fig. E.2a). The resulting fit indicates that 72% of the signal accounts to the  $Q^3$  sites and 6% for  $Q^3(1Al)$  sites. The remaining 22% accounts to the  $Q^4$  or  $Q^4(1Al)$  sites (broad peak at -106 ppm) pointing to the additional phase. This strongly suggests that the composition of the tetrahedral layer can be derived from chemical analyzes could be severely biased by non-negligible fraction of Si atoms located in an impurity that would not be detected by XRD due to its (presumably) amorphous nature.<sup>209</sup>

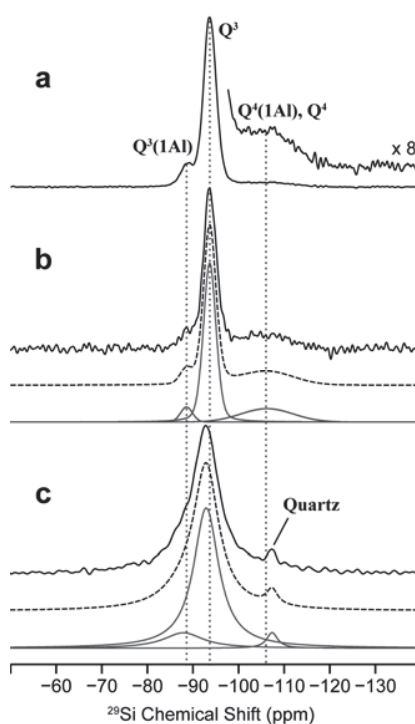


**Figure E.2** (a)  $^{29}Si$  [ $^1H$ ] CP-MAS NMR spectrum of synthetic Na-montmorillonite (Na-S-MMT) collected with a contact time of 10 ms. (b) Quantitative  $^{29}Si$  echo-MAS NMR spectrum recorded with a recycling delay of 1000 s. The spectrum is simulated (dashed line) by Dmfit program and the corresponding deconvolutions are shown below as gray solid lines. (c)  $^{29}Si$  echo-MAS NMR spectrum of natural Na-

montmorillonite recorded with a recycling delay of 200 ms. The simulated spectrum (dashed line) and the deconvolution (gray solid lines) showed at the bottom. The NMR spectra (a, b) of Na-S-MMT and (c) Na-MMT were collected at a magnetic field of 9.4T.

In contrast, the  $^{29}\text{Si}$  MAS NMR spectrum of Na-MMT as shown in Figure E.2c, is much less informative. This is mainly because of the fast transverse relaxation<sup>245</sup> and associated broadening of the  $^{29}\text{Si}$  NMR signal, which is strongly influenced by the neighboring paramagnetic species ( $\text{Fe}^{3+}$ ). Hence, a single broad  $^{29}\text{Si}$  peak is observed at -93 ppm and could be attributed to the  $Q^3$   $^{29}\text{Si}$  sites. The  $Q^3$  (1Al) chemical environment is indicated by a shoulder peak at -88 ppm. This is evidenced by fitting the spectrum (dotted lines) by Dmfit program using Lorentzian lines and a position of  $Q^3$ (Al) moieties fixed +5 ppm away from the position of  $Q^3$  moieties. The additional phase obtained in Na-S-MMT, which is identified by a broad  $^{29}\text{Si}$  peak at -106 ppm cannot be detected in the  $^{29}\text{Si}$  MAS NMR spectrum of Na-MMT, but its presence cannot be ruled out given the large spectral broadening of the dominant  $^{29}\text{Si}$  peak. The Na-MMT is associated with other kinds of impurities that are extremely difficult to eliminate, as illustrated for example by the small peak at -107.4 ppm, which can be attributed to the Quartz.<sup>201</sup>

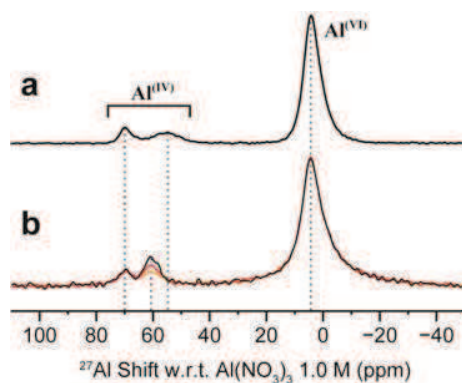


**Figure E.3** (a)  $^{27}\text{Al}$  MAS NMR spectrum of Na-S-MMT collected at 17.6 T (b)  $^{27}\text{Al}$  echo-MAS NMR spectra of Na-MMT recorded at 20 T with recycling delay of 0.01 (orange), 0.1 (red) and 1 second (black).

The  $^{27}\text{Al}$  MAS NMR measurements provide additional information regarding the location of Al atoms in the octahedral or tetrahedral layers. This could be determined by establishing the coordination state of Al atoms. As shown in the Figure E.3a, the  $^{27}\text{Al}$  echo-MAS NMR spectrum of Na-S-MMT consists of one intense peak and two weaker peaks, pointing to the Al atoms in the octahedral and tetrahedral environments, respectively. In particular, the  $^{27}\text{Al}$  peak at 70 ppm could be attributed to the four-coordinated  $\text{Al}^{(\text{IV})}$  chemical environments in the tetrahedral layer, which is consistent with the Si/ $\text{Al}^{(\text{IV})}$  substitution in the tetrahedral layer. The strong intense  $^{27}\text{Al}$  peak at 5 ppm can be assigned to six-

coordinated Al atoms present in the octahedral layer. The same two peaks are observed in the  $^{27}\text{Al}$  MAS NMR spectrum of Na-MMT as showed in the Figure E.3b. In addition, in both spectra a small peak has been observed, respectively at 55 and 60 ppm for Na-S-MMT and Na-MMT materials. This could be assigned to an extra phase, which is incompatible with the actual 2:1 clay minerals. This is confirmed by collecting a series of  $^{27}\text{Al}$  MAS NMR spectra for natural montmorillonite as a function of the recycling delay (0.01s - yellow, 0.1s - red and 1s - black). The signal due to  $\text{Al}^{\text{IV}}$  and  $\text{Al}^{\text{VI}}$  of the clay mineral are found to be fully relaxed within 10 ms but not the signal at 55 or 60 ppm. The longer longitudinal relaxation of  $^{27}\text{Al}$  peak at 55 or 60 ppm reveals that the corresponding Al atoms are not under the influence of the paramagnetic  $\text{Fe}^{3+}$  species.<sup>245</sup> Hence it could be assigned to an Al-containing extra phase containing little or no Fe.

It has been shown that the Na-S-MMT material contains impurity as revealed by  $^{29}\text{Si}$  and  $^{27}\text{Al}$  NMR studies, and we seek to verify that they have the same origin. This may be done by probing the spatial proximities between the Si and Al atoms. Few examples were found in the literature revealing the heteronuclear interactions between Al and Si atoms.<sup>211-213</sup> The spatial proximities between Al and Si atoms could be probed via heteronuclear  $^{29}\text{Si}$ - $^{27}\text{Al}$  dipolar couplings, for instance by collecting  $^{27}\text{Al}$  [ $^{29}\text{Si}$ ] dipolar-mediated HMQC.<sup>246</sup> This experiment makes a clear distinction between the impurity and the smectite phase for the sample of Na-S-MMT, as showed in Figure E.4.

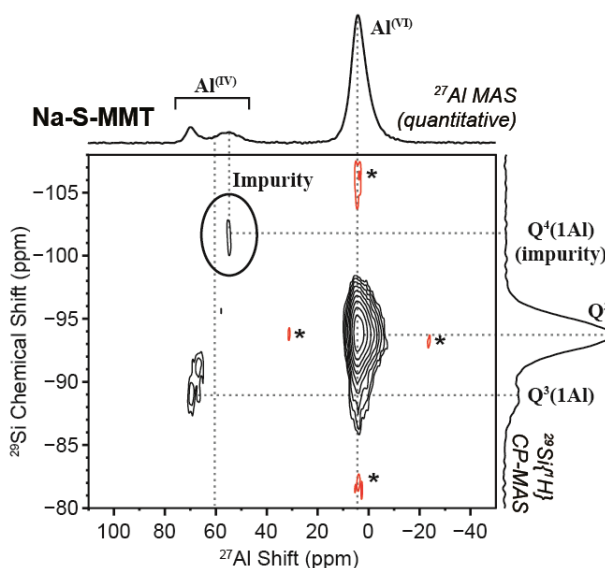


**Figure E.4**  $^{27}\text{Al}$  [ $^{29}\text{Si}$ ] dipolar-mediated HMQC collected at a magnetic field of 17.6 T at 5 kHz MAS for Na-S-MMT probing the spatial proximities between Si and Al atoms in the tetrahedral and octahedral layer of 2:1 clays.

As mentioned in the previous chapters, the heteronuclear dipolar couplings will be averaged to zero under magic angle spinning. Hence, we used symmetry based rotor-synchronized  $R4^2_1$  pulses<sup>181,189</sup> in order to reintroduce the heteronuclear dipolar couplings (See chapter B for more details). This allows probing the spatial proximities between Si and Al atoms. In spite of low natural abundance  $^{29}\text{Si}$  (4.7%), a 2D HMQC spectrum with decent signal to noise could be collected at a magnetic field of 17.6 T. As expected a strong correlation was observed between the signal corresponding to six-coordinated Al atoms in the direct dimension (F2) at 5 ppm and the  $Q^3$   $^{29}\text{Si}$  species in the indirect dimension (F1) at -93.7 ppm, which illustrates that the octahedral layered Al atoms are close to the four-coordinated Si atoms to which they are connected via apical O atoms. A second correlation is observed between the  $^{27}\text{Al}$  peak at 70 ppm corresponding to four-coordinated Al atoms and  $^{29}\text{Si}$  peak at -88.6 ppm corresponding to  $Q^3$  (1Al)  $^{29}\text{Si}$  species. This is a typical signature of Si/Al<sup>(IV)</sup> substitution in the tetrahedral layer. Finally, the correlation peak between the  $^{27}\text{Al}$  peak at 55 ppm and the broad  $^{29}\text{Si}$  peak centered at -102 ppm unambiguously confirms that the extra signals revealed previously in 1D  $^{29}\text{Si}$  and  $^{27}\text{Al}$  MAS spectra are the resultant of the same unknown aluminosilicate phase, which is basically constituted with  $Q^4$  and  $Q^4$ (1Al) Si sites and Al<sup>(IV)</sup> moieties.

Since, the paramagnetic species were absent in the Na-S-MMT, the line shape of each  $^{27}\text{Al}$  peak reveals the distribution of quadrupolar coupling constants, which originates from variations in the local symmetry. For instance, the signature of Al<sup>(IV)</sup> in the 2D HMQC spectrum indicates that the Al<sup>(VI)</sup> atoms in the octahedral layer may have connection with two Si atoms or one Si atom and one Al<sup>(IV)</sup> in the tetrahedral layer via apical oxygen atom. On the other hand, the ICP analyses indicate the presence of a significant amount of Mg atoms which indicate Mg/Al<sup>(VI)</sup> substitution in the octahedral layer. This may result, at a local level, in different Al<sup>(VI)</sup> environments such as, Al(Al)<sub>3</sub>, Al(Al)<sub>2</sub>(Mg), Al(Al)(Mg)<sub>2</sub>, Al(Mg)<sub>3</sub> according to the nature of their octahedral neighbors. The Al<sup>(IV)</sup> atoms may be connected with the octahedral neighbors via pairs of apical oxygen atoms or pairs of hydroxyl groups. These kinds of variation in the distribution of Al/Mg atoms in the octahedral or Si/Al in the tetrahedral layer, all affect in different ways the local symmetry. However, these environments are all embedded and impossible to distinguish from the Al<sup>(IV)</sup> NMR peak.

The distribution of cationic local environments can be established, for example by detecting  $^{25}\text{Mg}$  nuclei. Collecting  $^{25}\text{Mg}$  NMR spectra may be challenging for relatively low Mg contents (nuclear spin  $I=5/2$ ) because of its low natural abundance (10%) and low gyromagnetic ratio. In addition, large second-order quadrupolar coupling constant further contributes to the existing spectral broadening. These problems can however often be overcome by collecting the  $^{25}\text{Mg}$  NMR spectra at high magnetic field,<sup>247-248</sup> since second-order quadrupolar constant is inversely proportional to the magnetic field. Figure E.5a

and E.5b represent the  $^{25}\text{Mg}$  echo-MAS NMR spectra of Na-S-MMT and Na-MMT materials, respectively collected at a magnetic field of 19.9T. Similar to  $^{27}\text{Al}$  NMR measurements, the line shape of the  $^{25}\text{Mg}$  NMR spectrum of Na-S-MMT reveals the signature of distribution of quadrupolar coupling constant and isotropic chemical shifts. This is in fact the resultant of the Mg/Al substitution in the three adjacent octahedral sites or Si/Al substitution in the four adjacent tetrahedral sites. The  $^{25}\text{Mg}$  NMR spectrum of Na-S-MMT was simulated with a distribution of quadrupolar coupling constant and asymmetry parameter centered around  $C_Q = 3.35$  MHz and  $\eta_Q = 0.61$ , and a Gaussian distribution of  $^{25}\text{Mg}$  isotropic chemical shifts centered at 16 ppm. It is unfortunately not possible on the basis of  $^{25}\text{Mg}$  data to identify the different Mg environments associated with the  $\text{Al}^{(\text{VI})}/\text{Mg}$  or  $\text{Si}/\text{Al}^{(\text{IV})}$  distributions in the octahedral and tetrahedral layer. Another probe is thus needed to shed light onto the  $\text{Mg}/\text{Al}^{(\text{VI})}$  distribution in particular.

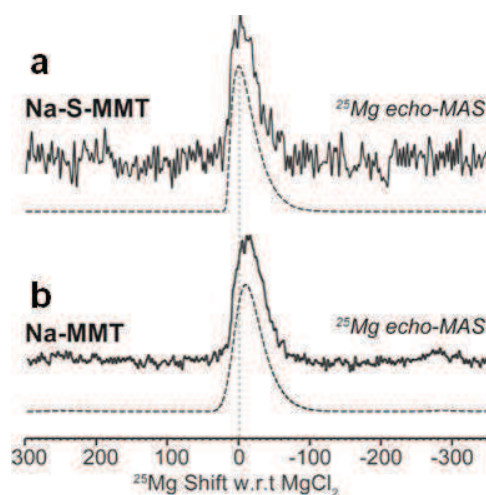


**Figure E.5** 1D  $^{25}\text{Mg}$  echo-MAS NMR spectra of (a) Na-S-MMT and (d) Na-MMT materials collected at a magnetic field of 19.9 T.

The  $^{25}\text{Mg}$  peak of Na-MMT as shown in the Figure E.5b also signifies the distribution of quadrupolar coupling constant and isotropic shifts. In addition, a slight broadening may be revealed as a result of the interactions between  $^{25}\text{Mg}$  nuclei and the paramagnetic  $\text{Fe}^{3+}$  species. In spite of all these complications, the corresponding  $^{25}\text{Mg}$  NMR spectrum has been simulated with the same parameters that used to model  $^{25}\text{Mg}$  NMR spectrum of Na-S-MMT, with the exception of the larger Lorentzian broadening. This confirms the existence of strong similarities between their interlayer molecular-scale structures.

### ***E.2.3 Distribution of Al and Mg atoms by $^1\text{H}$ MAS NMR***

The local structure of 2:1 clay minerals and their relative chemical composition could be successfully probed by  $^1\text{H}$  solid-state NMR studies. The availability of advanced NMR probes providing fast magic angle spinning and high magnetic fields enables to obtain a high resolution in the  $^1\text{H}$  NMR spectra. In the current studies, the  $^1\text{H}$  NMR measurement of (iron free) Na-S-MMT give a breakthrough to establish the various surface, intralayer and interlayer environments present in the clay minerals. For example, Figure E.6a shows the quantitative  $^1\text{H}$  NMR spectrum of Na-S-MMT collected at a magnetic field of 17.6T and at the MAS rate of 64 kHz. It shows three main peaks at 0.9, 2.2 and 3.7 ppm and a shoulder peak at ca. 4 ppm. These  $^1\text{H}$  peaks are specifically assigned with the help of  $^{27}\text{Al}$  and  $^{29}\text{Si}$  edited  $^1\text{H}$  MAS NMR spectra, as showed in the Figure E.6b and E.6c, respectively. The  $^{27}\text{Al}$  edited  $^1\text{H}$  spectrum was collected by using  $^1\text{H}[^{27}\text{Al}]$  CP-MAS sequence, where the magnetization is transferred from  $^{27}\text{Al}$  to nearby  $^1\text{H}$  nuclei via  $^{27}\text{Al}$ - $^1\text{H}$  dipolar couplings. It shows two main peaks at 0.9 and 2.2 ppm. This indicates that  $^1\text{H}$  peaks at 3.7 ppm and shoulder peak at 4 ppm are further away from the Al atoms. The  $^{29}\text{Si}$  edited  $^1\text{H}$  MAS spectrum also shows the same two main peaks at 0.9 and 2.2 ppm, with an additional broad peak at ca. 4 ppm. This is achieved by using double CP experiment, where the magnetization is initially transferred from  $^1\text{H}$  to  $^{29}\text{Si}$  nuclei, and then selectively transferred back to nearby  $^{29}\text{Si}$  nuclei. Hence, the peak at 4 and 3.7 ppm could be assigned to the water molecules adsorbed at the surface of the tetrahedral layer (or within the open cavities therein) and mobile water molecular present in the interlayer space, respectively. This is further confirmed by recording  $^1\text{H}$  MAS NMR for dehydrated clay mineral (overnight under vacuum at 100°C), as shown in the Figure E.6d. Here, the  $^1\text{H}$  peak at 3.7 ppm that assigned to mobile water molecules has completely disappeared.

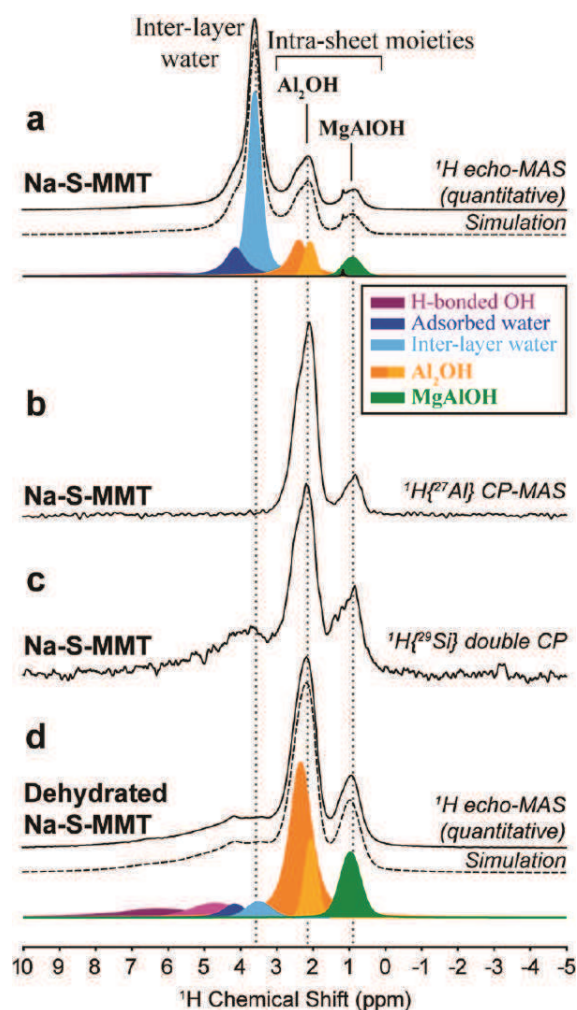


**Figure E.6** 1D  $^1\text{H}$  MAS NMR spectra of Na-S-MMT collected at a magnetic field of 17.6T by spinning the sample at 64 kHz. (a) Quantitative  $^1\text{H}$  echo-MAS NMR spectrum, (b)  $^1\text{H}[^{27}\text{Al}]$  CP-MAS NMR spectrum, (c)  $^1\text{H}[^{29}\text{Si}]$  double CP NMR spectrum and (d) Quantitative  $^1\text{H}$  echo-MAS NMR spectrum of dehydrated Na-S-MMT.

The  $^1\text{H}$  peaks at 0.9 and 2.2 ppm could be assigned to the intra-sheet hydroxyl groups connecting with Mg and Al atoms and present at the interface of the tetrahedral and octahedral sheets. This may include  $\text{Al}_2\text{OH}$  or  $\text{AlMgOH}$  species of the octahedral layer, the probability of  $\text{Mg}_2\text{OH}$  being lower given the Al/Mg ratio (5.2 based in ICP data). It seems reasonable to attribute the peak at 2.2 ppm to  $\text{Al}_2\text{OH}$  species and the peak at 0.9 ppm to the  $\text{AlMgOH}$  species. This hypothetical assignment is consistent with the various reported chemical shift ranges of intra-layer hydroxyl groups in dioctahedral and trioctahedral 2:1 clays.<sup>249</sup> These assignments are unambiguously confirmed by DFT calculations. As shown in the Figure E.7, the calculated  $^1\text{H}$  spectrum of a DFT-optimized structural model with chemical composition

of  $\text{Na}(\text{Al}^{\text{IV}}_7\text{Mg})(\text{Si}_{16})\text{O}_{40}(\text{OH})_8$  is compared with the  $^{27}\text{Al}$  edited  $^1\text{H}$  MAS NMR spectrum. Here one Al atom in octahedral layer is substituted with a Mg atom. Hence, out of 8 intralayer hydroxyl groups, six are  $\text{Al}_2\text{OH}$  and two are  $\text{AlMgOH}$  species (structural models are shown in Figure E.7a and b). The calculated  $^1\text{H}$  chemical shifts of the corresponding models are in good agreement with the experimental values (2.1 and 0.9 ppm) which are thus unambiguously assigned to  $\text{Al}_2\text{OH}$  and  $\text{AlMgOH}$  environments, respectively. The DFT calculations were further conducted on the models having two Mg atoms to verify the existence of  $\text{Mg}_2\text{OH}$  species in the octahedral layer. The resultant calculated  $^1\text{H}$  chemical shift was 0 ppm, and there was no signal observed in this region, which confirms the non-existence of  $\text{Mg}_2\text{OH}$  species in the structure of synthetic 2:1 clays.

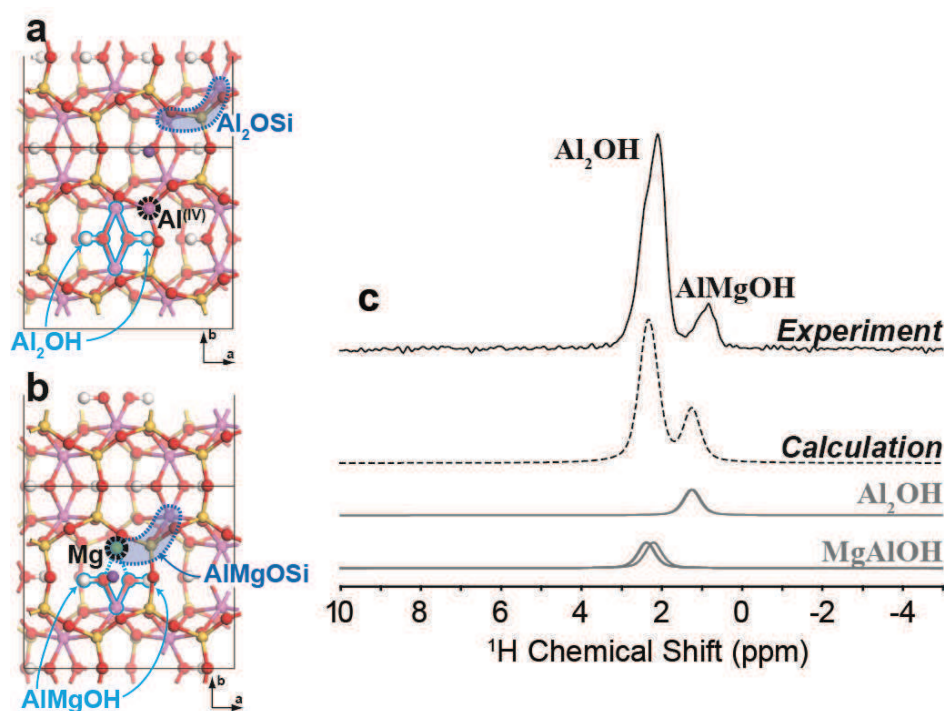


**Figure E.7** (a, b) Structural models of Na-montmorillonite used to calculate NMR parameters, here the Al atom is replaced by a Mg atom in the octahedral layer. Na, Al, Si, Mg, O, and H atoms are shown in dark purple, light purple, yellow, green, red, and white, respectively. (c) Experimental  $^{27}\text{Al}$  edited  $^1\text{H}$  MAS NMR spectrum of Na-S-MMT (solid line) and  $^1\text{H}$  NMR spectrum simulated (dotted line) by DFT calculation using the structural model  $\text{Na}(\text{Al}^{\text{IV}}_7\text{Mg})(\text{Si}_{16})\text{O}_{40}(\text{OH})_8$ .

The absence of  $\text{Mg}_2\text{OH}$  species in the Na-S-MMT does not necessarily exclude the possibility of having  $\text{Mg}_2\text{OSi}$  species. To confirm this, DFT calculations were conducted on the models with chemical composition of  $\text{Na}_2(\text{Al}^{\text{IV}}_6\text{Mg}_2)(\text{Si}_{16})\text{O}_{40}(\text{OH})_8$  associated with adjacent Mg atoms. The predicted energies for the models with adjacent Mg atoms connected via two  $\text{Mg}_2\text{OSi}$  units or two  $\text{Mg}_2\text{OH}$  units found to be

higher by 0.3 and 0.6 eV, respectively, as compared to the model where Mg atoms are not adjacent. This indicates the absence of  $\text{Mg}_2\text{OSi}$  or  $\text{Mg}_2\text{OH}$  species due to their less-favorable thermodynamics. Hence, there may be a general Mg-O-Mg avoidance trend in the octahedral layer leading to a nonrandom  $\text{Mg}^{2+}/\text{Al}^{3+}$  distribution. This is very similar to the case of Mg/Al LDH's (layered double hydroxide), i.e. clays with positively-charged layers consisting of a single octahedral sheet composed of  $\text{Al}^{3+}$  and  $\text{Mg}^{2+}$  cations, in which Al-O-Al avoidance has been observed.<sup>250-252</sup> It appears from these examinations that the entities responsible for the charge of the layer, whether this charge is positive or negative, have a tendency to avoid clustering in the octahedral layers of clays, as illustrated by  $\text{Al}^{3+}$  avoidance in LDH anionic clays and  $\text{Mg}^{2+}$  avoidance in cationic clays.

On the other hand,  $^1\text{H}$  NMR of Na-S-MMT (Figure E.6) are used to quantify selectively the composition of  $\text{Mg}^{2+}/\text{Al}^{3+}$  substitution and the resultant charge deficit in the octahedral layer. This is estimated based on quantification of the  $\text{Al}_2\text{OH}/\text{AlMgOH}$  ratio that obtained by deconvolution of the  $^1\text{H}$  spectra of hydrated (Fig. 6a) and dehydrated (Fig. 6d) Na-S-MMT. The color of each peak designates the different type of  $^1\text{H}$  environments. The overlap of  $^1\text{H}$  peaks of  $\text{Al}_2\text{OH}$  species in particular yields non-negligible uncertainty on the  $\text{Al}_2\text{OH}/\text{AlMgOH}$  ratio ( $3.4\pm 0.5$ ), however, the calculated  $\text{Al}^{(\text{VI})}/\text{Mg}$  ratio is  $8\pm 1$  which is more reliable in contrast with ratio obtained from  $^{29}\text{Si}$  NMR data ( $3\pm 3$ ). The relative chemical composition derived by solid-state NMR is compared with those obtained from EDS and ICP-EOS analyses. It seems the tetrahedral composition  $\text{Si}/\text{Al}^{(\text{IV})}$  derived from  $^1\text{H}$  ( $32\pm 2$ ) and  $^{29}\text{Si}$  ( $40\pm 9$ ) NMR is close to the real composition of clay minerals. In addition, since the material contain small amount of impurity, the EDS and ICP-EOS fail to distinguish the interlayer or intralayer Mg or the extent of Mg atoms in the impurity. Nevertheless, the  $^1\text{H}$  NMR (an indirect probe) selectively measures the amount of Mg atoms within the octahedral layer. This further explains why  $\text{Al}^{(\text{VI})}/\text{Mg}$  ratio measured by EDS ( $4.0\pm 0.2$ ) and ICP ( $5.2\pm 0.5$ ) is considerably lower than the ratio calculated by NMR ( $8\pm 1$ ), which is close to the real molecular composition.

### E.3 Solid-state NMR study of the new calcium borosilicate phase

#### E.3.1 General Introduction

A vast number of inorganic silicate based materials consist of aluminum or boron oxides. The molecular structures of these materials are profoundly different and strongly affect their physico-chemical properties. It mainly includes naturally-occurring zeolites. On the other hand, the calcium aluminosilicate or borosilicate minerals also have very diverse applications. The crystallinity or the purity of these materials may also depend on their chemical composition. These materials can be distinguished into several categories with respect to their chemical composition and extent of crystallinity and hence become a hot topic in glassy industry and geological field. For example, the boron-containing alkali and alkaline earth oxides are technologically very important in glass materials, such as, bioactive, optical and thermal shock-resistant glasses. In this context, this section focuses on the structural elucidation of a new crystalline calcium borosilicate phase ( $\text{CaSi}_{1/3}\text{B}_{2/3}\text{O}_{8/3}$ ) synthesized by annealing the corresponding glassy composition in the  $\text{CaO-SiO}_2\text{-B}_2\text{O}_3$  ternary system, as shown in the Figure E.8. This unknown phase has been primarily suggested by Bauer<sup>253</sup> in 1962 as the so called “X-phase” and was primarily observed during the boron substitution for aluminum in the naturally occurring mineral, known as gehlenite.

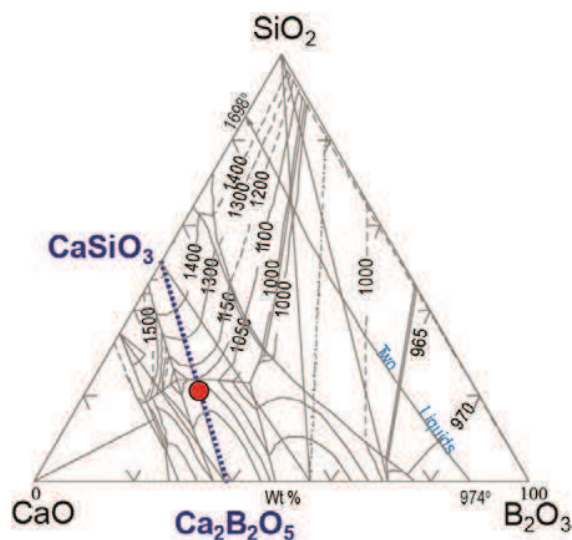


**Figure E.8** [Courtesy: Emmanuel Véron] The ternary diagram of  $\text{CaO-SiO}_2\text{-B}_2\text{O}_3$  system<sup>254</sup> showing the localization of the new calcium borosilicate oxide with  $\text{CaSi}_{0.33}\text{B}_{0.75}\text{O}_{2.79}$  nominal composition (red full circle symbol).

The main characterization methods involved in solving the crystal structure of this material are diffraction methods, such as in-situ neutron and synchrotron studies at high temperature and electron microscopy. As yet, diffraction methods provide only the average structure and fail to fully understand

the molecular ordering and Si/B distribution at the local level. This is because the reflections in the diffraction spectrum point to the average structure revealing the mixture of Si and B tetrahedral units. Hence, the solid-state NMR is a complimentary technique and investigates the local structure to make a clear distinction between Si to B molecular ordering. The local point of view of solid-state NMR, in combination with DFT calculations shed light onto seemingly distorted tetrahedral units, mixed Si/B compositions, and partial O occupations that are otherwise enigmatic in the average long-range structure.

### ***E.3.2 Solid-state NMR studies probing the local structure***

The diffraction measurements generally establish the long range molecular order and reveal the average structure. In the case of new calcium borosilicate material also, the diffraction data give the average long range structure, especially measured by means of in-situ neutron and synchrotron diffraction studies at 700°C, where this phase crystallizes. This provides the unit cell parameters, atomic positions, anisotropic thermal parameters and occupancies of all the atoms revealed by Rietveld refinement, which gives the actual chemical composition i.e.  $\text{CaSi}_{0.33}\text{B}_{0.66}\text{O}_{2.66}$  (or  $\text{CaSi}_{1/3}\text{B}_{2/3}\text{O}_{8/3}$ ). The refined structure is composed of one Ca, one Si/B mixed and three inequivalent O atoms and consists of linear chains (Figure E.9). It reveals the nature of distorted tetrahedra occupied by 1/3 (0.34 (3)) silicon and 2/3 (0.66(3)) boron atoms and are interconnected exclusively by O3 oxygen atoms, which according to Rietveld refinement of neutron powder diffraction data have a partial occupancy (0.67) in the unit cell. This shows that local crystal structure of  $\text{CaSi}_{1/3}\text{B}_{2/3}\text{O}_{8/3}$  phase contains finite chains along the *c* axis. The mixed Si/B composition and the partial occupancy of O3 oxygen atom lead to the ambiguities regarding the molecular structure at the local level. The solid-state NMR measurements, particularly the  $^{11}\text{B}$  and  $^{29}\text{Si}$  MAS NMR experiments probe the extent of B and Si molecular order at the local level.

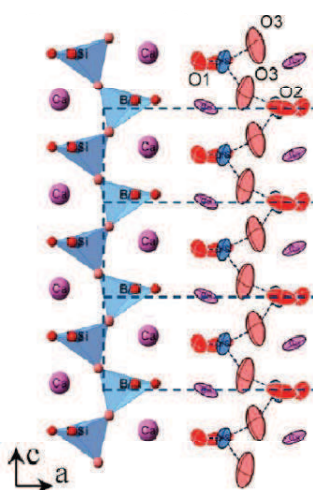


**Figure E.9** Average long range structure of  $\text{CaSi}_{1/3}\text{B}_{2/3}\text{O}_{8/3}$  phase proposed by diffraction measurements.

For example, as shown in the Figure E.10a, the  $^{11}\text{B}$  echo-MAS NMR spectrum determines the coordination state of the B atoms. The spin quantum number of  $^{11}\text{B}$  nucleus is  $3/2$  (quadrupolar nuclei). Hence, the observed  $^{11}\text{B}$  peak in the NMR spectrum reflects the signature of a second-order quadrupolar line shape. The Dmfit<sup>210</sup> program was used to simulate (Fig. E10a, in red) the  $^{11}\text{B}$  MAS spectrum to extract the isotropic  $^{11}\text{B}$  shift, quadrupolar coupling and the asymmetry parameter ( $\eta_Q$ ). The isotropic chemical shift:  $19.5 \pm 0.2$  ppm, quadrupolar coupling constant (QCC):  $2.62 \pm 0.05$  MHz and asymmetry parameter: 0.51, establish that the observed peak corresponds to a trigonal  $\text{BO}_3$  environment. The non-isotropic symmetry of  $\text{BO}_3$  units is related by large quadrupolar couplings accounting for anisotropic charge distribution and electric field gradient (EFG).<sup>255-256</sup>

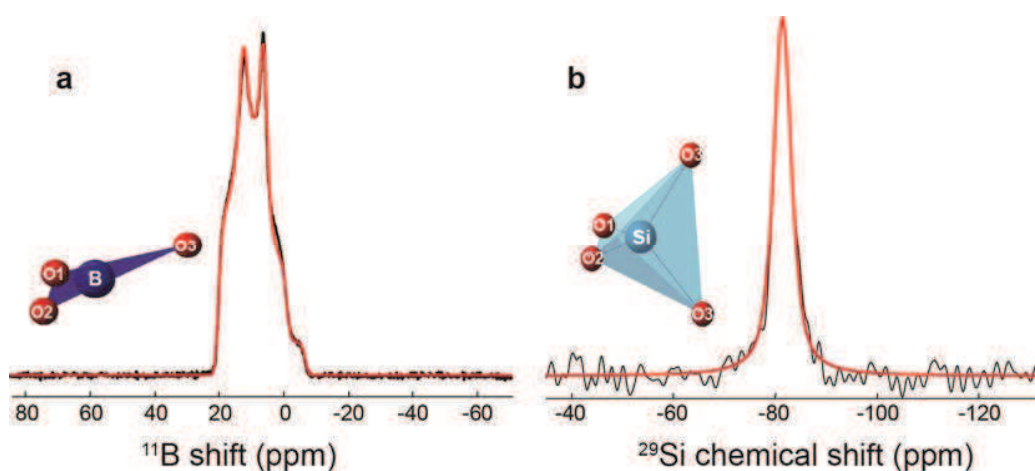


**Figure E.10** Solid-state NMR (a)  $^{11}\text{B}$  echo-MAS, (b)  $^{29}\text{Si}$  single-pulse spectra of  $\text{CaSi}_{1/3}\text{B}_{2/3}\text{O}_{8/3}$  (in black lines), collected at room temperature, at a magnetic field of 9.4 T (for  $^{11}\text{B}$  experiments) and 4.7 T (for  $^{29}\text{Si}$  experiments). Simulated Dmfit models are shown in red.

The asymmetry parameter further demonstrates the extent of deviation of EFG tensor from axial symmetry. In the present case, the value  $\eta_Q = 0.51$  suggests that  $\text{BO}_3$  units are connected to one or two other crystallographic sites via non-bridging oxygen atoms (NBO)<sup>257-258</sup> rather than isolated  $\text{BO}_3$  units (with 3 NBO's). This is also consistent with the  $\eta_Q$  for asymmetric  $\text{BO}_3$  units reported by Kriz et.al, in 1971, however for symmetric  $\text{BO}_3$  units it would be smaller than 0.3.<sup>259</sup> Computation of these data with the average long-range structure, where all B/Si sites have two non-bridging O atoms with full occupancy, it becomes clear that the  $\text{BO}_3$  units terminate the chains parallel to the c-axis. Each B atom contains an oxygen vacancy at one of the surrounding O3 oxygen sites along the chain. Therefore, the chain along the c-axis probably consists of  $\text{O}_2\text{B-O-BO}_2$ ,  $\text{O}_2\text{B-O}[\text{Si}(\text{O}_2)_n\text{-O}]\text{BO}_2$ , where  $n \geq 1$ . For simplicity, the chain is denoted as B-B, B-Si-B, B-Si-Si-B etc thereafter.

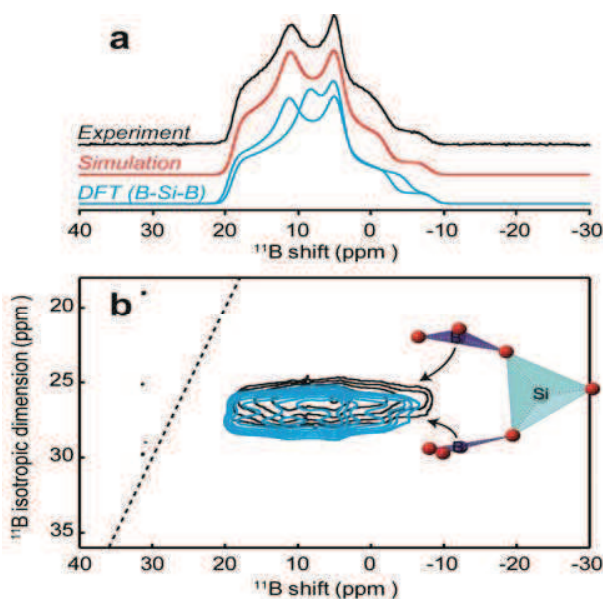


**Figure E.11** Solid-state NMR  $^{11}\text{B}$  multiple-quantum (MQ)-MAS of  $\text{CaSi}_{1/3}\text{B}_{2/3}\text{O}_{8/3}$ , collected at room temperature, at a magnetic field of 9.4 T. The spectrum is simulated (in red) by Dmfit program. The signature of  $^{11}\text{B}$  environments predicted with DFT calculations from local structural models containing “B-Si-B” units are shown in blue.

The Dmfit models of 1D  $^{11}\text{B}$  MAS NMR spectrum already suggest the presence of one type of  $\text{BO}_3$  environments. However, the model includes a broadening parameter that indicates a distribution of slightly distinct environments which we seek to understand. Such ambiguities can in principle be resolved by increasing the resolution, for example by collecting 2D multiple-quantum magic angle spinning (MQ-MAS) NMR spectrum.<sup>127</sup> In general, the half integer nuclei possess large quadrupolar interactions that include 1<sup>st</sup> order and 2<sup>nd</sup> order quadrupolar coupling. The 1<sup>st</sup> order quadrupolar interactions can be averaged by spinning the sample at the magic angle but the later fails to average the 2<sup>nd</sup> order quadrupolar interactions. The main reason behind the MQ-MAS experiment is averaging the 2<sup>nd</sup> order quadrupolar couplings, which shows highly resolved correlations in the indirect dimension, where the line width of each signal may be comparable to those observed for the spin  $\frac{1}{2}$  nuclei. This often makes it possible to distinguish different otherwise overlapping chemical environments on the basis of differences of isotropic chemical shift, quadrupolar coupling and asymmetry parameters. Figure E.11 shows the  $^{11}\text{B}$  MQ-MAS NMR spectrum of  $\text{CaSi}_{1/3}\text{B}_{2/3}\text{O}_{8/3}$  phase, collected at room temperature by spinning the sample at 10 kHz at a magnetic field of 9.4 T (black). The corresponding 2D NMR spectrum is simulated by a single peak using the Dmfit program with same NMR parameters that used to model the 1D MAS  $^{11}\text{B}$  echo-MAS spectrum (Fig. E.11a), although with a distribution  $^{11}\text{B}$  shifts in particular reveals the extent of variability in the local bonding geometry and/or the inter-chain arrangements. Because the position of the 2D

correlation peaks in the MQ-MAS NMR spectrum strongly depends on the NMR parameters such as  $\delta_{iso}$ ,  $C_Q$  and  $\eta_Q$ , such good fitting (Fig. E.11, red) obtained with a single peak confirms that only a single type of B environments is present. This ultimately suggests that the chain along the  $c$ -axis is composed of only B-Si-B units.

The  $^{29}\text{Si}$  MAS NMR spectrum collected at room temperature, as shown in the Figure E.10b depicts the nature of Si environments coordinated in the chain along the  $c$  axis. The presence of a single peak at -81 ppm points to a single type of  $^{29}\text{Si}$  environment present in the  $\text{CaSi}_{1/3}\text{B}_{2/3}\text{O}_{8/3}$  phase although its broadening of the spectrum reflects a distribution of  $^{29}\text{Si}$  environments. This is consistent with previous assignment made by  $^{11}\text{B}$  echo-MAS and  $^{11}\text{B}$  MQ-MAS NMR spectrum, that  $\text{CaSi}_{1/3}\text{B}_{2/3}\text{O}_{8/3}$  phase contains finite chains consisting of only B-Si-B units. Therefore, it confirms that each Si atom is connected to two three-coordinated B atoms via bridging oxygen atoms that can be denoted as Si (2B). Yet, the slight broadening at the bottom of  $^{29}\text{Si}$  MAS spectrum accounts to the deterioration of molecular order caused by variation in bonding geometries or differed inter-chain arrangements, which we seek to understand.

### ***E.3.3 $\text{CaSi}_{1/3}\text{B}_{2/3}\text{O}_{8/3}$ phase with $^{29}\text{Si}$ enrichment***

Advanced multi-pulse NMR experiments were performed in order to investigate the extent of local molecular order mainly affected by the inter chain arrangements. Performing these NMR experiments for the material with natural abundance  $^{29}\text{Si}$  is challenging (4.7%), since these experiments face sensitivity problems. In this context, the calcium borosilicate material ( $\text{CaSi}_{1/3}\text{B}_{2/3}\text{O}_{8/3}$  phase) was synthesized with 100% isotopic  $^{29}\text{Si}$  enrichment (one time crystallization at 650°C for 2 hours and quenched in water) to execute the advanced multi-pulse  $^{29}\text{Si}$  NMR experiments. The  $^{29}\text{Si}$  enrichment may leads to different behavior at the local level, which could be well established by solid-state NMR. The intention of these  $^{29}\text{Si}$  experiments is to establish the nature of  $^{11}\text{B}$  environments with respect to  $^{29}\text{Si}$  species confined within the chain along the  $c$  axis. As shown in the Figure E.13a, the  $^{29}\text{Si}$  echo-MAS NMR spectrum of  $^{29}\text{Si}$  enriched  $\text{CaSi}_{1/3}\text{B}_{2/3}\text{O}_{8/3}$  phase consists of two peaks. The  $^{29}\text{Si}$  peak at -81 ppm corresponds to the  $^{29}\text{Si}$  environments of the desired phase, which exhibits similar features as observed in the  $^{29}\text{Si}$  natural abundance material (Figure E.13e). However, the  $^{29}\text{Si}$  peak marked with a red star (at -76 ppm) reveals the existence of additional phase in the as-synthesized material, which could be assigned to an impurity. The line width of the corresponding  $^{29}\text{Si}$  peak is  $\approx 8$  ppm, in contrast with the  $^{29}\text{Si}$  peak at -81 ppm (FWHM  $\approx 4$  ppm) points to the amorphous nature of this phase. Moreover, the  $^{29}\text{Si}$  peak at -76 ppm may correspond to the  $Q^1$   $^{29}\text{Si}$  species, which indicates the availability of poorly polymerized  $^{29}\text{Si}$  tetrahedra. The difference between the amorphous and crystalline part of the material was well

understood by collecting a series of  $^{29}\text{Si}$  echo-MAS NMR experiments as a function of recycling delay. As shown in the Figure E.12 (plot of intensity v/s recycling delay), the red and green curves corresponds to the  $^{29}\text{Si}$  peak at -76 and -81 ppm, respectively. The maximum intensity of the  $^{29}\text{Si}$  peak at -76 ppm found to be almost stable beyond the recycling delay at 600 s. However, the intensity of the  $^{29}\text{Si}$  peak at -81 ppm is still increasing even beyond 600s recycling delay. Such a contrast in longitudinal relaxation ( $T_1$ ) delays is closely related to the extent of crystallinity in the two phases contained in the sample. The  $^{29}\text{Si}$  environments corresponding to the peak at -76 ppm have faster  $T_1$  relaxation rates than that of  $^{29}\text{Si}$  peak at -81 ppm, as shown in the Figure E.12, which supports the assignment of the former to an amorphous phase (indeed impurity), whereas the later is the crystalline  $\text{CaSi}_{1/3}\text{B}_{2/3}\text{O}_{8/3}$  phase. As mentioned before, most of the NMR experiments were collected with longer recycling delays accounting to the longer  $T_1$  relaxation rates of  $\text{CaSi}_{1/3}\text{B}_{2/3}\text{O}_{8/3}$  phase. This allows quantifying the relative composition of different  $^{29}\text{Si}$  environments. The amorphous phase is indicated by gray color and the crystalline phase is indicated by yellow color in the Figure E.13.

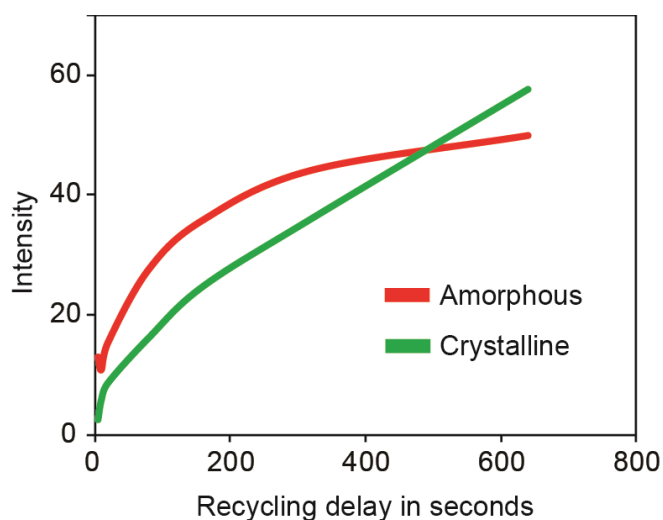


**Figure E.12** Plots of intensity v/s recycling delay of  $^{29}\text{Si}$  enriched  $\text{CaSi}_{1/3}\text{B}_{2/3}\text{O}_{8/3}$  phase extracted from series  $^{29}\text{Si}$  echo-MAS NMR spectrum as a function of recycling delay collected at a magnetic field of 9.4 T.

The nature of local molecular arrangement in the X-phase could also be established by probing the interactions between B and Si atoms. For example, the Figure E.13b shows the  $^{29}\text{Si}$  [ $^{11}\text{B}$ ] CP-MAS NMR spectrum of  $^{29}\text{Si}$  enriched  $\text{CaSi}_{1/3}\text{B}_{2/3}\text{O}_{8/3}$  phase. The idea of this experiment is to transfer the magnetization from  $^{11}\text{B}$  nuclei to the  $^{29}\text{Si}$  nuclei to reveal the interactions between  $^{29}\text{Si}$  and  $^{11}\text{B}$  species. Since the pulse sequence follows the excitation of  $^{11}\text{B}$  nuclei, the signal could be acquired with short recycling delay (1 second). This is because  $^{11}\text{B}$  is a quadrupolar nucleus (and high  $\gamma$  nuclei), which

possesses faster relaxation rates such that a short recycling delay allows to start with full  $^{11}\text{B}$  magnetization. As shown in the Figure E.13b, as expected the peak at -81 ppm contains similar spectral features as the  $^{29}\text{Si}$  peak obtained in the  $^{29}\text{Si}$  echo-MAS NMR spectrum. This confirms that all of the  $^{29}\text{Si}$  species in the crystalline  $\text{CaSi}_{1/3}\text{B}_{2/3}\text{O}_{8/3}$  phase are located next to the  $^{11}\text{B}$  species. A small contribution from the amorphous phase was again identified in the spectrum at -76 ppm, but it is comparatively weaker than in the echo-MAS spectrum. This may indicate a relative low B content in this additional phase a correspondingly small probability of B-Si proximities.

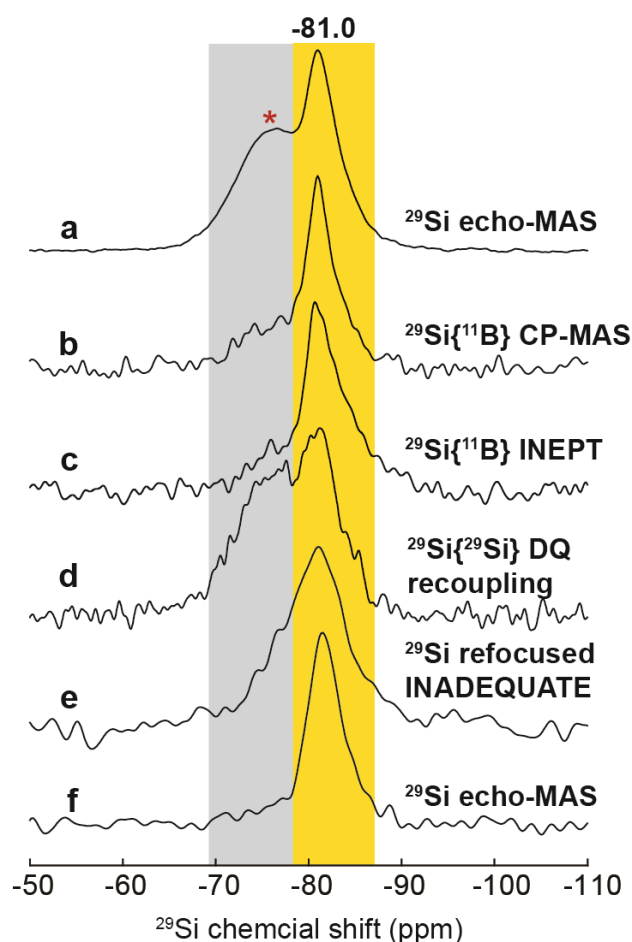


**Figure E.13** Solid-state NMR spectra of  $^{29}\text{Si}$  enriched  $\text{CaSi}_{1/3}\text{B}_{2/3}\text{O}_{8/3}$  phase collected at a magnetic field of 9.4 T. (a)  $^{29}\text{Si}$  echo-MAS NMR spectrum ( $d1 = 3600\text{s}$ ,  $ns = 4$ , 12.5 kHz MAS), (b)  $^{29}\text{Si}\{^{11}\text{B}\}$  CP-MAS NMR spectrum ( $d1 = 1\text{s}$ ,  $ns = 64$ , 18 kHz MAS), (c)  $^{29}\text{Si}\{^{11}\text{B}\}$  INEPT NMR spectrum ( $d1 = 8\text{s}$ ,  $ns = 7424$ , 18 kHz MAS), (d)  $^{29}\text{Si}\{^{29}\text{Si}\}$  DQ recoupling NMR spectrum ( $d1 = 3600\text{s}$ ,  $ns = 4$ , 8 kHz MAS). (e)  $^{29}\text{Si}$  refocused-INADEQUATE NMR spectrum ( $d1 = 3600\text{s}$ ,  $ns = 4$ , 12.5 kHz MAS) and (f)  $^{29}\text{Si}$  echo-MAS NMR spectrum of  $\text{CaSi}_{1/3}\text{B}_{2/3}\text{O}_{8/3}$  phase (with natural abundance  $^{29}\text{Si}$ ) collected at a magnetic field of 4.7T (same spectrum, Fig. E.10b).

Similarly, the  $^{29}\text{Si}$  [ $^{11}\text{B}$ ] Inensitive Nuclei Enhanced by Polarisation Transfer (INEPT)<sup>260-261</sup> NMR experiment reveals the extent of bonding interaction between the  $^{29}\text{Si}$  and  $^{11}\text{B}$  species. The idea of this experiment is very similar to the  $^{29}\text{Si}$  [ $^{11}\text{B}$ ] CP-MAS NMR experiment, however, the polarisation is transferred through chemical bonds from  $^{11}\text{B}$  to  $^{29}\text{Si}$  species via heteronuclear  $^{11}\text{B}$ -O- $^{29}\text{Si}$   $J$ -couplings. As shown in the Figure E.13c, the  $^{29}\text{Si}$  [ $^{11}\text{B}$ ] INEPT NMR spectrum shows a single  $^{29}\text{Si}$  peak at -81 ppm, which can be identified with the same spectral features that observed in the previous NMR measurements (Figure E.13a, E.10b). For example the relative intensity and the line shapes are almost identical to the  $^{29}\text{Si}$  [ $^{11}\text{B}$ ] CP-MAS NMR spectrum. This expands the understanding of molecular arrangements between  $^{29}\text{Si}$  and  $^{11}\text{B}$  units and confirms that all the  $^{29}\text{Si}$  species of the crystalline phase are connected with the trigonal  $\text{BO}_3$  units.

Furthermore, multi-pulse solid-state NMR measurements are capable of probing specifically the spatial or bonding interactions between the  $^{29}\text{Si}$  species within the crystallographic chain. This ultimately provides the local view of molecular arrangement associated with longer chain (B-Si-Si-B units or longer). For example, the  $^{29}\text{Si}$  [ $^{29}\text{Si}$ ] DQ recoupling NMR<sup>175,182</sup> spectrum is collected to probe the spatial proximities between the Si atoms. In fact, the homonuclear  $^{29}\text{Si}$ - $^{29}\text{Si}$  dipolar couplings (a measure of spatial interactions) between Si atoms have been averaged by spinning the sample at the magic angle. Hence, the symmetry based rotor-synchronized SR26<sub>4</sub><sup>11</sup> recoupling pulses were applied to reintroduce the homonuclear  $^{29}\text{Si}$ - $^{29}\text{Si}$  dipolar couplings (See Chapter B for experimental details). The Figure E.13d, represents the  $^{29}\text{Si}$  [ $^{29}\text{Si}$ ] DQ recoupling NMR spectrum collected at a recoupling duration of 6 ms. The  $^{29}\text{Si}$  peaks reveal the signature of spatially coupled Si atoms, no matter whether the  $^{29}\text{Si}$  species connected to each other or not. The  $^{29}\text{Si}$  peak at -81 ppm (yellow part) stands for the crystalline  $\text{CaSi}_{1/3}\text{B}_{2/3}\text{O}_{8/3}$  phase and the  $^{29}\text{Si}$  peak at -76 ppm (the gray part) corresponds again to the amorphous phase. In addition, the  $^{29}\text{Si}$ -O- $^{29}\text{Si}$  connectivities in the crystalline phase have been established by collecting  $^{29}\text{Si}$  refocused INADEQUATE NMR spectrum, as shown in the Figure E.13e. The echo-duration in the corresponding experiment is 44 ms, which point to the small  $^2J$   $^{29}\text{Si}$ -O- $^{29}\text{Si}$  couplings. A strong  $^{29}\text{Si}$  peak at -81 ppm reveals the signature of crystalline phase (yellow part). A small contribution from the amorphous phase (gray part) has also been observed. These two NMR experiments, probing the spatial proximities and connectivities between the  $^{29}\text{Si}$  species suggest the possibility of having a small amount of B-Si-Si-B units in the crystalline phase (less than 13%). Moreover, the INADEQUATE experiment indicates that B-Si-Si-B units show up at the same  $^{29}\text{Si}$  position as B-Si-B units. This is in contradiction with assignment made on the basis of  $^{11}\text{B}$  MAS and  $^{11}\text{B}$  MQ-MAS NMR measurements that, the crystalline material contains only B-Si-B units. In case, if the crystalline phase contains B-Si-Si-B units, then there should also be B-B units in the chain to maintain the global  $\text{CaSi}_{1/3}\text{B}_{2/3}\text{O}_{8/3}$  composition. These different  $^{11}\text{B}$

environments of B-Si-Si-B and B-B units could be expected to be clearly identified in the  $^{11}\text{B}$  MQ-MAS NMR spectrum, in the natural  $^{29}\text{Si}$  abundance material. However, the  $^{11}\text{B}$  MQ-MAS NMR spectrum shows the signature of one trigonal B atom that point to the presence of only B-Si-B units. Hence, the assignment still needs to be understood well, if we take into account the  $^{29}\text{Si}$  NMR experiments recorded on the  $^{29}\text{Si}$  enriched material (Figure E.13d and E.13e). However, the Dmfit model of 1D  $^{11}\text{B}$  MAS and  $^{11}\text{B}$  MQ-MAS spectrum of natural  $^{29}\text{Si}$  abundance  $\text{CaSi}_{1/3}\text{B}_{2/3}\text{O}_{8/3}$  phase suggest that the crystalline chain contains only B-Si-B units. The presence of B-Si-B or B-Si-Si-B units along the  $c$ -chain and the inter-chain arrangements is well established by DFT calculations.

### **E.3.3 Quantum chemical calculations of NMR parameters**

The DFT calculation of NMR parameters conducted on several possible borosilicate models further supports the interpretation made by  $^{11}\text{B}$  and  $^{29}\text{Si}$  MAS NMR experiments. As shown in the Figure E.14 and E.15, the DFT optimized models made a clear distinction between the local structure of  $\text{CaSi}_{1/3}\text{B}_{2/3}\text{O}_{8/3}$  phase consisting of  $\text{SiO}_4$  and  $\text{BO}_3$  units and the average structure predicted by powder X-ray and neutron diffraction data. The  $(\text{Si}_{1/3}\text{B}_{2/3})\text{O}_4$  tetrahedra is highly distorted (Fig E.15b), with large values of atomic displacement parameters, especially for the O3 oxygen (see the thermal ellipsoids in Fig E.15c). The calculated  $^{29}\text{Si}$   $\delta_{iso}$  and  $^{11}\text{B}$   $\delta_{iso}$ ,  $C_Q$  and  $\eta_Q$  and the respective calculated energies are summarized in Table 1.

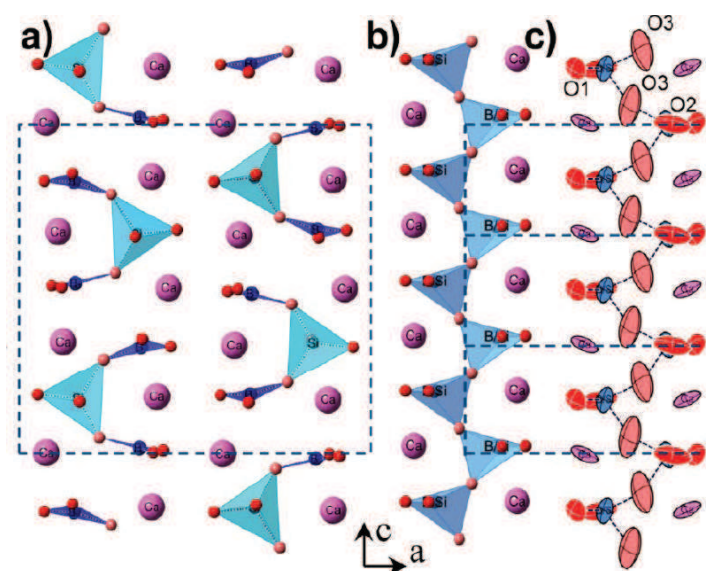


**Figure E.14** [Courtesy: Emmanuel Véron] Structural model of  $\text{CaSi}_{1/3}\text{B}_{2/3}\text{O}_{8/3}$  depicting the possible polyhedral arrangements along the  $c$  axis. (a) Average structure obtained by high-temperature powder diffraction structure determination, (b) average view of the proposed real structure represented on

several cells, explaining the high values of atomic displacement parameters, (c) thermal ellipsoids are drawn at the 50% probability level.

For the model containing B-Si-Si-B and B-B units (Fig E.15a), the calculated  $^{29}\text{Si}$  chemical shift of Si(1B) is -84.6 ppm, which is close to the  $^{29}\text{Si}$  chemical shift of Si(2B) moieties -84 ppm (Fig. E.15b). This suggests that the  $^{29}\text{Si}$  signal of such B-Si-Si-B units may overlap with the signature of B-Si-B units. The calculations confirm the absence of B-Si-Si-Si-B units, as the calculated  $^{29}\text{Si}$  chemical shift of  $Q^2$  (0B) found to be -87 ppm, which is not in good agreement with the experimental value. In fact, as mentioned before, the different intra-chain units, such as B-B or B-Si-B or B-(Si) $_n$ -B could be easily distinguished by comparing  $^{11}\text{B}$  MQ-MAS spectra simulated (with arbitrary intensities and broadening) based on the DFT-calculated  $^{11}\text{B}$  parameters. As shown in the Figure E.16, a large difference between the calculated (for models shown in Figure E.15, see also Table E.1) and experimental correlations confirms the absence of B-B (yellow) and B-Si-Si-B (red) units. Only the B-Si-B model (blue) whose calculated  $^{29}\text{Si}$  chemical shift (-84.1 and -83.9 ppm for models with different inter-chain arrangements) are in good agreement with the experimental spectrum (black) and confirms that the associated chains are composed of only B-Si-B units.

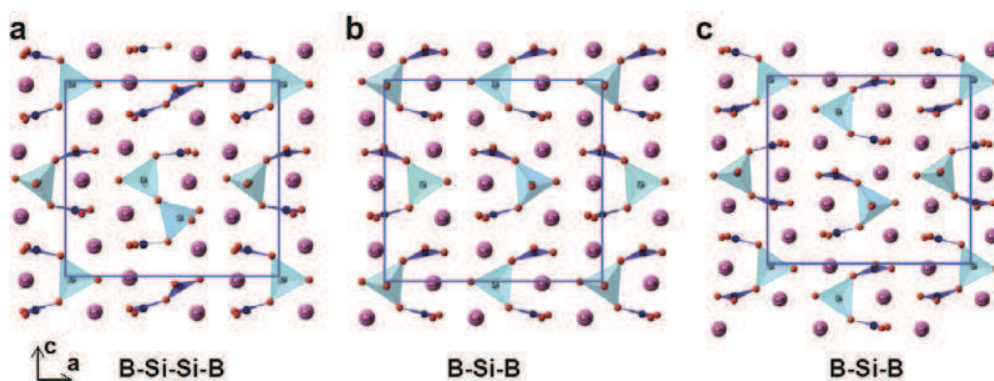


**Figure E.15** Structural model of  $\text{CaSi}_{1/3}\text{B}_{2/3}\text{O}_{8/3}$  depict the possible polyhedral arrangements along the  $c$  axis. (a) Borosilicate model showing B-Si-Si-B units, (b and c) Borosilicate models containing only B-Si-B units presenting different inter chain arrangements.

The calculated spectrum showed in the Figure E.11 (blue, also showed in the Figure E.16) corresponds to the B-Si-B units, for which the lowest energy is achieved. The calculated  $^{29}\text{Si}$  and  $^{11}\text{B}$  NMR parameters are also in good agreement with the experimental values. Notably, the models with B-Si-B units are just two simple examples of many possible inter-chain arrangements. All the models may co-exist in the structures at both room- and high-temperature, but  $^{11}\text{B}$  NMR data appear to be essentially

sensitive here to the type of local bonding unit and are unaffected by such differences in inter-chain arrangements.

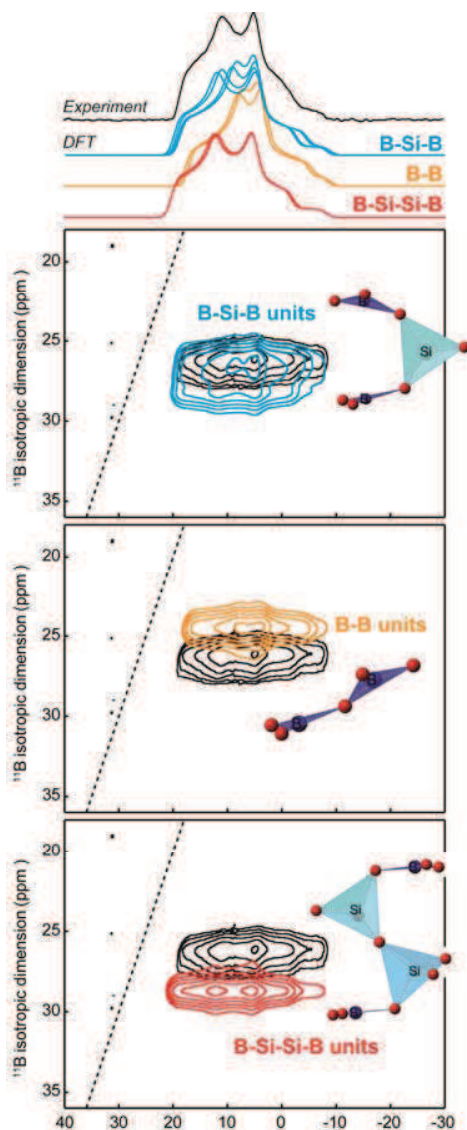


**Figure E.16**  $^{11}\text{B}$  MQ-MAS signatures calculated for a typical three-coordinated B environments described in the model of the  $\text{CaSi}_{11/3}\text{B}_{2/3}\text{O}_{8/3}$  showing B-Si-B (blue), B-B (yellow) and B-Si-Si-B (red) units. All these B environments are compared with the experimental MQ-MAS spectrum (in black, same in all plots). These simulated spectra are calculated from the average values of parameters calculated for all environments of a given type using the models shown Figures E.15. Calculated spectra are convoluted with Gaussian lines with full width at maximum (FWHM) of 4 ppm in the horizontal dimension and 2 ppm in the vertical dimension.

**Table E.1** NMR parameters calculated by DFT for models of the  $\text{CaSi}_{1/3}\text{B}_{2/3}\text{O}_{8/3}$  material.

Supercell	Calculated Energy (eV)	Local unit	$^{29}\text{Si}$ NMR parameters <sup>a</sup>		$^{11}\text{B}$ NMR parameters <sup>a</sup>		
			Site type	$\delta_{\text{iso}}$ (ppm)	$\delta_{\text{iso}}$ (ppm)	$C_Q$ (MHz)	$\eta_Q$
1x1x3 <sup>b</sup>	-27550.18	B-Si-B	Si(2B)	-83.9	20.0 ± 0.7	2.68 ± 0.06	0.58 ± 0.08
1x1x3 <sup>c</sup>	-27550.10	B-Si-B	Si(2B)	-84.2	19.9 ± 0.9	2.66 ± 0.06	0.62 ± 0.11
		B-B	-	N.A.	17.8 ± 0.3	2.55 ± 0.02	0.70 ± 0.08
1x1x3 <sup>c</sup>	-27549.93	B-Si-B	Si(2B)	-84.0 ± 0.5	20.0 ± 0.9	2.67 ± 0.08	0.60 ± 0.11
		B-Si-Si-B	Si(1B)	-84.6 ± 0.1	21.1 ± 0.1	2.74 ± 0.01	0.50 ± 0.02
1x1x6 <sup>c</sup>	-27549.74 <sup>d</sup>	B-Si-Si-Si-B	Si(2B)	-87.1			
			Si(1B)	-81.8 ± 2.1			
<b>Experimental<sup>e</sup></b>				-81(1)	19.5(2)	2.62(5)	0.51(1)

<sup>a</sup> Calculated NMR parameters are reported in the form  $a \pm b$ , where  $a$  is the average of the values calculated for all sites of a given type, and  $b$  is the standard deviation among these calculated values.

<sup>b</sup> Model shown in Figure E.14a, containing only B-Si-B units.

<sup>c</sup> Models shown in Figure E.15, B-B, B-Si-B, B-Si-Si-B units

<sup>d</sup> Scaled down (by a factor of 2) to the energy per  $\text{Ca}_{12}\text{Si}_4\text{B}_8\text{O}_{32}$  unit for comparison with other systems.

<sup>e</sup> Estimated uncertainties for the experimental parameters are indicated in parenthesis.

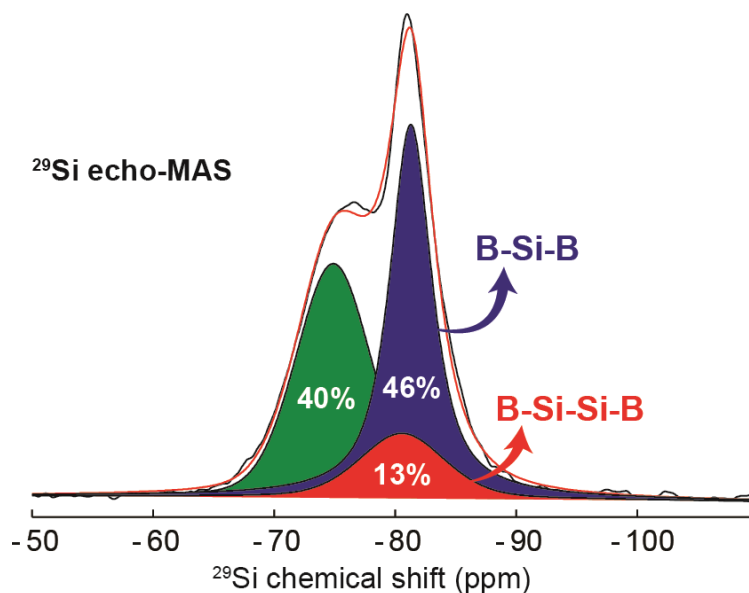


**Figure E.17**  $^{29}\text{Si}$  echo-MAS NMR spectrum of  $^{29}\text{Si}$  enriched  $\text{CaSi}_{1/3}\text{B}_{2/3}\text{O}_{8/3}$  phase deconvoluted by Dmfit program. The  $^{29}\text{Si}$  peak in red is extracted from the  $^{29}\text{Si}$  refocused-INADEQUATE NMR spectrum (Fig. E.13e) points to B-Si-Si-B units,  $^{29}\text{Si}$  peak in blue corresponds to B-Si-B units and peak in green corresponds to the amorphous phase.

Solid-state NMR measurements of  $^{29}\text{Si}$  natural abundance and DFT calculation results confirm the presence of only B-Si-B units along the *c*-chain. Calculations also suggest that B-Si-Si-B  $^{29}\text{Si}$  parameters might very well overlap with B-Si-B  $^{29}\text{Si}$  signature, as shown experimentally with the  $^{29}\text{Si}$  INADEQUATE spectrum of  $^{29}\text{Si}$  enriched  $\text{CaSi}_{1/3}\text{B}_{2/3}\text{O}_{8/3}$  phase. As shown in Figure E.17, the  $^{29}\text{Si}$  echo-MAS NMR spectrum of  $^{29}\text{Si}$  enriched  $\text{CaSi}_{1/3}\text{B}_{2/3}\text{O}_{8/3}$  phase is simulated by Dmfit program with three contributions. The  $^{29}\text{Si}$  peak at -81 ppm corresponding to crystalline phase is fitted with two contributions, where the red signal is fixed that extracted from  $^{29}\text{Si}$  refocused-INADEQUATE NMR spectrum (both spectra were collected with same experimental condition) and the blue signal is allowed to fit. This shows that 13% of the total Si accounts to B-Si-Si-B units and 46% are B-Si-B units. These findings provide the following insights for future research to exploit why such a difference in contrast to the  $\text{CaSi}_{1/3}\text{B}_{2/3}\text{O}_{8/3}$  phase studied at natural abundance sample, where only B-Si-B units are present.

#### **E.4 Conclusion**

Structural insights, at the local level, around heteroatoms in other types of materials are successfully revealed by using an approach somewhat similar to the case of the surfactant-directed layered silicates, with the combination of solid-state NMR and DFT calculations also playing a central role. Atomic substitutions indeed have great impact in many materials on the neighboring chemical environment, which may sometimes be turned into a probe of the amount or type of substitution. For example, the substitutions of Al by Mg atoms in the octahedral layer and of Si by Al atoms in the tetrahedral layers of montmorillonite are established by  $^{29}\text{Si}$ ,  $^{27}\text{Al}$  and  $^1\text{H}$  NMR. Notably, a clear distinction between  $\text{Al}_2\text{OH}$  and  $\text{AlMgOH}$  moieties revealed in  $^1\text{H}$  NMR is the key to our ability to describe the distributions of Al and Mg atoms in the octahedral layer. This Mg/Al distribution is found to be non-random, and appears to be driven by an avoidance of Mg-O-Mg pairs in favor of Al-O-Mg or Al-O-Al pairs. Spectral editing NMR experiments are particularly useful to probe the nature of different chemical environments within the octahedral and tetrahedral layers.

In a second example focusing on the new calcium borosilicate phase  $\text{CaSi}_{1/3}\text{B}_{2/3}\text{O}_{8/3}$ , the average long-range structure established by diffraction data seems to be disordered. When we push the structure determination to the local level by solid-state NMR, it is quite interesting to see that the structure is in fact composed of a single type of well-organized molecular unit. One-dimensional  $^{11}\text{B}$ ,  $^{29}\text{Si}$  and 2D  $^{11}\text{B}$  MQ-MAS NMR and DFT calculations demonstrate that the  $\text{CaSi}_{1/3}\text{B}_{2/3}\text{O}_{8/3}$  phase is essentially based on B-Si-B units with different inter-chain arrangements. These different arrangements of B-Si-B units ultimately result in what may be interpreted as disorder in the long-range structure, but the strongly localized point of view is essentially insensitive to this longer-range structure and provides a well-ordered local description of the material.

---

## ***Conclusions and Perspectives***

---

The main objective of this thesis is to understand what controls, at the molecular level, the distribution of heteroatoms into silicate materials, and how their incorporation modifies their otherwise molecularly-ordered frameworks. Only by obtaining a clear understanding of these fundamental structural can we hope to establish the structure-property relationship that will ultimately make it possible to rationally design new silicate-based catalysts. Several experimental techniques were used to address the difficult problematic of describing the local structural disorder around heteroatom sites, among which advanced solid-state NMR experiments, in combination with DFT calculations, played a decisive role. Al and B heteroatoms were incorporated into two strongly related layered silicates materials directed by  $C_{16}H_{33}Me_2EtN^+$ - and  $C_{16}H_{33}Me_3N^+$  surfactant molecules, respectively.<sup>22-24</sup> The insertion of such these heteroatoms into the layered silicate framework led to profound changes in the local structures, which nevertheless retained both the high extents of long-range lamellar order (probed by SAXS) and smaller extent of long-range molecular order (probed by SAXS) of their siliceous analogs. However, additional reflections in WAXS pattern of layered aluminosilicates at high aluminum content reveals that the global symmetry may very well be lost given the range of distortions associated with the cross-linking. In the case of boron incorporation, the resulting deterioration of the short-range molecular order cannot be detected in the WAXS pattern. While B atoms are significantly smaller than Si atoms, which in zeolites causes a reduction of the unit cell parameters proportional to the amount of B/Si substitution,<sup>109</sup> the maximum B loading attained here (Si/B = 60-140) is too small to give rise to detectable modifications of the poorly resolved WAXS pattern of these non-crystalline materials.

This lack of long-range crystallinity is not a limitation in solid-state NMR, whose local point of view provided crucial insights into the local structures around B and Al heteroatoms incorporated in the frameworks of  $C_{16}H_{33}Me_3N^+$ - and  $C_{16}H_{33}Me_2EtN^+$ - layered silicates. The alkyl-ammonium surfactants play a central role in these materials, both as templating and structure-directing agents to achieve mesoscopic and molecular order, respectively. These surfactants furthermore likely interact with the incorporated heteroatoms, since they can potentially compensate the negative charge resulting from the

## Conclusions and Perspectives

substitution of a tetravalent Si atom by a trivalent heteroatom. The other type of possible charge-compensating species are H<sup>+</sup>, which can be present as Brønsted acid Si-(OH)-B/Al sites or as silanols, BOH, or AlOH groups. These different possibilities were investigated by means of the <sup>11</sup>B transverse dephasing time measurements and heteronuclear correlation experiments probing the spatial proximities between <sup>1</sup>H and <sup>27</sup>Al or <sup>11</sup>B nuclei. This revealed the first remarkable differences between the local environments of Al and B incorporated in these materials. In the case of borosilicate materials, we were able to differentiate between B atoms incorporated in framework Q<sup>3</sup> and Q<sup>4</sup> sites. In the case of C<sub>16</sub>H<sub>33</sub>Me<sub>3</sub>N<sup>+</sup>-borosilicate, the boron is incorporated in both Q<sup>3</sup> and Q<sup>4</sup> sites, all of which giving rise to a well-identified <sup>11</sup>B NMR signature. In the case of C<sub>16</sub>H<sub>33</sub>Me<sub>2</sub>EtN<sup>+</sup>-borosilicates, in contrast, all B atoms are incorporated specifically in substitution of a single crystallographic Q<sup>3</sup> Si site. 2D NMR spectra shows the signature of B-OH moieties to compensate the charge of the Si/B substitution for both materials when the B is incorporated in a Q<sup>3</sup> site. The situation is completely different in the layered aluminosilicates, where though-space-mediated <sup>27</sup>Al-<sup>1</sup>H NMR spectra establish the absence of detectable Al-OH or Brønsted acidic sites, the charge compensation in these materials being ensured exclusively by the positively-charged alkylammonium surfactant molecules.

Another remarkable difference between the effects of Al and B incorporated in the same two layered silicate materials is the considerably larger extent of deterioration of the local structure caused by insertion of Al than B heteroatoms. This was established by multi-dimensional solid-state NMR experiments probing spatial proximities and connectivities between Si and Al or B atoms which selectively reveal the local environments around the incorporated heteroatoms, even at low heteroatom content. The large distribution of chemical shifts in both <sup>29</sup>Si and <sup>27</sup>Al dimensions for the C<sub>16</sub>H<sub>33</sub>Me<sub>2</sub>EtN<sup>+</sup>-aluminosilicate material in particular reflect the local disorder around Al atoms. The spatial interactions between Si atoms of disordered region around Al atoms and the molecularly-ordered “Al-free” regions located away from perturbation range of the incorporated Al were measured in <sup>29</sup>Si[<sup>29</sup>Si] correlation NMR experiments. They provide further confirmation that Al atoms are indeed incorporated into a well-ordered lamellar silicate material and have non-selective incorporation behavior. May be most importantly, the reduced number or absence of Q<sup>3</sup>(1Al) contributions in the <sup>27</sup>Al-<sup>29</sup>Si correlation experiments indicates that the incorporation of Al atoms modifies locally the silicate framework in such a way that the Al atoms are connected with only Q<sup>4</sup> Si sites, in contradiction with the well-known connectivity network of the siliceous analog (or of the “Al-free” regions of the layered aluminosilicates).

A similar type of structural modification also takes place in the case of the C<sub>16</sub>H<sub>33</sub>Me<sub>3</sub>N<sup>+</sup>-aluminosilicate material, whose simpler <sup>29</sup>Si MAS NMR signature makes it possible to understand in depth this phenomenon. Specifically, quantitative <sup>29</sup>Si MAS NMR spectra recorded for different Al

## Conclusions and Perspectives

contents present clear NMR signatures pointing to these structural rearrangements by means of relative populations of  $Q^n(mAl)$  contributions that are all spectrally-resolved. Models in which Al atoms are directly incorporated in either site without further modification of the framework predict numbers of incompletely-condensed  $Q^3$  and  $Q^3(1Al)$  species well above the experimental results. This led us to examine models where the incorporation of an Al atom is systematically associated with a condensation of two nearby  $Q^3$  sites (if Al is incorporated in a  $Q^4$  site) or of the Al and an adjacent  $Q^3$  Si site (if Al is incorporated in a  $Q^3$  site). While still imperfect, these models yield considerably improved agreement with the experimental  $^{29}Si$   $Q^n(mAl)$  populations, which strongly supports the hypothesis of a local condensation of the framework upon Al incorporation that was made for the other aluminosilicate material. Furthermore, the absence in both materials of charge-compensating Al-OH or Al-OH-Si species is another indication of such a structural rearrangement, since the condensation of two adjacent  $Q^3$  sites reduces the negative charge of the framework (by  $2e$ ), which makes it unnecessary for the Al/Si charge deficit to be compensated by a  $H^+$ .

This type of structural rearrangement occurs in only one of the borosilicate materials: the  $C_{16}H_{33}Me_3N^+$ - directed material, where B is incorporated non-specifically at different crystallographic site. And even in this material it does not occur systematically. In the majority of cases the B atom is in a  $Q^3$  environment with the charge deficit compensated by a BOH (or potentially a B-(OH)-Si) moiety and no detectable evidence of local framework condensation around this site. One particular  $^{11}B$  NMR peak assigned to B incorporated in a  $Q^4$  site, however, shows the absence of  $Q^3(1B)$  neighbor and of charge-compensating  $H^+$  nearby, which are both strong evidence that a cross-linking occurs upon incorporation of B at this site.

The case of the  $C_{16}H_{33}Me_2EtN^+$ - directed layered borosilicates silicates is thus remarkable in several respects. In contrast to the other borosilicate material and the two aluminosilicates, the B heteroatoms are clearly incorporated in a single crystallographic  $Q^3$  site (out of the two distinct  $Q^3$  and three distinct  $Q^4$  present in the framework) without further re-arrangement of the framework, a conclusion that was further supported by DFT calculations of  $^{11}B$  chemical shifts. The charge Si/B deficit is compensated in this case by the formation of a BOH group. The sharp NMR signatures in 1D and 2D  $^{11}B$  and  $^{29}Si$  correlation experiments indicate that the local structural effects of B atoms on neighboring  $^{29}Si$  environment are identical throughout this sample. These “defected” B sites, which are well isolated from each other given the low B loading, are thus in fact molecularly-ordered, although they lack the periodicity of a crystalline environment.

## *Conclusions and Perspectives*

Because all surfactant-directed materials were prepared in identical synthesis conditions, with very similar surfactant molecules, such a marked contrast in the consequences of the B or Al incorporation on the local structure raises many questions. Few hypothetical reasons in this respect corroborate why there has been preferential incorporation in one material and not in the other.

Because all surfactant-directed materials were prepared in identical synthesis conditions, with very similar surfactant molecules, such a marked contrast in the consequences of the B or Al incorporation on the local structure raises many questions. First, a few hypothetical reasons may be formulated to explain why there has been preferential incorporation in one borosilicate material and not in the other. The presence of B atoms with a significantly smaller size than the Si atom they replace is expected to create a certain amount of stress in the silicate framework, which must relax (through variations in the bonding geometry) to attain a stable conformation. This mechanism depends on the availability of sufficient degrees of freedom. In this context,  $C_{16}H_{33}Me_2EtN^+$ - material with 2/5 of  $Q^3$  sites is slightly more condensed than the  $C_{16}H_{33}Me_3N^+$ - material, which contains 50% of  $Q^3$  sites, which somehow seems to force the B atoms to be located in a single T site that can accommodate more easily than others such variations. The slightly more condensed framework of the  $C_{16}H_{33}Me_2EtN^+$ - material, in particular, it does not seem to allow the additional cross-linking that occurs in some cases for the other borosilicate (or systematically in the alumino-silicate materials). Another possible reason for such differences is the different ways in which the linear chains formed by the  $Q^3$  sites and their non-bridging oxygen atoms are arranged in the two different framework structures. These chains are aligned in the same direction above and below the plane in the  $C_{16}H_{33}Me_2EtN^+$ - material, whereas in  $C_{16}H_{33}Me_3N^+$ - material the chains of  $Q^3$  sites located on the top and bottom sides of each layer are perpendicular to each other. Possibly as a result of this difference, the lamellar structure of the  $C_{16}H_{33}Me_2EtN^+$ - material appears to be unable to bend such as to accommodate for a cross-linking, for example between the B atom and a nearby Si atom, whereas this can happen in some cases for the  $C_{16}H_{33}Me_3N^+$ - material.

The different consequences of the incorporation of Al or B heteroatoms in one given material are also striking. The main reasons for such discrepancies are most likely differences in atomic size (B = 0.88 Å, Al = 1.43 Å) and electronegativity: 1.61 for Al and 2.04 for B, closer to the value of Si: 1.9, which causes the B-O linkage in a B-O-Si sequence to be less polar as compared to the Al-O bond. Either or both differences may be used to explain why cross-linking is systematically observed for each Al incorporated in either material, whereas it never happens for B incorporated in the  $C_{16}H_{33}Me_2EtN^+$ - material and only in some cases in the other. The larger size of Al atoms as compared to B reduces the extent to which the framework needs to bend to accommodate for an additional cross-linking. Along the same line, it seems reasonable that the smaller size of the B atom may promote in favorable cases

## *Conclusions and Perspectives*

preferential incorporation in  $Q^3$  sites, since, being less-condensed, these sites have more degrees of freedom than  $Q^4$  sites to accommodate for the smaller size of the B atom. Finally, the similar polarities of B-O and Si-O bonds may explain why the B atom may “like” to sit in a  $Q^3$  site (as a B-OH unit) and to be connected via bridging O atoms to other  $Q^3$  Si sites, just like Si atoms in the siliceous framework, whereas this situation is unfavorable for Al atoms.

Such an analysis of the factors governing the respective incorporation behavior of B and Al atoms in the two surfactant-directed materials studied in this work could not have been possible without the combination of state-of-the-art multi-dimensional NMR techniques and methodologies and DFT calculations. They provide the keys to the deep understanding of Al and B heteroatom distributions in these molecularly-ordered layered silicates, even in the absence of long-range 3D crystallinity. The presence of chemically different types ( $Q^3$  and  $Q^4$ ) of T sites in these materials makes it possible to achieve and demonstrate the selective incorporation of B heteroatoms at a unique crystallographic site in one material. This opens the way to future work in which these or other layered silicate frameworks with the B heteroatoms selectively incorporated at specific crystallographic site(s) could be condensed to form (by topotactic transformation) a 3D zeolite where the heteroatom location(s) could also be controlled (and established using the same experimental and modeling approach) as a result. The new class of catalysts designed in this manner would represent an important step in towards the ultimately goal sought by so many materials scientists for decades, with little success.

The approach developed for these layered boro-and alumino-silicate materials are further extended to the study of atomic substitution in other materials, to understand the distribution of heteroatoms, the local structures around them, or re-examine the materials chemical compositions. In the 2:1 clay mineral montmorillonites,<sup>262</sup> for instance, tetrahedral layers are composed of four-coordinated Si occasionally substituted by Al atoms, while the octahedral layer contains six-coordinated Al substituted by Mg atoms. These substitutions at the origin of the charge layer that provide this material with its tremendously important cation exchange capacity. Signatures of such different environments are established by detecting  $^{29}\text{Si}$ ,  $^{27}\text{Al}$ ,  $^{25}\text{Mg}$  and  $^1\text{H}$  nuclei, which sheds light onto the Mg/Al cation ordering in the octahedral layer. Most decisive in this work was our ability to measure the chemical compositions using the local point of view of solid-state NMR, and in particular  $^1\text{H}$  NMR at fast MAS and high magnetic fields in combination with DFT calculations. These quantification results show that the  $\text{Mg}^{2+}/\text{Al}^{3+}$  distribution in the octahedral layer of montmorillonite is governed by an avoidance of Mg-O-Mg pairs.

### *Conclusions and Perspectives*

In a second example, solid-state NMR provides important information, highly complementary to diffraction data, to establish the local structure of new crystalline calcium borosilicate phase ( $\text{CaSi}_{1/3}\text{B}_{2/3}\text{O}_{8/3}$ ) with mixed Si/B compositions and partial occupancies at some crystallographic site.<sup>263</sup> Such complications in the average long-range structure determined by in-situ high temperature diffraction studies may give the impression (at first sight) that this structure is in fact disordered in this respect. But in reality, at the local level, this situation is the result of the contributions of a single type of well-organized B-Si-B units differing only (at a scale longer than probed by NMR) by their inter-chain arrangements.  $^{29}\text{Si}$  and  $^{11}\text{B}$  NMR experiments and DFT calculations demonstrate the presence of such B-Si-B units. The findings from these studies discussed in this manuscript, the heteroatoms (mainly Al and B) distribution in novel materials, their influence on the local structure and possibly the long-range structure provide new understanding of their molecular level properties.

## References

1. Corma, A. *Chemical Reviews* **1997**, *97*, 2373.
2. Palin, L.; Lamberti, C.; Kvick, A.; Testa, F.; Aiello, R.; Milanesio, M.; Viterbo, D. *Journal of Physical Chemistry B* **2003**, *107*, 4034.
3. Han, O. H.; Kim, C. S.; Hong, S. B. *Angewandte Chemie-International Edition* **2002**, *41*, 469.
4. Milanesio, M.; Lamberti, C.; Aiello, R.; Testa, F.; Piana, M.; Viterbo, D. *Journal of Physical Chemistry B* **2000**, *104*, 9951.
5. Van Bokhoven, J. A.; Lee, T. L.; Drakopoulos, M.; Lamberti, C.; Thiess, S.; Zegenhagen, J. *Nature Materials* **2008**, *7*, 551.
6. Fyfe, C. A.; Bretherton, J. L.; Lam, L. Y. *J. Am. Chem. Soc.* **2001**, *123*, 5285.
7. Sklenak, S.; Dedecek, J.; Li, C. B.; Wichterlova, B.; Gabova, V.; Sierka, M.; Sauer, J. *Angewandte Chemie-International Edition* **2007**, *46*, 7286.
8. Baerlocher, C.; Xie, D.; McCusker, L. B.; Hwang, S. J.; Chan, I. Y.; Ong, K.; Burton, A. W.; Zones, S. I. *Nature Materials* **2008**, *7*, 631.
9. Xie, D.; McCusker, L. B.; Baerlocher, C.; Gibson, L.; Burton, A. W.; Hwang, S. J. *Journal of Physical Chemistry C* **2009**, *113*, 9845.
10. MacKenzie, K. J. D.; Smith, M. E. *Multinuclear Solid-State Nmr of Inorganic Materials*; Pergamon, 2002.
11. Engelhardt, G.; Michel, D. *High-resolution solid-state NMR of silicates and zeolites*; Wiley, 1987.
12. Jeong, H.-K.; Nair, S.; Vogt, T.; Dickinson, L. C.; Tsapatsis, M. *Nat Mater* **2003**, *2*, 53.
13. Ikeda, T.; Akiyama, Y.; Oumi, Y.; Kawai, A.; Mizukami, F. *Angewandte Chemie International Edition* **2004**, *43*, 4892.
14. Ikeda, T.; Kayamori, S.; Mizukami, F. *Journal of Materials Chemistry* **2009**, *19*, 5518.
15. Palin, L.; Croce, G.; Viterbo, D.; Milanesio, M. *Chemistry of Materials* **2011**, *23*, 4900.
16. Yilmaz, B.; Muller, U.; Tijsebaert, B.; De Vos, D.; Xie, B.; Xiao, F. S.; Gies, H.; Zhang, W. P.; Bao, X. H.; Imai, H.; Tatsumi, T. *Chemical Communications* **2011**, *47*, 1812.
17. Li, Z.; Marler, B.; Gies, H. *Chemistry of Materials* **2008**, *20*, 1896.
18. Mochizuki, D.; Shimojima, A.; Imagawa, T.; Kuroda, K. *J. Am. Chem. Soc.* **2005**, *127*, 7183.
19. Moteki, T.; Chaikittisilp, W.; Shimojima, A.; Okubo, T. *J. Am. Chem. Soc.* **2008**, *130*, 15780.
20. Choi, M.; Na, K.; Kim, J.; Sakamoto, Y.; Terasaki, O.; Ryoo, R. *Nature* **2009**, *461*, 246.
21. Na, K.; Choi, M.; Park, W.; Sakamoto, Y.; Terasaki, O.; Ryoo, R. *J. Am. Chem. Soc.* **2010**, *132*, 4169.
22. Christiansen, S. C.; Zhao, D.; Janicke, M. T.; Landry, C. C.; Stucky, G. D.; Chmelka, B. F. *J. Am. Chem. Soc.* **2001**, *123*, 4519.

## References

23. Hedin, N.; Graf, R.; Christiansen, S. C.; Gervais, C.; Hayward, R. C.; Eckert, J.; Chmelka, B. F. *J. Am. Chem. Soc.* **2004**, *126*, 9425.
24. Brouwer, D. H.; Cadars, S.; Eckert, J.; Liu, Z.; Terasaki, O.; Chmelka, B. F. *J. Am. Chem. Soc.* **2013**.
25. Kickelbick, G. *Hybrid Materials: Synthesis, Characterization, and Applications*; John Wiley & Sons, 2007.
26. Coltrain, B. K.; Society, M. R. *Better ceramics through chemistry VII: organic/inorganic hybrid materials : symposium held April 8-12, 1996, San Francisco, California, U.S.A*; Materials Research Society, 1996.
27. Mark, J. E.; Lee, C. C. Y.; Bianconi, P. A. *Hybrid Organic-Inorganic Composites*; American Chemical Society, 1995.
28. Mark, J. E. *Heterogeneous Chemistry Reviews* **1996**, *3*, 307.
29. Schmidt, H.; Krug, H. In *Inorganic and Organometallic Polymers II: Advanced Materials and Intermediates*; WisianNeilson, P., Allcock, H. R., Wynne, K. J., Eds. 1994; Vol. 572, p 183.
30. Sharp, K. G. *Advanced Materials* **1998**, *10*, 1243.
31. Innocenzi, P.; Falcaro, P.; Grosso, D.; Babonneau, F. *The Journal of Physical Chemistry B* **2003**, *107*, 4711.
32. Innocenzi, P.; Brusatin, G.; Babonneau, F. *Chemistry of Materials* **2000**, *12*, 3726.
33. Baccile, N.; Laurent, G.; Bonhomme, C.; Innocenzi, P.; Babonneau, F. *Chemistry of Materials* **2007**, *19*, 1343.
34. Baccile, N.; Teixeira, C. V.; Amenitsch, H.; Villain, F.; Lindén, M.; Babonneau, F. *Chemistry of Materials* **2007**, *20*, 1161.
35. Coronado, E.; Palomares, E. *Journal of Materials Chemistry* **2005**, *15*, 3593.
36. Wehlius, T.; Korner, T.; Nowy, S.; Frischeisen, J.; Karl, H.; Stritzker, B.; Brutting, W. *Physica Status Solidi a-Applications and Materials Science* **2011**, *208*, 264.
37. Chen, C. M.; Sun, X. Q.; Wang, F.; Zhang, F.; Wang, H.; Shi, Z. S.; Cui, Z. C.; Zhang, D. M. *Ieee Journal of Quantum Electronics* **2012**, *48*, 61.
38. Eldada, L.; Fujita, J.; Radojevic, A.; Gerhardt, R.; Izuhara, T. **2005**, 200.
39. Diaz, U.; Cantin, A.; Corma, A. *Chemistry of Materials* **2007**, *19*, 3686.
40. Pergher, S. B. C.; Corma, A.; Fornes, V. *Quimica Nova* **1999**, *22*, 693.
41. Mammeri, F.; Bourhis, E. L.; Rozes, L.; Sanchez, C. *Journal of Materials Chemistry* **2005**, *15*, 3787.
42. Guo, X. M.; Canet, J. L.; Boyer, D.; Gautier, A.; Mahiou, R. *Journal of Materials Chemistry* **2012**, *22*, 6117.
43. Ahmed, A.; Clowes, R.; Myers, P.; Zhang, H. *Journal of Materials Chemistry* **2011**, *21*, 5753.

## References

44. Svec, F.; Tennikova, T. B.; Deyl, Z. *Monolithic Materials: Preparation, Properties and Applications*; Elsevier Science, 2003.
45. Comanescu, C.; Ficai, D.; Lacatusu, I.; Guran, C. *Revista De Chimie* **2011**, *62*, 37.
46. Gerardin, C.; Sundaresan, S.; Benziger, J.; Navrotsky, A. *Chemistry of Materials* **1994**, *6*, 160.
47. Klein, L. C.; Garvey, G. J. *Journal of Non-Crystalline Solids* **1980**, *38–39, Part 1*, 45.
48. Brinker, C. J.; Keefer, K. D.; Schaefer, D. W.; Ashley, C. S. *Journal of Non-Crystalline Solids* **1982**, *48*, 47.
49. Zanotto, E. D. *Journal of Non-Crystalline Solids* **1992**, *147*, 820.
50. Rivera-Munoz, E. M.; Huirache-Acuna, R. *International Journal of Molecular Sciences* **2010**, *11*, 3069.
51. Beretta, M. *PhD thesis* **2009**.
52. Ozin, G. A. *Canadian Journal of Chemistry* **1999**, *77*, 2001.
53. Ward, M. D.; Horner, M. J. *CrystEngComm* **2004**, *6*, 401.
54. Keppeler, M.; Holzbock, J.; Akbarzadeh, J.; Peterlik, H.; Hüsing, N. *Beilstein Journal of Nanotechnology* **2011**, *2*, 486.
55. Biz, S.; White, M. G. *Microporous and Mesoporous Materials* **2000**, *40*, 159.
56. Bae, J. A.; Hwang, S. H.; Song, K. C.; Jeon, J. K.; Ko, Y. S.; Yim, J. H. *Journal of Nanoscience and Nanotechnology* **2010**, *10*, 290.
57. Feng, P. Y.; Bu, X. H.; Stucky, G. D. *Nature* **1997**, *388*, 735.
58. Cundy, C. S.; Cox, P. A. *Chemical Reviews* **2003**, *103*, 663.
59. Corma, A.; Rey, F.; Rius, J.; Sabater, M. J.; Valencia, S. *Nature* **2004**, *431*, 287.
60. Freyhardt, C. C.; Tsapatsis, M.; Lobo, R. F.; Balkus, K. J.; Davis, M. E. *Nature* **1996**, *381*, 295.
61. Cundy, C. S.; Cox, P. A. *Microporous and Mesoporous Materials* **2005**, *82*, 1.
62. [http://en.wikipedia.org/wiki/Hydrothermal\\_synthesis](http://en.wikipedia.org/wiki/Hydrothermal_synthesis).
63. Groen, J. C.; Peffer, L. A. A.; Perez-Ramirez, J. *Microporous and Mesoporous Materials* **2003**, *60*, 1.
64. Tiemann, M.; Goletto, V.; Blum, R.; Babonneau, F.; Amenitsch, H.; Lindén, M. *Langmuir* **2002**, *18*, 10053.
65. Michaux, F.; Baccile, N.; Impéror-Clerc, M.; Malfatti, L.; Folliet, N.; Gervais, C.; Manet, S.; Meneau, F.; Pedersen, J. S.; Babonneau, F. *Langmuir* **2012**, *28*, 17477.
66. Gramm, F.; Baerlocher, C.; McCusker, L. B.; Warrender, S. J.; Wright, P. A.; Han, B.; Hong, S. B.; Liu, Z.; Ohsuna, T.; Terasaki, O. *Nature* **2006**, *444*, 79.
67. McCusker, L. B. *Acta Crystallographica Section A* **1991**, *47*, 297.
68. Peng, L.; Huo, H.; Liu, Y.; Grey, C. P. *J. Am. Chem. Soc.* **2007**, *129*, 335.
69. Huo, H.; Peng, L.; Grey, C. P. *Journal of Physical Chemistry C* **2011**, *115*, 2030.

## References

70. Bull, L. M.; Cheetham, A. K.; Anupold, T.; Reinhold, A.; Samoson, A.; Sauer, J.; Bussemer, B.; Lee, Y.; Gann, S.; Shore, J.; Pines, A.; Dupree, R. *J. Am. Chem. Soc.* **1998**, *120*, 3510.
71. Cadars, S.; Lesage, A.; Hedin, N.; Chmelka, B. F.; Emsley, L. *Journal of Physical Chemistry B* **2006**, *110*, 16982.
72. Shayib, R. M.; George, N. C.; Seshadri, R.; Burton, A. W.; Zones, S. I.; Chmelka, B. F. *J. Am. Chem. Soc.* **2011**, *133*, 18728.
73. Thomas, J. M.; Gonzalezcalbert, J. M.; Fyfe, C. A.; Gobbi, G. C.; Nicol, M. *Geophysical Research Letters* **1983**, *10*, 91.
74. Grimmer, A. R.; Wieker, W.; Vonlampe, F.; Fechner, E.; Peter, R.; Molgedey, G. *Zeitschrift Fur Chemie* **1980**, *20*, 453.
75. Nanba, T.; Nishimura, M.; Miura, Y. *Geochim. Cosmochim. Acta* **2004**, *68*, 5103.
76. Vogels, R.; Klopogge, J. T.; Geus, J. W. *Microporous and Mesoporous Materials* **2005**, *77*, 159.
77. Smith, J. V.; Blackwell, C. S. *Nature* **1983**, *303*, 223.
78. Ramdas, S.; Klinowski, J. *Nature* **1984**, *308*, 521.
79. Plévert, J.; Di Renzo, F.; Fajula, F. In *Studies in Surface Science and Catalysis*; A. Galarneau, F. F. F. D. R., Vedrine, J., Eds.; Elsevier: 2001; Vol. Volume 135, p 342.
80. Engelhardt, G.; Radeaglia, R. *Chemical Physics Letters* **1984**, *108*, 271.
81. Weiss, C. A.; Altaner, S. P.; Kirkpatrick, R. J. *American Mineralogist* **1987**, *72*, 935.
82. Grimmer, A. R.; Radeaglia, R. *Chemical Physics Letters* **1984**, *106*, 262.
83. Gibbs, G. V.; Hamil, M. M.; Louisnat, S.; Bartell, L. S.; Yow, H. *American Mineralogist* **1972**, *57*, 1578.
84. Xue, X.; Kanzaki, M. *The Journal of Physical Chemistry C* **2012**, *116*, 10714.
85. Massiot, D.; Fayon, F.; Deschamps, M.; Cadars, S.; Florian, P.; Montouillout, V.; Pellerin, N.; Hiet, J.; Rakhmatullin, A.; Bessada, C. *C. R. Chim.* **2010**, *13*, 117.
86. Kirmayer, S.; Dovgolevsky, E.; Kalina, M.; Lakin, E.; Cadars, S.; Epping, J. D.; Fernandez-Arteaga, A.; Rodriguez-Abreu, C.; Chmelka, B. F.; Frey, G. L. *Chemistry of Materials* **2008**, *20*, 3745.
87. <http://en.wikipedia.org/wiki/Montmorillonite>.
88. Firouzi, A.; Kumar, D.; Bull, L. M.; Besier, T.; Sieger, P.; Huo, Q.; Walker, S. A.; Zasadzinski, J. A.; Glinka, C.; Nicol, J.; Margolese, D.; Stucky, G. D.; Chmelka, B. F. *Science* **1995**, *267*, 1138.
89. Vortmann, S.; Rius, J.; Siegmann, S.; Gies, H. *Journal of Physical Chemistry B* **1997**, *101*, 1292.
90. Jansen, J. C.; Vandergaag, F. J.; Vanbekkum, H. *Zeolites* **1984**, *4*, 369.
91. Sitarz, M.; Mozgawa, W.; Handke, M. *Journal of Molecular Structure* **1997**, *404*, 193.
92. Sitarz, M.; Handke, M.; Mozgawa, W. *Spectrochimica Acta Part a-Molecular and Biomolecular Spectroscopy* **1999**, *55*, 2831.

## References

93. Chu, C. T. W.; Chang, C. D. *Journal of Physical Chemistry* **1985**, *89*, 1569.
94. Strodel, P.; Neyman, K. M.; Knozinger, H.; Rosch, N. *Chemical Physics Letters* **1995**, *240*, 547.
95. Stave, M. S.; Nicholas, J. B. *Journal of Physical Chemistry* **1995**, *99*, 15046.
96. Parrillo, D. J.; Lee, C.; Gorte, R. J.; White, D.; Farneth, W. E. *Journal of Physical Chemistry* **1995**, *99*, 8745.
97. Sulikowski, B. *Heterogeneous Chemistry Reviews* **1996**, *3*, 203.
98. Mihailova, B.; Valtchev, V.; Mintova, S.; Faust, A. C.; Petkov, N.; Bein, T. *Physical Chemistry Chemical Physics* **2005**, *7*, 2756.
99. Camblor, M. A.; Hong, S. B.; Davis, M. E. *Chemical Communications* **1996**, 425.
100. Fripiat, J. G.; Bergerandre, F.; Andre, J. M.; Derouane, E. G. *Zeolites* **1983**, *3*, 306.
101. Derouane, E. G.; Fripiat, J. G. *Zeolites* **1985**, *5*, 165.
102. Omalley, P. J.; Dwyer, J. *Zeolites* **1988**, *8*, 317.
103. Vetrivel, R.; Pal, S.; Krishnan, S. *Journal of Molecular Catalysis* **1991**, *66*, 385.
104. Han, S.; Schmitt, K. D.; Schramm, S. E.; Reischman, P. T.; Shihabi, D. S.; Chang, C. D. *The Journal of Physical Chemistry* **1994**, *98*, 4118.
105. Ione, K. G. V., L. A. *Uspechi Chimii* **1987**, *56*, 393.
106. Fricke, R.; Kosslick, H.; Lischke, G.; Richter, M. *Chemical Reviews* **2000**, *100*, 2303.
107. Pauling, L. *The Nature of the Chemical Bond and the Structure of Molecules and Crystals: An Introduction to Modern Structural Chemistry*; Cornell University Press, 1960.
108. Deka, R. C.; Tajima, N.; Hirao, K. *Journal of Molecular Structure: THEOCHEM* **2001**, *535*, 31.
109. Millini, R.; Perego, G.; Bellussi, G. *Topics in Catalysis* **1999**, *9*, 13.
110. Coudurier, G.; Auroux, A.; Vedrine, J. C.; Farlee, R. D.; Abrams, L.; Shannon, R. D. *Journal of Catalysis* **1987**, *108*, 1.
111. Taramasso, M., Perego, G. and Notari, B. *Proceedings of the 5th International Conference on Zeolites (Ed. L.V.C.Rees) Heyden, London* **1980**, 40.
112. Hoelderich, W. *Pure Appl. Chem.* **1986**, *58*, 1383.
113. Vetrivel, R. *Zeolites* **1992**, *12*, 424.
114. Van Nordstrand, R. A.; Santilli, D. S.; Zones, S. I.; in: Ocelli, M. L.; and Robson, H. E. *Molecular Sieves: Synthesis of Microporous Materials* **1992**, *1*.
115. Millini, R.; Perego, G.; Parker, W. O.; Bellussi, G.; Carluccio, L. *Microporous Materials* **1995**, *4*, 221.
116. Schwieger, W.; Pohl, K.; Brenn, U.; Fyfe, C. A.; Grondey, H.; Fu, G.; Kokotailo, G. T. In *Studies in Surface Science and Catalysis*; H.K. Beyer, H. G. K. I. K., Nagy, J. B., Eds.; Elsevier: 1995; Vol. Volume 94, p 47.

## References

117. Komura, K.; Murase, T.; Sugi, Y.; Koketsu, M. *Chemistry Letters* **2010**, *39*, 948.
118. Dorset, D. L.; Kennedy, G. J. *The Journal of Physical Chemistry B* **2005**, *109*, 13891.
119. [http://izasc.ethz.ch/fmi/xsl/IZA-SC/ftc\\_fw.xsl?-db=Atlas\\_main&-lay=web&STC=MVY&-find](http://izasc.ethz.ch/fmi/xsl/IZA-SC/ftc_fw.xsl?-db=Atlas_main&-lay=web&STC=MVY&-find).
120. Grünewald-Lüke, A.; Gies, H.; Müller, U.; Yilmaz, B.; Imai, H.; Tatsumi, T.; Xie, B.; Xiao, F.-S.; Bao, X.; Zhang, W.; De Vos, D. *Microporous and Mesoporous Materials* **2012**, *147*, 102.
121. Corma, A.; Diaz-Cabanas, M. J.; Jiang, J.; Afeworki, M.; Dorset, D. L.; Soled, S. L.; Strohmaier, K. G. *Proceedings of the National Academy of Sciences of the United States of America* **2010**, *107*, 13997.
122. 3702886, U. S. P.
123. Dedecek, J.; Balgová, V.; Pashkova, V.; Klein, P.; Wichterlová, B. *Chemistry of Materials* **2012**.
124. Dedecek, J.; Sobalik, Z.; Wichterlova, B. *Catalysis Reviews-Science and Engineering* **2012**, *54*, 135.
125. Van Bokhoven, J. A.; Lee, T.-L.; Drakopoulos, M.; Lamberti, C.; Thiess, S.; Zegenhagen, J. *Nature Materials* **2008**, *7*, 551.
126. Lippmaa, E.; Maegi, M.; Samoson, A.; Tarmak, M.; Engelhardt, G. *J. Am. Chem. Soc.* **1981**, *103*, 4992.
127. Frydman, L.; Harwood, J. S. *J. Am. Chem. Soc.* **1995**, *117*, 5367.
128. Sarv, P.; Wichterlova, B.; Cejka, J. *Journal of Physical Chemistry B* **1998**, *102*, 1372.
129. Sarv, P.; Fernandez, C.; Amoureux, J. P.; Keskinen, K. *Journal of Physical Chemistry* **1996**, *100*, 19223.
130. Sakellariou, D.; Le Goff, G.; Jacquinet, J. F. *Nature* **2007**, *447*, 694.
131. Levitt, M. H. *Spin Dynamics: Basics of Nuclear Magnetic Resonance*; John Wiley & Sons, 2008.
132. Laws, D. D.; Bitter, H. M. L.; Jerschow, A. *Angewandte Chemie-International Edition* **2002**, *41*, 3096.
133. Pake, G. E. *Journal of Chemical Physics* **1948**, *16*, 327.
134. Ernst, R. R.; Bodenhausen, G.; Wokaun, A. *Principles of Nuclear Magnetic Resonance in One and Two Dimensions*; Oxford University Press, USA, 1990.
135. <http://www.cryst.bbk.ac.uk/PPS2/projects/schirra/html/2dnmr.htm>.
136. Lesage, A.; Bardet, M.; Emsley, L. *J. Am. Chem. Soc.* **1999**, *121*, 10987.
137. De Paepe, G.; Hodgkinson, P.; Emsley, L. *Chemical Physics Letters* **2003**, *376*, 259.
138. De Paepe, G.; Lesage, A.; Emsley, L. *Journal of Chemical Physics* **2003**, *119*, 4833.
139. Elena, B.; de Paëpe, G.; Emsley, L. *Chemical Physics Letters* **2004**, *398*, 532.
140. De Paepe, G.; Lesage, A.; Steuernagel, S.; Emsley, L. *ChemPhysChem* **2004**, *5*, 869.
141. Andrew, E. R.; Bradbury, A.; Eades, R. G. *Nature* **1958**, *182*, 1659.
142. Lowe, I. J. *Phys. Rev. Lett.* **1959**, *2*, 285.
143. Facey, G. <http://u-of-o-nmr-facility.blogspot.fr/2007/11/magic-angle-spinning.html>.

## References

144. Sun, B. Q.; Baltisberger, J. H.; Wu, Y.; Samoson, A.; Pines, A. *Solid State Nuclear Magnetic Resonance* **1992**, *1*, 267.
145. Samoson, A.; Lippmaa, E.; Pines, A. *Molecular Physics* **1988**, *65*, 1013.
146. Chmelka, B. F.; Mueller, K. T.; Pines, A.; Stebbins, J.; Wu, Y.; Zwanziger, J. W. *Nature* **1989**, *339*, 42.
147. Wu, Y.; Sun, B. Q.; Pines, A.; Samoson, A.; Lippmaa, E. *J. Magn. Reson.* **1990**, *89*, 297.
148. Medek, A.; Harwood, J. S.; Frydman, L. *J. Am. Chem. Soc.* **1995**, *117*, 12779.
149. Bennett, A. E.; Rienstra, C. M.; Auger, M.; Lakshmi, K. V.; Griffin, R. G. *Journal of Chemical Physics* **1995**, *103*, 6951.
150. Fung, B. M.; Khitrin, A. K.; Ermolaev, K. *J. Magn. Reson.* **2000**, *142*, 97.
151. De Paepe, G.; Elena, B.; Emsley, L. *Journal of Chemical Physics* **2004**, *121*, 3165.
152. Detken, A.; Hardy, E. H.; Ernst, M.; Meier, B. H. *Chemical Physics Letters* **2002**, *356*, 298.
153. Pines, A.; Gibby, M. G.; Waugh, J. S. *Journal of Chemical Physics* **1973**, *59*, 569.
154. Hartmann, S. R.; Hahn, E. L. *Physical Review* **1962**, *128*, 2042.
155. Metz, G.; Wu, X. L.; Smith, S. O. *Journal of Magnetic Resonance Series A* **1994**, *110*, 219.
156. Iuga, D.; Kentgens, A. P. M. *Journal of Magnetic Resonance* **2002**, *158*, 65.
157. Iuga, D.; Schäfer, H.; Verhagen, R.; Kentgens, A. P. M. *J. Magn. Reson.* **2000**, *147*, 192.
158. Kentgens, A. P. M.; Verhagen, R. *Chemical Physics Letters* **1999**, *300*, 435.
159. Iuga, D.; Morais, C.; Gan, Z. H.; Neuville, D. R.; Cormier, L.; Massiot, D. *J. Am. Chem. Soc.* **2005**, *127*, 11540.
160. Sakellariou, D.; Emsley, L. In *Encyclopedia of Magnetic Resonance*; John Wiley & Sons, Ltd: 2007.
161. Fyfe, C. A.; Gies, H.; Feng, Y. *J. Am. Chem. Soc.* **1989**, *111*, 7702.
162. Fyfe, C. A.; Gies, H.; Feng, Y.; Kokotailo, G. T. *Nature* **1989**, *341*, 223.
163. Fyfe, C. A.; Grondey, H.; Feng, Y.; Kokotailo, G. T. *J. Am. Chem. Soc.* **1990**, *112*, 8812.
164. Fyfe, C. A.; Feng, Y.; Grondey, H.; Kokotailo, G. T.; Mar, A. *Journal of Physical Chemistry* **1991**, *95*, 3747.
165. Lesage, A.; Sakellariou, D.; Steuernagel, S.; Emsley, L. *J. Am. Chem. Soc.* **1998**, *120*, 13194.
166. Fyfe, C. A.; Wong-Moon, K. C.; Huang, Y.; Grondey, H.; Mueller, K. T. *The Journal of Physical Chemistry* **1995**, *99*, 8707.
167. Mao, K.; Wiench, J. W.; Lin, V. S. Y.; Pruski, M. *J. Magn. Reson.* **2009**, *196*, 92.
168. Schaller, T.; Buchele, U. P.; Klärner, F. G.; Blaser, D.; Boese, R.; Brown, S. P.; Spiess, H. W.; Koziol, F.; Kussmann, J.; Ochsenfeld, C. *J. Am. Chem. Soc.* **2007**, *129*, 1293.
169. Soubias, O.; Jolibois, F.; Reat, V.; Milon, A. *Chemistry-a European Journal* **2004**, *10*, 6005.

## References

170. Yates, J. R.; Pham, T. N.; Pickard, C. J.; Mauri, F.; Amado, A. M.; Gil, A. M.; Brown, S. P. *J. Am. Chem. Soc.* **2005**, *127*, 10216.
171. Mueller, L. J.; Elliott, D. W.; Kim, K. C.; Reed, C. A.; Boyd, P. D. W. *J. Am. Chem. Soc.* **2002**, *124*, 9360.
172. Cadars, S.; Sein, J.; Duma, L.; Lesage, A.; Pham, T. N.; Baltisberger, J. H.; Brown, S. P.; Emsley, L. *J. Magn. Reson.* **2007**, *188*, 24.
173. De Paepe, G.; Giraud, N.; Lesage, A.; Hodgkinson, P.; Bockmann, A.; Emsley, L. *J. Am. Chem. Soc.* **2003**, *125*, 13938.
174. Cadars, S.; Mifsud, N.; Lesage, A.; Epping, J. D.; Hedin, N.; Chmelka, B. F.; Emsley, L. *Journal of Physical Chemistry C* **2008**, *112*, 9145.
175. Kristiansen, P. E.; Carravetta, M.; Lai, W. C.; Levitt, M. H. *Chemical Physics Letters* **2004**, *390*, 1.
176. Kristiansen, P. E.; Carravetta, M.; van Beek, J. D.; Lai, W. C.; Levitt, M. H. *Journal of Chemical Physics* **2006**, *124*.
177. Raleigh, D. P.; Levitt, M. H.; Griffin, R. G. *Chemical Physics Letters* **1988**, *146*, 71.
178. Karlsson, T.; Popham, J. M.; Long, J. R.; Oyler, N.; Drobny, G. P. *J. Am. Chem. Soc.* **2003**, *125*, 7394.
179. Gregory, D. M.; Mitchell, D. J.; Stringer, J. A.; Kiihne, S.; Shiels, J. C.; Callahan, J.; Mehta, M. A.; Drobny, G. P. *Chemical Physics Letters* **1995**, *246*, 654.
180. Hohwy, M.; Jakobsen, H. J.; Eden, M.; Levitt, M. H.; Nielsen, N. C. *Journal of Chemical Physics* **1998**, *108*, 2686.
181. Brinkmann, A.; Levitt, M. H. *Journal of Chemical Physics* **2001**, *115*, 357.
182. Brouwer, D. H.; Darton, R. J.; Morris, R. E.; Levitt, M. H. *J. Am. Chem. Soc.* **2005**, *127*, 10365.
183. Marin-Montesinos, I.; Brouwer, D. H.; Antonioli, G.; Lai, W. C.; Brinkmann, A.; Levitt, M. H. *J. Magn. Reson.* **2005**, *177*, 307.
184. Vega, A. J. *Solid State Nuclear Magnetic Resonance* **1992**, *1*, 17.
185. Vega, A. J. *J. Magn. Reson.* **1992**, *96*, 50.
186. Grey, C. P.; Vega, A. J. *J. Am. Chem. Soc.* **1995**, *117*, 8232.
187. Bielecki, A.; Kolbert, A. C.; Levitt, M. H. *Chemical Physics Letters* **1989**, *155*, 341.
188. Levitt, M. H.; Oas, T. G.; Griffin, R. G. *Israel Journal of Chemistry* **1988**, *28*, 271.
189. Brinkmann, A.; Kentgens, A. P. M. *J. Am. Chem. Soc.* **2006**, *128*, 14758.
190. Hu, B.; Trebosc, J.; Amoureux, J. P. *J. Magn. Reson.* **2008**, *192*, 112.
191. Bonhomme, C.; Gervais, C.; Babonneau, F.; Coelho, C.; Pourpoint, F.; Azaïs, T.; Ashbrook, S. E.; Griffin, J. M.; Yates, J. R.; Mauri, F.; Pickard, C. J. *Chemical Reviews* **2012**, *112*, 5733.
192. Pickard, C. J.; Mauri, F. *Physical Review B* **2001**, *63*, 245101.

## References

193. Yates, J. R.; Pickard, C. J.; Mauri, F. *Physical Review B* **2007**, *76*, 024401.
194. Clark, S. J.; Segall, M. D.; Pickard, C. J.; Hasnip, P. J.; Probert, M. J.; Refson, K.; Payne, M. C. Z. *Kristall*. **2005**, *220*, 567.
195. Segall, M. D.; Lindan, P. J. D.; Probert, M. J.; Pickard, C. J.; Hasnip, P. J.; Clark, S. J.; Payne, M. C. *Journal of Physics-Condensed Matter* **2002**, *14*, 2717.
196. Hartree, D. R. *Mathematical Proceedings of the Cambridge Philosophical Society* **1928**, *24*, 111.
197. Hartree, D. R. *Mathematical Proceedings of the Cambridge Philosophical Society* **1928**, *24*, 89.
198. Hohenberg, P.; Kohn, W. *Physical Review B* **1964**, *136*, B864.
199. Perdew, J. P.; Burke, K.; Ernzerhof, M. *Phys. Rev. Lett.* **1996**, *77*, 3865.
200. Mackenzie, K. J. D.; Smith, M. E. *multinuclear solid-state NMR of inorganic materials*; Pergamon Press: Oxford, 2002.
201. Stebbins, J. F. In *Handbook of Physical Constants*; Ahrens, T. J., Ed.; American Geophysical Union: Washington D.C., 1995; Vol. 2.
202. Koller, H.; Engelhardt, G.; Kentgens, A. P. M.; Sauer, J. *J. Phys. Chem.* **1994**, *98*, 1544.
203. Martel, L.; Cadars, S.; Véron, E.; Massiot, D.; Deschamps, M. *Solid State Nucl. Mag.* **2012**, *45–46*, 1.
204. Massiot, D.; Fayon, F.; Alonso, B.; Trebosc, J.; Amoureux, J. P. *J. Magn. Reson.* **2003**, *164*, 160.
205. Florian, P.; Gervais, M.; Douy, A.; Massiot, D.; Coutures, J.-P. *The Journal of Physical Chemistry B* **2000**, *105*, 379.
206. Massiot, D. *Journal of Magnetic Resonance, Series A* **1996**, *122*, 240.
207. Alemany, L. B.; Massiot, D.; Sherriff, B. L.; Smith, M. E.; Taulelle, F. *Chem. Phys. Lett.* **1991**, *177*, 301.
208. Kirkpatrick, R. J.; Kinsey, R. A.; Smith, K. A.; Henderson, D. M.; Oldfield, E. *Am. Mineral.* **1985**, *70*, 106.
209. Le Forestier, L.; Muller, F.; Villieras, F.; Pelletier, M. *Applied Clay Science* **2010**, *48*, 18.
210. Massiot, D.; Fayon, F.; Capron, M.; King, I.; Le Calvé, S.; Alonso, B.; Durand, J.-O.; Bujoli, B.; Gan, Z.; Hoatson, G. *Magnetic Resonance in Chemistry* **2002**, *40*, 70.
211. Fyfe, C. A.; Wongmoon, K. C.; Huang, Y.; Grondey, H.; Mueller, K. T. *Journal of Physical Chemistry* **1995**, *99*, 8707.
212. DePaul, S. M.; Ernst, M.; Shore, J. S.; Stebbins, J. F.; Pines, A. *Journal of Physical Chemistry B* **1997**, *101*, 3240.
213. Edén, M.; Grins, J.; Shen, Z.; Weng, Z. *J. Magn. Reson.* **2004**, *169*, 279.
214. Kennedy, G. J.; Wiench, J. W.; Pruski, M. *Solid State Nuclear Magnetic Resonance* **2008**, *33*, 76.

## References

215. Ganapathy, S.; Kumar, R.; Montouillout, V.; Fernandez, C.; Amoureux, J. P. *Chemical Physics Letters* **2004**, *390*, 79.
216. Carravetta, M.; Eden, M.; Zhao, X.; Brinkmann, A.; Levitt, M. H. *Chemical Physics Letters* **2000**, *321*, 205.
217. Xia, Y. D.; Mokaya, R. *Microporous and Mesoporous Materials* **2006**, *94*, 295.
218. Christiansen, S. C.; Zhao, D. Y.; Janicke, M. T.; Landry, C. C.; Stucky, G. D.; Chmelka, B. F. *J. Am. Chem. Soc.* **2001**, *123*, 4519.
219. Bielecki, A.; Burum, D. P. *Journal of Magnetic Resonance Series A* **1995**, *116*, 215.
220. Fayon, F.; King, I. J.; Harris, R. K.; Evans, J. S. O.; Massiot, D. C. *R. Chim.* **2004**, *7*, 351.
221. Florian, P.; Fayon, F.; Massiot, D. *Journal of Physical Chemistry C* **2009**, *113*, 2562.
222. Klinowski, J.; Carr, S. W.; Tarling, S. E.; Barnes, P. *Nature* **1987**, *330*, 56.
223. Baerlocher, C., ; Mccusker, LB; *IZA database*.
224. Guegan, R. *Langmuir* **2010**, *26*, 19175.
225. Guegan, R.; Gautier, M.; Beny, J. M.; Muller, F. *Clays and Clay Minerals* **2009**, *57*, 502.
226. de Paiva, L. B.; Morales, A. R.; Diaz, F. R. V. *Applied Clay Science* **2008**, *42*, 8.
227. Ruiz-Hitzky, E.; Aranda, P.; Darder, M.; Ogawa, M. *Chemical Society Reviews* **2011**, *40*, 801.
228. Ruiz-Hitzky, E.; Aranda, P.; Darder, M.; Rytwo, G. *Journal of Materials Chemistry* **2010**, *20*, 9306.
229. DAVIDTZT JC, L. P. *Clays and Clay Minerals* **1970**, *18*, 325.
230. Ohkubo, T.; Saito, K.; Kanehashi, K.; Ikeda, Y. *Science and Technology of Advanced Materials* **2004**, *5*, 693.
231. Ferrage, E.; Lanson, B.; Sakharov, B. A.; Drits, V. A. *American Mineralogist* **2005**, *90*, 1358.
232. Karaborni, S.; Smit, B.; Heidug, W.; Urai, J.; vanOort, E. *Science* **1996**, *271*, 1102.
233. Gougeon, R. D.; Reinholdt, M.; Delmotte, L.; Miehe-Brendle, J.; Jeandet, P. *Solid State Nuclear Magnetic Resonance* **2006**, *29*, 322.
234. Lippmaa, E.; Maegi, M.; Samoson, A.; Engelhardt, G.; Grimmer, A. R. *J. Am. Chem. Soc.* **1980**, *102*, 4889.
235. Sanz, J.; Serratos, J. M. *J. Am. Chem. Soc.* **1984**, *106*, 4790.
236. Altaner, S. P.; Weiss, C. A.; Kirkpatrick, R. J. *Nature* **1988**, *331*, 699.
237. Ohkubo, T.; Kanehashi, K.; Saito, K.; Ikeda, Y. *Clays and Clay Minerals* **2003**, *51*, 513.
238. Espinosa, J.; Gomez, S.; Fuentes, G. A. In *Zeolites and Related Microporous Materials: State of the Art 1994*; Weitkamp, J., Karge, H. G., Pfeifer, H., Holderich, W., Eds.; Elsevier Science Publ B V: Amsterdam, 1994; Vol. 84, p 283.
239. Takahashi, T.; Ohkubo, T.; Suzuki, K.; Ikeda, Y. *Microporous and Mesoporous Materials* **2007**, *106*, 284.

## References

240. Tkac, I.; Komadel, P.; Muller, D. *Clay Minerals* **1994**, *29*, 11.
241. Alba, M. D.; Becerro, A. I.; Castro, M. A.; Perdigon, A. C. *Chemical Communications* **2000**, 37.
242. Alba, M. D.; Becerro, A. I.; Castro, M. A.; Perdigon, A. C. *Chemical Communications* **2001**, 249.
243. Alba, M. D.; Castro, M. A.; Naranjo, M.; Perdigon, A. C. *Physics and Chemistry of Minerals* **2004**, *31*, 195.
244. Alba, M. D.; Castro, M. A.; Chain, P.; Naranjo, M.; Perdigon, A. C. *Physics and Chemistry of Minerals* **2005**, *32*, 248.
245. Labouriau, A.; Kim, Y. W.; Earl, W. L. *Physical Review B* **1996**, *54*, 9952.
246. Trebosc, J.; Hu, B.; Amoureux, J. P.; Gan, Z. *J. Magn. Reson.* **2007**, *186*, 220.
247. Griffin, J. M.; Berry, A. J.; Ashbrook, S. E. *Solid State Nuclear Magnetic Resonance* **2011**, *40*, 91.
248. Pallister, P. J.; Moudrakovski, I. L.; Ripmeester, J. A. *Physical Chemistry Chemical Physics* **2009**, *11*, 11487.
249. Alba, M. D.; Becerro, A. I.; Castro, M. A.; Perdigon, A. C.; Trillo, J. M. *Journal of Physical Chemistry B* **2003**, *107*, 3996.
250. Sideris, P. J.; Nielsen, U. G.; Gan, Z. H.; Grey, C. P. *Science* **2008**, *321*, 113.
251. Sideris, P. J.; Blanc, F.; Gan, Z. H.; Grey, C. P. *Chemistry of Materials* **2012**, *24*, 2449.
252. Cadars, S.; Layrac, G. r.; Gérardin, C.; Deschamps, M. l.; Yates, J. R.; Tichit, D.; Massiot, D. *Chemistry of Materials* **2011**, *23*, 2821.
253. Bauer, H. *Neues Jahrb. Mineral. Mh.* **1962**, 127.
254. Fletcher, J. G.; Glasser, F. P. *Journal of Materials Science* **1993**, *28*, 2677.
255. Smith, H. D.; Wiersema, R. J. *Inorganic Chemistry* **1972**, *11*, 1152.
256. Turner, G. L.; Smith, K. A.; Kirkpatrick, R. J.; Oldfield, E. *J. Magn. Reson.* **1986**, *67*, 544.
257. Kroeker, S.; Stebbins, J. F. *Inorganic Chemistry* **2001**, *40*, 6239.
258. Konig, H.; Hoppe, R.; Jansen, M. *Zeitschrift Fur Anorganische Und Allgemeine Chemie* **1979**, *449*, 91.
259. Kriz, H. M.; Bray, P. J. *J. Magn. Reson.* **1971**, *4*, 76.
260. Morris, G. A.; Freeman, R. *J. Am. Chem. Soc.* **1979**, *101*, 760.
261. Fyfe, C. A.; Wong-Moon, K. C.; Huang, Y.; Grondey, H. *J. Am. Chem. Soc.* **1995**, *117*, 10397.
262. Cadars, S.; Guegan, R.; Garaga, M. N.; Bourrat, X.; Le Forestier, L.; Fayon, F.; Huynh, T.-V.; Allier, T.; Nour, Z.; Massiot, D. *Chemistry of Materials* **2012**.
263. Véron, E.; Garaga, M. N.; Pelloquin, D.; Cadars, S.; Suchomel, M.; Suard, E.; Massiot, D.; Montouillout, V.; Matzen, G.; Allix, M. *Inorganic Chemistry* **2013**.
264. Hediger, S.; Meier, B. H.; Kurur, N. D.; Bodenhausen, G.; Ernst, R. R. *Chemical Physics Letters* **1994**, *223*, 283.

### References

265. Massiot, D.; Fayon, F.; Capron, M.; King, I.; Le Calve, S.; Alonso, B.; Durand, J. O.; Bujoli, B.; Gan, Z. H.; Hoatson, G. *Magnetic Resonance in Chemistry* **2002**, *40*, 70.
266. Frydman, L.; Harwood, J. S. *Journal of the American Chemical Society* **1995**, *117*, 5367.
267. Amoureux, J. P.; Fernandez, C.; Steuernagel, S. *Journal of Magnetic Resonance Series A* **1996**, *123*, 116.

# Appendices

---

## *Appendix A*

### *Experimental Section*

---

All solid-state NMR spectra discussed in this manuscript were collected at 300, 400, 500, 750 and 850 MHz BRUKER NMR spectrometers at a magnetic field of 7, 9.4, 11.7, 17.6 and 20 tesla, respectively. The  $^{11}\text{B}$  [ $^{29}\text{Si}$ ] heteronuclear correlation experiments were collected at a magnetic field of 9.4T, with Larmor frequency of 400.17, 128.38, and 79.49 MHz for  $^1\text{H}$ ,  $^{11}\text{B}$ , and  $^{29}\text{Si}$  nuclei, respectively, by using 3.2 mm triple-resonance probehead. The  $^{27}\text{Al}$  [ $^{29}\text{Si}$ ] and  $^{11}\text{B}$  [ $^{29}\text{Si}$ ] heteronuclear correlation experiments were collected at a magnetic field of 17.6 ( $^1\text{H}$ ,  $^{11}\text{B}$ ,  $^{27}\text{Al}$ , and  $^{29}\text{Si}$  Larmor frequencies of 750.12, 240.66, 195.46 and 149.01 MHz, respectively) and 20 T ( $^1\text{H}$ ,  $^{11}\text{B}$ ,  $^{27}\text{Al}$ , and  $^{29}\text{Si}$  Larmor frequencies of 850.26, 272.80, 221.57 and 168.91 MHz, respectively) by using 4 mm and 3.2 mm probehead, respectively, in double- and triple resonance mode depend on the type of NMR experiments.  $^{29}\text{Si}$  [ $^{29}\text{Si}$ ] correlation experiments were collected at a magnetic field of 7 T ( $^1\text{H}$  and  $^{29}\text{Si}$  operating frequency of 300.15 and 59.62 MHz, respectively) using 4 mm double-resonance probehead. The magic angle setting ( $54.7^\circ$ ) of all the probes that used to conduct the NMR experiments studied in the manuscript was done by detecting  $^{79}\text{Br}$  or  $^2\text{H}$  nuclei for the sample potassium bromide KBr or DHMB, respectively. NMR  $^{29}\text{Si}$  -  $^1\text{H}$ ,  $^{11}\text{B}$  and  $^{27}\text{Al}$  chemical shifts were referenced to tetra methyl silane (TMS) and 1M  $\text{Al}(\text{NO}_3)_3$  and 1M  $\text{BF}_3\text{OEt}_2$ , respectively at 0.00 ppm.

## **Chapter C**

The 1D  $^{29}\text{Si}$  CP-MAS (**Figure D.4a**) and  $^{27}\text{Al}$  echo-MAS (**Figure D.4b**) NMR spectra of  $\text{C}_{16}\text{H}_{33}\text{Me}_2\text{EtN}^+$ -directed layered aluminosilicate ( $^{29}\text{Si}$  natural abundance) were collected at a magnetic field of 7T and 17.6 T, respectively by spinning the sample at 10 kHz MAS. The former spectrum was collected over 2k transients with 2 second recycling delay. The magnetization was transferred from  $^1\text{H}$  to  $^{29}\text{Si}$  nuclei via adiabatic passage by matching Hartmann-Hahn condition, contact time was set to 10 ms.  $^{27}\text{Al}$  NMR spectrum was acquired with 256 transients and a 1 second recycling delay. Double frequency sweep (DFS) pulses (1 ms) are used prior to excitation on  $^{27}\text{Al}$  channel to enhance the signal.  $^{29}\text{Si}$  [ $^{29}\text{Si}$ ] DQ-SQ recoupling NMR spectrum (**Figure D.4c**) of  $\text{C}_{16}\text{H}_{33}\text{Me}_2\text{EtN}^+$ -directed layered aluminosilicate ( $^{29}\text{Si}$  enriched) collected at a magnetic field of 7 T. The spinning frequency was set to 4.6 kHz in order to

### Experimental Section

use symmetry-based  $SR26_4^{11}$  recoupling pulses at a  $^{29}\text{Si}$  nutation frequency of  $\approx 30$  kHz ( $6.5 \nu_R$ ) within the probe limits. The recoupling duration was set to 3.5 ms (2 rotor periods) and 2D spectrum was collected over 224 increments in the indirect dimension (F1) for each of 64 transients in the direct dimension (F2) with 3.5 second recycling delay. 90 kHz  $^1\text{H}$  decoupling ( $3 \times ^{29}\text{Si}$  recoupling nutation frequency) and 60 kHz  $^1\text{H}$  decoupling were used during recoupling and acquisition, respectively.

The 2D  $^{27}\text{Al}[^{29}\text{Si}]$  dipolar-mediated HMQC<sup>190</sup> spectrum of  $\text{C}_{16}\text{H}_{33}\text{Me}_2\text{EtN}^+$ -directed layered aluminosilicate was collected for both samples at natural abundance  $^{29}\text{Si}$  (**Figure D.5**) and with 100%  $^{29}\text{Si}$  isotopic enrichment (**Figure D.6**) at a magnetic field of 17.6T and 11.7T, in a 4 mm triple-resonance probehead ( $^{27}\text{Al}$ - $^{29}\text{Si}$  insert) at the MAS rate of 7 and 8 kHz, respectively. The recoupling duration was set to 5.1 ms ( $6 R4_1^2$  symmetry cycles of 6 rotor period) for the former and 2.25 ms ( $6 R4_1^2$  symmetry cycles of 3 rotor period) for the later spectrum, before and after evolution period. The former spectrum was acquired over 32 increments in F1 dimension for each of 4480 transients in F2 dimension with a recycling delay of 1.5 second, while the later spectrum was collected over 28 increments in the F1 dimension for each of 2560 transients in the F2 dimension with a recycling delay of 1 second. 50 kHz  $^1\text{H}$  decoupling was used during both recoupling (CW) and acquisition (SPINAL64). The  $^{29}\text{Si}[^{27}\text{Al}]$  CP-HMQC spectrum shown in Figure D.5 (in red) was collected at a magnetic field of 17.6 T, firstly the magnetization is transferred from  $^1\text{H}$  to  $^{29}\text{Si}$  nuclei via cross-polarisation, and then HMQC sequence was implemented to detect  $^{29}\text{Si}$  in the direct dimension.

2D  $^{27}\text{Al}[^1\text{H}]$  HETCOR NMR spectrum (**Figure C.7**) of  $\text{C}_{16}\text{H}_{33}\text{Me}_2\text{EtN}^+$ -directed layered aluminosilicate ( $^{29}\text{Si}$  natural abundance) was collected at a magnetic field of 20.0 T in a 3.2 mm DBB triple-resonance probehead (3.5 turn coil used to tune  $^1\text{H}$  and  $^{27}\text{Al}$  larmor frequency) by spinning the sample at 18 kHz MAS. The cross-polarisation of  $^1\text{H}$  to  $^{27}\text{Al}$  nuclei (nutation frequency of 3.5 kHz for  $^{27}\text{Al}$  and 16 kHz for  $^1\text{H}$ ) was achieved with Ramp<sup>155</sup> on the  $^1\text{H}$  channel, with a contact time of (a) 0.5 ms, (b) 2 ms, (c) 6 ms and (d) 10 ms. The 2D spectrum acquired over 200 (a, c or d) or 240 (b) increments in the F1 dimension for each of 192 (a or c) or 128 (b or d) transients with 2 second recycling delay. 40 kHz  $^1\text{H}$  decoupling (SPINAL64) was used during acquisition. The total experimental time for collecting all the four 2D spectra is 76 hours.

1D  $^{29}\text{Si}[^1\text{H}]$  CP-MAS and  $^{29}\text{Si}$  quantitative MAS NMR spectra (**Figure C.7**) of  $\text{C}_{16}\text{H}_{33}\text{Me}_3\text{N}^+$ -directed layered aluminosilicate with Si/Al ratio of (b, f) 73, (c, g) 35 and (d, h) 15, were collected at a magnetic field of 9.4 T by spinning the sample at 10 kHz MAS. The contact time was set to 8 ms and each  $^{29}\text{Si}$  [ $^1\text{H}$ ] CP-MAS spectrum collected over 2k transients with a 2 second recycling delay. The  $^{29}\text{Si}$  quantitative MAS spectra were acquired over 144 transients with a recycling delay of 500 second. 50 kHz

### Experimental Section

$^1\text{H}$  decoupling (SPINAL64) employed during acquisition. 1D  $^{27}\text{Al}$  echo-MAS NMR spectra (**Figure C.11**) of  $\text{C}_{16}\text{H}_{33}\text{Me}_3\text{N}^+$ -directed layered aluminosilicate with Si/Al ratio of (a) 15, (b) 35 and (c) 73, were collected at a magnetic field of 20 T by spinning the sample at 18 kHz MAS with 1024 transients and a recycling delay of 1 second.

2D (a)  $^{29}\text{Si}[^{29}\text{Si}]$  refocused INADEQUATE<sup>136</sup> and (b)  $^{29}\text{Si}$  DQ-SQ recoupling NMR spectra of  $^{29}\text{Si}$  enriched  $\text{C}_{16}\text{H}_{33}\text{Me}_3\text{N}^+$ -surfactant directed layered aluminosilicate (**Figure C.12**) were collected at a magnetic field of 7.0 T with spinning frequency of 10 kHz and 4.6 kHz, respectively. The former spectrum acquired over 80 increments in the indirect dimension for each of 96 scans with a recycling delay of 2.2 second. The echo-period was set to 5 ms (50 rotor period) before and after the evolution period.  $^1\text{H}$  decoupling strength 60 kHz (SPINAL64) used during both acquisition and dephasing. While the later spectrum was collected over 80 increments (F1) for each 32 scans (F2) with recycling delay of 2 second. The recoupling duration was set to 3.5 ms (2 rotor period) before and after evolution period.  $^1\text{H}$  decoupling strength 60 and 90 kHz was used during acquisition (SPINAL64) and recoupling (CW), respectively. In both experiments adiabatic shape was used for the cross-polarisation and contact time was set to 5 and 7 ms, respectively.

2D  $^{27}\text{Al}[^1\text{H}]$  HETCOR NMR spectra (**Figure C.13**) of  $\text{C}_{16}\text{H}_{33}\text{Me}_3\text{N}^+$ -surfactant directed layered aluminosilicate synthesized (a) with  $^{29}\text{Si}$  enrichment and (b) at natural abundance  $^{29}\text{Si}$  collected at a magnetic field of 20.0T and sample was spun at a MAS rate of 10 and 18 kHz, respectively. The contact time was set to (a) 0.2 ms and (b) 6 ms. The spectrum was acquired over (a) 218 or (b) 200 increments in the indirect dimension for each of (a) 416 or (b) 32 transients, respectively in the F2 dimension with a recycling delay of 1.5 and 2 sec, respectively. 60 kHz  $^1\text{H}$  decoupling was used (SPINAL64) during acquisition.

2D (d)  $^{29}\text{Si}[^{27}\text{Al}]$  and (c)  $^{27}\text{Al}[^{29}\text{Si}]$   $J$ -mediated HMQC<sup>165</sup> NMR spectrum (**Figure C.14**) of  $^{29}\text{Si}$  enriched  $\text{C}_{16}\text{H}_{33}\text{Me}_3\text{N}^+$ -surfactant directed layered aluminosilicate were collected at a magnetic field of 20.0 T using 3.2 mm triple-resonance probehead ( $^{27}\text{Al}$ - $^{29}\text{Si}$  insert) at the MAS rate of 14 kHz. The former spectrum acquired over 30 increments and 2624 transients with recycling delay of 2 second. Here  $^{29}\text{Si}$  was detected in the direct dimension and  $^{27}\text{Al}$  in the indirect dimension. Magnetization was transferred from  $^1\text{H}$  to  $^{29}\text{Si}$  via adiabatic passage (contact time 7 ms) before the HMQC sequence. The later spectrum was acquired over 48 increments in the indirect dimension for each of 384 transients in the direct dimension where  $^{27}\text{Al}$  nuclei were detected with recycling delay of 2 second. The half-echo delay was set to 5 ms (70 rotor period) and 60 kHz  $^1\text{H}$  decoupling was used during both acquisition and dephasing in both type of experiments. DFS scheme is used prior to  $^{27}\text{Al}$  excitation(c).

## Chapter D

**Figure D.2 and D.3** represent  $^{11}\text{B}$  echo-MAS and  $^{29}\text{Si}$  CP-MAS NMR spectra of  $\text{C}_{16}\text{H}_{33}\text{Me}_3\text{N}^+$ - and  $\text{C}_{16}\text{H}_{33}\text{Me}_2\text{EtN}^+$ -directed layered borosilicates synthesized at natural  $^{29}\text{Si}$  abundance and with 100%  $^{29}\text{Si}$  isotopic enrichment, respectively. For all  $^{11}\text{B}$  excited NMR experiments, double frequency sweep (DFS)<sup>156</sup> preparation sequence was used to enhance the signal. For all  $^{11}\text{B}$  and  $^{29}\text{Si}$  NMR experiments, 50 kHz  $^1\text{H}$  decoupling (SPINAL64) employed during acquisition. **Figure D.2:**  $^{29}\text{Si}[^1\text{H}]$  CP-MAS and  $^{11}\text{B}$  echo-MAS NMR spectra were collected at 17.6 T at the spinning frequency of 7 and 10 kHz (using a 4 mm probehead), respectively.  $^{29}\text{Si}[^1\text{H}]$  CP-MAS spectra acquired with CP contact time of 8 ms and a recycling delay of 2s each, with 4k and 2k transients for  $\text{C}_{16}\text{H}_{33}\text{Me}_3\text{N}^+$ - and  $\text{C}_{16}\text{H}_{33}\text{Me}_2\text{EtN}^+$ -directed layered borosilicate, respectively.  $^{11}\text{B}$  echo-MAS spectra collected for over 4k and 1k transients with 1 and 2 second recycling delay, respectively for  $\text{C}_{16}\text{H}_{33}\text{Me}_3\text{N}^+$ - and  $\text{C}_{16}\text{H}_{33}\text{Me}_2\text{EtN}^+$ -directed layered borosilicate material. **Figure D.3:**  $^{29}\text{Si}[^1\text{H}]$  CP-MAS and  $^{11}\text{B}$  echo-MAS NMR spectra of  $\text{C}_{16}\text{H}_{33}\text{Me}_3\text{N}^+$ - and  $\text{C}_{16}\text{H}_{33}\text{Me}_2\text{EtN}^+$ -directed layered borosilicate were collected at 17.6 T and 9.4 T, respectively at 10 kHz MAS, while  $^{29}\text{Si}[^1\text{H}]$  CP-MAS NMR spectra acquired with contact time of 4 and 8 ms, number of scans 256 and 128 with recycling delay of 2 second, respectively and  $^{11}\text{B}$  echo-MAS spectra acquired for 2k and 4k transients with recycling delay of 2 and 1 second, respectively.

**Figure D.4:**  $^{29}\text{Si}$  [ $^{29}\text{Si}$ ] refocused INQDEQUATE NMR spectra of  $^{29}\text{Si}$  enriched (a)  $\text{C}_{16}\text{H}_{33}\text{Me}_3\text{N}^+$  - and (b)  $\text{C}_{16}\text{H}_{33}\text{Me}_2\text{EtN}^+$  - directed layered borosilicate materials were collected at a magnetic field of 7 T by spinning the sample at 10 kHz, half-echo delay was set to 6 ms. Former 2D spectrum was acquired for over 128 transients (F2) for each of 160 increments (F1) with 2.8 second recycling delay, while the later one is acquired over 96 transients (F2) for each of 184 increments (F1) with a repetition delay of 3.1 second, respectively.

**Figure D.5 and D.12:**  $^{11}\text{B}$  echo-MAS experiments were performed at 17.6 T, at the MAS rate of 14 kHz with recycling delay of 2 second. Transverse dephasing time measurements were done by collecting a series of  $^{11}\text{B}$  echo-MAS spectra with half-echo delay ranging between 0-12 ms (7 increments) over 1024 transients each. Heteronuclear  $^1\text{H}$  decoupling at a nutation frequency of 60 kHz (SPAINAL64) was alternatively turned on and off during the echo (and kept on during the acquisition).

$^{11}\text{B}[^1\text{H}]$  HETCOR NMR spectra were collected at a magnetic field of 17.6 T, at the spinning frequency 14 kHz (using a 4 mm probehead). The magnetization was transferred from  $^1\text{H}$  to  $^{11}\text{B}$  by using adiabatic passage through hartmann-hahn condition.<sup>264</sup> CP contact time was set to 1 and 0.1 ms to collect the spectra of  $\text{C}_{16}\text{H}_{33}\text{Me}_3\text{N}^+$ - (**Figure D.6**) and  $\text{C}_{16}\text{H}_{33}\text{Me}_2\text{EtN}^+$ - (**Figure D.13**) materials ( $^{29}\text{Si}$  natural

## Experimental Section

abundance), respectively. The signal in the 2D  $^1\text{H}$  dimension was accumulated over 96 increments with 176 transients each for the former and 128 increments with 64 transients each for the later. Heteronuclear  $^1\text{H}$  decoupling at a nutation frequency of 70 kHz was applied during acquisition. Both spectra were collected using a repetition delay of 2 second.

Two-dimensional  $^{11}\text{B}$  [ $^{29}\text{Si}$ ] dipolar- and  $J$ -mediated HMQC spectra were collected at 9.4 T on materials synthesized with  $^{29}\text{Si}$  enrichment, at a MAS frequency of 10 kHz (using 3.2 mm triple-resonance probehead). The heteronuclear dipolar couplings between  $^{11}\text{B}$  and  $^{29}\text{Si}$  species were reintroduced in dipolar-mediated  $^{11}\text{B}$  [ $^{29}\text{Si}$ ] HMQC by means of  $R4^2_1$  symmetry-based dipolar recoupling<sup>181,189-190,216</sup> scheme at a  $^{29}\text{Si}$  nutation frequency of 20 kHz ( $2\nu_R$ ). The recoupling durations were set to 6 ms (10 symmetry cycles of 6 rotor periods each) before and after the evolution period. Signal was acquired with 96 increments (1024 transients) and a repetition delay of 2.17 second for  $\text{C}_{16}\text{H}_{33}\text{Me}_2\text{EtN}^+$ - material (**Figure D.18, blue**) and 80 increments (1536 transients) with a repetition delay of 2.5 second for  $\text{C}_{16}\text{H}_{33}\text{Me}_3\text{N}^+$ - material (**Figure D.9**). The poor signal to noise of the 2D spectra as a result of long recoupling duration led to experimental duration of 61 hours for the former and 88 hours for the latter. The half-echo delay before and after the evolution period in the  $^{11}\text{B}$  [ $^{29}\text{Si}$ ]  $J$ -mediated HMQC<sup>165</sup> experiments were optimized experimentally to 10 and 12.5 ms for the  $\text{C}_{16}\text{H}_{33}\text{Me}_3\text{N}^+$ - (**Figure D.8**) and  $\text{C}_{16}\text{H}_{33}\text{Me}_2\text{EtN}^+$ - (**Figure D.18, red**) materials, respectively. Signal was accumulated in the indirect dimensions with 32 increments (2304 scans each) for the former and 96 increments for the latter (768 transients each) materials. Recycling delays of 3 second for both materials led to experimental durations of 62 and 63 hours, respectively. Heteronuclear  $^1\text{H}$  decoupling (SPINAL64 sequence) at a nutation frequency of ca. 60 kHz was applied during the whole sequence.

## Chapter E

$^{27}\text{Al}$  MAS NMR spectrum of synthetic (**Figure E.3a**) and natural (**Figure E.3b**) montmorillonite was collected a magnetic field of 17.6 and 20.0 T, respectively at the MAS rate 64 kHz. The signal was accumulated over 568 transients with 1 second recycling delay for the former material, while for the later longitudinal relaxation rates was generated through variations of the recycling delays from 0.01 s (with 2048 transients and 128 dummy transients to reach the steady state) to 0.1 s (with 1024 transients and 32 dummy transients) and 1s (512 transients, 8 dummy transients). Heteronuclear  $^1\text{H}$  low-power XiX decoupling at a  $^1\text{H}$  nutation frequency of 12.5 kHz was applied during acquisition.

**Figure E.2:** The quantitative  $^{29}\text{Si}$  MAS experiment of synthetic montmorillonite was performed at 7.0T magnetic field by spinning the sample at 10 kHz MAS frequency with a recycling delay of 1000 second

### Experimental Section

and 96 transients using SPINAL64 heteronuclear  $^1\text{H}$  decoupling.  $^{29}\text{Si}[^1\text{H}]$  CP-MAS was collected with same condition, where signal was accumulated over 2048 transients using contact time of 10 ms with an adiabatic CP condition, and a recycling delay of 2 second.  $^{29}\text{Si}$  NMR experiment of natural montmorillonite was obtained at 9.4 T, using a 7 mm double resonance probe at the MAS frequency of 5 kHz. The signal was accumulated over 10240 transients with 200 ms recycling delay, and  $^1\text{H}$  decoupling (SPINAL 64) was applied during acquisition.

**Figure E.4:** The 2D  $^{27}\text{Al}[^{29}\text{Si}]$  dipolar-mediated HMQC spectrum of synthetic montmorillonites was collected at 17.6 T, at a MAS frequency of 5 kHz. Four SR4 $^2_1$  blocks (24 rotor period) were used before and after detection at the  $^{29}\text{Si}$  nutation frequency of 10 kHz, in which the total recoupling duration was set to 9.6 ms. The signal was accumulated in the indirect dimension with 32 increments and 4096 transients for each increment. DFS preparation period is used to enhance the  $^{27}\text{Al}$  signal, with a pulse length of 1 ms and a sweep range of between 0.1 and 1.5 MHz.

**Figure E.5:**  $^{25}\text{Mg}$  NMR spectra of synthetic and natural montmorillonites were collected at 20 T, using a 4 mm double resonance probehead, at MAS frequency of 14 kHz and signal was accumulated over 32k and 1792 k transients with recycling delay of 1 s and 50 ms, respectively. Carr-Purcell-Meiboom-Gill (CPMG) acquisition and DFS pulse of 1 ms and sweep range between 0.1 and 1.5 MHz, was used to improve the signal to noise. The CPMG acquisition consisted here of 15 full echoes and 4 ms separations between central-transition-selective  $180^\circ$  pulses of 20  $\mu\text{s}$ , with a recycling delay of 250 ms, and 512 transients for signal accumulation. Direct Fourier transform of the CPMG echo-train leads to spectra consisting of multiple sharp lines whose envelope reproduces the ordinary spectrum. An alternative processing of the data set, performed with Dmfit,<sup>265</sup> consists in making the Fourier transform of the sum of individual echoes to recover a conventional powder pattern.

**Figure E.6:** 1D  $^1\text{H}$  experiments were performed at 17.6 T using a 1.3 mm double-resonance probehead by spinning the sample at 64 kHz. The quantitative  $^1\text{H}$  echo-MAS NMR experiment was performed with short echo duration of 8 rotor period to remove completely the background signals, using 16 transients with a recycling delay of 15 second. For  $^1\text{H}[^{27}\text{Al}]$  NMR experiment, cross-polarization of  $^1\text{H}$  to  $^{27}\text{Al}$  was achieved using amplitude ramps (50-100% of the maximum amplitude) with 1 ms contact time. The signal was acquired over 256 transients with 1 s recycling delay.  $^{29}\text{Si}[^1\text{H}]-^1\text{H}[^{29}\text{Si}]$  double CP experiment was collected by optimizing the contact time of  $^{29}\text{Si}[^1\text{H}]$  CP to 5 ms and  $^1\text{H}[^{29}\text{Si}]$  to 2 ms, in order achieve selective cross-polarisation to protons in close proximity to the  $^{29}\text{Si}$  nuclei. The signal was collected with 2048 transients, and a recycling delay of 2 s.

## Experimental Section

**Figure E.10:**  $^{11}\text{B}$  solid state echo-MAS NMR spectrum (**Figure E.10a**) was collected on a 9.4 T Bruker Avance I spectrometer at a Larmor frequency of 128.37 MHz using a 3.2 mm triple resonance probehead. Low-power selective  $90^\circ$  and  $180^\circ$  pulses of 13.5 and 27  $\mu\text{s}$  were used to excite the central transition. An echo delay of 0.06 ms was used to remove the  $^{11}\text{B}$  background signal due to the BN probe stator. The sample was spun at a MAS rate of 16 kHz, and signal enhancement was achieved by means of a double-frequency sweep (DFS) preparation.<sup>156</sup> The signal was accumulated over 16 transients with a relaxation delay of 8 seconds. The quantitative  $^{29}\text{Si}$  solid-state MAS NMR experiment (**Figure E.10b**) was performed at room temperature on 4.7 T Bruker Avance I wide bore spectrometer using a 7 mm MAS probehead at a Larmor frequency of 39.75 MHz. The signal was accumulated over 648 transients with a 3600 second recycling delay, at a spinning frequency of 5 kHz. Two dimensional  $^{11}\text{B}$  z-filtered MQ-MAS<sup>266,267</sup> NMR spectrum (**Figure E.11**) was collected on a 9.4 T Bruker Avance I spectrometer using 4 mm DR probehead. The excitation and conversion pulse lengths were optimized to 3.4 and 1.2  $\mu\text{s}$  respectively. The sample was spun at a MAS frequency of 14 kHz. A selective  $90^\circ$  pulse of 12  $\mu\text{s}$  was utilized to bring back magnetization to Z-axis before acquiring the signal. A z-filter delay of 0.5 ms was used. The signal was acquired over 24 scans for each of 192 increments with a separation delay of 1 second. The deconvolutions of NMR spectra were achieved with the Dmfit program.<sup>265</sup>

1D solid-state NMR experiments of  $^{29}\text{Si}$  enriched  $\text{CaSi}_{1/3}\text{B}_{2/3}\text{O}_{8/3}$  phase as shown in the **Figure E.13** were performed at a magnetic field of 9.4 T.  $^{29}\text{Si}$  echo-MAS NMR spectrum (**Figure E.13a**) was acquired over 4 transients with a recycling delay of 3600 second at the MAS rate of 12.5 kHz.  $^{29}\text{Si}[^{11}\text{B}]$  CP-MAS NMR spectrum (**Figure E.13b**) was collected over 64 scans with a recycling delay of 1 second by spinning the sample at 18 kHz MAS. The contact time was set to 10 ms.  $^{29}\text{Si}[^{11}\text{B}]$  INEPT NMR spectrum (**Figure E.13c**) collected over 7424 transients with 8 second recycling delay at the MAS rate of 18 kHz. The first and second half-echo delay was set to 12.5 ms and 29.1 ms, respectively.  $^{29}\text{Si}[^{29}\text{Si}]$  DQ recoupling NMR spectrum (**Figure E.12d**) was acquired over 4 transients with a recycling delay of 3600 second at the MAS rate of 8 kHz. The recoupling duration was set to 6 ms (6 symmetry cycles of 6 rotor period) before and after the evolution period.  $^{29}\text{Si}[^{29}\text{Si}]$  refocused-INADEQUATE NMR experiment (**Figure E.12e**) was carried in 4 transients with a recycling delay of 3600 second at the spinning frequency of 12.5 kHz.

---

## *Appendix B*

### *Symbols and abbreviations*

---

NMR	Nuclear Magnetic Resonance
1D	One-dimensional
2D	Two-dimensional
I	Spin quantum number
J	Scalar coupling
$\gamma$	Gyromagnetic ratio
$B_0$	External magnetic field
$J_{IS}$	<i>J</i> -coupling between spins I and S
CSA	Chemical Shift Anisotropy
EFG	Electric Field Gradient
MAS	Magic Angle Spinning
SQ	Single Quantum
DQ	Double Quantum
INADEQUATE	Incredible Natural Abundance Double QUAntum Transfer Experiment
HMQC	Heteronuclear multiple-quantum correlation
HETCOR	Heteronuclear correlation
CP-MAS	Cross polarization magic angle spinning
SP	Single Pulse
DFT	Density Functional Theory
ppm	Parts per million
GIPAW	Gauge Including Projector Augmented Waves
eV	Electron Volt
SPINAL	Small-Phase INcremental ALteration (decoupling)

*Symbols and abbreviations*

EPR	Electron spin resonance
ICP	Inductively Coupled Plasma
IR	Infrared
XRD	X-ray diffraction
TEM	Transmission electron microscopy
SEM	Scanning electron microscopy
FWHM	Full width at half maximum

**Résumé de thèse  
en Français**

# Table des Matières

Introduction	3
Chapitre A. Revue de la littérature sur les matériaux silicates poreux et lamellaires	5
Chapitre B. Méthodes et matériaux	10
Chapitre C. Etude de la structure locale autour d'hétéroatomes d'Al dans les silicates en Feuillet auto-assemblés en présence de surfactants	14
Chapitre D. Structure locale résultant de l'incorporation de bore dans les silicates en feuillet non-cristallins	20
Chapitre E. Extension à l'étude de la substitution atomique dans d'autres matériaux	27
Conclusions et Perspectives	34
Résumé des annexes	35
Symboles et Abréviations	35
Résumé court (en Anglais et en Français)	37

## ***Introduction***

La compréhension fine de la structure de matériaux permet de contrôler leurs propriétés, et donc leur impact sur notre vie quotidienne. Les matériaux silicatés (basés sur la composition  $\text{SiO}_2$ ) forment l'une des classes les plus importantes de matériaux qui ont été et continuent d'être étudiés en raison de leur faible coût et toxicité. Ils incluent des exemples aussi célèbres que les zéolites, les argiles, ou les silices (méso-)poreuses. L'incorporation au sein de matrices silicatées d'hétéroatomes leur confèrent une vaste gamme de propriétés qui ont été exploitées dans de nombreux domaines d'application, parmi lesquels figure notamment la catalyse hétérogène, qui représente un énorme enjeu industriel. Des exemples importants d'hétéroatomes utilisés dans ce contexte sont les atomes trivalents (Al, Ga,  $\text{Fe}^{\text{III}}$ ) dont le déficit de charge par rapport aux atomes de Si (tétravalents) qu'ils substituent génère une acidité locale, source d'activité catalytique. La présence de tels atomes est susceptible de modifier la structure locale du réseau du fait des différences de rayon ionique et/ou de la nécessité de compenser cette charge. Cela induit généralement un désordre local qui rend la caractérisation structurale de ces environnements locaux particulièrement délicate. Pourtant le contrôle de la localisation des hétéroatomes au sein du réseau et des modifications structurales locales qu'ils engendrent est fondamental pour optimiser les propriétés macroscopiques, et cela reste aujourd'hui un défi majeur en science des matériaux.

L'incorporation préférentielle d'hétéroatomes au sein d'un site cristallographique unique et bien défini dans les réseaux de silicates ordonnés à l'échelle moléculaire, en particulier dans les zéolites, est une tâche extrêmement complexe. Cela est dû en partie à la difficulté de caractériser à l'échelle moléculaire la structure locale résultant de cette incorporation. Les méthodes les plus puissantes de caractérisation structurales disponibles actuellement, basées sur la diffraction, reposent sur l'existence d'une répétition à plus ou moins longue distance de motifs structuraux locaux, lesquels sont perturbés par la présence d'hétéroatomes. Dans ce contexte, les méthodes de caractérisation locales, et notamment la résonance magnétique nucléaire (RMN) ont en principe la capacité de jouer un rôle déterminant pour répondre à cette problématique. Pourtant, en dépit de nombreuses études menées au cours des dernières décades, l'environnement local autour des hétéroatomes dans les matériaux silicates est encore mal connu. Un autre obstacle pour le contrôle des sites d'incorporation d'hétéroatomes dans les zéolites est la grande similitude chimique des différents sites cristallographiques correspondant aux sites de substitution potentiels. Les zéolites sont en effet constituées de réseaux de tétraèdre de  $\text{SiO}_4$  entièrement interconnectés, c'est-à-dire que chaque atome de Si est connecté à quatre autres par des oxygènes pontant (et désignés par le symbole  $Q^4$ ) de sorte que les différents sites cristallographiques ne diffèrent que par l'arrangement géométrique des tétraèdres adjacents.

Une voie alternative pour contrôler la distribution d'hétéroatomes dans les zéolites consiste à les incorporer d'abord dans les silicates lamellaires, dont les feuillets peuvent ensuite être condensés de manière à obtenir des zéolites de structures 3D proches du réseau 2D de départ. A la différence des zéolites, les silicates en feuillet présentent des sites connectés à seulement 3 atomes Si voisins par des oxygènes pontant, le dernier oxygène du tétraèdre  $\text{SiO}_4$  étant dit non-pontant ; de tels environnements sont désignés par le symbole  $Q^3$ . La présence de tels environnements, en plus des sites  $Q^4$ , dont ils diffèrent chimiquement, au sein du réseau, permet de supposer que des préférences marquées pour la substitution d'hétéroatomes pourraient apparaître dans les silicates en feuillet, et la démonstration de ce principe a été l'un des objectifs principaux de cette thèse.

Les travaux ont porté essentiellement sur l'incorporation d'hétéroatomes de B ou d'Al au sein d'un type particulier de silicates en feuillet auto-assemblés en présence de surfactants alkyl-ammonium, qui sont en quelque sorte les « ancêtres » d'une nouvelle classe de matériaux : les zéolites nanostructurées, sur lesquels se focalise un grand intérêt aujourd'hui (suite aux travaux de Ryoo et collaborateurs). Le chapitre A replace ces travaux de thèse dans son contexte à travers une revue de la littérature sur la synthèse, la caractérisation, et les applications des matériaux silicatés poreux et lamellaires. Le chapitre B donne les grandes lignes des techniques expérimentales et computationnelles utilisées dans le contexte de cette thèse, et décrit la synthèse des matériaux boro- et aluminosilicates étudiés. Les chapitres C et D décrivent respectivement l'étude de l'incorporation d'hétéroatomes d'Al et de B au sein de nos systèmes modèles de silicates en feuillet. Enfin, le dernier chapitre (E) ouvre ces travaux sur une perspective plus large en montrant comment des approches similaires peuvent être appliquées pour caractériser les substitutions atomiques dans d'autres classes de matériaux : une nouvelle phase borosilicate de calcium synthétisée à haute température et une argile de synthèse étudiée notamment comme barrière de polluant: la montmorillonite.

---

## **Chapitre A: Revue de la littérature sur les matériaux silicates poreux et lamellaires**

---

**A.1 Introduction.** L'objectif de ce chapitre est de survoler les avancées principales, les applications et enjeux de la recherche sur les matériaux silicatés poreux et lamellaires, afin de définir le contexte notre étude portant sur la structure locale autour d'hétéroatomes.

**A.2 Matériaux silicates poreux et RMN à l'état solide.** On donne dans cette section une définition générale des matériaux hybrides organiques-inorganiques, et présente une classification de ces matériaux en fonction du (ou des) type(s) d'interactions sévissant aux interfaces organiques-inorganiques (Van-der-Waals, électrostatiques, liaisons hydrogène, liaisons covalentes...), de leurs architectures, et de leurs compositions. Les principes généraux, les avantages et les inconvénients des principales méthodes de synthèse de matériaux silicatés hybrides organiques-inorganiques y sont brièvement décrits :

- la voie sol-gel basée sur la tendance des milieux de synthèse contenant à la fois des particules solides et du liquide à former des gels,
- la synthèse hydrothermale, dans lesquels le matériau se forme sous pression dans un autoclave porté à température relativement élevée (typiquement autour de 150°C pour les zéolites, généralement préparées par cette voie).

Dans ces deux approches, la fraction organique joue un rôle de « template » autour duquel le réseau inorganique se forme, ce qui confèrera éventuellement au matériau sa structure de pores, après élimination de la fraction organique. La fonctionnalisation de ces matériaux peut intervenir directement au cours de la synthèse ou par voie post-synthétique.

Enfin, un dernier volet de la section A.2 précise le rôle joué par la caractérisation locale par la spectroscopie de RMN d'abord dans la science des matériaux en général, en complément des principales autres méthodes de caractérisation, puis appliquée à l'étude de matériaux silicatés. On y liste, sans rentrer dans les détails de la technique, les différents noyaux observables et le type d'informations qui peuvent être obtenues : coordinence, nombre et type d'atomes voisins (connectés ou non), l'existence de liaisons chimiques, les proximités spatiales...

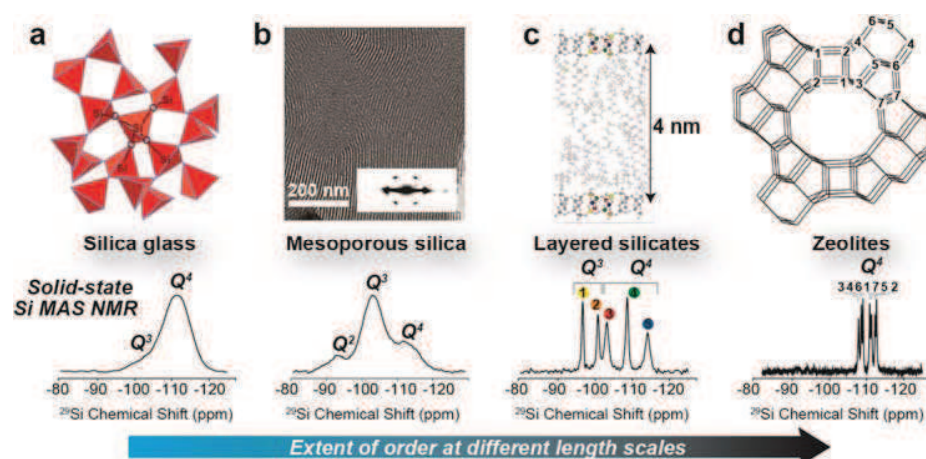


**Figure A.1** [Ref: Massiot et.al. C.R. Chimie 2010] Différents types de matériaux silicatés classés par degré croissant d'ordre à différentes échelles, avec les spectres RMN du  $^{29}\text{Si}$ , qui renseignent sur le degré d'ordre à l'échelle moléculaire et le degré de polymérisation du réseau.

**A.3 Les matériaux composites à base de silicates en feuillet.** Cette section présente un survol de la conception et de la caractérisation structurale de matériaux composites à base de silicates. On présente brièvement les différents type de matériaux qui peuvent entrer dans cette catégorie, parmi lesquels figurent notamment les argiles, avant de se focaliser plus spécifiquement sur les silicates auto-assemblés en présence de surfactants alkyl-ammonium, qui constituent le principal objet d'étude de ce travail de thèse.

Comme dans de nombreux matériaux mésoporeux, les molécules amphiphiles (comportant une partie hydrophile et une partie hydrophobe) de surfactants alkyl-ammonium jouent un rôle fondamental dans la formation de la structure lamellaire de tels matériaux : c'est le rôle de « template » décrit plus haut. De plus, la charge (positive) de leur tête hydrophile et ses interactions avec le réseau inorganique (chargé négativement) sont la clé du développement d'un fort degré d'ordre atomique moléculaire au sein de chaque feuillet. Ces concepts fondamentaux sont présentés à travers la revue de plusieurs études antérieures à ces travaux de thèse, et portant sur les différentes étapes de la formation de ces matériaux. Elles portent sur deux exemples particuliers : les silicates en feuillets auto-assemblés en présence de surfactants (i)  $\text{C}_{16}\text{H}_{33}\text{Me}_3\text{N}^+$  et (ii)  $\text{C}_{16}\text{H}_{33}\text{Me}_2\text{EtN}^+$ , au sein desquels l'incorporation d'hétéroatomes d'Al et de B a été étudiée au cours de cette thèse.

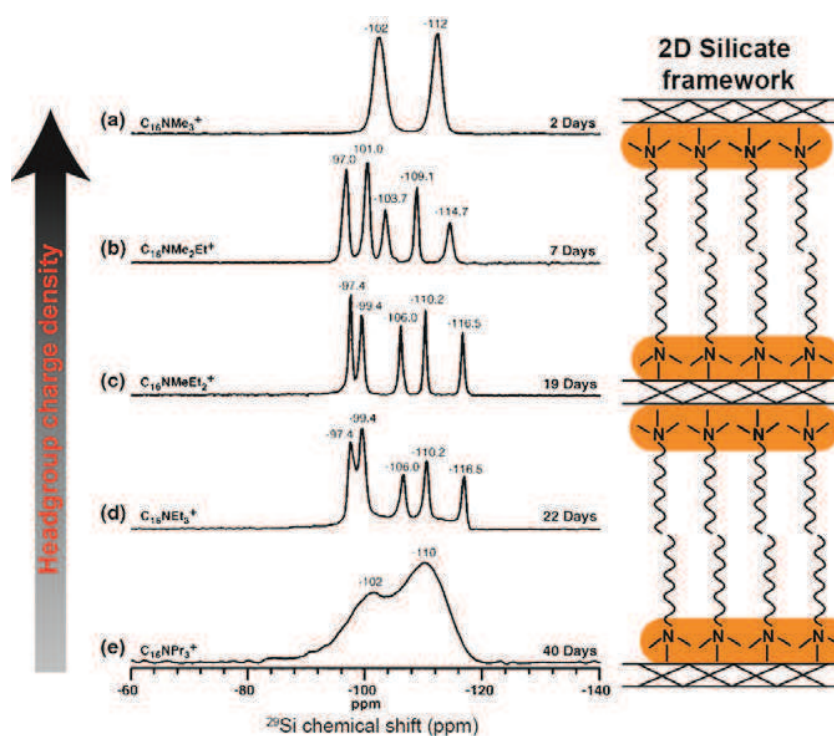


**Figure A.2** [Ref: Christiansen et.al. *J. Am. Chem. Soc.* 2001] Spectres RMN du  $^{29}\text{Si}$  de silicates en feuillets auto-assemblés en présence de surfactants qui diffèrent par la densité de charge de leur tête hydrophile : (a)  $\text{C}_{16}\text{H}_{33}\text{Me}_3\text{N}^+$  (b)  $\text{C}_{16}\text{H}_{33}\text{Me}_2\text{EtN}^+$  (c)  $\text{C}_{16}\text{H}_{33}\text{MeEt}_2\text{N}^+$  (d)  $\text{C}_{16}\text{H}_{33}\text{Et}_3\text{N}^+$  and (e)  $\text{C}_{16}\text{H}_{33}\text{Pr}_3\text{N}$ , avec les temps nécessaires pour la cristallisation complète (lorsque cela est possible) des feuillets. Le schéma de droite est une représentation grossière de la structure lamellaire de ces matériaux.

L'absence quasi complète d'ordre cristallographique tridimensionnel (3D) à longue distance dans ces matériaux limite fortement la quantité d'information qui peut être obtenue par les méthodes de diffraction. Cette section montre comment la structure moléculaire, ordonnée à courte échelle, au sein des feuillets, a cependant pu être déterminée (là encore au cours de travaux antérieurs à cette thèse) en combinant des méthodes multidimensionnelles avancées de RMN à l'état solide combinées au calcul moléculaire, et notamment le calcul par la théorie de la fonctionnelle de la densité (DFT).

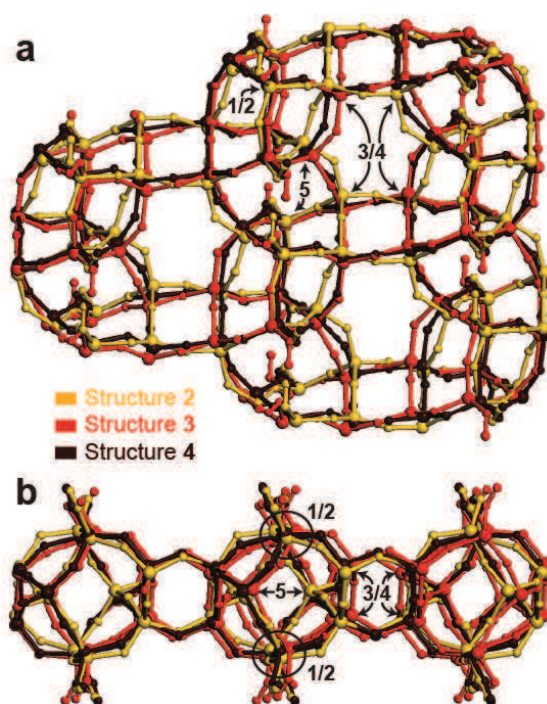


**Figure A.3** [Ref: Brouwer et.al. *J. Am. Chem. Soc.* 2013] Superposition (en vue de haut et de côté) de 3 structures de réseau possibles établies pour les silicates en feuillet auto-assemblés en présence de surfactants  $C_{16}H_{33}Me_2EtN^+$  à partir de données croisées de DRX, RMN et calcul DFT.

**A.4 Les hétéroatomes et leur rôle dans les matériaux silicates poreux et lamellaires.** L'un des champs d'application les plus importants des matériaux silicatés poreux et lamellaires est la catalyse hétérogène. Leur activité catalytique est directement liée à l'acidité découlant de leur composition, et notamment du type et de la quantité d'hétéroatomes incorporés au sein du réseau. Les conséquences de la présence de tels hétéroatomes au sein de matrices silicatées poreuses ou lamellaires sont présentées dans cette section. On y passe également en revue une partie des intenses efforts de recherche qui ont été et sont encore aujourd'hui consacrés à la possibilité de contrôler l'incorporation préférentielle, voire sélective, de ces hétéroatomes au sein de sites cristallographiques spécifiques.

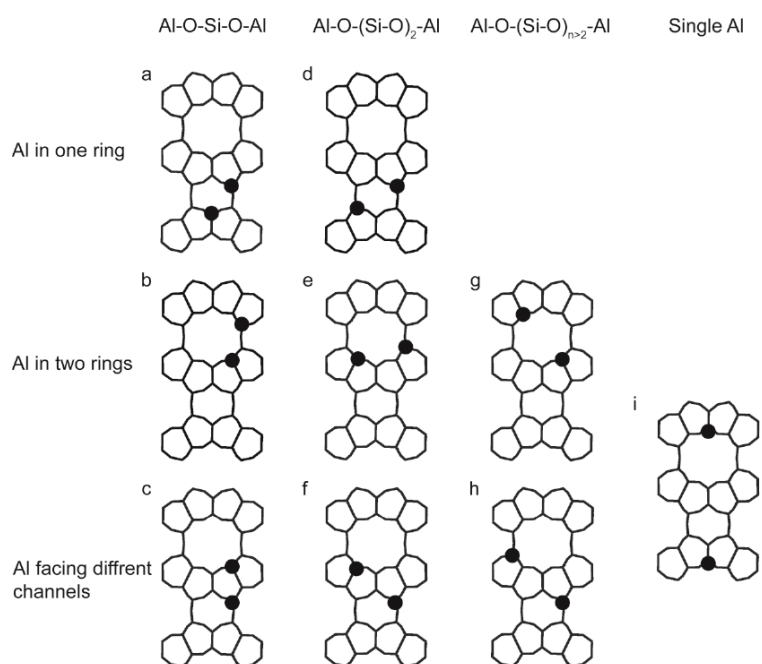


**Figure A.4** [Ref: Dedecek et. al. Chem. Mater. 2012] Distribution d'atomes d'Al dans différentes structures cycliques au sein de zéolites.

La substitution sélective de sites cristallographiques judicieusement choisis est en effet supposée offrir un degré de contrôle encore jamais atteint de la réactivité de ces matériaux. Quelques exemples de résultats particulièrement intéressants obtenus sur cette voie dans le cas des zéolites sont discutés. Ces exemples se concentrent plus particulièrement sur le cas de l'incorporation d'hétéroatomes d'Al et de B qui font l'objet de ce travail de thèse.

---

## Chapitre B : Méthodes et Matériaux

---

**B.1 Introduction.** Le développement de puissantes méthodes de caractérisation ouvre la voie d'une compréhension toujours plus fine, à différentes échelles, de la structure des matériaux silicatés. Ce chapitre se focalise sur les concepts de base des différentes techniques expérimentales et théoriques utilisées dans le cadre de cette thèse, ainsi que sur les méthodes de synthèses mises en jeu lors de la préparation des matériaux.

**B.2. La mesure et l'exploitation des interactions de RMN.** La RMN étant la principale technique utilisée dans ce travail, une large section lui est consacrée. Elle passe en revue les différentes interactions potentiellement mises en jeu dans une expérience de RMN, en comparant leurs ordres de grandeur, leurs effets sur les spectres, et les différents moyens technique ou méthodologiques permettant soit de s'en affranchir lorsqu'elles sont gênantes, soit de les exploiter lorsqu'elles sont en mesure de fournir des informations structurales pertinentes. Ces interactions incluent notamment :

- l'interaction Zeeman qui sépare en fréquence tous les noyaux actifs en RMN ( $^1\text{H}$ ,  $^{29}\text{Si}$ ,  $^{17}\text{O}$ ,  $^{27}\text{Al}$ ,  $^{11}\text{B}$ ...) proportionnellement au champ magnétique externe appliqué et permet de détecter les signaux correspondants de manière indépendante,
- le déplacement chimique qui détermine (dans les cas les plus simples) la position des pics sur un spectre de RMN, et qui traduit dépend fortement de l'environnement local d'un noyau donné,
- l'interaction quadripolaire, résultant de l'interaction entre les gradients de champ électrique locaux et le moment quadripolaire (Figure B.1) des noyaux de spin nucléaire  $I > \frac{1}{2}$  ( $^{17}\text{O}$ ,  $^{27}\text{Al}$ ,  $^{11}\text{B}$ ). Elle constitue une signature de l'environnement local souvent complémentaire de l'interaction de déplacement chimique dans les solides, mais peut aussi être source d'élargissement très problématique des spectres.

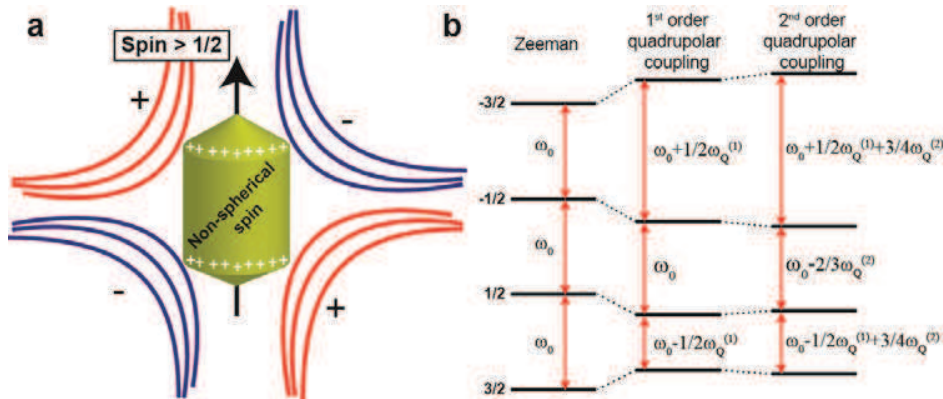


**Figure B.3** (a) Interaction de d'un spin à "non-sphérique" (de  $spin > 1/2$ ) avec le gradient de champ électrique local. (b) Diagramme de niveaux d'énergie pour un spin-3/2 sujet à l'interaction quadripolaire de premier et second ordre.

- l'interaction dipôle-dipôle (ou dipolaire) entre noyaux du même type (« homonucléaire ») ou de types différents (« hétéronucléaires ») à travers l'espace. Cette interaction est directement liée aux distances internucléaires et peut être exploitée pour sonder les proximités spatiales, et même mesurer des distances internucléaires.

- L'interaction de couplage scalaire (J) est une sonde directe de l'existence de liaisons chimiques (covalentes ou liaisons H), qu'elle permet de mettre en évidence. Son utilisation dans le cas des solides peut être plus délicate que l'interaction dipolaire du fait de sa plus faible intensité.

Toutes ces interactions peuvent être mises en jeu simultanément ou (ce qui est souvent préférable) séparément dans des méthodes basées sur des séries d'impulsions radiofréquences (RF) de durée, intensité et phase judicieusement choisies. Cette section décrit le principe général permettant de collecter des expériences de RMN bidimensionnelles (2D) dans lesquels deux types d'information différents peuvent être corrélés pour décupler la quantité d'information locale pouvant être obtenue sur le système considéré. La mise en œuvre de telles techniques dans les systèmes à l'état solide nécessite toutefois l'emploi de nombreuses astuces technologiques et méthodologiques aujourd'hui bien établies, et qui sont également présentées dans cette section. Elles ont pour but de s'affranchir des interactions responsables d'élargissement spectral et/ou de perte de cohérence du signal, qui se traduisent par des pertes parfois dramatique de résolution et/ou de sensibilité. Ces techniques incluent par exemple la rotation à l'angle magique (MAS) permettant de s'affranchir des composantes anisotropes des interactions de déplacement chimique (réduite à sa composante isotrope) et dipolaire (annulée dans la plupart des cas, ce qui veut dire qu'elle doit être réintroduite par le biais d'impulsions RF si on souhaite l'exploiter). Le découplage

hétéronucléaire permet de s'affranchir des couplages entre noyaux dits « rares » ( $^{29}\text{Si}$  par exemple) et/ou de bas rapport gyromagnétique et les spins abondants à fort  $\gamma$  comme les  $^1\text{H}$ . Enfin, la polarisation croisée permet de transférer le signal de ces spins abondants à fort  $\gamma$  vers les spins (éventuellement rares) à faible  $\gamma$  et d'augmenter ainsi considérablement le signal associé.

Les deux sections suivantes sont dédiées à la description du principe général des expériences les plus récentes (et les plus performantes) dédiées à l'exploitation des couplages scalaires et des couplages dipolaires pour sonder respectivement l'existence de liaisons chimiques et les proximités spatiales. On distingue dans les deux cas les expériences homo-nucléaires des expériences hétéro-nucléaires, les dernières étant particulièrement intéressantes lorsqu'on souhaite sonder la structure locale du réseau silicaté (via les noyaux de  $^{29}\text{Si}$ ) autour d'hétéroatomes de (B ou Al par exemple), ce qui représente un des points principaux de cette thèse.

**B.2. Autres méthodes expérimentales et computationnelles.** Cette section présente les différentes techniques qui ont été employées en complément de la RMN pour analyser les matériaux étudiés. On y présente tout d'abord la diffraction des rayons X, qui, dans le cadre de systèmes lamellaires non-cristallins donne un accès direct à l'ordre mésoscopique (empilement des feuillettes) et à la distance inter-feuillettes. Elle permet aussi de sonder l'existence d'un degré même assez faible d'ordre moléculaire à longue distance au sein des feuillettes de silicates. Les quantités relatives de Si, Al et/ou B dans les échantillons ont été mesurées par la méthode « Inductively Coupled Plasma » (ICP) dont le principe général est également brièvement décrit.

Une section importante est dédiée à la présentation des grands principes régissant la modélisation moléculaire par la théorie de la fonctionnelle de la densité (DFT), et notamment l'approche sur base d'ondes planes, qui permet de traiter des solides infinis grâce aux conditions aux limites périodiques. Couplée avec l'utilisation de pseudo-potentiels pour décrire les électrons de cœur, et leurs interactions avec les électrons de valence, cette approche permet de calculer les propriétés fines de systèmes comportant des nombres d'atomes relativement grands (plusieurs centaines). On décrit ensuite l'approche « Gauge-Including Projector-Augmented Waves » (GIPAW) qui permet la prédiction dans le cadre de ce formalisme des tenseurs d'écrantage magnétique, qui peuvent ensuite être reliés aux déplacements chimiques pour une comparaison avec les paramètres RMN expérimentaux. Pour une plus grande précision des calculs, la relation entre le déplacement chimique et l'écrantage est estimée empiriquement à partir de séries de calculs réalisés sur des composés modèles cristallins de structure et de paramètres RMN connus, ce qui permet d'établir les courbes de calibrations présentées dans la Figure B.2. Elles permettent notamment de s'affranchir d'erreurs systématiques résultant des approximations de la DFT.

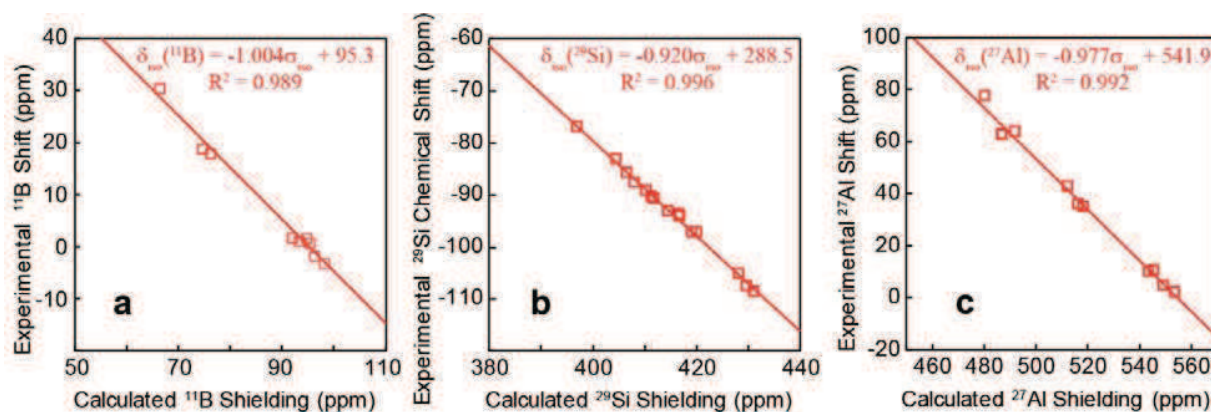


**Figure B.2** Courbes de corrélation entre déplacement chimique expérimental et écrantage calculé par la méthode GIPAW, établies à partir de composés cristallins de référence de structures connues pour les noyaux de (a)  $^{29}\text{Si}$ , (b)  $^{11}\text{B}$  et (c)  $^{27}\text{Al}$ .

**B.4 Synthèses des matériaux étudiés.** Les silicates en feuillet étudiés dans le cadre de ce travail ont tous été synthétisés en conditions hydrothermales à partir de notamment de différents précurseurs de silicium (silice, tétraméthoxy orthosilicate : TMOS) et de surfactants alkyl ammonium ( $\text{C}_{16}\text{H}_{33}\text{Me}_2\text{EtN}^+$ ,  $\text{Br}^-$  ou  $\text{C}_{16}\text{H}_{33}\text{Me}_3\text{N}^+$ ,  $\text{Br}^-$ ) commerciaux dans un mélange méthanol-eau. Le pH du mélange est ajusté à 11.5, puis la mixture est chauffée à  $135^\circ\text{C}$  dans un autoclave pendant plusieurs jours (entre 2 et 14 suivant les matériaux) avant d'être lavé, filtré, et séché à l'air. L'incorporation de B ou Al est obtenue en rajoutant des précurseurs ( $\text{B}(\text{OH})_3$  ou  $\text{NaAlO}_2$ , respectivement) choisis à la suite de différents essais (réalisés à UC Santa Barbara). L'enrichissement isotopique en  $^{29}\text{Si}$  a fait l'objet de gros efforts d'optimisation du fait de la nature du précurseur (de la silice enrichie à 99.9% en  $^{29}\text{Si}$ ), et de la grande difficulté à l'hydrolyser entièrement (contrairement au TMOS qui s'hydrolyse très facilement). Un protocole relativement robuste permettant d'obtenir des comportements de synthèse assez similaires en utilisant de la silice non-enrichie et celle enrichie (de morphologies et propriétés macroscopiques parfois très différentes) a pu être établi. Il permet de tester les synthèses avant d'utiliser la couteuse silice enrichie (6 k€ par gramme de  $^{29}\text{Si}$ ).

La synthèse du borosilicate de calcium étudié dans le Chapitre E est effectuée par recristallisation (pendant 2h) à  $750^\circ\text{C}$  d'un verre de composition  $\text{Ca}_3\text{B}_2\text{SiO}_8$ . Le verre initial est obtenu par trempé d'un mélange vitrifiable des oxydes primaires porté à  $1300^\circ\text{C}$ .

---

## Chapitre C : Etude de la structure locale autour d'hétéroatomes d'Al dans les aluminosilicates en feuillet auto-assemblés en présence de surfactants

---

**C.1 Introduction.** L'aluminium est l'hétéroatome le plus employé pour conférer aux catalyseurs solides à base de silicate leur réactivité. Dans ce chapitre, nous étudions l'incorporation d'Al dans les silicates en feuillets auto-assemblés en présence de surfactant, dans le but notamment de vérifier l'hypothèse selon laquelle la présence de sites cristallographiques Si de type  $Q^3$  et  $Q^4$  assez différents chimiquement pourrait induire une substitution préférentielle. On y décrit d'abord les aspects relatifs à la synthèse, et notamment au contrôle du taux d'incorporation et du degré d'ordre aux échelles mésoscopique et moléculaire avant de se pencher sur l'étude de la structure locale autour de ces hétéroatomes. Nos études ont montré que, bien qu'assez similaires en termes de morphologie, les matériaux synthétisés à partir des deux types de surfactants étudiés voient leur structure locale modifiée de manière assez différente autour des hétéroatomes d'Al. Il a été choisi de présenter chaque matériau dans une section différente.

**C.2 Incorporation d'hétéroatomes d'Al dans les réseaux 2D de silicate.** Cette section décrit l'incorporation d'Al dans les deux types de matériaux silicates 2D synthétisés à partir de surfactants  $C_{16}H_{33}Me_2EtN^+$  ou  $C_{16}H_{33}Me_3N^+$ . L'incorporation d'Al et la capacité de contrôler sa quantité au sein du matériau final (entre  $Si/Al = 15$  et  $\infty$ ) est démontrée à partir des mesures ICP. La conservation de degrés d'ordre mésoscopique et moléculaire au sein des feuillets comparables au matériau silicates de référence est mise en évidence grâce à la DRX à bas et à hauts angles, respectivement (figure C.1)

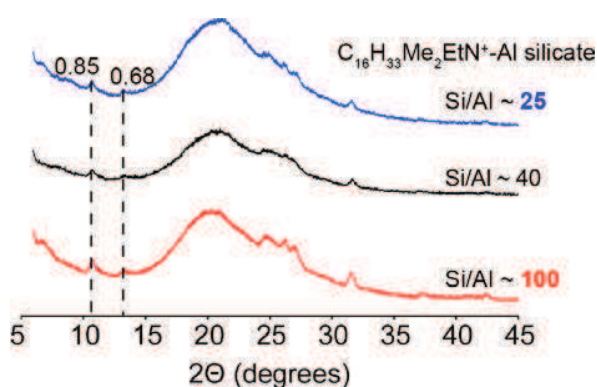


**Figure C.1** Diffractogrammes RX (grands angles) d'aluminosilicates en feuillets synthétisés à partir de surfactants  $C_{16}H_{33}Me_2EtN^+$  avec différents rapports Si/Al (100, 40 et 25) et qui témoignent du faible degré d'ordre moléculaire à longue distance existant au sein des feuillets.

**C.3 Distribution des hétéroatomes d'Al au sein des feuillets de silicates synthétisés à partir de surfactants  $C_{16}H_{33}Me_2EtN^+$ .** La spectroscopie RMN fournit toute une série d'informations à l'échelle locale, qui permettent tout d'abord de confirmer que les hétéroatomes d'Al sont bien incorporés au sein du réseau silicatés. Le spectre  $^{29}Si$  (Figure C.2a) présente la signature d'environnements Si situés suffisamment loin de l'Al pour conserver la signature du matériau de silicate de référence (composantes bleues dans la décomposition). Superposés à ces signaux, on observe un signal large (en vert) correspondant à des régions plus désordonnées, qui peuvent raisonnablement être attribués aux atomes de Si situés dans les premières sphères de coordinence autour de l'Al. Le spectre  $^{27}Al$  confirme en effet que l'Al est présent uniquement en coordinence 4, ce qui suggère que tous les atomes d'Al se sont substitués à un atome de Si au sein du réseau au cours de la synthèse.

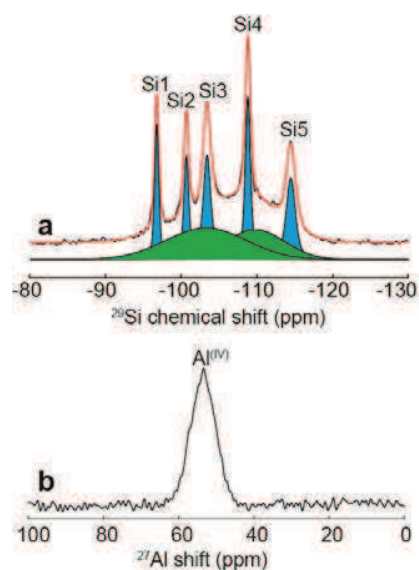


**Figure C.2** Spectres RMN (a) du  $^{29}Si$  (en noir) (b) et de l' $^{27}Al$  collectés pour le matériau aluminosilicate en Feuillet auto-assemblé en présence de surfactant  $C_{16}H_{33}Me_2EtN^+$ , avec un rapport Si/Al de 40.

L'environnement local autour des hétéroatomes d'Al incorporés dans ces matériaux a pu être sondé de manière directe et **sélective** par des expériences RMN de corrélation établissant les proximités spatiales ou les connectivités (via des O pontants) entre noyaux de  $^{29}Si$  et de  $^{27}Al$ , expériences grandement facilitées par l'enrichissement isotopique en  $^{29}Si$ . Sur la figure C.3, la projection dans la direction  $^{29}Si$  du spectre (à droite en noir) est la signature directe des atomes de Si situés à une distance de moins de 4 à 5

À (environ) d'un Al incorporé au sein du réseau. Elle correspond à la contribution large observée sur le spectre  $^{29}\text{Si}$  1D montrant l'intégralité des atomes de Si, et confirme l'état fortement désordonné de la structure locale autour de ces atomes.

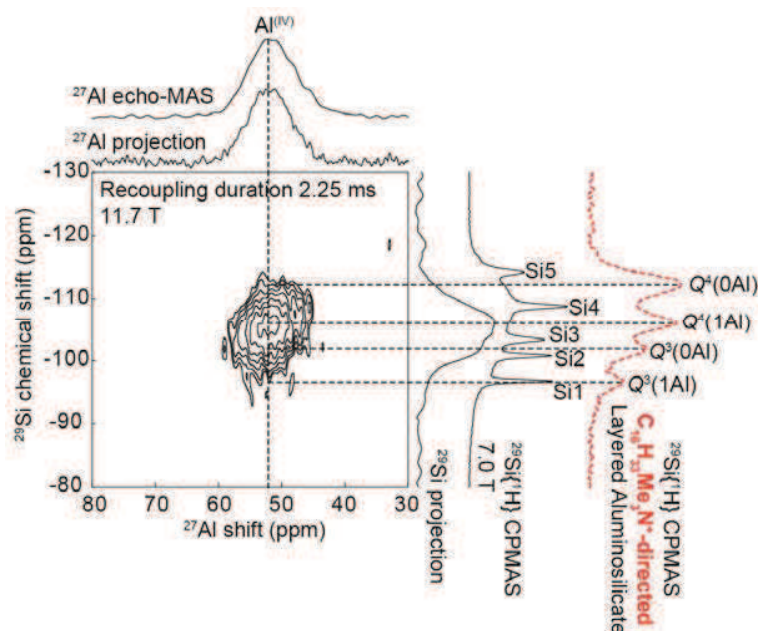


**Figure C.3** Spectre RMN 2D de corrélation  $^{27}\text{Al}[^{29}\text{Si}]$  via l'interaction dipolaire collecté sur un échantillon enrichi en  $^{29}\text{Si}$  de aluminosilicate en feuillets auto-assemblé en présence de surfactant  $\text{C}_{16}\text{H}_{33}\text{Me}_2\text{EtN}^+$ , avec un rapport Si/Al (mesuré) de 70. Les projections dans les dimensions  $^{29}\text{Si}$  et  $^{27}\text{Al}$  sont montrées à droite et en haut du spectre 2D pour comparaison avec les spectres 1D correspondants.

Ces mesures ont ensuite été combinées à des expériences sondant les noyaux de  $^1\text{H}$  localisés à proximité des Al. Elles ont montré que la charge négative introduite au sein du réseau par la substitution  $\text{Si}^{4+}/\text{Al}^{3+}$  n'est pas compensée par la présence d'un  $\text{H}^+$  supplémentaire (sous forme de  $\text{Al}(\text{OH})\text{-Si}$ , de  $\text{Al-OH}$  pour de  $\text{Si-OH}$ ) mais uniquement par la proximité de molécules de surfactants. Cette observation est à mettre en relation avec une autre observation surprenante qui peut être dégagée du spectre 2D  $^{27}\text{Al}\text{-}^{29}\text{Si}$  de la figure C.3 et d'autres sondant directement l'existence de liaisons  $\text{Si-O-Al}$ . La gamme de déplacement chimique des noyaux de  $^{29}\text{Si}$  Si connectés à un atome de Si indique qu'ils sont tous connectés à 4 voisins : 3 Si et 1 Al, unités désignées par le symbole  $Q^4(1\text{Al})$ . Ceci est en contradiction avec la structure silicatée de référence, dans laquelle tous les atomes de Si ont au moins un voisin de type  $Q^3$  (avec seulement 3 voisins Si) de sorte que, quel que soit son site de substitution, un aluminium devrait nécessairement être connecté à des atomes de Si connectés à seulement 2 Si et 1 Al, désignés par l'expression  $Q^3(1\text{Al})$ . Or ce n'est pas le cas, ce qui suggère que, au cours de la cristallisation du feuillet (dans des conditions

hydrothermales permettant aux liaisons de se rompre et de se reformer), la structure locale autour des atomes de Al se distingue profondément de la structure de référence par un degré de condensation plus élevé. Tous les atomes Si situés autour de l'Al sont ainsi des tétraèdres de type  $Q^4(1Al)$  entièrement polymérisés.

Cette observation importante (dont jamais aucun autre exemple n'a été reporté auparavant à notre connaissance) a ensuite été corroborée par des calculs DFT. Les calculs montrent que lorsqu'on crée artificiellement des connectivités entre unités de type  $Q^3$  (ou  $Q^3(1Al)$ ) pour les transformer en unités  $Q^4$  (ou  $Q^4(1Al)$ ), la structure du feuillet est capable de se courber légèrement de manière à s'adapter à cette nouvelle connectivité et ainsi retrouver des géométries de tétraèdres assez régulières à proximité du défaut ainsi créé. La présence d'une connectivité supplémentaire par rapport à la structure silicatée de référence rend moins nécessaire la compensation locale de la charge de l'Al, puisque deux unités Si-O<sup>-</sup> (ou une unité Si-O<sup>-</sup> et une entité Al-O<sup>-</sup>) ont été converties en une seule unité Si-O-Si (ou Si-O-Al) ce qui génère un excès de 2 charges positives. La présence de surfactants à proximité est alors largement suffisante pour compenser la charge négative associée à l'Al incorporé, en accord avec les expériences RMN de corrélation <sup>1</sup>H-<sup>27</sup>Al.

**C.3 Distribution des hétéroatomes d'Al au sein de feuillets de silicates synthétisés à partir de surfactants C<sub>16</sub>H<sub>33</sub>Me<sub>3</sub>N<sup>+</sup>.** Une étude tout à fait similaire menée sur les matériaux aluminosilicates auto-assemblés en présence du second type de surfactant C<sub>16</sub>H<sub>33</sub>Me<sub>3</sub>N<sup>+</sup> (plus hydrophile) renforce encore ces interprétations. L'incorporation d'Al dans ce système est plus facile que le précédent, ce qui a permis une étude quantitative systématique en fonction de la quantité d'Al. La figure C.4 montre comment les espèces  $Q^3(1Al)$  et  $Q^4(1Al)$  croissent systématiquement au dépend des espèces  $Q^3$  et  $Q^4$  avec la quantité d'Al incorporé.

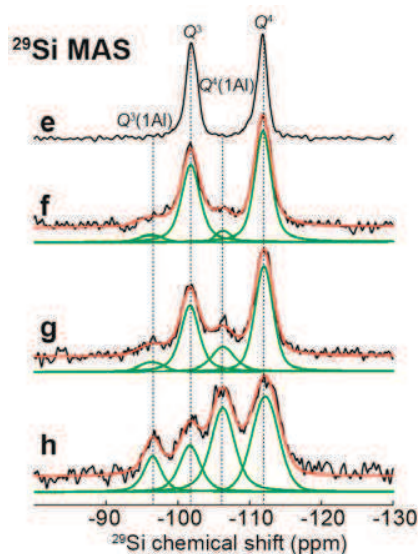


**Figure C.4** Spectres RMN 1D  $^{29}\text{Si}$  quantitatifs (en noir) d'aluminosilicates en feuillets auto-assemblés en présence de surfactants  $\text{C}_{16}\text{H}_{33}\text{Me}_3\text{N}^+$  avec des rapports Si/Al (e)  $\infty$ , (f) 73, (g) 35 et (h) 15. Les spectres simulés (en rouge) sont la somme des contributions individuelles (en vert) attribuées (de gauche à droite) aux espèces  $\text{Q}^3(1\text{Al})$ ,  $\text{Q}^3$ ,  $\text{Q}^4(1\text{Al})$ ,  $\text{Q}^4$ .

Comme dans le cas du matériau précédent, les expériences RMN de corrélation  $^{29}\text{Si}$ - $^{27}\text{Al}$  révèlent une très forte majorité d'environnements Si de type  $\text{Q}^4(1\text{Al})$  dans les premiers voisins tétraédriques des Al incorporés, qui indique une augmentation de la polymérisation du réseau autour de ces sites. Là encore comme dans le cas précédent, les expériences de corrélation  $^1\text{H}$ - $^{27}\text{Al}$  montrent une compensation de la charge associée à la substitution  $\text{Al}^{3+}/\text{Si}^{4+}$  assurée exclusivement par les têtes polaires de surfactants. Cela corrobore l'interprétation selon laquelle, à proximité directe d'atomes d'Al, les oxygènes non-pontant présents dans la structure de référence condensent deux à deux au cours de la cristallisation pour former une structure localement plus polymérisée, ce qui rend la compensation de charge de l'Al par des  $\text{H}^+$  supplémentaires (par exemple) inutile. La figure C.5 montre la comparaison d'une structure de feuillet sans Al et d'une structure avec Al obtenue après relaxation en partant d'une structure où les oxygènes non-pontant de l'Al (incorporé ici en substitution d'un site  $\text{Q}^3$ ) et d'un Si initialement  $\text{Q}^3$  adjacent ont été connectés manuellement. Là encore, même avec une super-cellule de taille limitée, le feuillet s'avère suffisamment flexible pour s'adapter localement au nouveau pont Si-O-Al ainsi créé (en jaune sur la figure C.5b).

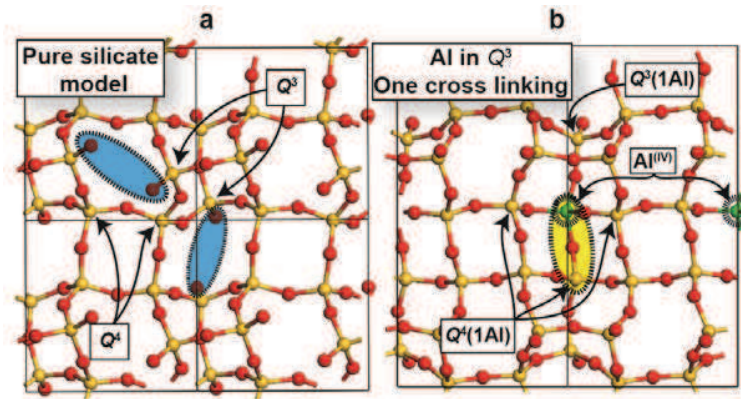


**Figure C.5** Structures optimisées par DFT (a) d'un silicate en feuillet et (b) de l'aluminosilicate obtenu par substitution d'un Si (initialement  $Q^3$ ) et connexion « manuelle » de l'Al avec l'oxygène non-pontant du Si (initialement) en  $Q^3$  le plus proche, créant ainsi 4 unités  $Q^4(1Al)$  et causant la perte de 2  $Q^3$ .

L'exemple de la figure C.5 montre comment cette nouvelle connectivité modifie le nombre d'espèces Si présentes dans l'échantillon de départ en supprimant 2 sites Si  $Q^4$  (l'un substitué par Al, l'autre condensé avec un Si adjacent) et en générant 4 sites de type  $Q^4(1Al)$ . Un bilan similaire peut ainsi être établi pour les différentes situations en fonction du site de substitution de l'Al (à la place d'un Si initialement en  $Q^4$  ou en  $Q^4$ ) et du nombre (0, 1 ou 2) et du type de nouvelles connectivités formées (Si-O-Si ou Si-O-Al). On peut ensuite utiliser ces observations pour prédire l'évolution des différentes populations  $Q^n(mAl)$  d'environnements Si (avec  $n = 3$  ou  $4$  et  $m = 0$  ou  $1$ ) en fonction du rapport Si/Al. La comparaison de ces prédictions avec l'évolution des populations mesurées expérimentalement (figure C.4) démontre que l'incorporation d'un atome d'Al s'accompagne systématiquement d'une augmentation locale de la polymérisation du réseau. Ce phénomène se traduit par une structure localement plus désordonnée que celle qui pourrait être attendue si l'incorporation était une simple substitution Si/Al sans autre modification profonde de la structure du feuillet.

---

## **Chapitre D: Structure locale résultant de l'incorporation de bore dans les silicates en feuillet non-cristallins**

---

**D.1 Introduction.** Le bore est un hétéroatome beaucoup moins utilisé que l'aluminium pour les catalyseurs solides silicatés, mais il est pourtant intéressant à plusieurs titres. Son acidité plus faible que celle de l'Al peut permettre de jouer sur la sélectivité de certaines réactions chimiques. D'autre part, il est possible de le substituer grâce à des traitements post-synthèse par d'autres hétéroatomes tout en conservant la structure de départ. Ainsi, certaines zéolites aluminosilicates ne peuvent être synthétisés qu'en synthétisant d'abord une zéolite borosilicate puis en substituant les atomes de B par des atomes d'Al. Dans ce chapitre, nous étudions l'hypothèse selon laquelle les propriétés radicalement différentes du bore pourraient conduire à une incorporation plus sélective que l'aluminium dans les silicates en feuillet, toujours dans l'idée de pouvoir ensuite obtenir, par condensation des feuillets, une zéolite 3D dans laquelle la position des hétéroatomes au sein du réseau serait bien contrôlée. L'organisation de ce chapitre est similaire à celle du précédent, avec une première section démontrant l'incorporation de bore dans les deux types de silicates en feuillet formés en présence des surfactants  $C_{16}H_{33}Me_2EtN^+$  ou  $C_{16}H_{33}Me_3N^+$ , puis deux chapitres traitant séparément de la structure locale autour des hétéroatomes dans chaque matériau.

**D.2 Incorporation d'hétéroatomes de bore dans les réseaux 2D de silicate.** Comme dans le chapitre précédent la présence de bore dans les échantillons de borosilicates est établie grâce à des mesures d'ICP. Elles montrent que, contrairement au cas de l'aluminium, seuls de faibles taux de bore peuvent être incorporés au sein de ces matériaux sans détériorer la structure ou former de phases annexes (comme établi grâce aux analyses DRX). Comme le montre la figure D.1, la RMN du  $^{29}Si$  confirme dans les deux matériaux que la structure du matériau de référence est conservée, et les spectres  $^{11}B$  indiquent que le tout le bore présent dans les matériaux est bien incorporé au réseau sous forme de bore en coordinence 4 (désigné par l'expression  $B^{(IV)}$ ). Mais ces spectres  $^{11}B$  fournissent d'autres informations capitales. Tout d'abord, et contrairement au cas de l'aluminium, les spectres bore donnent des signatures très fines témoignant d'un fort degré d'ordre à l'échelle moléculaire au sein de ces environnements. Ceci permet en outre de mettre en évidence des différences radicales d'un système borosilicate à l'autre, avec notamment plusieurs composantes  $^{11}B$  très bien séparées dans le cas du matériau synthétisé avec du  $C_{16}H_{33}Me_3N^+$

(Figure D.1b) et une composante unique dans celui synthétisé avec du  $C_{16}H_{33}Me_2EtN^+$  (Figure D.1d). Les deux sections suivantes se focalisent, matériau par matériau, sur les causes, au niveau de la structure locale de ces remarquables différences.

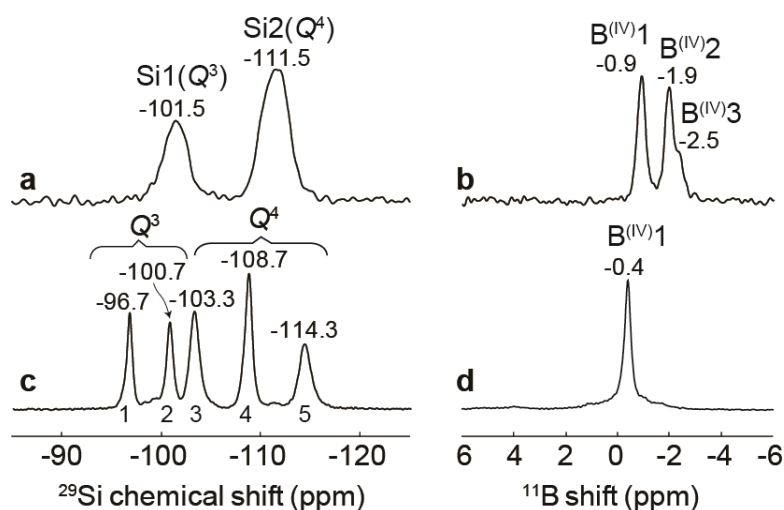


**Figure D.1** Spectres RMN (à gauche)  $^{29}Si$  et (à droite)  $^{11}B$  de borosilicates en feuillet auto-assemblés en présence de (a-b)  $C_{16}H_{33}Me_3N^+$  et (c-d)  $C_{16}H_{33}Me_2EtN^+$ .

**D.3 Distribution des hétéroatomes de bore au sein de feuillets de borosilicates synthétisés à partir de surfactants  $C_{16}H_{33}Me_3N^+$ .** De premiers éléments d'information importants sur l'environnement local autour des hétéroatomes de bore ont été fournis en sondant à l'aide de différentes expériences de RMN les proximités spatiales entre noyaux de  $^{11}B$  et de  $^1H$ . Elles mettent notamment en évidence (figure D.2) des mécanismes de compensation de charge différents d'un environnement  $^{11}B$  à l'autre. On distingue ainsi des sites (B1), attribués à des atomes de bore en substitution d'un site Si de type  $Q^3$ , dans lesquels la charge est compensée par la présence d'un  $H^+$  pour former une entité B-OH, et des sites  $^{11}B$  (sites B2 et B3) qui n'interagissent (beaucoup plus faiblement) qu'avec les protons des molécules de surfactants, et attribués à des atomes de B en substitution de Si de type  $Q^4$ .

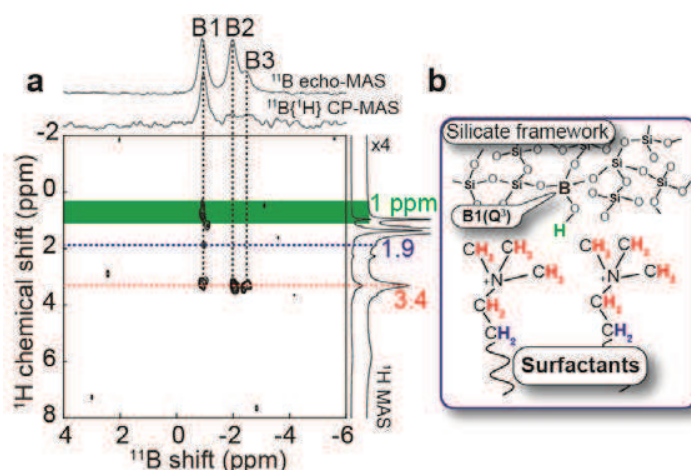


**Figure D.2** (a) Spectre RMN de corrélation  $^{11}\text{B}-^1\text{H}$  de borosilicate en feuillet synthétisé en présence de surfactants  $\text{C}_{16}\text{H}_{33}\text{Me}_3\text{N}^+$  et établissant les proximités spatiales entre noyaux de  $^{11}\text{B}$  et de  $^1\text{H}$ . La zone en vert indique la présence de protons autres que ceux du surfactant, impliqués dans la compensation de charge du site B1, attribué à des espèces B-OH.

Ces interprétations sont là encore confirmées grâce à la modélisation moléculaire. De nombreux modèles dans lesquels un atome de Si est substitué par un atome de B ont été construits et optimisés grâce à la DFT. Dans l'exemple de la figure D.3, la charge négative associée à la substitution  $\text{Si}^{4+}/\text{B}^{3+}$  est compensée par addition d'un  $\text{H}^+$  pour former un environnement BOH, mais d'autres mécanismes ont été également étudiés (formation de groupements silanols, addition d'une molécule de surfactant...). Les calculs de déplacement chimique  $^{11}\text{B}$  réalisés sur ces modèles par la méthode GIPAW prédisent des différences importantes entre des environnements  $(\text{SiO})_3\text{B-OH}$  et  $(\text{SiO})_4\text{B}$ , et des valeurs de déplacement en bon accord avec l'attribution des pics expérimentaux.

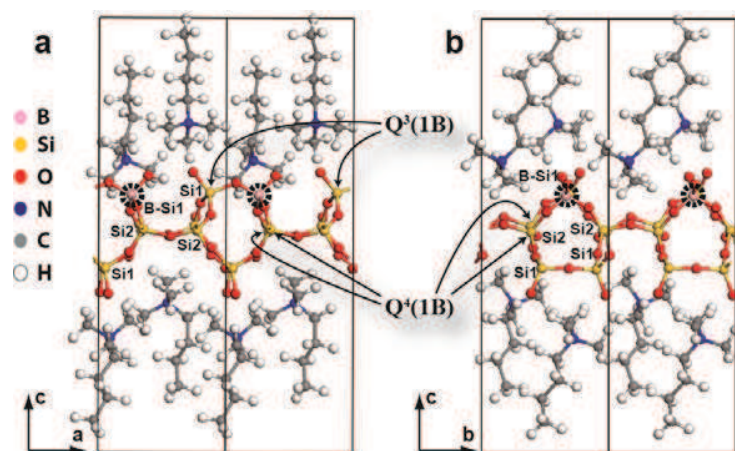


**Figure D.3** Exemple de modèle structural optimisé par DFT (vu selon deux directions différentes) utilisé pour décrire la structure de borosilicate en feuillet synthétisé avec des surfactants  $C_{16}H_{33}Me_3N^+$ . Un atome de Si sur les 8 présent dans la super-maille est échangé par un atome de B et le déficit de charge correspondant est compensé par l'addition d'un  $H^+$  pour former une entité B-OH.

L'environnement direct du B au sein du feuillet est sondé grâce aux expériences de corrélation  $^{11}B$ - $^{29}Si$ . Elles montrent comme dans le cas des aluminosilicates discuté dans le chapitre précédent une forte tendance de l'hétéroatome à s'entourer d'atomes de Si entièrement condensé, en dépit des réorganisations profondes de la structure locale que la création de connectivités Si-O-B ou Si-O-Si supplémentaire nécessite. La figure D.4 illustre ce principe à travers un exemple de structure qui s'est déformée au cours de l'optimisation de géométrie (D.4b) pour s'adapter à la présence d'une connectivité Si-O-Si supplémentaire impliquant un premier voisin Si initialement en  $Q^3$  du bore. Les différentes possibilités de réarrangement qui peuvent être envisagées permettent d'expliquer la présence de 3 sites  $^{11}B$  distincts dans le spectre (Figure D.1b) alors que la structure de référence ne compte que deux sites cristallographiques distincts (un de type  $Q^3$  et un de type  $Q^4$ ).

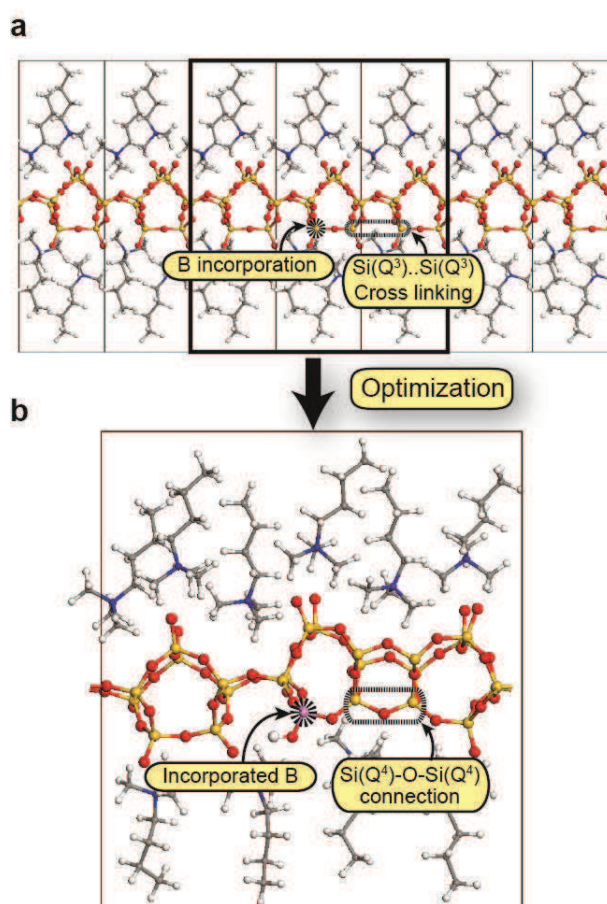


**Figure D.4** (a) Modèle silicaté optimisé par DFT, utilisé comme point de départ pour former (b) une super-maille (ici 3x1x1 mailles de départ) permettant de décrire les réarrangements structuraux susceptibles d'intervenir autour d'un hétéroatome de bore (en rose) associé à une nouvelle connectivité Si-O-Si.

**D.4 Distribution des hétéroatomes de bore au sein de feuillets de borosilicates synthétisés à partir de surfactants  $C_{16}H_{33}Me_2EtN^+$ .** Cette section présente les résultats d'une étude tout à fait similaire effectuée pour le matériau borosilicate en feuillet auto-assemblé à partir du deuxième type de surfactant : le  $C_{16}H_{33}Me_2EtN^+$ . Le point principal dans le cas de ce matériau est l'observation d'un pic RMN  $^{11}B$  unique qui suggère une incorporation préférentielle d'un l'un des cinq sites cristallographiques distincts présents dans le matériau silicaté de référence. On y établit que le déficit de charge associé à ce site est compensé par un proton formant vraisemblablement une unité B-OH (comme le site B1 du matériau précédent), le bore étant incorporé en substitution d'un site Si de type  $Q^3$ . La figure D.5 montre des expériences de corrélation  $^{11}B$ - $^{29}Si$  à travers les ponts B-O-Si (en rouge) et à travers l'espace (en bleu), collectés à partir d'un échantillon enrichi en  $^{29}Si$  (avec un rapport Si/B = 70). La superposition de ces

deux spectres permet de distinguer clairement les premiers voisins Si du bore (on en dénombre trois en accord avec l'interprétation selon laquelle le bore est en substitution d'un site  $Q^3$ ) et les atomes de Si proches (moins de 4 à 5 Å) mais pas connectés.

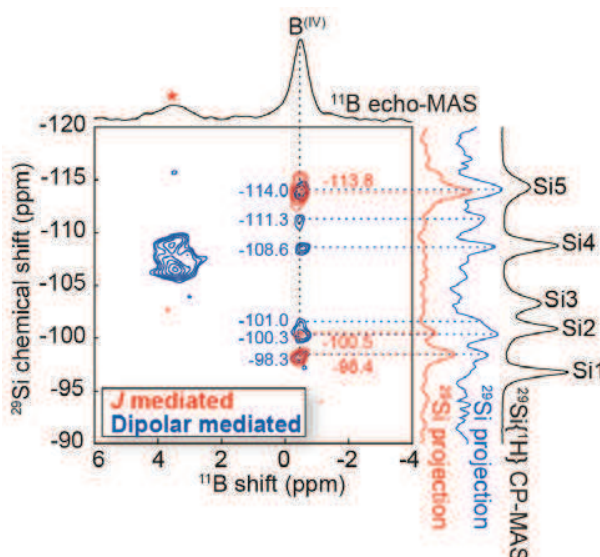


**Figure D.5** Superposition de spectres RMN de corrélation  $^{11}\text{B}$ - $^{29}\text{Si}$  utilisant (en bleu) les interactions dipolaires pour sonder les proximités spatiales et (en rouge) les couplages scalaires pour sonder les connectivités Si-O-B. Les projections en couleur sur la droite sont les signatures sélectives des Si connectés ou à proximité du B, qui représentent une infime fraction des Si de l'échantillon (spectre 1D en noir tout à droite).

La très faible largeur de tous les pics associés aux noyaux de  $^{29}\text{Si}$  dans la proximité directe du bore indique un très fort degré d'ordre à l'échelle moléculaire, qui signifie que la structure locale autour de ce type unique de défaut est répétée à l'identique dans tout le matériau. Il s'agit pourtant bien là de défauts qui, s'ils interviennent toujours au sein du même site cristallographique, ne sont cependant pas répétés de façon périodique à plus longue échelle. C'est ce concept qui est illustré dans la figure D.6. On ne peut pas parler d'environnements cristallins au sens strict du terme, mais la similitude de structure locale de tous ses sites dans tout l'échantillon suggère néanmoins que leurs propriétés physico-chimiques, et notamment leur réactivité est probablement identique au sein de l'échantillon. Une petite parenthèse : si vous lisez ces lignes, alors peut-être n'avait-on peut-être pas tout à fait tort de nous demander d'écrire ce résumé en Français... Merci dans ce cas de nous le faire savoir : [sylvian.cadars@cnrs-orleans.fr](mailto:sylvian.cadars@cnrs-orleans.fr).

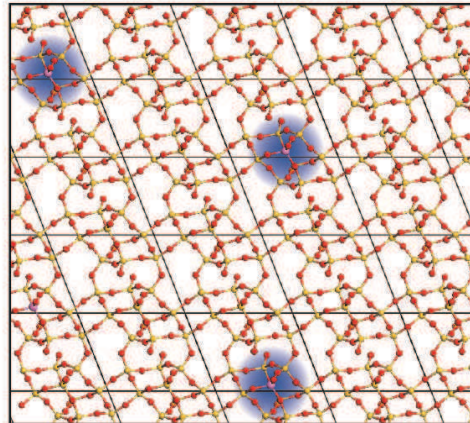


**Figure D.6** *Modèle fictif de feuillet (vue de haut) dans lequel un site cristallographique Si donné (toujours le même) est substitué par un atome de B dans des répétitions aléatoirement réparties de la maille unitaire. Les modifications de courte portée de la structure du réseau (halo bleu) associées à ces défauts se répètent à l'identique dans tout l'échantillon en dépit de leur répartition probablement aléatoire.*

---

## **Chapitre E: Extension à l'étude de la substitution atomique dans d'autres matériaux**

---

**E.1 Introduction.** Les substitutions atomiques  $\text{Si}^{4+}/\text{M}^{3+}$  intervenant dans les catalyseurs solides silicatés abordées dans les chapitres précédents ne représentent qu'un petit exemple parmi la vaste gamme de substitutions (et/ou de lacunes) susceptibles d'intervenir dans les matériaux. De telles substitutions génèrent du désordre structural à l'échelle locale, y compris dans des matériaux dont la structure périodique moyenne à longue distance (telle que déterminée à partir des méthodes de diffraction) est bien définie, et jouent très souvent des rôles clés dans les propriétés physico-chimiques. Ce chapitre montre comment un certain nombre des approches utilisées pour les aluminosilicates et borosilicates en feuillet peuvent être étendues à d'autres types de systèmes et de substitutions atomiques. La première section focalise sur une argile de synthèse : la montmorillonite, et la seconde sur une nouvelle phase borosilicate de calcium synthétisée à haute température.

**E.2 Exploration de la structure locale d'une argile de type 2:1: la montmorillonite.** Les argiles de synthèses sont des systèmes intéressants du point de vue de la RMN car elles permettent de mener des études poussées sur leur structure locale en s'affranchissant des difficultés liées notamment à la présence quasi-systématique de  $\text{Fe}^{(\text{III})}$  paramagnétique dans les minéraux d'origine naturelle. La montmorillonite est une argile dite de type 2:1, c'est-à-dire que chaque feuillet d'argile est composé d'une couche octaédrique constituée d'une majorité d'entités  $\text{AlO}_6$ , et prise en sandwich entre deux couches tétraédriques composées majoritairement d'entités  $\text{SiO}_4$ . La substitution d'une proportion relativement importante d' $\text{Al}^{3+}$  par des  $\text{Mg}^{2+}$  dans la couche octaédrique et d'une faible quantité  $\text{Si}^{4+}$  par des  $\text{Al}^{3+}$  dans la couche tétraédrique se traduit par un déficit de charge qui est compensé par la présence de cations entre les feuillets (majoritairement du sodium dans la plupart des montmorillonites d'origine naturelle). Un des grands intérêts des argiles pour une vaste gamme d'applications provient de la possibilité d'échanger les cations de l'espace inter-foliaire par une grande variété d'espèces cationiques, qui ouvre la voie à toutes sortes de propriétés macroscopiques.

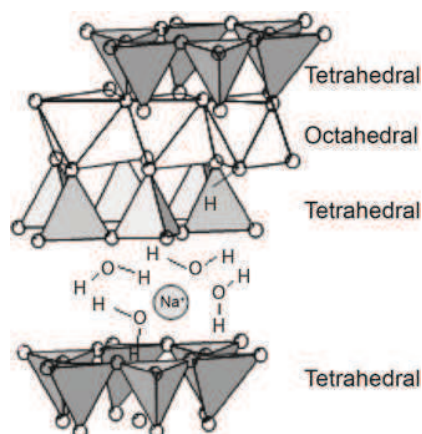


**Figure E.1** [Ref: Gougeon R.D. et al., S.S.N.M.R. 2006] Représentation schématique de la montmorillonite.

Nos études ont porté sur une argile synthétisée d'après la méthode de Leforestier *et al.*, [ref : Appl. Clay. Sc. 2010] dont la composition estimée par une combinaison d'analyse chimique et d'ICP est  $(\text{Na}_{0.68}\text{Mg}_{0.03})(\text{Al}_{3.35}\text{Mg}_{0.65})(\text{Si}_{7.91}\text{Al}_{0.09})\text{O}_{20}(\text{OH}_4)$ . Dans ce système la RMN combinée du  $^{29}\text{Si}$  et du  $^{27}\text{Al}$  permet de révéler de manière quantitative la substitution Si/Al dans la couche tétraédrique. Le gros avantage par rapport aux analyses quantitatives macroscopiques est que cette quantification est faite spécifiquement sur les contributions attribuables à l'argile, en s'affranchissant des contributions dues à une impureté aluminosilicate qui a pu être identifiée au sein de cette argile de synthèse. Cette impureté est peu ou pas cristalline et n'avait donc pas pu être mise en évidence auparavant par diffraction. Les signaux attribuables à cette impureté sont clairement mis en évidence sur le spectre de corrélation (à travers l'espace) de la figure E.2. Ce spectre permet bien d'identifier la faible contribution (en bas à gauche du spectre) attribuable aux Al localisés dans la couche tétraédrique (désignés  $\text{Al}^{(\text{IV})}$ ), qui sont connectés (et donc proches) de Si de type  $Q^3(1\text{Al})$ , dont la position se distingue de la majorité des Si de l'argile: de type  $Q^3$ .

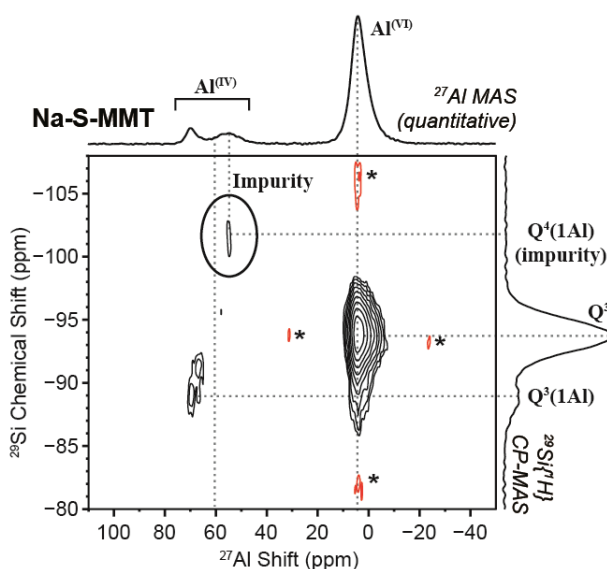


**Figure E.2** Spectre RMN de corrélation  $^{27}\text{Al}$ - $^{29}\text{Si}$  exploitant l'interaction dipolaire, collecté pour la montmorillonite de synthèse (Na-S-MMT).

Les différentes espèces  $^{27}\text{Al}$  et  $^{29}\text{Si}$  identifiées au sein de l'argile montrent en outre un élargissement assez important qui traduit une grande variabilité d'environnements locaux (également traduite dans les spectres RMN du  $^{25}\text{Mg}$ ), et qui est attribuable aux substitutions Mg/Al au sein de la couche octaédrique. Or dans ce système, c'est justement la substitution Al/Mg qui a la plus grande influence sur la charge des feuillets, et donc sur les propriétés macroscopiques. Nous avons démontré que cette substitution peut être quantifiée en utilisant la RMN du  $^1\text{H}$  à haut champ magnétique et haute vitesse de rotation à l'angle magique (MAS), seules conditions dans lesquelles la résolution spectrale est suffisante pour séparer les différents types de groupements hydroxyles situés au sein du feuillet. Ces groupements se présentent sous la forme d'oxygène tri-coordonnés qui connectent entre eux deux sites octaédriques, pour former des espèces de type  $\text{Al}_2\text{OH}$  (dominantes étant donné le rapport Al/Mg),  $\text{MgAlOH}$ , et éventuellement  $\text{Mg}_2\text{OH}$ . Les différents spectres RMN  $^1\text{H}$  de la figure E.3, combinés avec le calcul DFT, ont permis d'identifier clairement les espèces  $\text{Al}_2\text{OH}$  et  $\text{MgAlOH}$  et de confirmer que les espèces  $\text{Mg}_2\text{OH}$  sont absentes (dans les limites de la détection par RMN) dans ce système. Cela a permis de revisiter la composition de la couche octaédrique dans ce système, et surtout de mettre en évidence une tendance à l'évitement des espèces porteuses de la charge du feuillet : les cations  $\text{Mg}^{2+}$ .

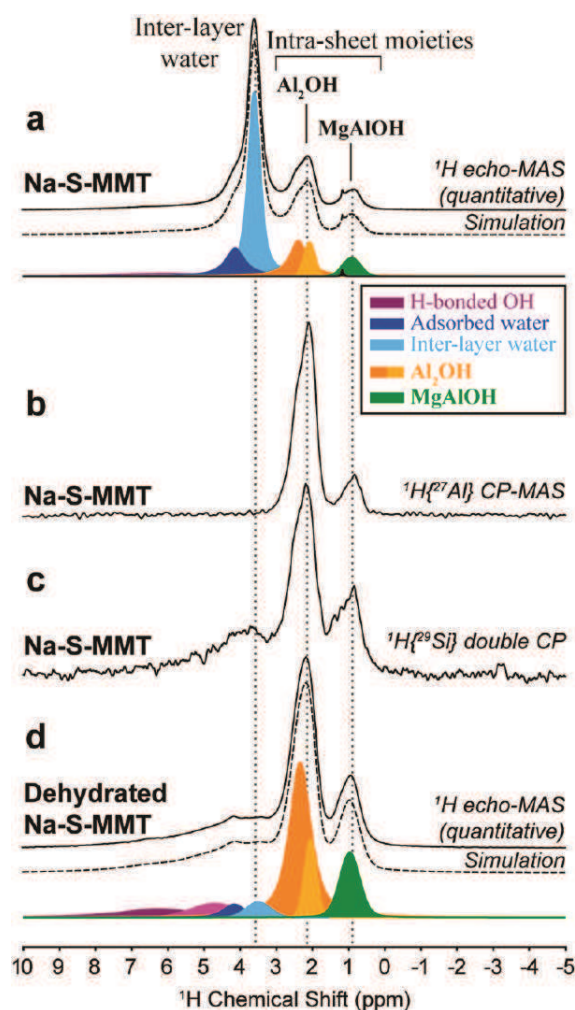


**Figure E.3** Spectres RMN  $^1\text{H}$  collectés à haute vitesse de rotation à l'angle magique (64 kHz) et haut champ magnétique (17.6T) dans des conditions (a) quantitatives, ou permettant de révéler sélectivement les protons localisés à proximité de noyaux (b)  $^{27}\text{Al}$  ou (c)  $^{29}\text{Si}$ . (d) Spectre quantitatif collecté pour l'argile déshydratée.

**E.3 Etude par RMN à l'état solide d'une nouvelle phase borosilicate de calcium.** Cette section se focalise sur la caractérisation à l'échelle locale d'une nouvelle phase borosilicate de calcium caractérisée pour la première fois dans le système ternaire (pourtant très étudié)  $\text{CaO} \cdot \text{SiO}_2 \cdot \text{B}_2\text{O}_3$ . Cette phase, de composition  $\text{CaSi}_{1/3}\text{B}_{2/3}\text{O}_{8/3}$ , a été synthétisée par recuit à  $750^\circ\text{C}$  d'un verre de même composition. La structure cristalline est conservée après refroidissement à température ambiante, malgré un degré d'ordre à longue distance plus faible (identifiée par la largeur des pics de diffraction) qu'à  $750^\circ\text{C}$ , conditions dans lesquelles la structure a pu être déterminée en combinant la diffraction des rayons-X sur synchrotron et des neutrons. Cette structure est à première vue très simple puisqu'elle est

composée de 2 chaînes identiques (reliées par symétrie) parallèles à l'axe *c*, et consistant en une succession de tétraèdres là aussi équivalents par symétrie. Mais la situation est en fait plus complexe, puisque la qualité de l'affinement basé sur les données combinées neutrons et synchrotron révèle que chacun des sites tétraédrique est en fait composé d'un mélange de 2/3 - 1/3 de B et Si, respectivement. L'oxygène pontant O3 est de plus caractérisé par une occupation partielle (de 2/3) qui indique une rupture des chaînes à l'échelle locale. Ceci peut être interprété comme un désordre de composition, qui s'accompagne de plus de distorsions géométriques, puisque les tétraèdres sont fortement déformés. Ces observations traduisent le fait que la diffraction fournit une image moyennée à longue distance de la structure, et qui ne reflète pas nécessairement la structure locale.

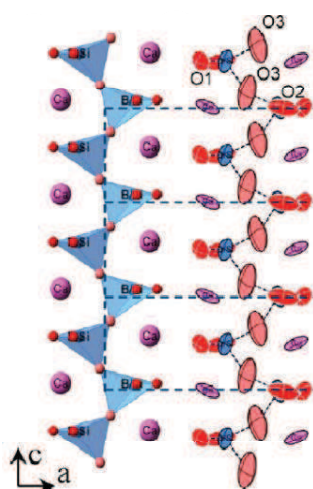


**Figure E.4** Structure moyenne à longue distance de la phase  $\text{CaSi}_{1/3}\text{B}_{2/3}\text{O}_{8/3}$  déterminée par diffraction.

La RMN est ainsi très complémentaire de la diffraction puisqu'elle donne au contraire une vision purement locale de la structure, qui permet dans ce cas précis de clarifier immédiatement un certain nombre d'aspects structuraux. Les spectres RMN  $^{11}\text{B}$  et  $^{29}\text{Si}$  de la figure E.5 révèlent ainsi que tous les atomes de bore de la structure sont présents sous forme d'unités  $\text{BO}_3$  (aucun  $\text{BO}_4$  détectable) qui sont donc directement associés à des lacunes d'oxygène O3 et correspondent donc à des bouts de chaîne. Les paramètres de l'interaction quadripolaire  $^{11}\text{B}$  (obtenus par ajustement de modèles, en rouge sur la figure) renseignent en outre sur la symétrie locale et permettent d'affirmer que ces unités  $\text{BO}_3$  ne sont pas isolées mais sont toujours connectés le long de la chaîne à une unité  $\text{SiO}_4$  ou une autre unité  $\text{BO}_3$ .

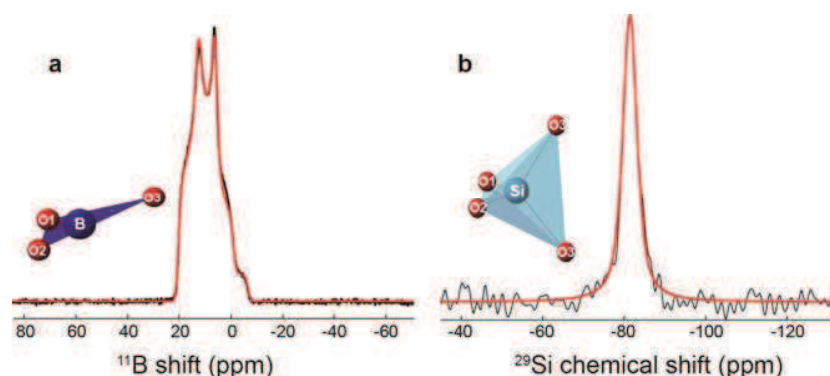


**Figure E.5** Spectres RMN (a)  $^{11}\text{B}$  et (b)  $^{29}\text{Si}$  de la phase  $\text{CaSi}_{1/3}\text{B}_{2/3}\text{O}_{8/3}$  (en noir). Les spectres en rouge correspondent aux modèles permettant l'extraction des paramètres RMN.

Une étude approfondie a ensuite été conduite en combinant diverses expériences plus avancées de RMN avec la modélisation moléculaire, dans le but de déterminer la longueur des chaînes ( $\text{O}_2\text{B-O-BO}_2$  et/ou  $\text{O}_2\text{B-O-}[\text{Si}(\text{O}_2)\text{-O-}]_n\text{BO}_2$ , avec  $n \geq 1$ ) et éventuellement leurs arrangements, et ainsi clarifier notre vision de la structure locale de ce système. Les différentes expériences de RMN avaient pour objectifs d'augmenter la résolution spectrale  $^{11}\text{B}$ , ou encore de sonder les proximités et connectivités entre noyaux de  $^{29}\text{Si}$  et/ou  $^{11}\text{B}$  pour essayer de distinguer différents types d'environnements locaux. Nous avons pour cela eu recours à la fois à l'échantillon utilisé pour la caractérisation par diffraction et à des échantillons enrichis en  $^{29}\text{Si}$  (de pureté moindre que le premier, pour une raison encore indéterminée). Ces études ont permis de conclure que la phase  $\text{CaSi}_{1/3}\text{B}_{2/3}\text{O}_{8/3}$  est composée en très grande majorité à l'échelle locale d'un seul type de fragment moléculaire : des unités  $\text{O}_2\text{B-O-Si}(\text{O}_2)\text{-O-BO}_2$  séparées le long de l'axe c par des lacunes d'oxygène  $\text{O}_3$ . La figure E.6a donne un exemple parmi les nombreux modèles permettant de décrire en partie les géométries locales résultant de cette composition. La relaxation par DFT confère à ce modèle une géométrie très différente de la structure moyenne à longue distance (Figure E.6b). Les autres modèles plausibles de cette structure, tous caractérisés par la répétition de la même entité  $\text{O}_2\text{B-O-Si}(\text{O}_2)\text{-O-BO}_2$  de base, diffèrent en fait par l'arrangement des chaînes les unes par rapport aux autres. Nous suspectons que ce désordre inter-chaîne qui est responsable de désordre résiduel observé (à travers les largeurs de raies  $^{29}\text{Si}$  et  $^{11}\text{B}$ ) dans ce système à température ambiante.

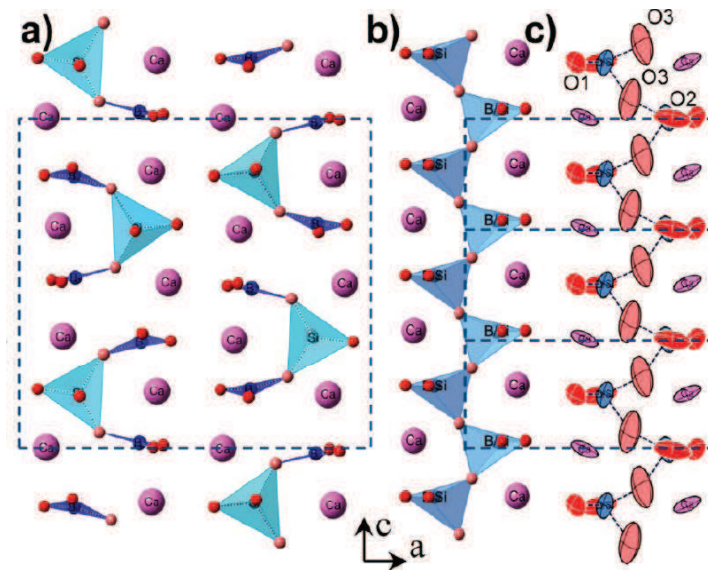


**Figure E.6** Comparaison selon le même point de vue et à la même échelle (a) d'un des nombreux exemples possibles de modèle de la structure locale et (b) de la structure moyenne à longue distance de la phase  $\text{CaSi}_{1/3}\text{B}_{2/3}\text{O}_{8/3}$ . Les polyèdres en (a) correspondent à des structures locales réelles alors que les tétraèdres déformés représentés en (b) traduisent un environnement moyen à longue distance, avec des compositions mixtes B/Si et des occupations partielles (site O3).

Cette exemple souligne ainsi la grande complémentarité d'une approche combinant les méthodes basées sur la répétition d'un ordre à longue distance, qui n'ont pas d'équivalent pour déterminer la structure cristalline d'un matériau, mais n'en fournissent néanmoins qu'une vision moyennée, et les méthodes sondant la structure locale telles que la RMN, couplées à la modélisation moléculaire. Cette démarche se diffuse d'autant plus vite en science des matériaux qu'elle permet également déterminer (ou d'appréhender) la structure moléculaire de matériaux peu ou pas cristallins, tels que les silicates en feuillet décrits dans les chapitres précédents, ou encore les assemblages macromoléculaires complexes.

---

## **Conclusions et Perspectives**

---

Ces travaux de thèse ont permis de comprendre avec un degré de détail sans précédent (à notre connaissance) la structure locale autour d'hétéroatomes incorporés dans des silicates en feuillets. La combinaison de techniques d'analyse, de diffraction et de la modélisation moléculaire avec des méthodologies de RMN de pointe capables de sonder directement l'environnement à proximité directe des hétéroatomes d'Al et de B (même en faibles quantités) révèlent un certain nombre de faits inattendus. Des différences radicales apparaissent en fonction de la nature de l'hétéroatome incorporé (Al ou B), mais aussi, pour un type d'hétéroatome, entre les deux types de matériaux silicatés de référence étudiés, ce en dépit de fortes similitudes au niveau de leurs morphologies et de leur compositions. On a ainsi mis en évidence dans le cas de l'incorporation d'Al des modifications assez profondes de la structure locale autour des hétéroatomes, avec une plus forte polymérisation du réseau qui se traduit par un important désordre structural local, le reste du matériau conservant le fort degré d'ordre moléculaire (à courte portée) au sein des feuillets. Ce désordre local semble beaucoup moins important dans le cas de l'incorporation de bore, notamment pour un matériau dans lequel l'incorporation intervient sélectivement au sein d'un seul type de site cristallographique parmi les 5 que comptent les feuillets dans ce système. Dans ce cas, on constate au contraire un très fort degré d'ordre moléculaire, les déformations structurales autour de chaque hétéroatome étant identiques au sein de l'ensemble de l'échantillon. La conclusion de cette thèse offre l'occasion de formuler des hypothèses sur les origines de ces différences, en se basant sur les différences connues entre les deux systèmes de référence (hydrophobicité des têtes de surfactant, degré de polymérisation du réseau, positions relatives des oxygènes non-pontant...) et les différences de propriétés de l'aluminium et du bore.

La possibilité d'incorporer le bore sélectivement dans l'un de ces matériaux ouvre la voie à un travail futur qui consistera à condenser les feuillets de borosilicates adjacents pour former une zéolite de structure reliée dans laquelle le bore sera localisé à des positions bien particulière. L'idée serait d'ensuite comparer la réactivité de ce matériau pour différentes réactions test typiques à celle mesurée pour un échantillon de référence dans lequel le bore serait distribué aléatoirement. Les premiers tests pour condenser ce type de silicates n'ont pas été concluant, mais plusieurs types de silicates en feuillet de structures proches existent, qui peuvent être utilisés comme précurseurs de zéolites. Certains de ces systèmes peuvent être synthétisés avec du bore (ou de l'aluminium) et une démarche tout à fait similaire à celle décrite ici pourrait leur être appliquée.

## Résumé des Annexes

---

### *Annexe A: Section expérimentale*

---

Cette annexe décrit chapitre par chapitre les conditions expérimentales utilisées pour les expériences de RMN dont les résultats sont présentés dans la thèse. Des références aux figures correspondantes sont données systématiquement.

---

### *Annexe B: Symboles and abréviations*

---

RMN	Résonance Magnétique Nucléaire
1D, 2D, 3D	Uni-, bi- tri-dimensionnel(le)
I	Nombre quantique de spin
J	Couplage scalaire
$\gamma$	Rapport gyromagnétique
$B_0$	Champ magnétique externe
CSA	anisotropie de déplacement chimique
EFG	Gradient de champ électrique
MAS	Rotation à l'angle magique
SQ	Simple Quantum
DQ	Double Quanta
INADEQUATE	Incredible Natural Abundance Double QUAntum Transfer Experiment
HMQC	Heteronuclear multiple-quantum correlation
HETCOR	Heteronuclear correlation
CP-MAS	Cross polarization magic angle spinning
SP	Expérience de simple impulsion (Single Pulse)
DFT	Théorie de la fonctionnelle de la densité
ppm	Parties par million

*Annexes*

GIPAW	Gauge Including Projector Augmented Waves
eV	Electron Volt
SPINAL	Small-Phase INcremental ALteration (decoupling)
RPE	Résonance de spin électronique
ICP	Inductively Coupled Plasma
IR	Infra-rouge
DRX	Diffraction des rayons X
MET	Microscopie électronique à transmission
MEB	Microscopie électronique à balayage

**Mounesha N. GARAGA**

## **Structure local autour d'Hétéroatomes dans des Matériaux Alumino- et Borosilicates pour la Catalyse**

En dépit de l'importance considérable des matériaux alumino- et borosilicates pour la catalyse, l'origine moléculaire de leur activité demeure mal comprise. Ceci tient à la difficulté de caractériser le désordre structural local généré au sein du réseau silicaté par l'incorporation d'hétéroatomes. Le caractère local de la résonance magnétique nucléaire (RMN) à l'état solide en fait une technique adaptée pour résoudre cette question majeure.

Les silicates en feuillets auto-assemblés en présence de surfactants sont d'excellents systèmes modèles pour l'étude de la structure locale autour d'hétéroatomes de B ou d'Al car la synthèse, la structure moléculaire et la signature RMN  $^{29}\text{Si}$  simple de leurs formes siliceuses sont parfaitement maîtrisées. L'incorporation dans leurs réseaux silicatés de différentes quantités d'Al ou de B et leurs conséquences ont été étudiées par des méthodologies avancées de RMN permettant de sonder les interactions à travers l'espace ou les liaisons chimiques entre noyaux de  $^{29}\text{Si}$ ,  $^{27}\text{Al}$ ,  $^{11}\text{B}$  et/ou  $^1\text{H}$ , une approche qui peut être étendue à la substitution atomique dans une argile aluminosilicate et un nouveau borosilicate de calcium.

Ces résultats ont été combinés à la modélisation moléculaire pour construire et valider des modèles structuraux capables de décrire les distorsions et les réarrangements parfois profonds du réseau résultant de la substitution. Cela a révélé des différences frappantes entre les conséquences de l'incorporation d'Al ou de B dans deux matériaux de morphologie semblables mais de structures moléculaires différentes, et offre une occasion unique de comprendre les propriétés régissant l'incorporation d'hétéroatomes dans les silicates.

Mots clés: RMN à l'état solide, silicates en feuillet, hétéroatome, sites actifs, structure locale

## **Locale Structure around Heteroatoms in Alumino- and Borosilicates for Catalysis**

While alumino- and borosilicate materials have paramount importance in catalysis, the molecular origin of their activity is not completely understood. This is mainly because the incorporation of heteroatoms into the silicate framework deteriorates the molecular order by generating local disorder that is particularly difficult to establish. Because of its local vision of ordered and disordered environments, solid-state nuclear magnetic resonance (NMR) can play a key role to solve this long-standing issue.

Surfactant-directed layered silicate materials with short-range molecular order are particularly interesting model systems to study the local structures around Al or B heteroatoms because the synthesis, molecular structures, and simple  $^{29}\text{Si}$  NMR signatures of their pure-silicate forms are well understood. Various amounts of Al and B atoms were incorporated into their frameworks, and their consequences on the local structure were investigated by state-of-the-art multidimensional NMR measurements probing spatial proximities or bonding interactions between  $^{29}\text{Si}$ ,  $^{11}\text{B}$ ,  $^{27}\text{Al}$ , and  $^1\text{H}$  nuclei, an approach that could be extended to atomic substitution in an aluminosilicate clay and a new calcium borosilicate.

These results were combined with molecular modeling to build and evaluate structural models that capture the local framework distortions and sometimes profound rearrangements resulting from the atomic substitutions. This reveals remarkable differences between the consequences of the incorporation Al or B in two distinct frameworks of otherwise strongly-related materials, and offers a unique opportunity to understand the properties that drive heteroatom incorporation.

Keywords: solid-state NMR, layered silicates, heteroatoms, active sites, local structure



**CEMHTI – CNRS UPR3079**  
**Conditions extrêmes et Matériaux : Haute Température et Irradiation**  
1D avenue de la Recherche Scientifique  
45 071 Orléans Cedex 2

